Active Vibration Isolation for Controlled Flexible Structures

by

Gary H. Blackwood

S.B. Massachusetts Institute of Technology (1986)
S.M. Massachusetts Institute of Technology (1988)

SUBMITTED TO THE DEPARTMENT OF
AERONAUTICS AND ASTRONAUTICS
IN PARTIAL FULFILLMENT OF THE REQUIREMENTS
FOR THE DEGREE OF
Doctor of Philosophy
at the
Massachusetts Institute of Technology
February, 1994

Signature of Author _____
Department of Aeronautics and Astronautics
October 1, 1993

Certified by _____
Professor Andreas von Flotow
Thesis Committee Chairman, University of Washington

Certified by _____
Professor John Dugundji
Department of Aeronautics and Astronautics

Certified by _____
Professor Nesbitt Hagood IV
Department of Aeronautics and Astronautics

Certified by _____
Professor Michael Athans
Department of Electrical Engineering and Computer Science

Certified by _____
Dr. James Fanson
Jet Propulsion Laboratory, California Institute of Technology

Accepted by _____
Professor Harold Y. Wachman
Chairman, Department Graduate Committee

Active Vibration Isolation for Controlled Flexible Structures

by

Gary H. Blackwood

Submitted to the Department of Aeronautics and Astronautics
on Oct 1, 1993, in Partial Fulfillment of the
Requirements for the Degree of
Doctor of Philosophy

Abstract

The general problem of active vibration isolation for flexible structures is investigated in order to determine the impact of structural flexibility on the performance of passive and active mounts. A mechanical and control design approach is proposed in which compensators are first designed for an active isolator mounted to a rigid base, and then re-implemented with little or no changes when the actuator is later attached to a flexible structure. A general model for an isolator mount is developed and used to characterize the impact of structural flexibility in terms of a dimensionless parameter that is a function of isolated mass, modal damping and modal mass. It is shown that for values of the dimensionless parameter small compared to one, the effect of flexibility on the isolator transfer functions and passive performance can be ignored. For values of the parameter large compared to one, a parametric multiplicative error model is proposed to bound the perturbations to the nominal (rigid base) plant model. Low order dereverberated mobility models, based on a frequency average of complex base or equipment mobility, are proposed as a means to incorporate knowledge of the approximate base structural dynamics into the nominal plant model. The individual effects of mechanical design, passive isolation, and choice of output sensor on the degree of modal decoupling are described.

Three active isolators are constructed for the purpose of reducing structural vibrations at optics mounting locations on the SERC Interferometer Testbed. Open loop tests of the active mount illustrate the advantages of a mechanical design that decouples uncertain base dynamics from the loop transfer function. LQG compensators employing acceleration feedback are implemented stably with the active mount attached to both a rigid test stand and to the flexible testbed. The impact of base flexibility, and the performance limitations of modes within the active mount itself, are quantified. Three simultaneous, independent pathlength control actuators mounted to the same flexible testbed are shown to each provide 12 dB of broadband vibration improvement over 10 to 500 Hz in three laser pathlength outputs. The individual and combined contributions of mechanical redesign, passive vibration

isolation, passive damping and active pathlength control to the improvement of the testbed performance metric are shown. Results of this thesis emphasize the advantages of mechanical design for control in which the open loop plant is conditioned to robustly accept low order, high gain compensation.

Thesis Committee: Dr. Andreas von Flotow
Thesis Committee Chairman
Adjunct Professor of Aeronautics, University of Washington
Dr. John Dugundji
Professor of Aeronautics and Astronautics
Dr. Nesbitt Hagood IV
Assistant Professor of Aeronautics and Astronautics
Dr. Michael Athans
Professor of Electrical Engineering
Dr. James Fanson
Member of the Technical Staff, NASA Jet Propulsion Laboratory

To Myrtle Folsom

Through her love of teaching and of life,
she inspired her students
to wonder, learn and explore

Acknowledgements

I would like to begin by thanking my thesis supervisor Professor Andreas von Flotow for guiding and encouraging me throughout my graduate career. His broad-minded approach to engineering and his penchant for fresh insight have strongly contributed to the work presented in this thesis. To Dr. James Fanson I am deeply grateful for his early guidance in the field of experimental structural control. Dr. Fanson has provided inspiration to me through his meticulous approach to problem solving and by his engineering perspective.

I wish to thank Professor Michael Athans for his well taught course on multivariable control design, and for assisting me in defining the control design problem addressed in this thesis. To Professor Nesbitt Hagood and Professor John Dugundji I am grateful for their help in defining the scope and contributions of this work. I also want to thank Professor Edward Crawley for creating and fostering a truly rewarding research environment at the MIT Space Engineering Research Center.

Several individuals deserve recognition for their direct assistance in the laboratory experiments of this thesis. Carl Blaurock performed initial testing of the active mount and integrated the instrumentation on the testbed. To Ruth Huang, Alfredo Colon and Maya Federman, I am grateful for their skilled assembly of detailed analog circuitry. I also wish to thank Frank Aguirre for his assistance in the laboratory during the past year, and to thank Etienne Balmes for the use of his identification software.

I owe special thanks to Yoshi Hyodo, who as a visiting engineer from the Nissan Motor Corporation, contributed heavily to the design testing of the precision actuator hardware. Finally, Mark Andersson deserves credit for his expert assistance in the formatting and layout of this document.

Contents

List of Figures

List of Tables

Chapter 1

Introduction

1.1 A Controlled Structures Design Framework

The problem of vibration reduction in flexible mechanical systems is encountered in numerous aerospace, industrial and commercial applications: instrument pointing and microgravity processing aboard spacecraft, rider comfort and interior noise in passenger vehicles, machinery isolation within submarines, precision machining operations, and many others. Design solutions – historically using passive means but increasingly employing active control – enable the product, process or system to meet a desired level of performance in the presence of disturbances. Within the aerospace industry the set of analysis and design tools for active and passive control of structural vibration is known as Controlled Structures Technology (CST). The use of CST to enhance or enable the successful mission performance of future spacecraft designs has been the focus of significant research effort for more than a decade. A number of laboratory testbeds [10, 56, 53, 18, 72] and at least one shuttle flight experiment [50] have been dedicated to this topic.

A framework for CST design [10] is shown in Figure 1.1. Subdisciplines are pictorially arranged in relation to the way in which the disturbance enters the structure (input conditioning and isolation), is transmitted (structural design, passive damping), and is modified by active control (high and low authority control, sensor and actuator dynamics, output isolation). It is expected that a layered synthesis of passive

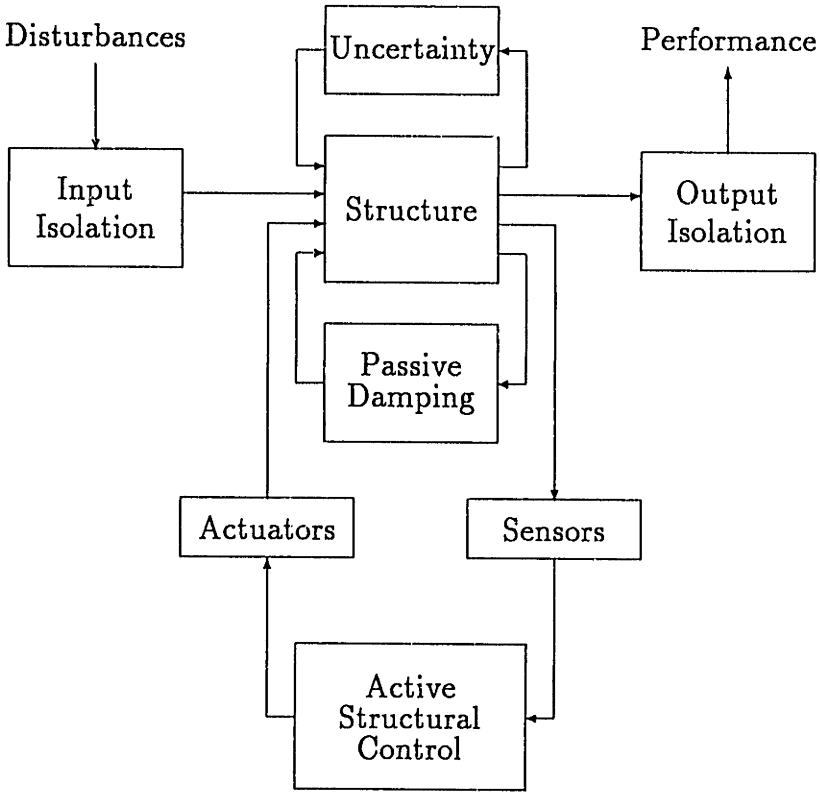

Figure 1.1: Controlled Structures Technology (CST) design framework.

and active control will be required to meet the stringent disturbance environments required for many proposed precision optical spacecraft missions [40]. An alternate representation of the CST design approach is illustrated in Figure 1.2 [72] which emphasizes a layered control approach: isolation of disturbance at its source, structural quieting, and output compensation. The structural quieting layer generally requires a distributed implementation of passive damping and low authority control (LAC), while the isolation layer is fundamentally a local design problem. The third layer in Figure 1.2, output compensation, may consist of either local isolation of sensitive equipment or a global high authority control (HAC) architecture using distributed actuators to control a stated performance metric.

Early research in CST addressed different aspects of the structural quieting layer in Figure 1.2: sensor and actuator design, structural plant modelling, identification, and passive and active damping (or LAC). Structural quieting is accomplished by the

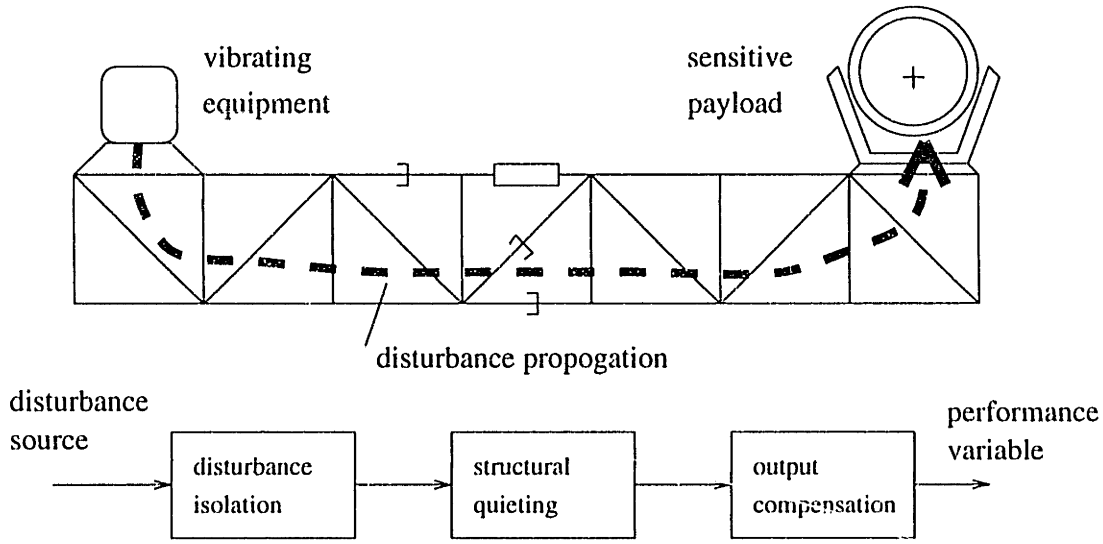

Figure 1.2: Three layer approach to disturbance minimization in structures.

dissipation of vibrational energy within the structure; special hardware such as the passive D-Strut [2] and active piezoelectric struts using collocated force and strain feedback [42] have been developed for truss structures. The performance improvement due to structural quieting is limited, however, and once the base structural resonant peaks have been significantly reduced by active and passive damping, further treatment will yield small increases in performance [5]. To achieve greater disturbance rejection additional high authority control layers are added to the plant to modify the structural frequencies and mode shapes. One option is the use of distributed induced strain actuators for high authority control; this approach has been investigated for beam and plate structures [3, 41] as well as for truss structures [21, 54]. While significant performance improvements have been demonstrated, the resulting HAC control designs have been characterized by high model and compensator order and a high sensitivity to plant uncertainty and plant variations, which has made general application of this approach difficult.

Recently there has been renewed interest in passive and active isolation in controlled structures design, both at the disturbance source (Figure 1.2) and at the output compensation stage. Isolation is attractive because it can be applied directly

at disturbance sources or at critical output locations. In principle, the active isolation open loop plant will be collocated and will be dominated by local mount dynamics, permitting the design of low order compensators that neglect base dynamics. The presence of base resonant flexibility, however, can influence the performance and stability of the active mount and the isolation design must be considered as part of a coupled CST design. Open research questions, to be investigated in this thesis, are: when must active isolation be considered a control-structure interaction (CSI) problem, how does base or equipment modal flexibility influence active isolation design for controlled structures, and how are sensors, actuators and local mechanical design features selected to permit robust implementation of low order, high gain compensation.

1.2 The Isolation Concept

The purpose of mechanical isolation is to attenuate the transmission of disturbances between equipment and a structural foundation by inserting a compliant mount at the interface, as illustrated in Figure 1.3 for a single degree of freedom system. The two classical isolation problems are presented: in Figure 1.3(a), the mount blocks the transmission of base motion from the sensitive equipment; while in Figure 1.3(b), the compliant mount isolates the foundation from forces generated by vibrating equipment. In the simplest idealization, the foundation is assumed to have infinite impedance (compared to the isolator or equipment impedance), and the equipment blocked disturbance force $F_E^b(s)$ and base free disturbance velocity v_B^f are assumed to be prescribed.

One measure of the performance of an isolation mount is the transmissibility of force or displacement across the interface, defined by

$$T(s) = \frac{v_E(s)}{v_B^f(s)} = \frac{F_t(s)}{F_E^b(s)} \tag{1.1}$$

The characteristic transmissibility for a passive isolation system is illustrated qualitatively in Figure 1.4, and represents the case in which the equipment is modelled

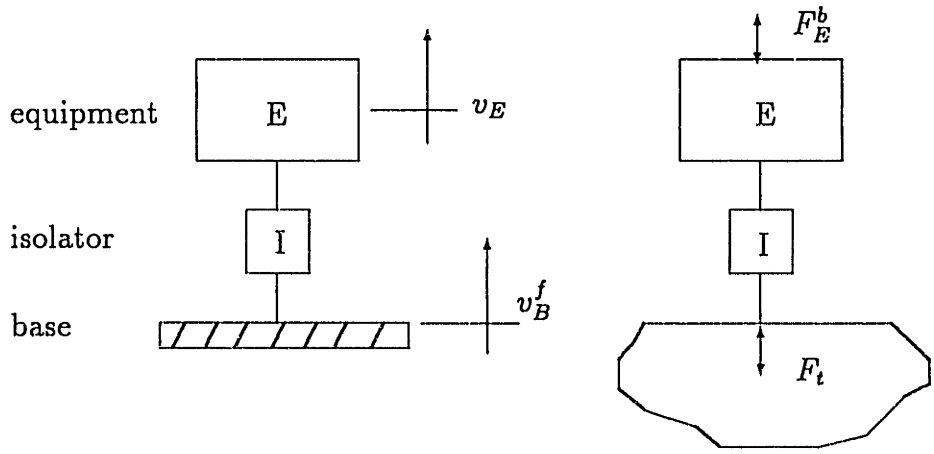

(a) base vibration (b) equipment vibration

Figure 1.3: The two standard disturbance isolation problems: (a) compliant mount I used to isolate base motion v_B^f from sensitive equipment E, and (b) compliant element used to isolate machinery blocked disturbance force F_E^b from foundation.

as a rigid mass and the isolator is modelled as a massless viscously damped spring. The mount attenuates disturbance frequencies above $\sqrt{2}\omega_o$ where ω_o is the mount natural frequency, and amplifies disturbances for all frequencies below $\sqrt{2}\omega_o$. The design tradeoff is to make ω_o low enough to provide low transmissibility at high frequencies, while limiting static deflection and transient dynamic deflections due to impulse disturbances. A second tradeoff involves the level of viscous damping in the isolator interface: damping is required to limit the transmissibility at resonance, yet the presence of isolator damping degrades the performance of the isolator at high frequencies. Harris [31] provides an extensive reference for passive isolation design.

Active control can be used to enhance the transmissibility provided by a passive mount, or to provide a level of isolation when the passive mount is stiff. Sensor measurements such as equipment or base acceleration, interface force or gap are used to command an actuator (represented by blocks labeled "A"), arranged in one of the configurations illustrated in Figure 1.5. Actuators may be electromagnetic, piezoelectric, pneumatic, hydraulic, electromechanical, or other, and will have finite output impedance which governs the load carrying ability at zero power and determines whether the actuator may be considered to command force or displacement. Fig-

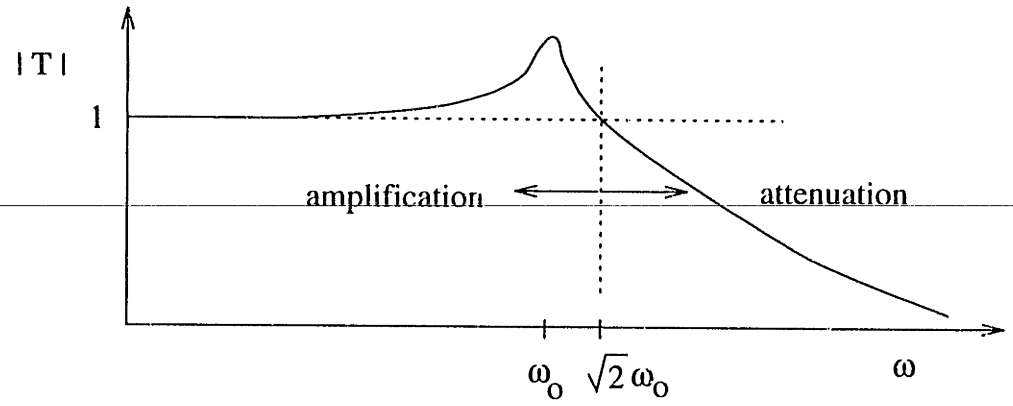

Figure 1.4: Qualitative transmissibility of a passive isolation mount.

ure 1.5(a) is a typical configuration for a force actuator used to soften an already soft passive mount. In Figure 1.5(b), the series passive isolation element may provide isolation for a stiff displacement actuator, or perhaps provide decoupling of the active element reaction force from the base. In both Figure 1.5(a) and Figure 1.5(b), the equipment is used as the reaction mass for the active stage; in Figure 1.5(c) and Figure 1.5(d), a separate mass is used for the reaction force. The two latter instances might be termed *momentum compensation* and *force cancellation* instead of isolation, but the control objective remains the same – to modify the passive transmissibility of disturbances using an active control force applied at or near the mount interface. Examples of each of the cases shown in Figure 1.5 may be found in the literature [82, 15, 79, 78].

Because an active mount is not constrained by the constitutive relations of passive materials, active control permits much greater freedom in the design of mount transmissibility. Figure 1.6 illustrates the qualitative effects of broadband and narrowband control on the closed loop transmissibility. Reasons for using active mounts include the following:

(i) the passive mount natural frequency can be reduced while eliminating static deflection

(ii) addition of inertial damping to reduce resonant transmissibility without degrading high frequency attenuation

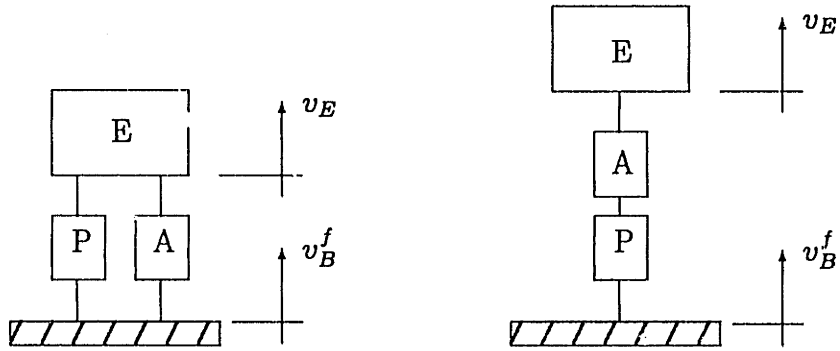

(a) parallel actuation

(b) series actuation

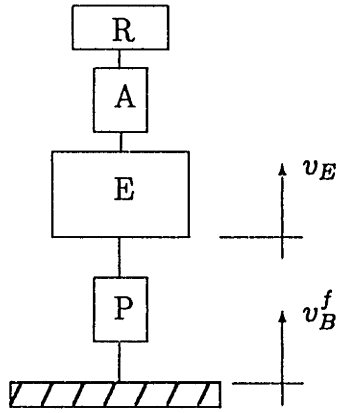

(c) momentum compensation

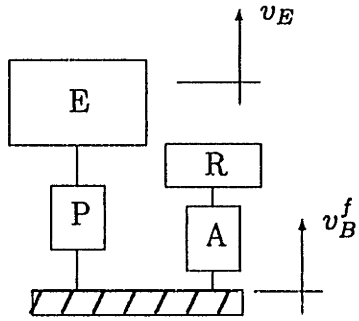

(d) force compensation

Figure 1.5: Four actuator configurations used to modify the passive transmissibility between a vibrating base and sensitive equipment E (with output velocity v_e). P and A represent passive and active elements, while R represents a reaction mass. Configurations (c) and (d) are not typically considered to be isolators, but can be used to modify the passive transmissibility between base motion and output velocity, which is the active isolation problem. These configurations also apply directly to the force isolation problem, in which the equipment is the vibration source and the base is the receiver.

(iii) more flexibility in tailoring frequency dependence of the transmissibility

(iv) ability to create time-varying notches in the transmissibility for narrowband disturbances

(v) possible weight or size improvements.

A number of authors have investigated the effects of feedback on local mount transmissibility [75], [60], [26]. Numerous demonstrations of broadband control can be found in the literature [60], [71], [82], which has been demonstrated to eliminate

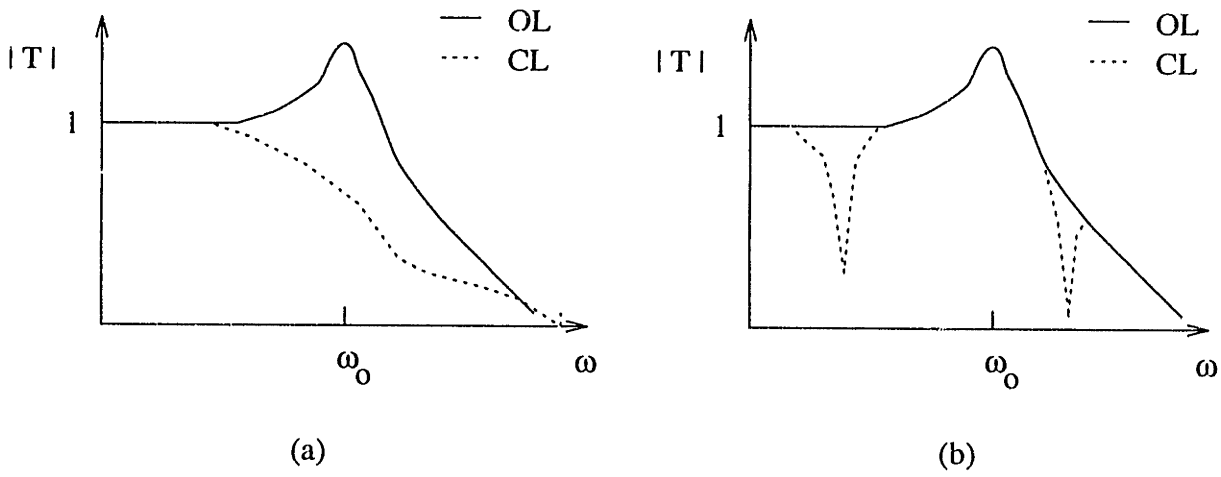

Figure 1.6: Qualitative effects of active control on the isolator transmissibility: (a) broadband and (b) narrowband compensation.

resonant amplification and to reduce the mount natural frequency up to a factor of 25 for single stage systems [80], limited mainly by sensor dynamic range and mount or foundation resonances. The literature in narrowband control is extensive; design approaches using classical, higher harmonic, LMS feedforward, and modern control have been developed; Sievers and von Flotow [67] review and show the equivalence between these narrowband design methods.

1.3 Literature Review

1.3.1 Examples of Isolation for Spacecraft

Passive isolation has been utilized in spacecraft missions where the disturbance environments required by cameras or telescopes are particularly stringent. The three-thousand pound HEAO-B X-ray telescope was isolated from its host spacecraft by four silicone elastomeric mounts [29]. The mounts were designed with 21-35 Hz natural frequency to attenuate shock loadings during handling, provide controlled spacecraft-telescope interface during launch, and to minimize spacecraft induced thermal loading during on-orbit operation. A more well known example is the passive isolation of HST reaction wheel assemblies (RWAs) using viscoelastic fluid dampers [58]. Due to ro-

tational imbalances and bearing imperfections, each RWA would generate multi-axis disturbances up to 0.12 N at numerous harmonics of wheel speed, which could range from zero to 3000 rpm (50 Hz). Each 48-kg RWA was mounted on 3 pairs of isolators which provided a 20 Hz axial corner frequency and 50 percent improvement in telescope jitter, while allowing control torques generated by the RWAs to be passed to the spacecraft. Passive isolation has been considered for a base mounting for space station gimbal systems [84] as well as for low pass filters within high precision payload pointing systems [69].

An active magnetopneumatic mount has been used to isolate a 400 pound missile guidance platform during launch [60] in which the mount had a 5 Hz corner frequency and zero static deflection. Active isolation was proposed [35] for the isolation of attitude control system disturbances from a quiet spacecraft and telescope structure. Most spacecraft applications of active isolation have been for vernier stages or image motion compensation stages of precision pointing systems such as the Annular Suspension and Pointing System and the Instrument Pointing System [37,32]. A multilayer design approach is necessary because main gimbal actuators are low bandwidth (0.5 Hz) and because the gimbal mounts are stiff above this frequency [39,63]. Magnetic isolation mounts [30,25] are typically used to isolate the vernier stage in these applications. Recently interest in micro-g isolation of shuttle and space station payloads has motivated work on ultra-low frequency active isolation using magnetic and piezoelectric bimorph actuators [1,26,73,34,22,68]. Active narrowband momentum compensation and isolation are currently under investigation for the attenuation of disturbances for the Oxford cryogenic cooler which is being considered for numerous remote sensing spacecraft instruments [14,15].

1.3.2 Isolation of Non-Rigid Structures

Flexibility of the base structure, isolated equipment or the isolation mount itself can degrade the performance of passive and active mounts. The transmissibility defined in Eqn. 1.1 will overestimate the performance of a passive isolation mount, and base resonant dynamics will participate in the local plant dynamics leading to a

risk of instability with active control, unless measures are taken to compensate these dynamics in the controller or by mechanical redesign. Base flexibility first became important in the isolation of vibrating machinery from ship hulls and is of current interest for machinery isolation and precision pointing aboard spacecraft.

The concept of passive isolator effectiveness was introduced in the 1950's as a dimensionless measure of vibration reduction defined as the ratio of *unisolated* mount variables (force and velocity) to the *isolated* variables [17]. Sykes [77] used mechanical impedance methods to calculate the effectiveness of isolation of machines (both rigid and flexible) isolated from non-rigid foundations modelled as a general impedance as well as by simple mechanical analogies: spring, mass, damper, and single resonator. The effectiveness of the isolator was found in almost all cases to decrease above the machine-foundation resonance when the foundation exhibited flexibility. Ruzicka and Cavanaugh [59] analyzed the problem of isolation of flexible equipment from a rigid base and compared results to a flexible beam experiment. Swanson, Miller and Norris [76] extended the analysis of Sykes to a multidimensional isolation of flexible structures and used singular values to express bounds on the isolator effectiveness based on the measured impedances of a flexible engine and structural frame.

The active isolation of rigid equipment from a flexible base has been investigated in several recent papers. Watters *et al.* [82] regulated the transmitted force from a machine to a flexible base using an electromagnetic actuator and showed that base dynamics are nearly decoupled from the force measurement, yet base acceleration exhibited strong interaction with base modes, prohibiting simple broadband control design with this sensor. However in an analytical study, Kaplow and Velman [35] used base acceleration effectively for active isolation of machinery vibration, although in this case resonant dynamics occurred well above the passive mount corner frequency. Scribner *et al.* [62] demonstrated isolation of force from a modally rich plate using piezoelectric actuators and found that an active control solution is simplified when the base input mobility has high modal overlap, a function of both damping and relative modal density. Isolation of equipment vibration from the JPL Phase B Testbed using gap feedback was implemented by Spanos *et al.* [72]. Interaction with structural

resonances was minimal due to the high level modal damping (5 percent); resonances internal to the passive flexure within the isolation hardware were found to limit the active isolator performance. A second implementation using force feedback on an undamped structure showed the same type of base flexibility decoupling as in the study by Watters *et al.* In each of these cases, the compensators were designed using plant models based on measurements taken with the isolator already mounted to a flexible structure.

Isolation and positioning of sensitive equipment mounted to flexible bases has also been investigated. Garcia, Sievers and von Flotow [24] experimentally demonstrated the broadband isolation of a lightweight mirror bonded to a multilayer piezoceramic actuator mounted to the tip of a flexible cantilevered beam. They found that the participation of base flexibility in the transfer function from piezoelectric actuator voltage to laser output was governed by the dimensionless parameter

$$\frac{1}{\zeta_b}\frac{m}{\overline{m}_b} \tag{1.2}$$

where m is the mass of the mirror and ζ_b and $\overline{m}_b$ are the damping and modal mass of the base resonance. The result indicates that if the actuated mass is small relative to the modal mass, or if structural damping is large, then the mass can be actively isolated from base motion with little risk of unstable interaction with base modes. In another study, Spanos *et al.* [72] used two layers of output isolation – reactionless piezoelectric actuation and voice coil – as the fine and coarse pathlength control of a lightweight mirror on the JPL Phase B Testbed, achieving a factor of 137 reduction in disturbance level. Base resonances were evident in the voice coil loop; their effects on the loop stability were lessened by the addition of 5 percent damping to the base modes by a structural quieting layer. Lurie *et al.* have also investigated the use of bridge feedback to modify the impedance of a piezoelectric actuator for use as an active isolator [43]. Base flexibility will also interact with the control of gimballed payloads when the gimbal axis is not through the payload center of gravity [57, 69].

The inclusion of a passive isolation stage can reduce the degree to which base flexibility appears in the plant transfer function for active isolation or payload pointing.

Watters *et al.* [82] chose a soft passive mount, in the parallel configuration of Figure 1.5(a), to reduce frequency response variations due to base resonances in the open loop transfer function using transmitted force as the regulated variable. A passive isolation stage in series with an active stage (Figure 1.5(b)) may be used to decouple the foundation dynamics from the plant transfer function above some frequency if the passive stage includes an inertia against which the force actuator can react. Complete decoupling is ideally provided by reactionless linear piezoelectric actuators [72, 48], and reactionless gimbals for payload pointing [38, 9] have been designed and tested.

In each of these applications, the objective of the design is to dynamically decouple the unknown resonant base dynamics from the open loop plant, such that the active isolation or pathlength control is low order and need only account for local mount dynamics, and is relatively insensitive to changes in the base structure. Passive isolation stages, therefore, provide not only open loop disturbance attenuation (add performance) but also can be designed to condition the open loop transfer functions (add robustness) for the active stage by decoupling unknown base dynamics from the more well known local mount dynamics.

The dual performance/robustness roles of passive and active isolation are compared to the familiar performance/robustness roles of passive and active damping in Tables 1.1 and 1.2. Passive damping has a dual role of attenuating disturbance transmission while also adding adding phase lead to lightly damped structural poles, thus adding robustness to low and high authority control loops. Low authority control fulfills a similar role in disturbance rejection and addition of robustness to high authority loops. Active isolation attenuates high frequency structural disturbances and thus limits the required control bandwidth of other global high authority control loops in the CST design architecture.

1.4 Thesis Objectives and Contributions

While passive and active vibration isolation of equipment from rigid foundations has been well developed in the literature, a shortcoming is the treatment of active

Table 1.1: The roles of passive and local control – for both performance and added robustness for active control – are analogous to the performance and stability roles of passive isolation.

Role	Passive Damping	Local Control
Performance	reduce disturbance to performance output	reduce disturbance to performance output
Robustness	add stability margin to LAC and HAC	add stability to HAC

Table 1.2: Passive isolation provides both disturbance attenuation and robustness for local isolation control by decoupling flexible modes from the loop transfer function. Active isolation removes control burden from other (HAC) loops in a CST design.

Role	Passive Isolation	Active Isolation
Performance	reduce disturbance to performance output	reduce disturbance to performance output
Robustness	decouple base flexible modes from active isolation plant model	reduce control authority required for HAC loops in CST design

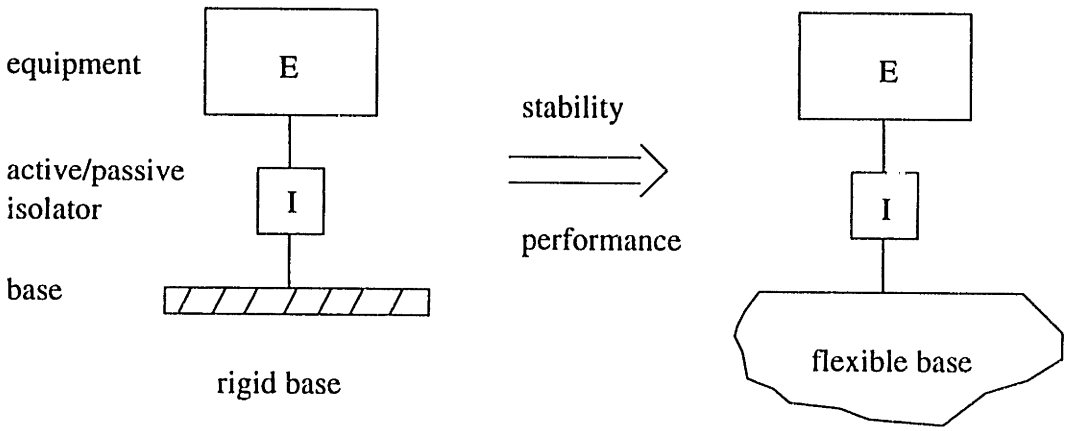

Figure 1.7: The proposed design approach is to design compensators for the active mount based on the rigid base transfer functions, to validate stability and performance on a rigid test stand, and then to implement the active mount (with the same compensator) on a flexible structure.

isolation for flexible structures, for both force and displacement transmissibility. The degradation of performance and degree of coupling with base flexibility has been investigated for passive mounts only (effectiveness concept) and not for active mounts; additionally the issue of stability must be considered for active systems.

Although active isolation for flexible structures has been demonstrated in recent papers [82,72,71], in each case the compensation has been designed using plant models based on *in situ* measurements of the isolated mounted to the flexible structure. Thus, a central research issue is to test and model an active mount first on a rigid test stand, and to develop a controller that will remain stable and provide known performance in the presence of structural flexibility in the foundations to which the mount will later be attached, as illustrated in Figure 1.7. Given this design approach, a natural extension of the research is to determine what information about the base structure could (or should) be added to the rigid based design model to either improve stability or enhance performance.

The plant to be controlled is described by the coupling of two mechanical systems: the local mount (well known and low order) and the base structure (usually of high order, with uncertainty in modal parameters of natural frequency, damping and mode

shapes, particularly at higher frequencies). For a large class of isolation problems, the local mount dynamics dominate the loop transfer function for the active control, and two modelling options are obvious: (1) augmentation of the plant dynamics to account for the poorly known, weakly coupled base flexibility, or (2) the local mount dynamics are chosen as the known model and base dynamics are treated as parametric and unstructured uncertainty in the plant. Parametric uncertainties arise because the base flexibility changes the frequency, damping, or mode shape of the local mount resonances, while unstructured uncertainty arises because base modes add unmodelled dynamics to the true open loop plant. The approach taken in this thesis is to include parametric "backbone" mobility models of the base structure in the isolator plant transfer function, and to treat base resonances as unstructured uncertainty.

Objectives: The objective of this thesis is to first investigate the impact that mechanical flexibility, in the base structure or isolated equipment, has on the performance and stability of active isolation. A second objective is to demonstrate, in analysis and experiment, the importance of mechanical design for an active mount to permit robust implementation of low order, high gain control that is insensitive to the presence of unmodelled modal flexibility in the base structures to which the mount is attached. The experimental objective of this thesis is to demonstrate that an active mount can be first controlled on a rigid test stand, and then installed on a flexible structure with little or no modifications to the compensator.

Contributions: The power of mechanical design for control, as opposed to control design for difficult mechanical systems, is demonstrated in this thesis. In analysis and experiment it is demonstrated how the decoupling inherent in isolation architectures, enhanced by mechanical design of the active mount, permits a control design approach in which base modal flexibility is ignored (within certain limitations) during the design process. Work by Sykes [77] and Ruzicka [59] on passive isolation for flexible structures is extended in two ways: first, a dimensionless coupling parameter is introduced to describe the perturbations due to base and equipment flexibility on the passive isolator

effectiveness; second, frequency averaged mobility models (dereverberated and linear magnitude average) of complex base structures or equipment, are added to improve the accuracy of passive isolator performance using a modified effectiveness function.

The thesis further demonstrates the impact of base and equipment structural flexibility on the active mount transfer functions, for two actuator configurations and a set of sensor outputs. The perturbations in magnitude and phase are characterized in terms of a dimensionless parameter, which can be used for mechanical design to quantify the level of decoupling provided by the mount. A new parametric multiplicative error model based on the coupling parameter is introduced for control design, and dereverberated mobility models of the base or equipment are shown to improve the nominal plant transfer functions. Finally, laboratory experiments on the SERC Interferometer Testbed demonstrate multiple, independent isolation and pathlength control on a flexible structure.

1.5 Thesis Description

A general model for passive isolation is developed in Chapter 2 which allows the study of mechanical flexibility in the base structure or isolated equipment, using four-pole mobility methods. It is shown how the mount *passive sensitivity* function (the inverse of the mount effectiveness) is most useful for characterizing mount performance. Several examples are shown that illustrate the impact of base and equipment flexibility on this function, parameterized by the dimensionless coupling parameter. A new method using averaged mobility models of the base structure is shown to improve the models of mount passive sensitivity when an isolator is mounted to base structure with high modal content.

In Chapter 3 the dimensionless coupling parameter is used to characterize the effects of structural flexibility on the magnitude and phase of the local mount transfer functions. The general mobility analysis reveals a great deal of similarity between the effects of base and equipment flexibility, leading to simplifications in the presentation

and in development of a simple multiplicative error model. Both parallel and series actuation configurations are studied.

The SERC Interferometer Testbed is described in Chapter 4, and the testbed performance metric is motivated by the requirements of proposed orbiting observatories. Measurements of the tested performance metric are shown, and a modal test of the test block demonstrates that it is effectively rigid for the purpose of the isolator component tests.

Chapter 5 presents the design and open loop tests of three hardmount and softmount actuators used for active isolation and pathlength control. Transfer functions of the actuators, measured both on the rigid test block and on the testbed, illustrate the advantages of softmount or reactionless mechanical design, for both individual and multiple isolator control.

Control designs for acceleration feedback and pathlength control are presented for the three active mounts in Chapter 6. LQG design methods are used to design compensators for isolator plant models derived from rigid test block measurements. The compensators are implemented stably on the actuator, mounted first to the test block, and then to the testbed with little or no modifications to the compensators. Pathlength control using three independent mounts demonstrates a dramatic improvement in the testbed performance metric. A summary of the thesis results and a discussion of the contributions is provided in Chapter 7.

Chapter 2

Passive Isolation

2.1 Objectives

The objective of this chapter is to develop a general model for passive mechanical isolation, which can be used to investigate the effect that modal flexibility – in the base structure or isolated equipment – has on mount transmissibility and passive sensitivity. Frequency domain analysis based on a four-pole mobility representation is used to develop equations of motion and to determine dimensionless parameters governing isolator performance and the impact of flexibility. State space methods are then introduced for numerical simulations of isolation. Finally, it is shown how frequency averaged mobility models of complex base dynamics can provide simple yet accurate models of mount passive sensitivity when isolators are mounted to flexible base structures.

2.2 Review of Mobility Analysis Methods

This section presents, in a consistent notation, mechanical mobility and impedance, concepts used throughout this thesis. Frequency domain analysis is useful for providing insight for low order problems, which can then easily be extended to more complex structures. Within the frequency domain framework, a mobility representation is preferred to that of impedance because of the similarity between mobility

and the form of plant transfer functions used for control design. In particular, this section presents mobility concepts using four-pole mobility methods [51], a method that facilitates the derivation of system equations and aids in their interpretation.

Basic Definitions: Figure 2.1 illustrates a free body diagram of a linear mechanical system that is acted upon by two sinusoidal forces at points i and j. Consider first the case in which only $f_i(t)$ acts on the system and represent that force by a magnitude and phase

$$f_i(t) = |f_i|\, e^{j\omega t} \tag{2.1}$$

The velocity at point i (in the same direction as f_i) at the driving frequency is

$$\begin{aligned} v_i(t) &= |v_i|\, e^{j(\omega t+\phi)} \\ &= |v_i|\, e^{j\phi} e^{j\omega t} \end{aligned} \tag{2.2}$$

Velocity v_i, displacement $x_i = v_i/j\omega$ and acceleration $\ddot{x}_i = j\omega v_i$ all occur with fixed phase relative to the driving force. Let $f_i(s)$ and $v_i(s)$ be the Laplace transforms of the force and velocity. Mechanical impedance is defined as the ratio of the driving force to the resulting velocity of the system; when the force and velocity are collocated this ratio is termed the mechanical *driving point impedance* or simply the *point impedance*

$$Z_{ii}(s) = \frac{f_i(s)}{v_i(s)} \tag{2.3}$$

where $s = j\omega$. The mechanical *driving point mobility*, or *point mobility*, is defined by the ratio of velocity to the collocated force

$$Y_{ii}(s) = \frac{v_i(s)}{f_i(s)} \tag{2.4}$$

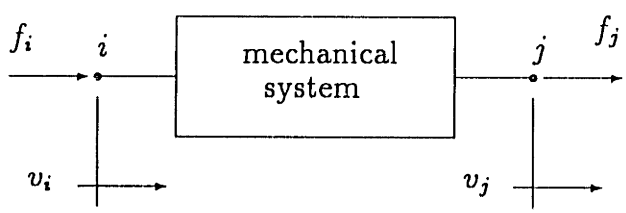

Figure 2.1: General passive linear mechanical free body diagram. Forces f_i and f_j act on the system.

Similarly, the mechanical *transfer mobility* is defined by the ratio of the noncollocated velocity $v_j(s)$ to the force $f_i(s)$

$$Y_{ji}(s) = \frac{v_j(s)}{f_i(s)} \tag{2.5}$$

In matrix notation the mobility matrix $\mathbf{Y}$ relates the two velocities and forces

$$\begin{bmatrix} v_i \\ v_j \end{bmatrix} = \begin{bmatrix} Y_{ii} & Y_{ij} \\ Y_{ji} & Y_{jj} \end{bmatrix} \begin{bmatrix} f_i \\ f_j \end{bmatrix} \tag{2.6}$$

Dependence on the Laplace variable s is suppressed below for brevity. A passive linear system exhibits reciprocity which implies that $Y_{ij} = Y_{ji}$. A thorough treatment of mechanical impedance and mobility, including representations for many lumped parameter models and rules for assembling system equations, can be found in references by Hixson [33] and Crandall [16].

Four-Pole Mobility Method: The four-pole representation of mechanical mobility [51] applies to systems with two identifiable connection points. Here the most general framework is introduced, followed by four simple examples. Figure 2.2 illustrates the four-pole conventions for the same mechanical system shown in Figure 2.1. F_i is a force which acts *upon* the system at input point i, and F_j is the force exerted *by* the system at output point j on an external load; the reaction force on the system is $-F_j$. Comparison with Figure 2.1, in which both f_i and f_j act *on* the system, yields

$$\begin{aligned} F_i &= f_i \\ F_j &= -f_j \end{aligned} \tag{2.7}$$

With these definitions the mobility matrix of Eq. 2.6 can be rearranged to the input-output form known as the four-pole representation:

$$\begin{aligned} \begin{bmatrix} F_i \\ v_i \end{bmatrix} &= \begin{bmatrix} \dfrac{Y_{jj}}{Y_{ji}} & \dfrac{1}{Y_{ji}} \\ \dfrac{Y_{ii}Y_{jj} - Y_{ij}Y_{ji}}{Y_{ji}} & \dfrac{Y_{ii}}{Y_{ji}} \end{bmatrix} \begin{bmatrix} F_j \\ v_j \end{bmatrix} \\ &= \begin{bmatrix} \alpha_{11} & \alpha_{12} \\ \alpha_{21} & \alpha_{22} \end{bmatrix} \begin{bmatrix} F_j \\ v_j \end{bmatrix} = \alpha \begin{bmatrix} F_j \\ v_j \end{bmatrix} \end{aligned} \tag{2.8}$$

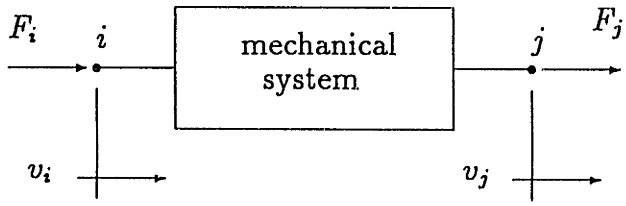

Figure 2.2: Conventions for four-pole mobility representation. Force F_i acts on the system, and F_j is the force exerted *by* the system.

For all passive linear systems $\det(\alpha) = 1$ since $Y_{ij} = Y_{ji}$, which can be checked by Eq. 2.8. Using the notation of Ruzicka [59], the four-pole parameters α_{kl} can be expressed in terms of the system velocity transmissibility $(T_v)_{ji}^{jf}$ and free transfer mobility $(Y)_{ij}^{jf}$ when station j is free ($F_j = 0$), defined by

$$\alpha_{12} = \left.\frac{F_i}{v_j}\right|_{F_j=0} = \frac{1}{(Y)_{ij}^{jf}} \tag{2.9}$$

$$\alpha_{22} = \left.\frac{v_i}{v_j}\right|_{F_j=0} = \frac{1}{(T_v)_{ij}^{jf}} \tag{2.10}$$

and in terms of the system force transmissibility $(T_F)_{ji}^{jb}$ and blocked transfer mobility $(Y)_{ij}^{jb}$ when station j is blocked ($v_j = 0$), defined by

$$\alpha_{11} = \left.\frac{F_i}{F_j}\right|_{v_j=0} = \frac{1}{(T_F)_{ij}^{jb}} \tag{2.11}$$

$$\alpha_{21} = \left.\frac{v_i}{F_j}\right|_{v_j=0} = (Y)_{ij}^{jb} \tag{2.12}$$

Based on the reciprocity theorem [27] the transfer mobilities between points i and j are the same in both directions, so the order of the subscripts in the blocked and free transfer mobilities does not matter:

$$(Y)_{ij}^{jb} = (Y)_{ji}^{ib} = Y_{ij}^{b} \tag{2.13}$$

$$(Y)_{ij}^{jf} = (Y)_{ji}^{if} = Y_{ij}^{f} \tag{2.14}$$

According to the transmissibility theorem [77] the velocity and force transmissibilities in opposite directions across the mechanical element are identical

$$(T_v)_{ji}^{if} = (T_F)_{ij}^{jb} \tag{2.15}$$

therefore the parameter α_{11} can be expressed as

$$\alpha_{11} = \frac{1}{(T_F)_{ij}} = \frac{1}{(T_v)_{ji}} \tag{2.16}$$

where in Eq. 2.16 it is assumed in the definition of force transmissibility that station j is blocked, and in the definition of velocity transmissibility that station i is free. In general $(T_v)_{ij}$ does not equal $1/(T_v)_{ji}$. Using the notation of Eqs. 2.11 to 2.16, the four-pole representation of Eq. 2.8 becomes simply

$$\begin{bmatrix} F_i \\ v_i \end{bmatrix} = \begin{bmatrix} \dfrac{1}{(T_v)_{ji}} & \dfrac{1}{Y_{ij}^f} \\ Y_{ij}^b & \dfrac{1}{(T_v)_{ij}} \end{bmatrix} \begin{bmatrix} F_j \\ v_j \end{bmatrix} \tag{2.17}$$

The four-pole matrices for four simple examples are shown below.

mass: A rigid mass exhibits no flexibility between points i and j so $v_i = v_j$. The constitutive relation $F_i - F_j = msv_i$ expressed in four-pole representation is

$$\begin{bmatrix} F_i \\ v_i \end{bmatrix} = \begin{bmatrix} 1 & ms \\ 0 & 1 \end{bmatrix} \begin{bmatrix} F_j \\ v_j \end{bmatrix} \tag{2.18}$$

spring: A massless spring has unity transmissibility of force $F_i = F_j$ and the constitutive equation $k(v_i - v_j)/s = F_i$. The four-pole form is

$$\begin{bmatrix} F_i \\ v_i \end{bmatrix} = \begin{bmatrix} 1 & 0 \\ \dfrac{s}{k} & 1 \end{bmatrix} \begin{bmatrix} F_j \\ v_j \end{bmatrix} \tag{2.19}$$

damper: Similarly for a massless damper, $F_i = F_j$ and the constitutive equation $c(v_i - v_j) = F_i$ expressed in four-pole form is

$$\begin{bmatrix} F_i \\ v_i \end{bmatrix} = \begin{bmatrix} 1 & 0 \\ \dfrac{1}{c} & 1 \end{bmatrix} \begin{bmatrix} F_j \\ v_j \end{bmatrix} \tag{2.20}$$

spring and damper in parallel: Applying the rule for four-pole elements in parallel [51] to Eqs. 2.19 and 2.20 the four-pole matrix becomes

$$\begin{bmatrix} F_i \\ v_i \end{bmatrix} = \begin{bmatrix} 1 & 0 \\ \dfrac{s}{k+sc} & 1 \end{bmatrix} \begin{bmatrix} F_j \\ v_j \end{bmatrix} \tag{2.21}$$

The four-pole representation of 2.17 is in a convenient form for symbolic manipulation, although in some instances an alternate representation for α_{11} and α_{22} is required. Using the notation of Ruzicka [59], the point mobilities of Eq. 2.4 are expressed as

$$Y_{ii} = \left.\frac{v_i}{f_i}\right|_{f_j=0} = \left.\frac{v_i}{F_i}\right|_{F_j=0} = Y_i^{jf} \qquad (j \text{ free}) \tag{2.22}$$

$$Y_{jj} = \left.\frac{v_j}{f_j}\right|_{f_i=0} = -\left.\frac{v_j}{F_j}\right|_{F_i=0} = Y_j^{if} \qquad (i \text{ free}) \tag{2.23}$$

The point mobility Y_{ii} is often referred to as the system *input* mobility, and Y_{jj} as the system *output* mobility. Comparison of Eqs. 2.8 and 2.17, along with the notation of Eqs. 2.22 and 2.23, leads to the following representation of the α_{11} and α_{22} four-pole parameters:

$$\alpha_{11} = \frac{1}{(T_v)_{ji}} = \frac{Y_{jj}}{Y_{ji}} = \frac{Y_j^{if}}{Y_{ij}^f} \tag{2.24}$$

$$\alpha_{22} = \frac{1}{(T_v)_{ij}} = \frac{Y_i}{Y_{ji}} = \frac{Y_{ii}^{jf}}{Y_{ij}^f} \tag{2.25}$$

Vibration Source Modelling: Figure 2.3 illustrates a vibration source modelled as a mechanical system with output (point) mobility denoted simply as Y_S, which when connected to an external system, exerts a force F_j on that system with velocity v_j at the interface. The output force and velocity are related by the equation

$$F_j = F_S^b - \frac{1}{Y_S} v_j \tag{2.26}$$

where F_S^b is defined as the *blocked force*, or that force exerted by the source on an infinitely rigid external system ($v_j = 0$). When point j is not connected to a load, $F_j = 0$ and the velocity v_j from Eq. 2.26 becomes the free velocity v_S^f of the vibration source

$$v_S^f = Y_S F_S^b \tag{2.27}$$

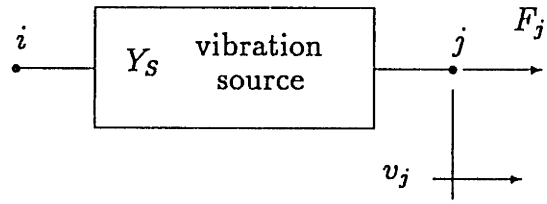

Figure 2.3: Vibration source model. The output mobility of the source at terminal j is Y_S. The boundary conditions on input terminal i may be unspecified as long as Y_S is known.

In matrix form Eq. 2.26 becomes

$$F_S^b = \begin{bmatrix} 1 & \frac{1}{Y_S} \end{bmatrix} \begin{bmatrix} F_j \\ v_j \end{bmatrix} \tag{2.28}$$

or

$$v_S^f = \begin{bmatrix} Y_S & 1 \end{bmatrix} \begin{bmatrix} F_j \\ v_j \end{bmatrix} \tag{2.29}$$

Model of Force Actuator: A force actuator can be modelled using four-pole methods as illustrated in Figure 2.4, in which the actuator is represented by a passive actuator mobility in parallel with a commanded force pair f_a. The four-pole matrix for the passive component of the actuator is

$$\begin{bmatrix} F_i \\ v_i \end{bmatrix} = \begin{bmatrix} \frac{1}{(T_v)_{ji}} & \frac{1}{Y_{ij}^f} \\ Y_{ij}^b & \frac{1}{(T_v)_{ij}} \end{bmatrix} \begin{bmatrix} F_j \\ v_j \end{bmatrix} \tag{2.30}$$

Using velocity continuity $v_i' = v_i$ and $v_j' = v_j$, and force equilibrium

$$F_i = F_i' - f_a \tag{2.31}$$

$$F_j = F_j' - f_a \tag{2.32}$$

the four-pole representation of the actuator with both active and passive elements included is expressed as

$$\begin{bmatrix} F_i' \\ v_i' \end{bmatrix} = \begin{bmatrix} \frac{1}{(T_v)_{ji}} & \frac{1}{Y_{ij}^f} \\ Y_{ij}^b & \frac{1}{(T_v)_{ij}} \end{bmatrix} \begin{bmatrix} F_j' \\ v_j' \end{bmatrix} + \begin{bmatrix} 1 - \frac{1}{(T_v)_{ji}} \\ -Y_{ij}^b \end{bmatrix} f_a \tag{2.33}$$

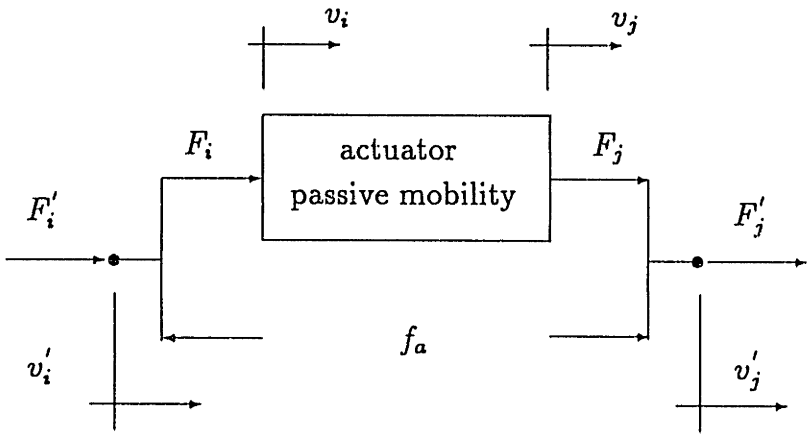

Figure 2.4: General actuator model, useful for describing either force or induced strain actuation.

Eq. 2.33 can be used to represent both force and displacement actuators.

For the special case in which the passive actuator mobility is that of a massless spring, the blocked transfer mobility $Y_{ij}^b = s/k$, the free transfer mobility $Y_{ij}^f = \infty$, and $1/(T_v)_{ji} = 1/(T_v)_{ij} = 1$. Substitution into Eq. 2.33 yields

$$F_i = F_j = F \tag{2.34}$$

$$(v_i - v_j) = \frac{s}{k}(F - f_a) \tag{2.35}$$

Eq. 2.35 indicates that when one or both ends of the actuator are free (or when the mobility of the external system is very large compared to that of the actuator), $F = 0$ and $(v_i - v_j) = -sf_a/k$, or

$$(x_i - x_j) = \frac{f_a}{k} \qquad \text{(free displacement)} \tag{2.36}$$

In this instance the actuator is considered to be a displacement actuator. Conversely, when both junctions of the actuator are attached to external systems of zero mobility (or when the mobility of the external system is very small compared to that of the actuator), $v_1 = v_2 = 0$ and the actuator generates the blocked force

$$F = f_a \qquad \text{(blocked force)} \tag{2.37}$$

In this case the actuator is considered to be a force actuator.

2.3 General Model for Passive Isolation

In this section four-pole mobility methods are used to derive functions that describe the performance of a general passive isolation mount, in particular the functions of mount transmissibility and mount passive sensitivity. A sufficiently general model is developed to investigate how the classical isolation model – based on the assumptions of rigid base, rigid equipment mass, and ideal massless isolator – is affected by mechanical flexibility in the base or isolated mass. This analysis approach helps in identifying connections between different isolation problems, leading to simplifications that will be used throughout the thesis. This section follows the work of Sykes [77] and Ruzicka and Cavenaugh [59] in the derivation of mount passive sensitivity, but is cast in terms of component mobility (instead of impedance) and further explores the dimensionless parameters governing the effects of modal flexibility. Importantly, this section is used for comparison with the models of active isolation mounts developed in Chapter 3.

2.3.1 Mount Transmissibility

Transmissibility of Velocity (Vibrating Base): Figure 2.5 illustrates the general velocity isolation problem. Equipment E is to be mounted to a moving base B that exhibits a free velocity v_B^f; the base free velocity is measured at the mounting location before the equipment or isolator is attached. An isolator I is a mechanical element placed between the equipment and base to attenuate the disturbance velocity that is transmitted to the equipment. The transmissibility function T_{v_3} for the velocity isolation problem is defined as the ratio of velocity at the equipment output terminal 3 to the free velocity of the foundation:

$$T_{v_3}(s) = \frac{v_3(s)}{v_B^f(s)} \tag{2.38}$$

Only when the base structure is rigid does the velocity v_1 of the coupled structure equal v_B^f; otherwise, these velocities are different.

Four-pole mobility methods are used to determine the velocity transmissibility from the base disturbance to the equipment output point 3. No assumptions (other

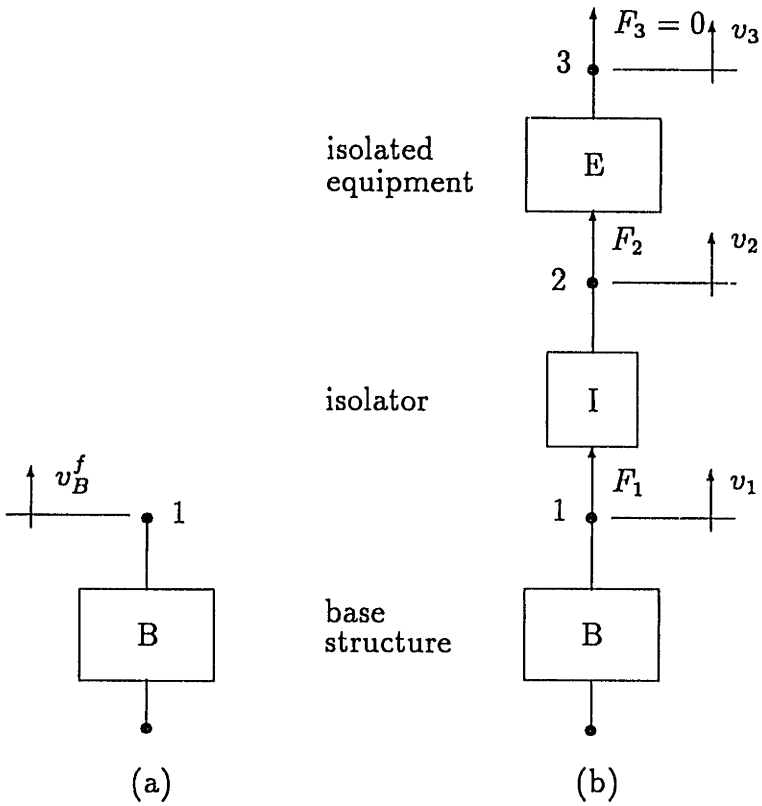

Figure 2.5: The general velocity isolation problem. The unloaded base B exhibits a free velocity v_B^f, which is equal to the loaded velocity v_1 when the base is rigid.

than the connectivity shown in Figure 2.5) have been placed on the mobility properties of E, I and B. Using notation developed in the previous section, and suppressing dependence on the Laplace variable s for brevity, the general four-pole matrix for the equipment illustrated in Figure 2.6(a) is expressed as

$$\begin{bmatrix} F_2 \\ v_2 \end{bmatrix} = \begin{bmatrix} \dfrac{1}{(T_v)_{32}} & \dfrac{1}{Y_{23}^f} \\ Y_{23}^b & \dfrac{1}{(T_v)_{23}} \end{bmatrix} \begin{bmatrix} F_3 \\ v_3 \end{bmatrix} \tag{2.39}$$

In the velocity isolation problem, the output terminal 3 is assumed to be free, therefore $F_3 = 0$ and Eq. 2.39 becomes

$$\begin{bmatrix} F_2 \\ v_2 \end{bmatrix} = \begin{bmatrix} \dfrac{1}{Y_{23}^f} \\ \dfrac{1}{(T_v)_{23}} \end{bmatrix} v_3 \tag{2.40}$$

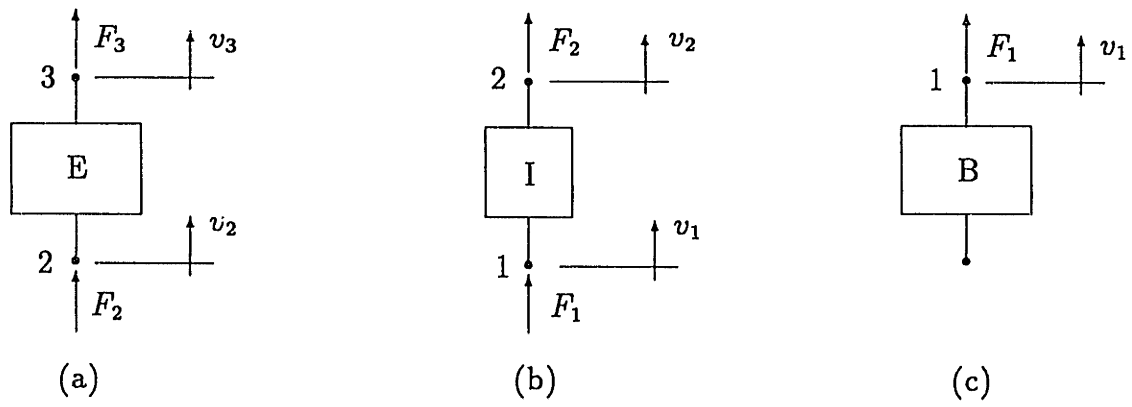

Figure 2.6: Four-pole models of system components.

The passive isolator in Figure 2.6(b) is represented by

$$\begin{bmatrix} F_1 \\ v_1 \end{bmatrix} = \begin{bmatrix} \dfrac{1}{(T_v)_{21}} & \dfrac{1}{Y_{12}^f} \\ Y_{12}^b & \dfrac{1}{(T_v)_{12}} \end{bmatrix} \begin{bmatrix} F_2 \\ v_2 \end{bmatrix} \tag{2.41}$$

The base structure in Figure 2.6(c) is modelled as a velocity disturbance source in accordance with Eq. 2.29

$$v_B^f = \begin{bmatrix} Y_B & 1 \end{bmatrix} \begin{bmatrix} F_1 \\ v_1 \end{bmatrix} \tag{2.42}$$

The velocity v_1 at terminal 1 only equals v_B^f when the base is rigid ($Y_B = 0$) or when terminal 1 is free ($F_1 = 0$). The coupled system equations are obtained by applying the rule for four-pole systems arranged in series [51] to Eqs. 2.40, 2.41, and 2.42:

$$v_B^f = \begin{bmatrix} Y_B & 1 \end{bmatrix} \begin{bmatrix} \dfrac{1}{(T_v)_{21}} & \dfrac{1}{Y_{12}^f} \\ Y_{12}^b & \dfrac{1}{(T_v)_{12}} \end{bmatrix} \begin{bmatrix} \dfrac{1}{Y_{23}^f} \\ \dfrac{1}{(T_v)_{23}} \end{bmatrix} v_3 \tag{2.43}$$

which upon expansion leads to the velocity transmissibility function T_{v_3}

$$T_{v_3}(s) = \frac{v_3}{v_B^f} = \frac{1}{\dfrac{1}{(T_v)_{12}(T_v)_{23}} + \dfrac{Y_{12}^b}{Y_{23}^f} + Y_B\left(\dfrac{1}{(T_v)_{21}Y_{23}^f} + \dfrac{1}{(T_v)_{23}Y_{12}^f}\right)} \tag{2.44}$$

The expression is simplified by multiplying the numerator and denominator by $(T_v)_{23}$ and applying Eq. 2.25

$$(T_v)_{23} = \frac{Y_{23}^f}{Y_2^{3f}} \tag{2.45}$$

where $Y_2^{3f} = Y_E$ is simply the input mobility of the equipment at terminal 2 when terminal 3 is free ($F_3 = 0$). With these simplifications Eq. 2.44 becomes

$$T_{v_3}(s) = \frac{v_3}{v_B^f} = \frac{(T_v)_{23}}{\frac{1}{(T_v)_{12}} + \frac{Y_{12}^b}{Y_E} + Y_B\left(\frac{1}{(T_v)_{21}Y_E} + \frac{1}{Y_{12}^f}\right)} \tag{2.46}$$

where

Y_E = the input mobility of the equipment at terminal 2; the ratio of velocity at terminal 2 due to force F_2 applied to the equipment

Y_B = the output mobility of the base structure at terminal 1; the ratio of velocity at terminal 1 due to $f_1 = -F_1$ applied to the base

Y_{12}^b = the isolator point mobility at terminal 1 when terminal 2 is blocked

Y_{12}^f = the isolator point mobility at terminal 1 when terminal 2 is free

$(T_v)_{12}$ = the velocity transmissibility across the isolator; the ratio of velocity at terminal 2 due to imposed velocity at terminal 1 with terminal 2 free

$(T_v)_{21}$ = the velocity transmissibility in the opposite direction across the isolator; the ratio of the velocity at terminal 1 due to an imposed velocity at terminal 2 with terminal 1 free

$(T_v)_{23}$ = the velocity transmissibility across the equipment; the ratio of velocity at terminal 3 due to imposed velocity at terminal 2 with terminal 3 free.

If only the velocity transmissibility to the input terminal 2 of the equipment is desired, terminals 2 and 3 in Figure 2.6 are allowed to coincide. In this case $(T_v)_{23} = 1$ and the transmissibility of Eq. 2.44 becomes

$$T_{v_2}(s) = \frac{v_2}{v_B^f} = \frac{1}{\frac{1}{(T_v)_{12}} + \frac{Y_{12}^b}{Y_E} + Y_B\left(\frac{1}{(T_v)_{21}Y_E} + \frac{1}{Y_{12}^f}\right)} \tag{2.47}$$

Eq. 2.47 differs from Eq. 2.46 only by the factor $(T_v)_{23}$.

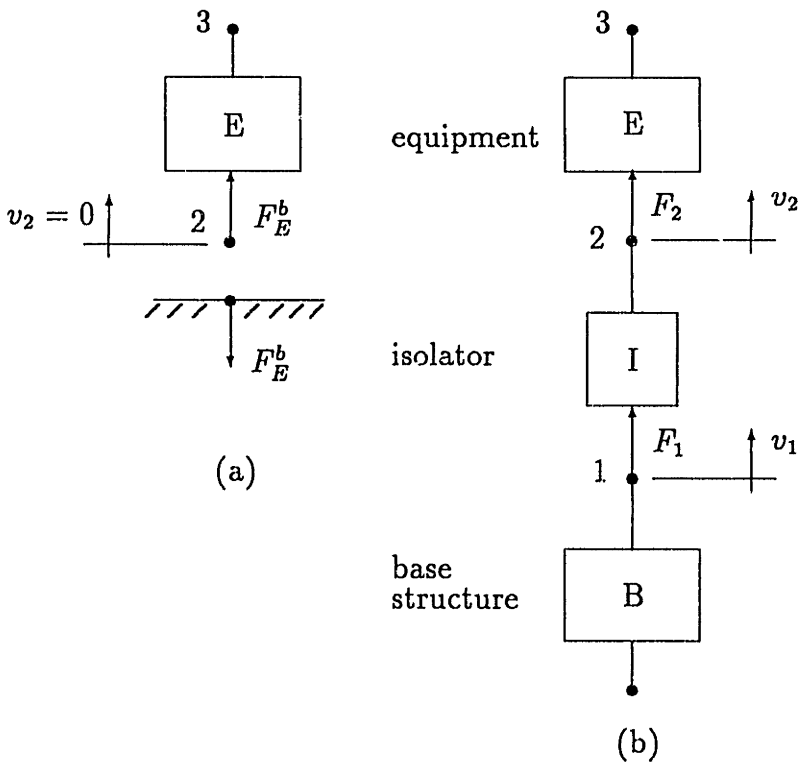

Figure 2.7: The general force isolation problem. Terminal 3 is assumed to be free ($F_3 = 0$).

Transmissibility of Force (Due to Vibrating Equipment): The similarity between the velocity isolation problem and the force isolation problem illustrated in Figure 2.7 is now shown. In the force isolation problem, vibrating equipment E generates a blocked force F_E^b, measured by the force transmitted to a rigid base when the equipment input terminal 2 is blocked ($v_2 = 0$), as shown in Figure 2.7(a). An isolator is used to attenuate the force F_1 transmitted to a base structure, which may be rigid or flexible. The equipment output terminal 3 is assumed to be free.

The transmissibility function T_F for the force isolation problem is defined as the ratio of force F_1 at the base interface to the blocked force generated by the vibrating equipment:

$$T_F(s) = \frac{F_1(s)}{F_E^b(s)} \tag{2.48}$$

Unlike the definition of component force transmissibility in Eq. 2.11, in Eq. 2.48 it is not assumed that force F_1 is measured at the input to a rigid base.

The source model for the vibrating equipment is slightly different from that of

vibrating base model because the blocked force F_E^b is measured at the input terminal to the equipment (Figure 2.7(a)), instead of at the output terminal (Figure 2.5(a)). The point mobility (input mobility) of the nonvibrating equipment at terminal 2 is $Y_E = v_2/F_2$. The relationship between the force F_2 and velocity v_2 when the vibrating equipment is connected to any external system at terminal 2 is expressed as

$$F_2 = F_E^b + \frac{1}{Y_E} v_2 \tag{2.49}$$

or

$$F_E^b = \begin{bmatrix} 1 & -\frac{1}{Y_E} \end{bmatrix} \begin{bmatrix} F_2 \\ v_2 \end{bmatrix} \tag{2.50}$$

When terminal 2 is blocked, $v_2 = 0$ and $F_2 = F_E^b$. If terminal 2 is free, $F_2 = 0$ and the equipment has free velocity $v_2^f = -Y_E F_E^b$.

To assemble the four-pole equations for the force isolation problem, the inverse of the four-pole matrix is required. Since $\det(\alpha) = 1$ for all passive linear systems, the inverse is easily found to be

$$\begin{bmatrix} F_j \\ v_j \end{bmatrix} = \begin{bmatrix} \frac{1}{(T_v)_{ij}} & -\frac{1}{Y_{ij}^f} \\ -Y_{ij}^b & \frac{1}{(T_v)_{ji}} \end{bmatrix} \begin{bmatrix} F_i \\ v_i \end{bmatrix} \tag{2.51}$$

The inverse four-pole matrix for the passive isolator in Figure 2.6(b) is therefore

$$\begin{bmatrix} F_2 \\ v_2 \end{bmatrix} = \begin{bmatrix} \frac{1}{(T_v)_{12}} & -\frac{1}{Y_{12}^f} \\ -Y_{12}^b & \frac{1}{(T_v)_{21}} \end{bmatrix} \begin{bmatrix} F_1 \\ v_1 \end{bmatrix} \tag{2.52}$$

The mobility of the base Y_B relates the force F_1, exerted by the base on an external system, to the velocity of the interface at point 1 in Figure 2.6(c)

$$v_1 = -Y_B F_1 \tag{2.53}$$

Eqs. 2.50, 2.52 and 2.53 are assembled to express the force transmissibility T_F

$$F_E^b = \begin{bmatrix} 1 & -\frac{1}{Y_E} \end{bmatrix} \begin{bmatrix} \frac{1}{(T_v)_{12}} & -\frac{1}{Y_{12}^f} \\ -Y_{12}^b & \frac{1}{(T_v)_{21}} \end{bmatrix} \begin{bmatrix} 1 \\ -Y_B \end{bmatrix} F_1 \tag{2.54}$$

$$T_F(s) = \frac{F_1}{F_E^b} = \frac{1}{\frac{1}{(T_v)_{12}} + \frac{Y_{12}^b}{Y_E} + Y_B\left(\frac{1}{(T_v)_{21}Y_E} + \frac{1}{Y_{12}^f}\right)} \tag{2.55}$$

A comparison of Eq. 2.55 to Eq. 2.47 leads to the conclusion

$$T_{v_2}(s) = T_F(s) \tag{2.56}$$

The presence of flexibility in the base, isolator or equipment does not affect this result, since these effects are captured by the general four-pole mobility representation. However, when the output terminal of the equipment is not collocated with the interface point to the isolator, then the velocity transmissibility T_{v_3} differs from the force transmissibility T_F by the factor $(T_v)_{23}$, representing the equipment velocity transmissibility between terminals 2 and 3.

2.3.2 Mount Passive Sensitivity

Passive Sensitivity (For a Vibrating Base): Alternate measures of isolator performance are the mount passive effectiveness $\mathcal{E}(s)$ [77] and its inverse function the mount passive sensitivity $\mathcal{P}(s)$, defined below, which relate the velocity of the isolated equipment to the equipment velocity when hardmounted to the base. The effectiveness concept is most easily understood by example, as illustrated for the general velocity isolation problem in Figure 2.8. As before, the base structure, with output mobility Y_B, produces a free disturbance velocity v_B^f in Figure 2.8(a). When the equipment is rigidly mounted to the base in Figure 2.8(b), the resulting velocity of the (unisolated) equipment at terminal 3 is denoted by $v_3^{(u)}$. An isolator, installed between equipment and base in Figure 2.8(c), produces the (isolated) equipment velocity $v_3^{(i)}$. The mount effectiveness $\mathcal{E}_{v_3}$ is defined as the ratio of the *unisolated* velocity to the *isolated* velocity at terminal 3

$$\mathcal{E}_{v_3}(s) = \frac{v_3^{(u)}(s)}{v_3^{(i)}(s)} \tag{2.57}$$

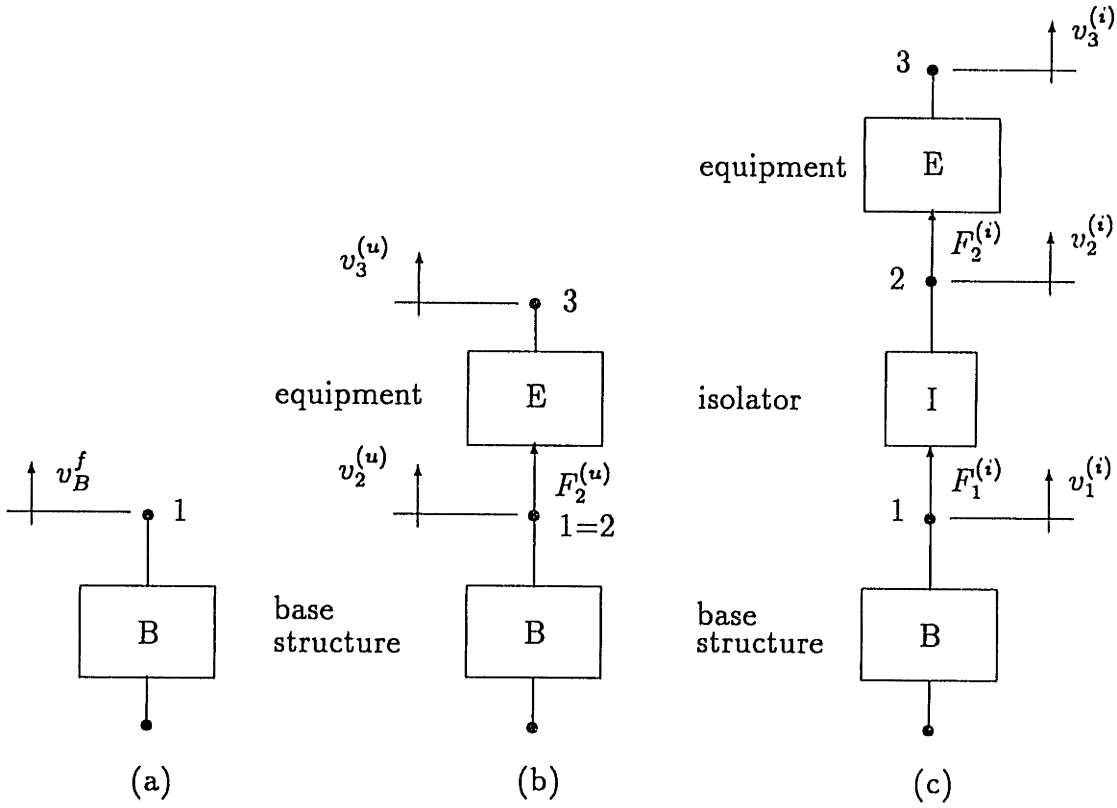

Figure 2.8: The general velocity isolation problem: definitions for mount passive sensitivity $\mathcal{P}(s)$, defined by the ratio of isolated velocity $v_3^{(i)}$ to unisolated velocity $v_3^{(u)}$.

The two velocities in the definition for mount effectiveness cannot be simultaneously observed in the mount; the addition or removal of the isolator I is required between measurements. The definition of effectiveness in Eq. 2.57 is somewhat undesirable, since at high frequencies the function is unbounded. The inverse of Eq. 2.57 is used to define the mount *passive sensitivity* function $\mathcal{P}_{v_3}$ for velocity v_3

$$\mathcal{P}_{v_3}(s) = \frac{v_3^{(i)}(s)}{v_3^{(u)}(s)} \tag{2.58}$$

The term passive sensitivity is selected because of the similarity of this function to the closed loop sensitivity function $S(s)$, which relates the closed loop output to the open loop output of a standard regulator with output y:

$$S(s) = \frac{y^{CL}(s)}{y^{OL}(s)} \tag{2.59}$$

The form of Eq. 2.58 is also preferable for the reason that as the base mobility decreases to zero, the familiar rigid base transmissibility function T_{v3} is recovered. An

important advantage of the passive sensitivity definition is that it does not require a measurement of the free velocity of the base v_B^f, measured when the equipment E is removed, which is an important consideration when the base is flexible. In other cases, a measurement of the free velocity v_B^f may be available and the mount transmissibility T_{v_3} of Eq. 2.38 can be used.

The passive sensitivity function may also be interpreted as the ratio of two transmissibility functions. Define the *softmount* transmissibility T_S as T_{v_3} from Eq. 2.38 and Figure 2.8(a)

$$T_S(s) = \frac{v_3^{(i)}(s)}{v_B^f(s)} \tag{2.60}$$

and the *hardmount* transmissibility T_H (corresponding to Figure 2.8(b)) as

$$T_H(s) = \frac{v_3^{(u)}(s)}{v_B^f(s)} \tag{2.61}$$

The passive sensitivity function of Eq. 2.58 is the ratio of these two transmissibilities:

$$\mathcal{P}_{v_3}(s) = \frac{T_S(s)}{T_H(s)} \tag{2.62}$$

The passive sensitivity $\mathcal{P}_{v_3}$ for the general model in Figure 2.8 is derived in this manner. Using Eqs. 2.40 and 2.42 and setting $[F_1 \;\; v_1]^T = [F_2 \;\; v_2]^T$, the expression for the unisolated velocity at terminal 3 is (with s dependence suppressed)

$$v_3^{(u)} = \frac{1}{\dfrac{Y_B}{Y_{23}^f} + \dfrac{1}{(T_v)_{23}}} v_B^f \tag{2.63}$$

By multiplying numerator and denominator by $(T_v)_{23}$, and by using the definitions of Eq. 2.45 and $Y_2^{3f} = Y_E$, the unisolated velocity is expressed as

$$v_3^{(u)} = \frac{(T_v)_{23}}{\dfrac{Y_B}{Y_E} + 1} v_B^f \tag{2.64}$$

The isolated velocity $v_3^{(i)}$ can be determined from Eq. 2.46, and when substituted along with Eq. 2.64 into Eq. 2.58, leads to the passive sensitivity for the mount velocity v_3

$$\mathcal{P}_{v_3}(s) = \frac{v_3^{(i)}}{v_3^{(u)}} = \frac{\dfrac{Y_B}{Y_E} + 1}{\dfrac{1}{(T_v)_{12}} + \dfrac{Y_{12}^b}{Y_E} + Y_B\left(\dfrac{1}{(T_v)_{21}Y_E} + \dfrac{1}{Y_{12}^f}\right)} \tag{2.65}$$

In a comparison of Eq. 2.46 and Eq. 2.65 it can be seen that the functions $\mathcal{P}_{v_3}$ and T_{v_3} will be identical when two conditions are satisfied: 1) the base mobility Y_B is zero, and 2) the equipment transmissibility $(T_v)_{23}$ equals 1, which occurs when the equipment output terminal 3 coincides with input terminal 2.

The passive sensitivity for velocity at the input location of the equipment is found in a similar manner. The unisolated velocity at terminal 2 is found by letting terminals 2 and 3 coincide in Eq. 2.64, so that $Y_{23}^f = Y_2^{3f} = Y_E$ and $(T_v)_{23} = 1$

$$v_2^{(u)} = \frac{1}{\dfrac{Y_B}{Y_E} + 1} v_B^f \tag{2.66}$$

which together with Eq. 2.47 yields the expression for the passive sensitivity of velocity at terminal 2

$$\mathcal{P}_{v_2}(s) = \frac{v_2^{(i)}}{v_2^{(u)}} = \frac{\dfrac{Y_B}{Y_E} + 1}{\dfrac{1}{(T_v)_{12}} + \dfrac{Y_{12}^b}{Y_E} + Y_B\left(\dfrac{1}{(T_v)_{21}Y_E} + \dfrac{1}{Y_{12}^f}\right)} \tag{2.67}$$

An important observation is that Eq. 2.67 is identical to Eq. 2.65, therefore $\mathcal{P}_{v_2} = \mathcal{P}_{v_3}$.

Passive Sensitivity (For Vibrating Equipment): The mount force effectiveness $\mathcal{E}_F$ for transmitted force is defined in the literature as the ratio of the base interface force, when isolated, to the base interface force when the equipment is hardmounted (as illustrated in Figure 2.9):

$$\mathcal{E}_F(s) = \frac{F_1^{(u)}(s)}{F_1^{(i)}(s)} \tag{2.68}$$

The passive sensitivity of force $\mathcal{P}_F$ is defined here as the inverse of the mount force effectiveness

$$\mathcal{P}_F(s) = \frac{F_1^{(i)}(s)}{F_1^{(u)}(s)} \tag{2.69}$$

The unisolated interface force $F_1^{(u)}$ is found by assembling the equipment vibration source model of Eq. 2.50 with the output mobility of the base structure, given by $v_1 = -Y_B F_1^{(u)} = -Y_B F_2^{(u)}$, to produce

$$F_E^b = \left[\, 1 - \frac{1}{Y_E} \,\right] \begin{bmatrix} 1 \\ -Y_B \end{bmatrix} F_1 \tag{2.70}$$

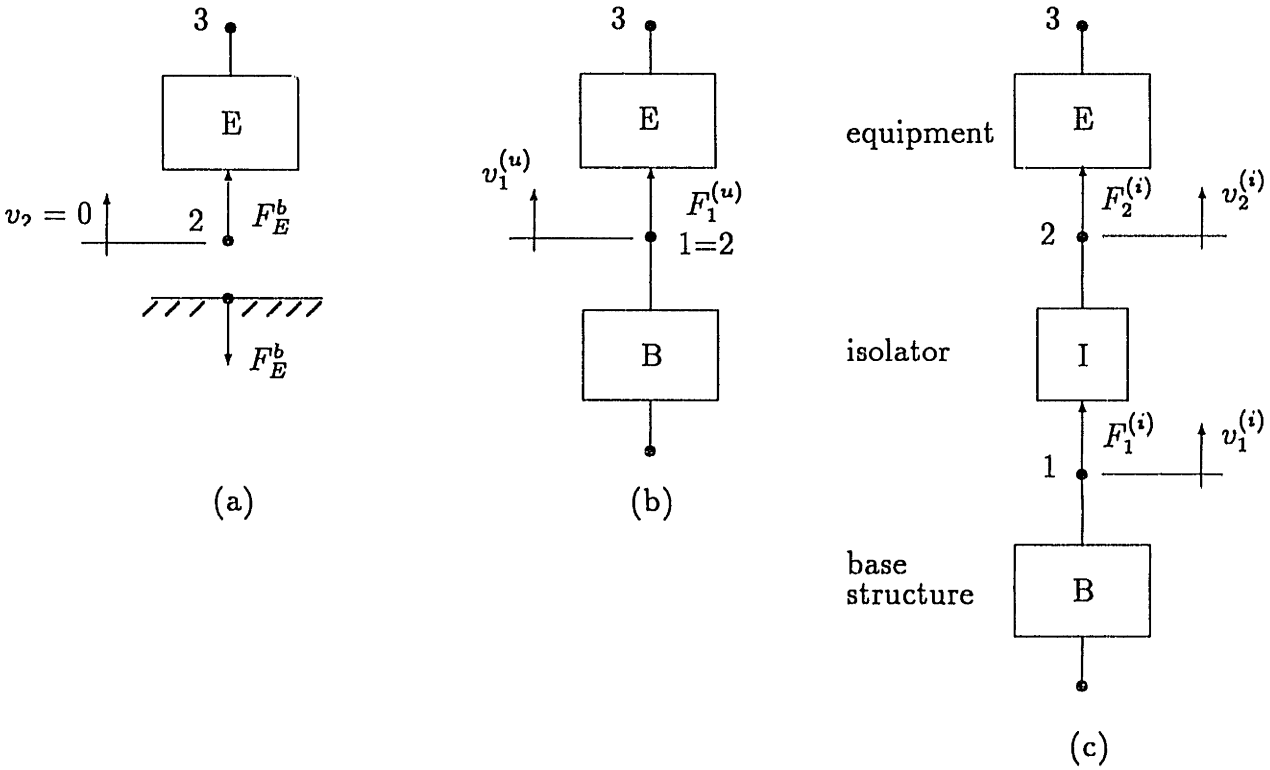

Figure 2.9: The general force isolation problem: definitions for mount passive sensitivity $\mathcal{P}(s)$, defined by the ratio of isolated force $F_1^{(i)}$ to unisolated force $F_1^{(u)}$.

$$\frac{F_1^{(u)}}{F_E^b} = \frac{1}{1 + \dfrac{Y_B}{Y_E}} \tag{2.71}$$

Substitution of Eq. 2.71 and Eq. 2.55 into Eq. 2.69 leads to the following expression for the mount passive sensitivity for force

$$\mathcal{P}_F(s) = \frac{F_1^{(i)}}{F_1^{(u)}} = \frac{\dfrac{Y_B}{Y_E} + 1}{\dfrac{1}{(T_v)_{12}} + \dfrac{Y_{12}^b}{Y_E} + Y_B\left(\dfrac{1}{(T_v)_{21}Y_E} + \dfrac{1}{Y_{12}^f}\right)} \tag{2.72}$$

which is identical to the velocity passive sensitivity functions $\mathcal{P}_{v_2}$ and $\mathcal{P}_{v_3}$. Continuing with the force isolation problem of Figure 2.9, the base output mobility $v_1 = -Y_B F_1$ at terminal 1 is unchanged by the mounted equipment or isolator. Therefore, the mount passive sensitivity for force $\mathcal{P}_F$ not only represents the ratio of isolated to unisolated interface force F_1, but also represents the ratio of isolated to unisolated

interface velocity v_1 [77]

$$\mathcal{P}_F(s) = \frac{F_1^{(i)}}{F_1^{(u)}} = \frac{v_1^{(i)}}{v_1^{(u)}} \tag{2.73}$$

This is an important result, since the ultimate objective of force isolation is usually to attenuate the base structure response due to the vibrating equipment; the interface force is just an intermediate variable. In addition, the result of Eq. 2.73 holds for any point on the base structure (not only at the interface terminal 1), since the relation of velocity at any other point in the base is fixed by a four-pole matrix to the force and velocity at terminal 1. This conclusion is not affected by the presence of structural flexibility in the base, isolator or equipment. Structural flexibility will, however, affect the achievable performance by the isolation mount, as is investigated in Sections 2.5 to 2.7.

2.3.3 Summary

Table 2.1 summarizes the results of this section. For the velocity isolation problem, it was shown that the passive sensitivity function $\mathcal{P}_v$ is the same for both terminals 2 and 3 of the equipment. This function is identical to the force and velocity passive sensitivity functions $\mathcal{P}_F$ of the force isolation problem. The symbol $\mathcal{P}$ will be used to represent all four functions:

$$\mathcal{P}(s) = \frac{\dfrac{Y_B}{Y_E} + 1}{\dfrac{1}{(T_v)_{12}} + \dfrac{Y_{12}^b}{Y_E} + Y_B\left(\dfrac{1}{(T_v)_{21}Y_E} + \dfrac{1}{Y_{12}^f}\right)} \tag{2.74}$$

In this section it is also shown that the transmissibility function T_{v_2} for the velocity isolation problem is identical to the transmissibility function T_F of the force isolation problem; the symbol T is chosen to represent both of these functions:

$$T(s) = \frac{1}{\dfrac{1}{(T_v)_{12}} + \dfrac{Y_{12}^b}{Y_E} + Y_B\left(\dfrac{1}{(T_v)_{21}Y_E} + \dfrac{1}{Y_{12}^f}\right)} \tag{2.75}$$

The transmissibility T is equal to the passive sensitivity $\mathcal{P}$ when $Y_B = 0$ (rigid base). Further, $T_{v3} = T$ when the velocity transmissibility across the equipment $(T_v)_{23} = 1$.

Table 2.1: Definitions of isolator performance.

Symbol	Functions Represented	
	velocity isolation problem (vibrating base)	force isolation problem (vibrating equipment)
Passive Sensitivity $\mathcal{P}(s)$	$\frac{v_2^{(i)}}{v_2^{(u)}}$ $\frac{v_3^{(i)}}{v_3^{(u)}}$	$\frac{F_1^{(i)}}{F_1^{(u)}}$ $\frac{v_1^{(i)}}{v_1^{(u)}}$
Transmissibility $T(s)$	$\frac{v_2}{v_B^f}$	$\frac{F_1}{F_E^b}$
Transmissibility $T_{v_3}(s)$	$\frac{v_3}{v_B^f}$	-

In the next section, the passive sensitivity $\mathcal{P}$ is investigated for the classical isolation problem.

2.4 Classical Passive Isolation Model

The classic velocity and force passive isolation model is a subset of the general model of Figures 2.8 and 2.9 with the following additional assumptions:

(i) base structure B is rigid

(ii) equipment E modelled as a rigid mass m

(iii) passive isolator I is massless

(iv) passive isolator I modelled as a viscously damped spring. The spring and viscous damping constants are frequency independent.

Figure 2.10 illustrates the classical velocity isolation model. The assumptions simplify the general expression for the mount passive sensitivity $\mathcal{P}$ given by Eq. 2.74. A rigid base implies $Y_B = 0$, therefore the passive sensitivity $\mathcal{P}$ is equal to the transmissibility T. Assumption (ii) implies that $Y_E = 1/ms$ and that the velocities at terminals 2

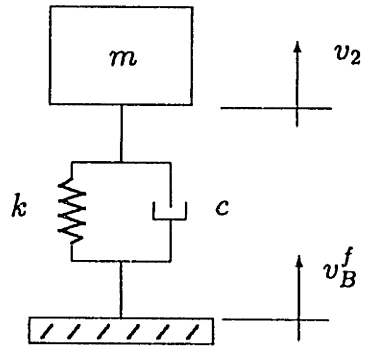

Figure 2.10: Classical passive isolation model: velocity isolation. The vibrating base is assumed to be infinitely stiff, and the isolator and equipment are modelled by simple lumped-parameter elements.

and 3 are identical. When the isolator is modelled as massless,

$$(T_v)_{12} = (T_v)_{21} = 1 \tag{2.76}$$

and

$$Y_{12}^f = \infty \tag{2.77}$$

Finally, the four-pole representation for a massless viscously damped spring is given by Eq. 2.21

$$Y_{12}^b = s/(cs + k) \tag{2.78}$$

As before, the isolator blocked transfer mobility Y_{12}^b is denoted simply by Y_I. With these definitions the passive sensitivity becomes

$$\begin{aligned} \mathcal{P}_r(s) &= \frac{1}{1 + \dfrac{Y_I}{Y_E}} \\ &= \frac{cs + k}{ms^2 + cs + k} \end{aligned} \tag{2.79}$$

where the symbol $\mathcal{P}_r$ is adopted to highlight that this function is the rigid base passive sensitivity, which will serve as a basis for comparison. By defining the following dimensionless parameters

$$\omega_o^2 = \frac{k}{m} \qquad \zeta_o = \frac{c}{2m\omega_o} \tag{2.80}$$

the rigid base passive sensitivity $\mathcal{P}_r$ can be represented in modal form

$$\mathcal{P}_r(s) = \frac{2\zeta_o\omega_o s + \omega_o^2}{s^2 + 2\zeta_o\omega_o s + \omega_o^2} \tag{2.81}$$

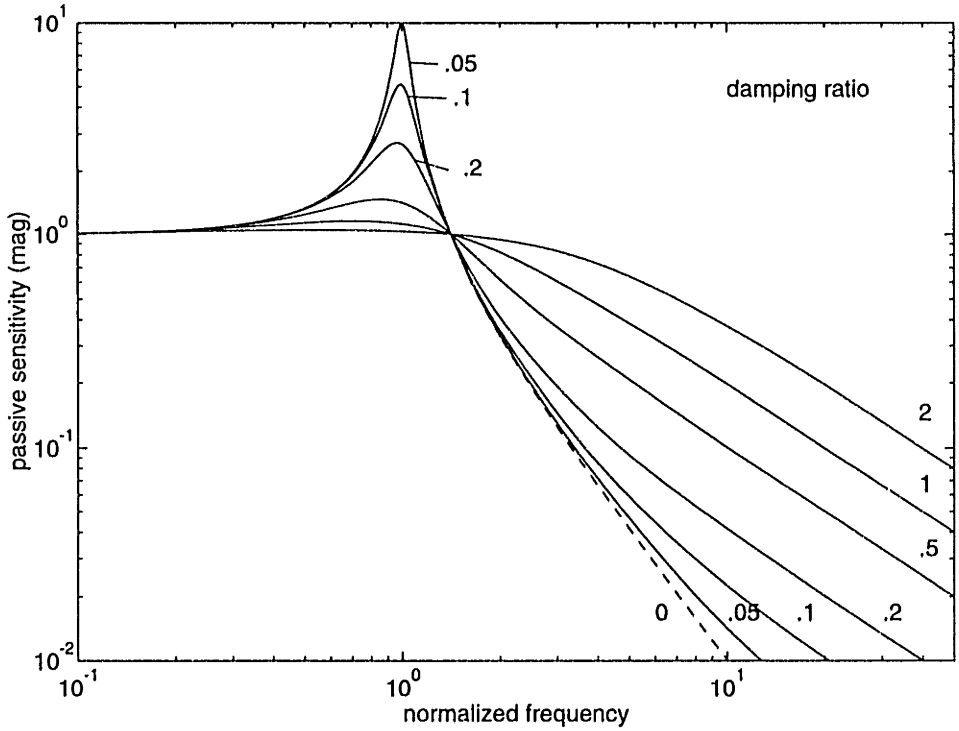

Figure 2.11: Passive sensitivity $\mathcal{P}_r(\bar{s})$ for classic isolation model for various mount damping ratios ζ_o.

Finally, the passive sensitivity can be expressed in terms of the normalized frequency $\bar{s} = j\bar{\omega} = j\omega/\omega_o$:

$$\mathcal{P}_r(\bar{s}) = \frac{2\zeta_o\bar{s} + 1}{\bar{s}^2 + 2\zeta_o\bar{s} + 1} \tag{2.82}$$

The magnitude of $\mathcal{P}_r$ is plotted in Figure 2.11 for several values of damping ζ_o. As shown in the previous section (summarized by Table 2.1), this function describes not only the passive sensitivity for the velocity isolation problem, but also the passive sensitivity for the force isolation problem as well. Figure 2.11 shows that regardless of the level of interface damping, the passive sensitivity magnitude at $\bar{\omega} = \sqrt{2}$ equals unity. At all greater frequencies the mount attenuates disturbance; at all lower frequencies, the mount amplifies.

The effect of increasing interface damping ratio ζ_o is to attenuate the resonance near $\bar{\omega} = 1$ at the cost of increased sensitivity at high frequencies. For zero damping, $\mathcal{P}_r$ rolls off with a logarithmic slope of -2; at finite values of damping a real zero at $\bar{\omega} = 1/(2\zeta_o)$ increases the logarithmic slope of the high frequency asymptote to -1.

The magnitude of the passive sensitivity at high frequency is

$$|\mathcal{P}_r(\infty)| = \frac{2\zeta_o}{\bar{\omega}} \tag{2.83}$$

and at the damped resonance $\bar{\omega}_d$ is approximated (to within 10% for $\zeta_o \leq 0.2$) as [61]

$$|\mathcal{P}_r(j\omega_o)| \approx \frac{1}{2\zeta_o} \qquad (\zeta_o \leq 0.2) \tag{2.84}$$

An additional performance metric is the static deflection in a 1-g field

$$\Delta = \frac{g}{\omega_o^2} \tag{2.85}$$

For example, for a mount with corner frequency of 20 Hz the static deflection is 0.6 mm, and at 1 Hz the static deflection is 25 cm. For microgravity mounts with passive corner frequencies on the order of 0.1 to 0.3 Hz, the static deflection is in the range of 2.8 to 24 meters, which poses obvious difficulties for multi-axis ground test and validation.

The classical isolation problem has been investigated thoroughly by many researchers. Ruzicka and Derby [61] have analyzed the effects of damping mechanisms other than viscous on the mount transmissibility, such as coulomb, quadratic, viscous with deadband, and elastically coupled damping. Elastically coupled or viscoelastic damping models are important in that many mount materials such as rubber exhibit these types of damping.

It is desirable to design a mount with elastically coupled damping since its performance is superior to that of a viscously damped mount. An isolator mount with elastically coupled damping is modelled using the Zener model (also called the standard linear solid) shown in Figure 2.12. At low frequencies the mount has spring stiffness $k_1 k_2/(k_1 + k_2)$, while at high frequencies the damper "locks up" and the mount stiffness increases to k_1. For an isolation mount modelled with a Zener spring, the high frequency rolloff of the passive sensitivity function approaches a logarithmic slope of -2, superior to the viscously damped mount. The Zener model parameters can be tuned to provide high damping near mount resonance while allowing recovery of a logarithmic slope of -2 at high frequency. A full treatment of this model is given

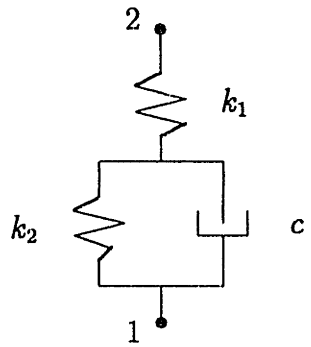

Figure 2.12: Zener model for isolator.

by Ruzicka and Derby [61]. In this thesis, viscously damped mounts will be used for simplicity in the analysis, and the results obtained are applicable to tuned elastically damped mounts. The Zener model for isolator mounts could be incorporated into the frequency domain analysis framework of this thesis with some minor added complexity of calculation.

2.5 Effects of Flexibility on Passive Isolation

The passive mount passive sensitivity $\mathcal{P}$, for cases in which the base or equipment exhibit flexibility, is compared to the rigid base effectiveness $\mathcal{P}_r$ for the classical isolation model of Section 2.4. For purpose of comparison, the classical model is assumed to have a mount damping ratio of 10%. Insights drawn from studying the effects of simple flexibility models on the function $\mathcal{P}$ are useful for interpreting experimental data in which the base or equipment mobility are more complicated functions of frequency.

2.5.1 Base Flexibility

Consider a passive isolation mount that is identical to that of the classical model, with the exception that the base structure exhibits flexibility. Beginning with the general expression for the mount passive sensitivity $\mathcal{P}$ in Eq. 2.74, the assumption of a flexible base implies that $Y_B \neq 0$. Assumptions (ii), (iii) and (iv) of the classical model still hold: therefore $(T_v)_{12} = (T_v)_{21} = 1$ and $Y_{12}^f = \infty$, and the blocked transfer

Table 2.2: Base mobility models and perturbation term.

base model	mobility	perturbation	
	$Y_B(s)$	$\frac{Y_B(s)}{Y_E(s)}$	$\frac{Y_B(\bar{s})}{Y_E(\bar{s})}$
mass	$\frac{1}{Ms}$	$\frac{m}{M}$	$\frac{m}{M}$
damper	$\frac{1}{C}$	$\frac{ms}{C}$	$\left(\frac{m\omega_o}{C}\right)\bar{s}$
spring	$\frac{s}{K}$	$\frac{s^2m}{K}$	$\left(\frac{k}{K}\right)\bar{s}^2$

mobility Y_{12}^b of the massless, viscously damped spring is again denoted by Y_I. With these assumptions, the passive sensitivity function becomes

$$\mathcal{P}(s) = \frac{1 + \frac{Y_B}{Y_E}}{1 + \frac{Y_I}{Y_E} + \frac{Y_B}{Y_E}} \tag{2.86}$$

where $Y_I = s/(k + cs)$ and $Y_E = 1/(ms)$. By comparing Eq. 2.86 with Eq. 2.79 it is evident that the perturbation term in Eq. 2.86 is Y_B/Y_E; when the perturbation is very small, the rigid base passive sensitivity $\mathcal{P}_r$ function is recovered. The degree of "smallness" of this term is considered for four cases of base flexibility: the base modelled as a (a) mass, (b) damper, (c) spring, and (d) single resonant mode. Table 2.2 lists the output base mobility models (at terminal 1 in Figures 2.8 and 2.9) and perturbation term Y_B/Y_E for the first three cases. The perturbation is expressed in terms of the dimensionless frequency $\bar{s} = j\omega/\omega_o$ in the third column. The dimensionless coefficients of powers of $\bar{s}$ in the last column appear in the expressions for the passive sensitivity $\mathcal{P}(\bar{s})$ derived below, and are treated as the variable parameter in plots of the passive sensitivity function. It is reasonable to expect that for values of each coefficient much less than one the rigid base passive sensitivity $\mathcal{P}_r(\bar{s})$ will be nearly recovered.

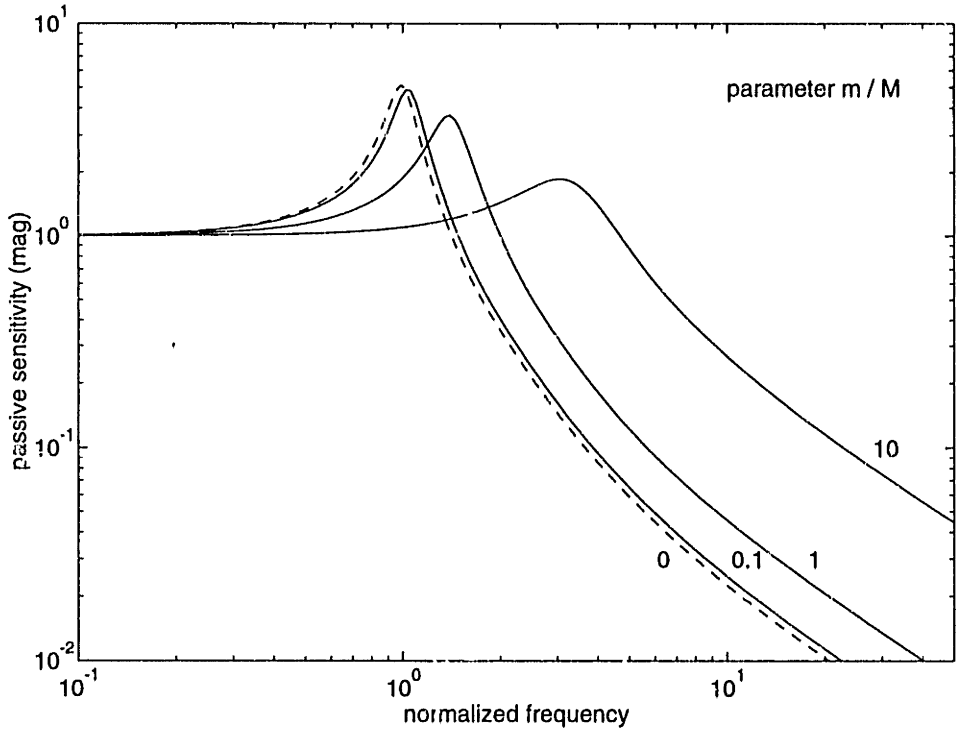

Figure 2.13: Passive sensitivity $\mathcal{P}(\bar{s})$ for base modelled as rigid mass M.

Base Modelled as a Mass: The base mobility model for a mass from Table 2.2 and the expressions for Y_I and Y_E are substituted into Eq. 2.86. Using the definitions of modal parameters ω_o and ζ_o defined in Eq. 2.80, the passive sensitivity as a function of normalized frequency becomes

$$\mathcal{P}(\bar{s}) = \frac{\left(1+\frac{m}{M}\right)(2\zeta_o\bar{s})+1}{\bar{s}^2+2\zeta_o\left(1+\frac{m}{M}\right)\bar{s}+\left(1+\frac{m}{M}\right)} \tag{2.87}$$

Figure 2.13 is a plot of the magnitude of the passive sensitivity $\mathcal{P}$ for different values of the parameter m/M. For base masses that are more than a factor of 10 greater than that of the isolated mass, the change in the passive sensitivity $\mathcal{P}$ is small. However, when the base is of comparable or smaller mass than the isolated mass, the resonant frequency of $\mathcal{P}$ occurs at a higher frequency and is more heavily damped. The base mass mobility has no effect on the real zero of the passive sensitivity $\mathcal{P}$ in Eq. 2.87, and thus no effect on the *slope* of the high frequency rolloff, although the magnitude is clearly increased.

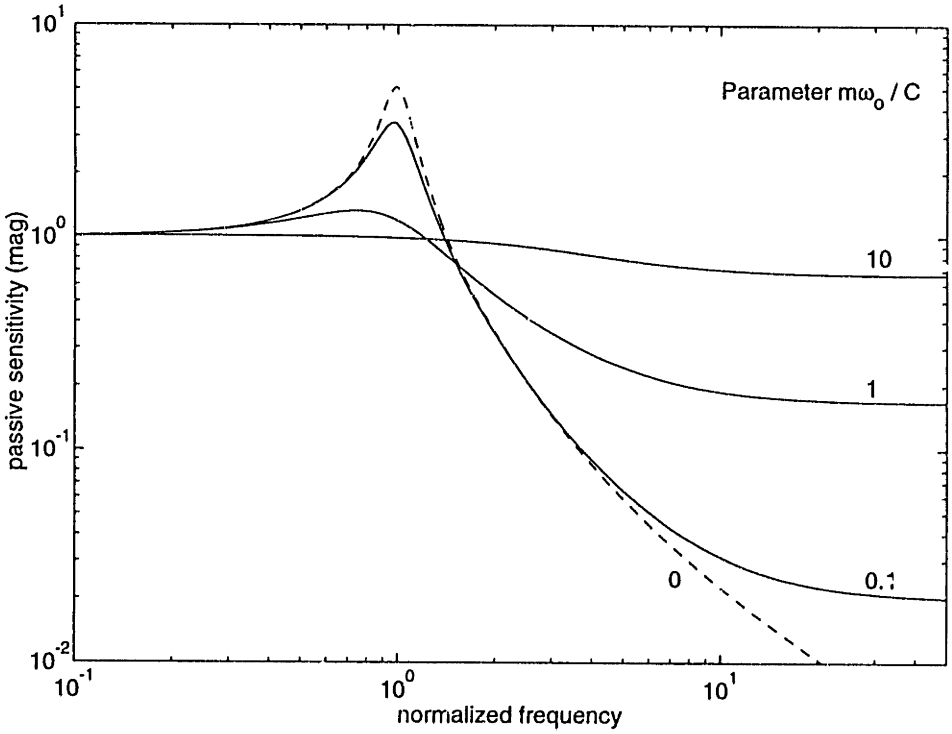

Figure 2.14: Passive sensitivity $\mathcal{P}(\bar{s})$ for base modelled as massless damper C.

Base Modelled as a Damper: Substitution of the base mobility model for a damper into Eq. 2.86 leads to

$$\mathcal{P}(\bar{s}) = \frac{2\zeta_o\left(\frac{m\omega_o}{C}\right)\bar{s}^2 + \left(2\zeta_o + \frac{m\omega_o}{C}\right)\bar{s} + 1}{\left(1 + 2\zeta_o\frac{m\omega_o}{C}\right)\bar{s}^2 + \left(2\zeta_o + \frac{m\omega_o}{C}\right)\bar{s} + 1} \tag{2.88}$$

For large $\bar{s}$ and finite values of mount damping ζ_o, this function approaches the constant

$$\mathcal{P}(\infty) = \frac{1}{1 + \frac{C}{2\zeta_o m\omega_o}} \tag{2.89}$$

where $2\zeta_o m\omega_o$ is equal to the mount interface damping factor, c. The passive sensitivity $\mathcal{P}$ is plotted in Figure 2.14 for several values of the dimensionless parameter $m\omega_o/C$. As the base damping factor C is decreased, the passive sensitivity resonance becomes more heavily damped, and the high frequency magnitude is increased, reaching a constant value determined by Eq. 2.89.

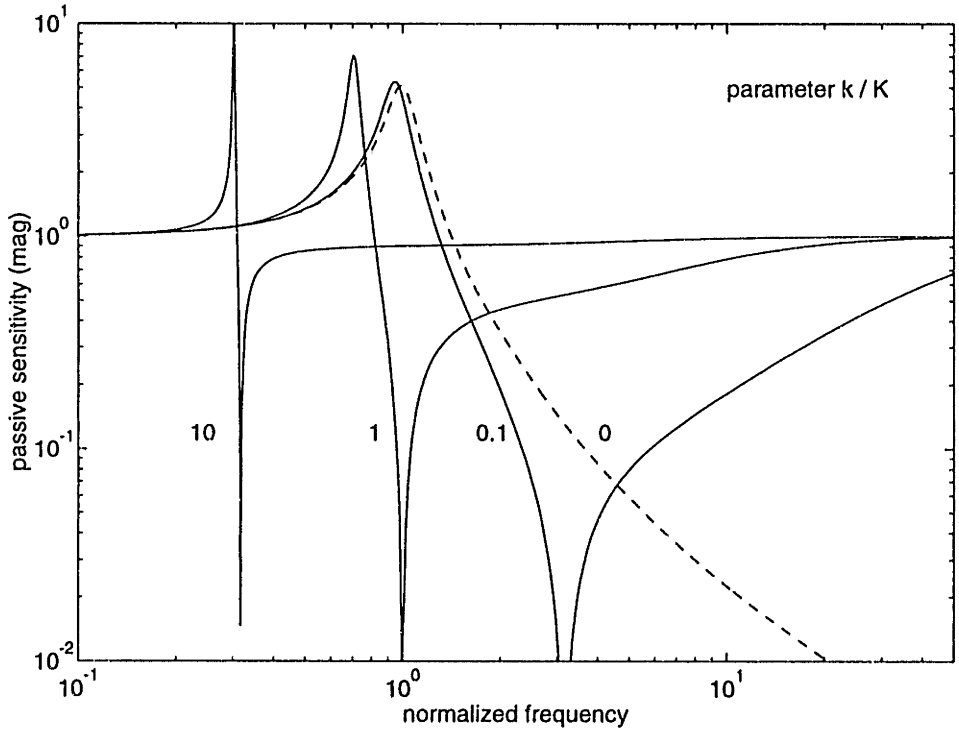

Figure 2.15: Passive sensitivity $\mathcal{P}(\bar{s})$ for base modelled as massless spring K.

Base Modelled as a Spring: For the base modelled as a spring K, the passive sensitivity $\mathcal{P}$ becomes

$$\mathcal{P}(\bar{s}) = \frac{\left(2\zeta_o \frac{k}{K}\right)\bar{s}^3 + \left(\frac{k}{K}\right)\bar{s}^2 + 2\zeta_o \bar{s} + 1}{\left(2\zeta_o \frac{k}{K}\right)\bar{s}^3 + \left(1 + \frac{k}{K}\right)\bar{s}^2 + 2\zeta_o \bar{s} + 1} \tag{2.90}$$

For finite values of mount damping, $\mathcal{P}(\infty) = 1$. Figure 2.15 is a plot of the passive sensitivity magnitude for several values of the parameter k/K. A zero occurs at a frequency that corresponds to the resonance of the equipment hardmounted to the undamped base spring. As the base spring constant K decreases relative to k, the resonance in $\mathcal{P}$ decreases in frequency and becomes more lightly damped, a trend that is opposite to the case illustrated in Figure 2.13, in which the base is modelled as a rigid mass.

A conclusion from from these three examples is that any finite mobility in the base reduces the performance of the isolation mount at high frequencies. In the case of the spring base mobility, the performance is band limited.

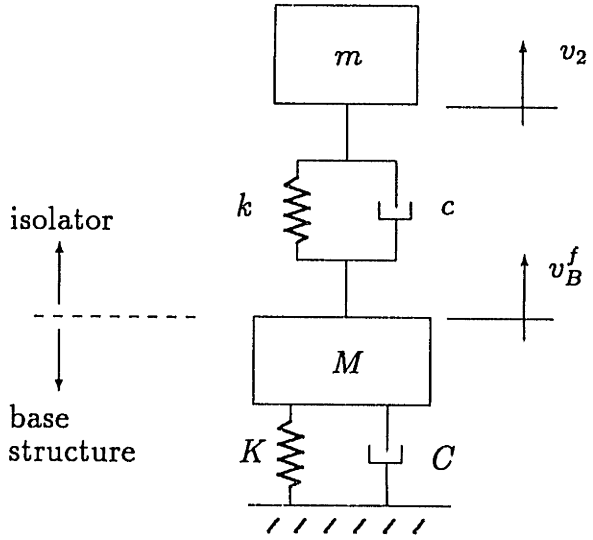

Figure 2.16: Passive isolator mounted to base modelled as a single resonant mode.

Base Modelled as a Resonant Mode: In this case the base mobility is expressed in standard second order modal form

$$Y_B(s) = \frac{s\phi_b^2}{s^2 + 2\zeta_b\omega_b s + \omega_b^2} \tag{2.91}$$

where ζ_b and ω_b are the modal damping and frequency of the (uncoupled) base resonance, and ϕ_b is the mass normalized mode eigenvector of the (uncoupled) base at output terminal 1. Figure 2.5.1 illustrates a passive isolator mounted to a base modelled as a single resonant mode.

The real-valued term ϕ_b^2 is defined as the modal residue A_b, which is the inverse of the driving point modal mass $\bar{m}_b$:

$$\phi_b^2 = A_b = \frac{1}{\bar{m}_b} \tag{2.92}$$

In the expression for the passive sensitivity $\mathcal{P}$ of Eq. 2.86, the perturbation is the dimensionless term Y_B/Y_E. In terms of the dimensionless frequency $\bar{s} = j\omega/\omega_o$, this term is expressed as

$$\frac{Y_B}{Y_E}(\bar{s}) = \frac{\bar{s}^2 m\phi_b^2}{\bar{s}^2 + 2\zeta_b\bar{\omega}_b\bar{s} + \bar{\omega}_b^2} \tag{2.93}$$

where $\bar{\omega}_b = \omega_b/\omega_o$. This function is plotted in Figure 2.17 for two values of $\bar{\omega}_b = \omega_b/\omega_o$: the plot resembles that of the accelerance of a single resonator with natural frequency $\bar{\omega}_b$, damping ζ_b and residue $m\phi_b^2$. For small ζ_b, the resonance frequency of the base

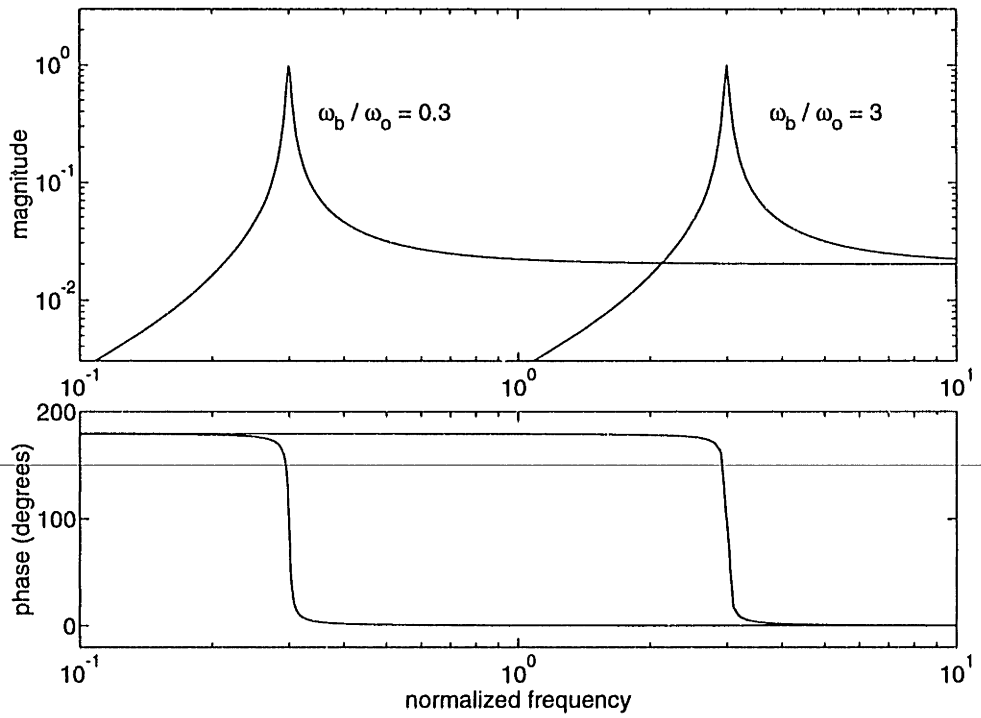

Figure 2.17: Perturbation term $Y_B(\bar{s})/Y_E(\bar{s})$ for two values of ω_b/ω_o.

mobility is well approximated by $\bar{\omega} = \bar{\omega}_b$ and the function in Eq. 2.93 reaches a maximum gain of

$$\begin{aligned} \beta_b &= \max_{\bar{s}} \left| \frac{Y_B}{Y_E}(\bar{s}) \right| \\ &= \frac{m\phi_b^2}{2\zeta_b} \end{aligned} \tag{2.94}$$

The coefficient β_b is dimensionless because ζ_b is dimensionless and $m\phi_b^2$ is the ratio of isolated mass m to base modal mass $\bar{m}_b = 1/\phi_b^2$. In Figures 2.18, 2.19, and 2.20 the passive sensitivity $\mathcal{P}$ is plotted for three different values of $\bar{\omega}_b$. The base modal damping ratio ζ_b is assumed to be 1%, the mount damping is assumed to have 10% damping (defined for a rigid base mounting) and each figure is parameterized by β_b.

Figure 2.18 shows the magnitude of $\mathcal{P}$ for $\bar{\omega}_b = 3$. The base resonance contributes a closely spaced pole-zero pair to $\mathcal{P}$: the zero corresponds to the resonant frequency of the equipment mass hardmounted to the flexible base, and the pole corresponds to the (higher) frequency of the isolated equipment on the flexible base. For $\beta_b < 1$ (the ratio of equipment mass to modal mass is less than twice the base modal damping ratio ζ_b) the perturbation to $\mathcal{P}$ is small, but as the modal mass is decreased relative to

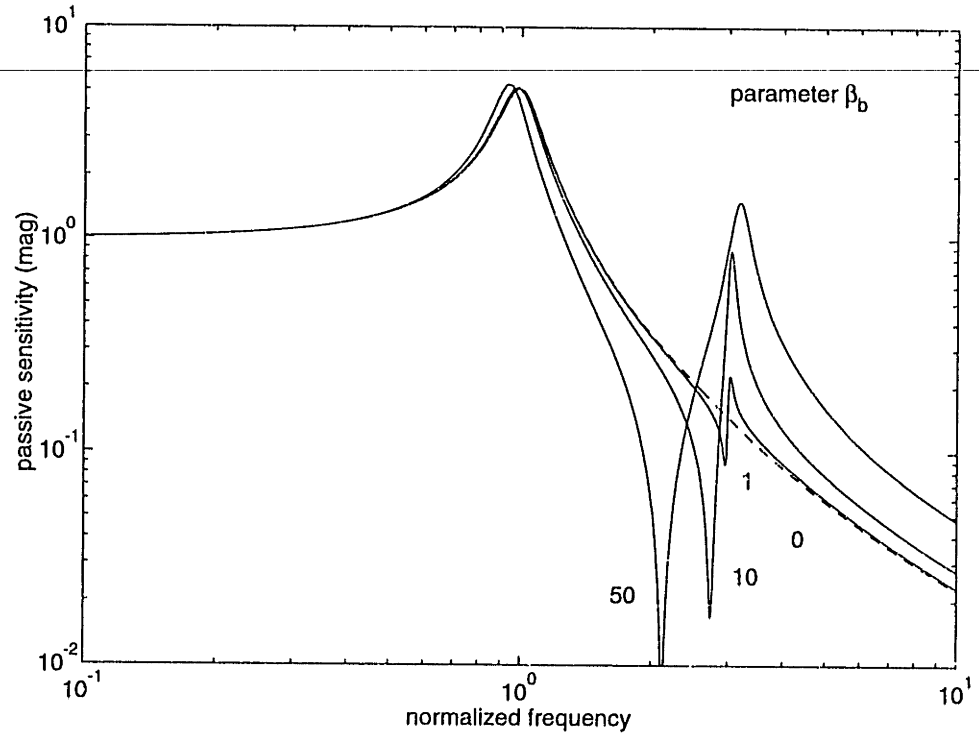

Figure 2.18: Passive sensitivity $\mathcal{P}(\bar{s})$ for base modelled as resonant mode. Parameters: $\beta_b = m\phi_b^2/(2\zeta_b)$, $\omega_b/\omega_o = 3, \zeta_o = 0.1, \zeta_b = 0.01$.

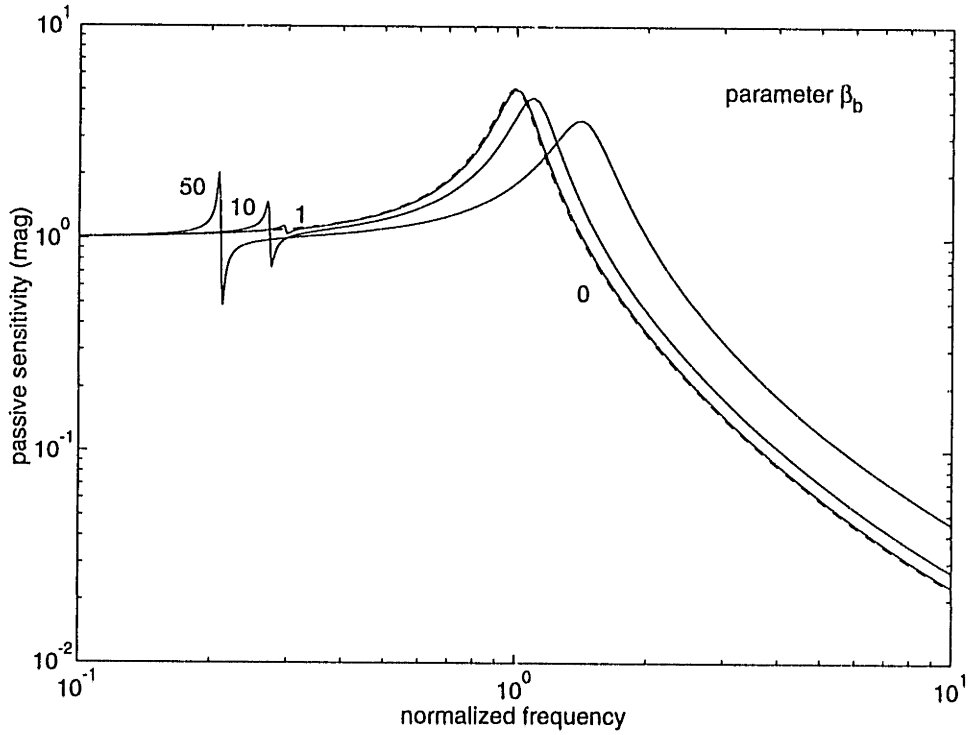

Figure 2.19: Passive sensitivity $\mathcal{P}(\bar{s})$ for base modelled as resonant mode. Parameters: $\beta_b = m\phi_b^2/(2\zeta_b)$, $\omega_b/\omega_o = 0.3, \zeta_o = 0.1, \zeta_b = 0.01$.

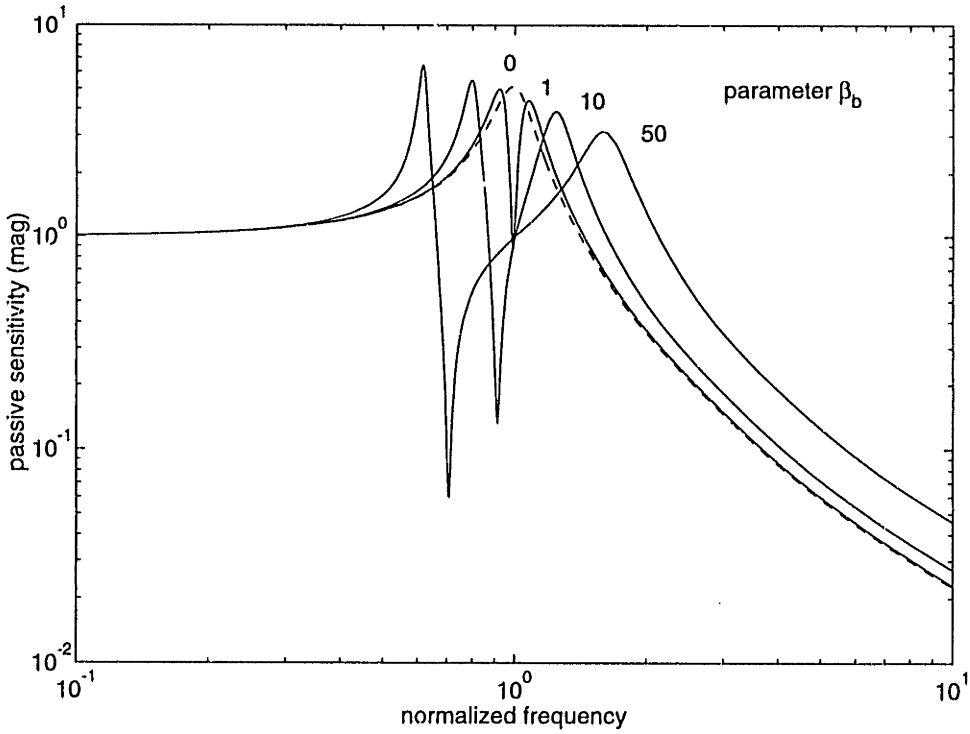

Figure 2.20: Passive sensitivity $\mathcal{P}(\bar{s})$ for base modelled as resonant mode. Parameters: $\beta_b = m\phi_b^2/(2\zeta_b)$, $\omega_b/\omega_o = 1, \zeta_o = 0.1, \zeta_b = 0.01$.

m, the pole-zero separation grows wider and the magnitude perturbation increases. The zero frequency decreases because the unisolated equipment loads the lighter base mode more strongly, and the pole frequency increases slightly because the base modal mass $\bar{m}_b$ has decreased relative to the constant isolator spring stiffness k. The isolator resonance at $\bar{\omega}_o = 1$ decreases and becomes more lightly damped as β_b is increased, since below $\bar{\omega}_b$ the base mobility appears to be that of a spring of constant $k_b = \bar{m}_b\omega_b^2$. The observed effect on the isolator resonance is consistent with that for the base spring model plotted in Figure 2.15.

In Figure 2.19, the base modal frequency is at frequency $\bar{\omega}_b = 0.3$. The pole-zero pair separation frequency, and the perturbation to the magnitude of $\mathcal{P}$, are smaller compared to Figure 2.18 for a given value of β_b, because in this frequency range the isolator has little or no effect, and the equipment velocity v_3 or interface force F_1 are nearly identical before and after addition of the passive isolator. Above $\bar{\omega}_b$, the base mobility appears to be that of a mass $\bar{m}_b$, and as expected from Figure 2.13, the mount resonance near $\bar{\omega}_o = 1$ increases and becomes more heavily damped for modal

masses that are of comparable size to the mass of the isolated equipment. When Figures 2.18 and 2.19 are compared, it is observed that for a given value of β_b, the effect on the frequency and damping of the mount resonance at $\bar{\omega}_o = 1$ is greatest when the base resonance occurs below mount resonance. However, the effect on the passive sensitivity function near $\bar{\omega}_b$ is greatest when the base resonance occurs above mount resonance.

In Figure 2.20 the base resonance is at $\bar{\omega}_b = 1$ and the effect of this mode on the amplitude of $\mathcal{P}$ is shown for different values of β_b. Even in this case, for values of β_b that are less than one, the effect on the passive sensitivity magnitude is small. As β_b increases, the mount resonance splits into two distinct modes, and behaves like a slightly mistuned proof mass damper.

2.5.2 Equipment Flexibility

In this section the magnitude of $\mathcal{P}$ for the classical model is compared to that for situations in which the equipment itself exhibits flexibility (in addition to the free body mobility of a rigid mass). In this case Y_B is set to zero, and the isolator blocked transfer mobility Y_I is the same as for the classical model. The equipment input mobility at terminal 2 is modelled as the sum of the free body mobility and the mobility of a flexible mode:

$$Y_E(s) = \bar{Y}_E(s) + Y_{e2}(s) \tag{2.95}$$

where

$$Y_{e2}(s) = \frac{s\phi_{e2}^2}{s^2 + 2\zeta_e\omega_e s + \omega_e^2} \tag{2.96}$$

$$\bar{Y}_E(s) = \frac{1}{ms} \tag{2.97}$$

The parameters ζ_e and ω_e are the modal damping and frequency of the (uncoupled) equipment resonance, and ϕ_{e2} is the mass normalized equipment mode eigenvector at input terminal 2. The term ϕ_{e2}^2 is the inverse of the equipment driving point modal mass $\bar{m}_{e2}$. With the assumed equipment mobility of Eq. 2.95 and the above assumptions for base and isolator mobility, the general expression of the passive sensitivity

$\mathcal{P}$ of Eq. 2.74 reduces to

$$\mathcal{P}(s) = \frac{1 + \dfrac{Y_{e2}}{\bar{Y}_E}}{1 + \dfrac{Y_I}{\bar{Y}_E} + \dfrac{Y_{e2}}{\bar{Y}_E}} \tag{2.98}$$

The perturbation to this equation is the term $Y_e/\bar{Y}_E$. In terms of the dimensionless frequency $\bar{s} = j\omega/\omega_o$, this term is expressed as

$$\frac{Y_{e2}}{\bar{Y}_E}(\bar{s}) = \frac{\bar{s}^2 m\phi_{e2}^2}{\bar{s}^2 + 2\zeta_e\bar{\omega}_e\bar{s} + \bar{\omega}_e^2} \tag{2.99}$$

where $\bar{\omega}_e = \omega_e/\omega_o$. For light damping ζ_e, this function reaches a maximum at $\bar{\omega}_e$ with gain

$$\begin{aligned} \beta_{e2} &= \max_{\bar{s}} \left| \frac{Y_{e2}}{\bar{Y}_E}(\bar{s}) \right| \\ &= \frac{m\phi_{e2}^2}{2\zeta_e} \end{aligned} \tag{2.100}$$

This dimensionless parameter, a function of equipment modal damping and the ratio of equipment rigid body mass m to equipment modal mass $\bar{m}_{e2}$ at the interface location, governs the degree to which equipment modal flexibility affects the passive sensitivity $\mathcal{P}$ of the classical isolation model.

At this point an important observation can be made by comparing the passive sensitivity and perturbation functions of of Eqs. 2.98 and 2.99 with those for the flexible base in Eqs. 2.86 and 2.93: these two sets of functions are identical if the following substitutions are made:

$$\phi_b \rightarrow \phi_{e2} \tag{2.101}$$

$$\zeta_b \rightarrow \zeta_e \tag{2.102}$$

$$\omega_b \rightarrow \omega_e \tag{2.103}$$

$$Y_E \rightarrow \bar{Y}_E \tag{2.104}$$

where $Y_E = \bar{Y}_E = 1/ms$. The dimensionless parameters β_{e2} and β_b in Eqs. 2.100 and 2.94 are also identical using these substitutions. Therefore, the effect of equipment resonances on the passive sensitivity $\mathcal{P}$ is identical to that illustrated in Figures 2.18, 2.19, and 2.20, with the substitution of β_{e2} for β_b. This is a new result

which complements the work by Sykes [77] on the effect of resonances in the base structure.

It is worth noting that the passive sensitivity $\mathcal{P}$ for equipment resonances holds for all four cases listed in Table 2.1 – in particular for the ratio of isolated to unisolated velocity at both equipment terminals 2 and 3. The effect of equipment flexibility on $\mathcal{P}$ depends only on the equipment input mobility at the interface terminal 2, and does not depend on whether terminals 2 and 3 remain in phase for frequencies above the equipment resonance $\bar{\omega}_e$. Thus, the equipment mode may be of either the global or appendage type [70].

2.6 State Space Methods

In the previous sections the transmissibility and isolator passive sensitivity of mechanical isolation systems were derived in the frequency domain, primarily to develop insight for low order problems. State space methods provide an alternate means to describe the isolator system dynamics, and are attractive for high order systems and for situations in which the isolator is attached to base structures that are also modelled in state space form. The analysis in this section is restricted to that of the classical passive isolator of Section 2.4, mounted to bases of different mobility. Isolators mounted to rigid bases are modelled first, and then the state models are modified to permit base flexibility.

Isolation on a Rigid Base: When the base is rigid, the problem of finding the mount passive sensitivity reduces to that of finding the mount transmissibility since the two functions are identical. For the passive isolation problem, a state model is formed by selecting a suitable state vector and by correctly modelling the way in which the disturbance drives the system dynamics. The simplest example of state space transmissibility is for force isolation on a rigid base. From Section 2.3, the force transmissibility of Eqs. 2.48 and 2.82 is

$$T_F(s) = \frac{F_1}{F_E^b} = \frac{2\zeta_o\omega_o s + \omega_o^2}{s^2 + 2\zeta_o\omega_o s + \omega_o^2} \tag{2.105}$$

where F_E^b is the blocked (disturbance) force that acts on the isolated mass, and F_1 is the reaction force on the base, as shown in Figure 2.7. The state space model of this simple second order system is realized in phase-variable (or observability) canonical form as

$$\begin{bmatrix} \dot{\eta}_2 \\ \ddot{\eta}_2 \end{bmatrix} = \begin{bmatrix} 0 & 1 \\ -\omega_o^2 & -2\zeta_o\omega_o \end{bmatrix} \begin{bmatrix} \eta_2 \\ \dot{\eta}_2 \end{bmatrix} + \begin{bmatrix} 0 \\ 1 \end{bmatrix} F_E^b$$

$$F_1 = \begin{bmatrix} \omega_o^2 & 2\zeta_o\omega_o \end{bmatrix} \begin{bmatrix} \eta_2 \\ \dot{\eta}_2 \end{bmatrix} \tag{2.106}$$

or

$$\begin{aligned} \dot{\boldsymbol{\eta}} &= A\boldsymbol{\eta} + Lu \\ y &= C\boldsymbol{\eta} \end{aligned} \tag{2.107}$$

where the state vector $[\eta_2 \quad \dot{\eta}_2]^T$ is equal to the physical state vector $[x_2 \quad \dot{x}_2]^T$. Note that the disturbance F_E^b enters the system as a single force on the mass, while the output F_1 is the sum of the force both in the spring and the damper. The transmissibility is expressed as

$$T_F(s) = C\left(sI - A\right)^{-1} L \tag{2.108}$$

The velocity isolation problem from a vibrating, rigid base illustrated in Figure 2.10 has the identical transmissibility function to Eq. 2.105, but the state space must be constructed differently: the force on the isolated mass is due to the force in both the spring and the damper, which in turn are functions of both the base disturbance velocity v_B^f and position $x_B^f = v_B^f/s$. The differential equation for the second order mechanical system is recovered from the transmissibility of Eq. 2.105 using the fact that $T_F = T_{v_2}$ and that $T_{v_2} = v_2/v_B^f = x_2/x_B^f$:

$$s^2x_2 + 2\zeta_o\omega_o s x_2 + \omega_o^2 x_2 = \omega_o^2 x_B^f + 2\zeta_o\omega_o v_B^f \tag{2.109}$$

This differential equation can be represented by a two-state model (used widely in the literature for active suspension of road vehicles [36]) in which the state vector is chosen as $\boldsymbol{\eta} = [x_2 - x_B^f \quad v_2]^T$, representing the spring deflection and mass velocity:

$$\begin{bmatrix} \dot{x}_2 - \dot{x}_B^f \\ \dot{v}_2 \end{bmatrix} = \begin{bmatrix} 0 & 1 \\ -\omega_o^2 & -2\zeta_o\omega_o \end{bmatrix} \begin{bmatrix} x_2 - x_B^f \\ v_2 \end{bmatrix} + \begin{bmatrix} -1 \\ 2\zeta_o\omega_o \end{bmatrix} v_B^f$$

$$v_2 = \begin{bmatrix} 0 & 1 \end{bmatrix} \begin{bmatrix} x_2 - x_B^f \\ v_2 \end{bmatrix} \tag{2.110}$$

The transmissibility is calculated again by Eq. 2.108 with the appropriate substitutions for the system matrices. One disadvantage of this state representation is that the mass position x_2 cannot be calculated directly; for this reason an alternate three-state model is proposed in which both mass position and velocity are states. Given the prescribed disturbance v_B^f, an additional right hand side forcing term x_B^f is required, but in order to preserve observability in the system equations the pure integration must be approximated by a stable integrator. A disturbance state z is introduced that approximates the base motion x_B^f:

$$\dot{z} = \frac{1}{s + \omega_z} v_B^f \qquad \omega_z << \omega_o \tag{2.111}$$

$$z \approx x_B^f \qquad \omega >> \omega_z \tag{2.112}$$

In practice, ω_z can be set much lower than ω_o (say $0.001\omega_o$) so that in the vicinity of passive mount resonance, z very nearly equals x_B^f. Had the prescribed disturbance been a base acceleration, then a two-state stable integrator would be constructed. Using Eq. 2.111, the state dynamics of Eq. 2.110 become

$$\begin{bmatrix} \dot{x}_2 \\ \ddot{x}_2 \\ \dot{z} \end{bmatrix} = \begin{bmatrix} 0 & 1 & 0 \\ -\omega_o^2 & -2\zeta_o\omega_o & \omega_o^2 \\ 0 & 0 & \omega_z \end{bmatrix} \begin{bmatrix} x_2 \\ \dot{x}_2 \\ z \end{bmatrix} + \begin{bmatrix} 0 \\ 2\zeta_o\omega_o \\ 1 \end{bmatrix} v_B^f$$

$$y = \begin{bmatrix} 0 & 1 & 0 \end{bmatrix} \begin{bmatrix} x_2 \\ \dot{x}_2 \\ z \end{bmatrix} \tag{2.113}$$

The transmissibility is calculated using Eq. 2.108.

Velocity Isolation on a Flexible Base: To derive expressions for the mount passive sensitivity, the velocity transmissibility for both hardmounted and softmounted

equipment will first be expressed in state space form, and the ratio of these transmissibilities provides the mount passive sensitivity according to Eq. 2.62. When the base exhibits dynamics, the base displacement and velocity are no longer treated as exogenous inputs, but are instead modelled as states (or outputs that are linear combinations of states) of a dynamic system.

Consider the general model for velocity isolation illustrated in Figure 2.8. It is assumed that the structural input mobility Y_B at terminal 1 is known, as well as the hardmounted disturbance velocity $v_2^{(u)}$ at the equipment input terminal (which is coincident with terminal 1 for the hardmount case). In order to simplify the analysis, it is assumed that the hardmount velocity $v_2^{(u)}$ is due to a fictitious external force f_e that acts at the base output terminal 1. A general n^{th} order state space model of the (uncoupled) base structure is expressed as

$$\begin{aligned} \dot{\eta}_b &= A_b \eta_b + B_b u_b \\ x_1 &= C_p \eta_b \\ \dot{x}_1 &= C_v \eta_b \end{aligned} \tag{2.114}$$

The system outputs are position and velocity of terminal 1; in most cases a feedthrough term can be avoided in the output equation by appending a high frequency second-order rolloff to any true displacement feedthrough terms, without loss of accuracy at low frequency ranges of interest. For the uncoupled beam the input u_b represents the external force f_e applied to terminal 1.

When the beam is coupled to a softmount isolator, the input u_b at the interface point 1 is the sum of the fictitious external disturbance force f_e and the internal reaction force f_1

$$u_b = f_e + f_1 \tag{2.115}$$

where f_1 is determined by the spring and damping forces

$$\begin{aligned} f_1 &= k(x_2 - x_1) + c(\dot{x}_2 - \dot{x}_1) \\ &= kx_2 - c\dot{x}_2 - kC_p\eta_b - cC_v\eta_b \end{aligned} \tag{2.116}$$

When this expression for f_1 is substituted into Eq. 2.115 and Eq. 2.114 the state

dynamics of the base become

$$\dot{\eta}_b = (A_b - B_b k C_p - B_b c C_v)\eta_b + B_b k x_2 + B_b c \dot{x}_2 + B_b f_e \tag{2.117}$$

The differential equation for the isolator is then modified by substituting the output equation of Eq. 2.106 into Eq. 2.109

$$s^2 x_2 = -\omega_o^2 x_2 - 2\zeta_o \omega_o s x_2 + (\omega_o^2 C_p + 2\zeta_o \omega_o C_v)\eta_b \tag{2.118}$$

The last two equations can now be assembled in state space form for the softmounted isolator. To remain consistent with previous derivations, the substitutions $k = m\omega_o^2$ and $c = 2\zeta_o m \omega_o$ are made in the assembled matrices A_a, B_a, C_a:

$$\begin{bmatrix} \dot{x}_2 \\ \ddot{x}_2 \\ \dot{\eta}_b \end{bmatrix} = \begin{bmatrix} 0 & 1 & 0 \\ -\omega_o^2 & -2\zeta_o\omega_o & (\omega_o^2 C_p + 2\zeta_o \omega_o C_v) \\ B_b m \omega_o^2 & B_b 2\zeta_o \omega_o m & \tilde{A}_b \end{bmatrix} \begin{bmatrix} x_2 \\ \dot{x}_2 \\ \eta_b \end{bmatrix} + \begin{bmatrix} 0 \\ 0 \\ B_b \end{bmatrix} f_e$$

$$\dot{x}_2 = \begin{bmatrix} 0 & 1 & 0 \end{bmatrix} \eta_b \tag{2.119}$$

where

$$\tilde{A}_b = A_b - B_b m \omega_o^2 C_p - B_b 2\zeta_o \omega_o m C_v \tag{2.120}$$

From here it is straightforward to calculate the transfer function from disturbance to output

$$G(s) = C_a (sI - A_a)^{-1} B_a \tag{2.121}$$

as well as the softmount velocity autospectrum at terminal 2

$$\Phi_{22}^{SM}(s) = |G(s)|^2 \, \Phi_{f_e f_e}(s) \tag{2.122}$$

where $\Phi_{f_e f_e}(s)$ is the autospectrum of the disturbance force. Output variance can be calculated in state space form using Lyapunov methods or in the frequency domain by integrating the autospectrum $\Phi_{22}^{SM}(s)$ over all frequencies.

In order to calculate mount passive sensitivity, the autospectrum for the hard-mounted equipment is required. In this situation there are no dynamics in the isolator, but the equipment mass loads the interface terminal 1 of the base by the inertial

reaction force

$$\begin{aligned} f_1 &= -m\ddot{x}_1 \\ &= -mC_v\dot{\eta}_b \\ &= -mC_vA\eta_b - mC_vBu \\ &= -mC_vA\eta_b - mC_vBf_1 - mC_vBf_e \end{aligned} \tag{2.123}$$

or

$$f_1 = -\frac{mC_vA}{1+mC_vB}\eta_b - \frac{mC_vB}{1+mC_vB}f_e \tag{2.124}$$

leading to the hardmount state equations for the base

$$\dot{\eta}_b = \left[I - \frac{mBC_v}{1+mC_vB} \right] A\eta_b + B\left[I - \frac{mC_vB}{1+mC_vB} \right] f_e$$

$$y = \left[1 \quad 0 \right] \eta_b \tag{2.125}$$

The hardmount output autospectrum is calculated using Eqs. 2.121 and 2.122. Finally, the magnitude of the passive sensitivity function at each frequency is expressed as

$$|\mathcal{P}(s)| = \left[\frac{\Phi_{22}^{SM}(s)}{\Phi_{22}^{HM}(s)} \right]^{1/2} \tag{2.126}$$

This equation produces the same passive sensitivity magnitude as Eq. 2.86, using base mobility Y_B calculated from Eq. 2.114:

$$Y_B(s) = C_v(sI - A)^{-1}B_b \tag{2.127}$$

Example 1: Base Modelled as Resonant Mode: Let the base be modelled by a single mode as in Eq. 2.91, only here let the output of the state model be both position and velocity at terminal 1:

$$\begin{aligned} \begin{bmatrix} \dot{\eta}_1 \\ \ddot{\eta}_1 \end{bmatrix} &= \begin{bmatrix} 0 & 1 \\ -\omega_b^2 & -2\zeta_b\omega_b \end{bmatrix} \begin{bmatrix} \eta_1 \\ \dot{\eta}_1 \end{bmatrix} + \begin{bmatrix} 0 \\ \phi_b^2 \end{bmatrix} u \\ \begin{bmatrix} x_1 \\ \dot{x}_1 \end{bmatrix} &= \begin{bmatrix} 1 & 0 \\ 0 & 1 \end{bmatrix} \begin{bmatrix} \eta_1 \\ \dot{\eta}_1 \end{bmatrix} \end{aligned} \tag{2.128}$$

When this state space model for the base is substituted into the coupled isolator/base state equations of Eq. 2.119, the assembled state space matrices A_a, B_a, and C_a for this example become

$$\begin{bmatrix} \dot{x}_2 \\ \ddot{x}_2 \\ \dot{\eta}_1 \\ \ddot{\eta}_1 \end{bmatrix} = \begin{bmatrix} 0 & 1 & 0 & 0 \\ -\omega_o^2 & -2\zeta_o\omega_o & \omega_o^2 & 2\zeta_o\omega_o \\ 0 & 0 & 0 & 1 \\ (\omega_o^2 m\phi_b^2) & (2\zeta_o\omega_o m\phi_b^2) & (-\omega_b^2 - \omega_o^2 m\phi_b^2) & (-2\zeta_b\omega_b - 2\zeta_o\omega_o m\phi_b^2) \end{bmatrix} \begin{bmatrix} x_2 \\ \dot{x}_2 \\ \eta_1 \\ \dot{\eta}_1 \end{bmatrix} + \begin{bmatrix} 0 \\ 0 \\ 0 \\ \phi_b^2 \end{bmatrix} f_e$$

$$\begin{bmatrix} y \end{bmatrix} = \begin{bmatrix} 1 & 0 & 0 & 0 \end{bmatrix} \begin{bmatrix} x_2 \\ \dot{x}_2 \\ \eta_1 \\ \dot{\eta}_1 \end{bmatrix} \tag{2.129}$$

Similarly, the hardmount state and output equations become

$$\begin{bmatrix} \dot{\eta}_1 \\ \ddot{\eta}_1 \end{bmatrix} = \begin{bmatrix} 0 & 1 \\ -\dfrac{\omega_b^2}{1+m\phi_b^2} & -\dfrac{2\zeta_b\omega_b}{1+m\phi_b^2} \end{bmatrix} \begin{bmatrix} \eta_1 \\ \dot{\eta}_1 \end{bmatrix} + \begin{bmatrix} 0 \\ \dfrac{\phi_b^2}{1+m\phi_b^2} \end{bmatrix} f_e$$

$$\begin{bmatrix} y \end{bmatrix} = \begin{bmatrix} 1 & 0 \end{bmatrix} \begin{bmatrix} \eta_1 \\ \dot{\eta}_1 \end{bmatrix} \tag{2.130}$$

It can be observed in the state equations for the hardmounted and softmounted isolator that as the dimensionless ratio $m\phi_b^2$ goes to zero, the original uncoupled isolator and beam equations are recovered. The output position and velocity of the base, driven by external disturbance f_e, become exogenous disturbance inputs to the uncoupled isolator states $[\ x_2 \quad \dot{x}_2\ ]^T$.

Example 2: Base Modelled as a Bernoulli-Euler Beam: Let the base to which the isolator is mounted be modelled as a Bernoulli-Euler beam that includes translational and rotational rigid body modes. Figure 2.21 illustrates the beam free

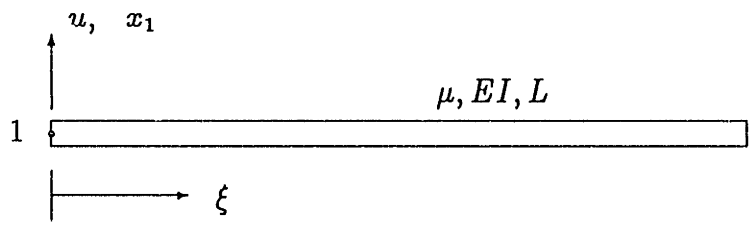

Figure 2.21: Base structure modelled as free-free Bernoulli-Euler beam. The isolator interface is at the beam tip $\xi = 0$.

body diagram, in which isolator interface terminal 1 of Figure 2.8 is assumed to be at spanwise coordinate $\xi = 0$. The beam transverse deflection at $\xi = 0$ is interface motion x_1, and as before the force u acting on the base is the sum of external disturbance and internal reaction forces $u = f_e + f_1$. The collocated beam transfer function from force u to position x_1 is first expressed in modal form:

$$\frac{x_1(s)}{u(s)} = \frac{A_r}{s^2} + \sum_{i=1}^{k} \frac{\phi_i(0)\phi_i(0)}{s^2 + 2\zeta_i\omega_i s + \omega_i^2} \tag{2.131}$$

The residue A_r of the rigid body mode is determined from the contributions of the translational and rotational modes to be

$$A_r = \phi_r(0)\phi_r(0) = \frac{4}{\mu L} \tag{2.132}$$

where μL equals the beam mass M_b, and $\phi_r(0)$ is defined as the rigid body mode shape evaluated at $\xi = 0$. The mass normalized eigenvectors are defined by

$$\phi(\xi) = \frac{1}{\sqrt{\mu L}}\psi_i(\xi) \tag{2.133}$$

$$\int_0^L \phi_i(\xi)\phi_j(\xi) = \delta_{ij} \tag{2.134}$$

where the free-free modeshapes $\psi_i(\xi)$ are from Blevins [13], normalized such that $\psi_i(0) = 2$. The residue A_i of each flexible mode is

$$A_i = \phi_i(0)\phi_i(0) = \frac{4}{\mu L} \tag{2.135}$$

Therefore the driving point modal mass $\bar{m}_i$ for each mode (including the rigid body mode) are the same and equal to

$$\bar{m}_i = \frac{1}{\phi_i(0)\phi_i(0)} = \frac{\mu L}{4} \tag{2.136}$$

For the following simulations, two dimensionless ratios are chosen to scale the beam mass and first natural frequency with respect to the mass m and (rigid base) resonance of the passive mount:

$$\frac{m}{\mu L} = 0.1 \tag{2.137}$$

$$\frac{\omega_o}{\omega_1} = 0.5 \quad \text{or} \quad 2.0 \tag{2.138}$$

The base structure state matrices become

$$A_b = \begin{bmatrix} 0 & I \\ -\Omega^2 & -2\zeta_i\Omega \end{bmatrix} \qquad B_b = \begin{bmatrix} 0 \\ \Phi^T \end{bmatrix} \tag{2.139}$$

$$C_b = \begin{bmatrix} C_p \\ C_v \end{bmatrix} = \begin{bmatrix} \Phi & 0 \\ 0 & \Phi \end{bmatrix} \qquad D_b = \begin{bmatrix} 0 \\ 0 \end{bmatrix} \tag{2.140}$$

where

$$\Omega^2 = \text{diag}\begin{bmatrix} 0 & \omega_1^2 & \omega_2^2 & \cdots & \omega_k^2 \end{bmatrix} \tag{2.141}$$

$$-2\zeta_i\Omega = \text{diag}\begin{bmatrix} 0 & -2\zeta_1\omega_1 & -2\zeta_2\omega_2 & \cdots & -2\zeta_k\omega_k \end{bmatrix} \tag{2.142}$$

$$\Phi = \begin{bmatrix} \phi_r(0) & \phi_1(0) & \phi_2(0) & \ldots & \phi_k(0) \end{bmatrix} \tag{2.143}$$

The effect of truncating the number of modes to k creates a nonzero D_b matrix, but this can be avoided by including a high frequency mode that has as its residue the residual displacement feedthrough term, or by including sufficiently many modes in the plant model (20 were used in the current simulation) so that the feedthrough term becomes negligible. The state matrices A_b, B_b and C_b can be substituted into the coupled isolator/base state equations of Eq. 2.119 and Eq. 2.125. Using Eqs. 2.121 and 2.122, the autospectrum of the mass output velocity v_2 can be calculated for both the hardmount and softmount cases, as shown in Figure 2.22. Damping on all flexible modes is assumed to be 1%, and the first beam resonance is assumed to occur at $2\omega_o$. The functions are plotted versus frequency normalized by the isolator resonance ω_o. In the simulation, the disturbance force autospectrum is modelled as a white noise signal with constant power spectral density $\Phi_{f_e f_e} = 1\text{N}^2/\text{Hz}$. The coupling parameter

β_b is the same for each mode, and is expressed as

$$\beta_b = \frac{m\phi_i^2}{2\zeta_i} = \frac{2m}{\zeta_i \mu L} \qquad i = 0, 1, 2, \ldots k \tag{2.144}$$

Given $\zeta_i = 0.01$ and $m/\mu L = 0.1$, this results in $\beta_b = 20$. This level of modal coupling is rather high, but it helps to illustrate the effect of base flexibility. Also shown in Figure 2.22 is an approximation to the softmount autospectrum, calculated by applying the rigid base passive sensitivity of Eq. 2.105 to the hardmount data:

$$\hat{\Phi}_{22}^{SM}(s) = |\mathcal{P}_r(s)|^2 \, \Phi_{22}^{HM}(s) \tag{2.145}$$

The actual mount passive sensitivity $\mathcal{P}$ – calculated by either Eq. 2.64 or Eq. 2.126 – is compared in Figure 2.23 to the passive sensitivity for an isolator mounted to a rigid base. It can be seen in both figures that the effect of the base flexibility is to shift the mount mode higher (since at ω_o the beam mobility is due primarily to its rigid body mode) which is consistent with the prior example in Figure 2.13. When isolated, each resonant mode shifts to a higher frequency, and except for the lowest beam mode at $\bar{\omega} = 2$, the damping in each mode is essentially unchanged. These observations are also consistent with the effects observed for the single mode example in Figure 2.18, which differs from the current simulation in that no rigid body mode is included. It is also evident in Figure 2.22 that the rigid base passive sensitivity, when applied to the original hardmount data, overestimates the isolator performance (underestimates the remaining energy) at high frequencies, and overestimates the energy remaining in the mode near $\bar{\omega} = 2$.

It should be noted here that while the passive sensitivity functions plotted in Figure 2.23 have been derived for the velocity isolation problem, the functions apply equally well to the force isolation problem, as is shown in Section 2.3.3. Additionally, the passive sensitivity functions in Figure 2.23 apply to the situation in which the base is rigid but the equipment exhibits modal flexibility, using the substitutions derived in Section 2.3.3.

Based on this example, it is worth asking whether an approximation for the isolator passive sensitivity can be determined based on our knowledge of the average base

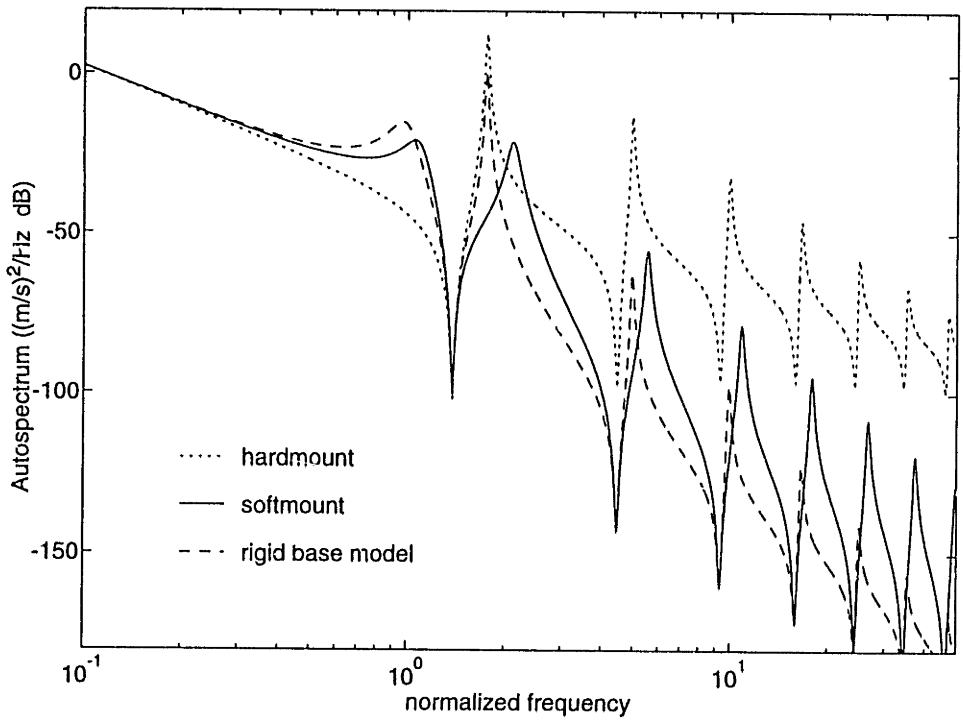

Figure 2.22: Velocity autospectra of equipment mounted to a B-E beam. Parameters: $m/M_b = 0.1$, $\omega_1/\omega_o = 2$, $\beta_b = 20$. Softmount trace represents sensitivity $\mathcal{P}_r(\bar{s})$ applied to hardmount spectrum.

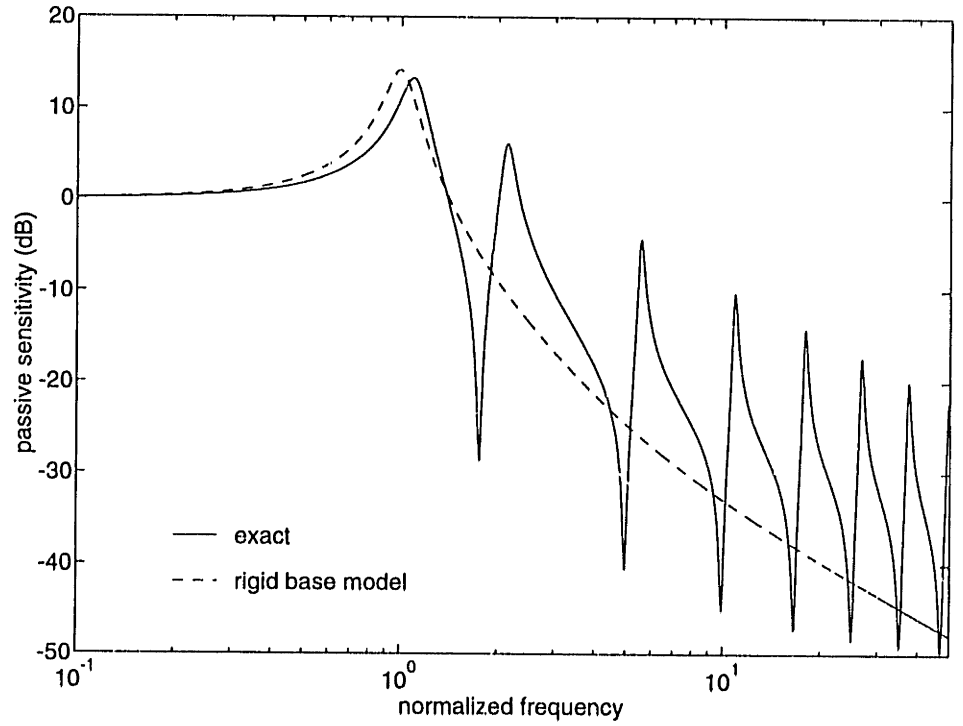

Figure 2.23: Passive sensitivity $\mathcal{P}(\bar{s})$ for base modelled as B-E beam, vs rigid base sensitivity $\mathcal{P}_r(\bar{s})$. Parameters: $m/M_b = 0.1$, $\omega_1/\omega_o = 2$, $\beta_b = 20$.

mobility, one that will be more accurate than the rigid base approximation but less complicated than including the full n^{th} order expression for the base mobility. The next section explores using two different types of averaged base mobility models – namely, the dereverberated mobility and the average magnitude models – to improve the softmount passive sensitivity prediction beyond that provided by the rigid base model.

2.7 Average Mobility Models for Isolator Passive Sensitivity

In this section it is shown how frequency averaged models of the base input mobility can be used in the expression for mount passive sensitivity to account for the performance reduction caused by base flexibility. Specifically, we wish to find an average base mobility $\tilde{Y}_B$ to be used in computing a modified passive sensitivity function $\tilde{\mathcal{P}}$ based on Eq. 2.86

$$\tilde{\mathcal{P}}(s) = \frac{1 + \dfrac{\tilde{Y}_B}{Y_E}}{1 + \dfrac{Y_I}{Y_E} + \dfrac{\tilde{Y}_B}{Y_E}} \tag{2.146}$$

that is both more accurate than that based on the hardmount approximation ($Y_B = 0$) and much simpler than the passive sensitivity based on the full order expression for Y_B. The modified effectiveness $\tilde{\mathcal{P}}$ can then be used with a model of the hardmount autospectrum (obtained by simulation or measurement) to make an estimate of the resulting softmount autospectrum at input terminal 2 of the isolated equipment:

$$\hat{\Phi}_{22}^{SM}(s) = \left|\tilde{\mathcal{P}}(s)\right|^2 \Phi_{22}^{HM}(s) \tag{2.147}$$

The motivation for this is that in practice, although the local equipment and isolator mobilities Y_E and Y_I are well characterized, the base structure to which the isolator is attached may not be. The base structure uncertainty lies primarily with the individual modal parameters – that is, individual modal damping, frequency and residue are not known – yet it may be possible to model the average properties of the structure. For

example, stiffness or mass may be approximated over certain frequency ranges, or reasonable bounds may be placed on the magnitude of eigenvectors, damping, or lowest natural frequency. In addition, the average RMS disturbance motion of the base structure may be estimated or bounded as a function of frequency.

Use of averaged structural models is prevalent in the literature. Statistical Energy Analysis [44], or SEA, employs models of average structure input impedance to investigate power dissipation and power flow between dynamic systems. Models are based on estimates of modal density, damping and eigenvector magnitude over frequency intervals (typically octave or third octave bands); prediction accuracy of these methods increases as the modal density increases relative to the chosen frequency intervals. For modally dense structures, Skudrzyk [65] characterized the magnitude of structural input mobility with respect to the mean-value response. MacMartin [45] showed experimentally how a dereverberated mobility model of a structure could be used to actively match the impedance of an actuator to maximize energy dissipation when the structural mobility is highly uncertain. In a similar experiment, Lurie et. al. [42] used feedback to match the impedance of an active piezoelectric strut to the backbone of the collocated structural impedance in order to maximize energy dissipation in a truss structure. However, the use of averaged base mobility models has not yet been applied to the passive isolation problem. In the remainder of this section, the Bernoulli-Euler beam example introduced in Section 2.5 is used as an illustration.

Average Autospectrum: Consider the hardmount velocity autospectrum Φ_{22}^{HM} for the beam example in Figure 2.22. In Figure 2.24 this function is compared to a histogram representing the linear average of this positive and real valued function in each of 12 logarithmically spaced frequency intervals. The number of frequency bins was chosen such that over the range of flexible modes, most bins contained at least one resonant peak. In each frequency bin, the linear area under each curve (representing velocity variance) is identical to that of the exact model. A similar average can be performed for the softmount autospectrum Φ_{22}^{SM} of Figure 2.22, and based on Eq. 2.126, an averaged mount passive sensitivity in each frequency interval

i can be defined as

$$|\mathcal{P}_a(\Delta\omega_i)| = \left[\frac{\Phi_{22}^{SM}(\Delta\omega_i)}{\Phi_{22}^{HM}(\Delta\omega_i)}\right]^{1/2} \tag{2.148}$$

The symbol $\mathcal{P}_a$ is used to represent the histogram based on the ratio of these individual frequency averages. In effect, this averaged function represents a type of "truth" test for the isolator, in that the purpose of the isolator is to reduce energy transmission from the vibrating base to the sensitive equipment. The averaged mount passive sensitivity $\mathcal{P}_a$ is plotted in Figure 2.25 versus the full order passive sensitivity $\mathcal{P}$ and the rigid base passive sensitivity $\mathcal{P}_r$. The discrepancy between $\mathcal{P}_r$ and $\mathcal{P}_a$ is large above mount resonance ω_o (at $\bar{\omega} = 1$) due to the presence of significant mobility in the base structure.

Passive Sensitivity Based on Dereverberated Base Mobility: A dereverberated, or log-magnitude frequency average, model of the base input mobility provides a convenient low order model $\tilde{Y}_B$ for substitution into the modified passive sensitivity function $\tilde{\mathcal{P}}$ in Eq. 2.146. The term *dereverberated* is drawn from the literature in wave modelling of flexible structures [45], [49] in which the local response of a structure due to an applied force is modelled as the sum of the direct response from outgoing waves, and the reverberant response due to waves that have reflected off boundaries and returned to the input terminal. The dereverberated response includes only the direct field response, which corresponds to a structure that is infinite in extent, or to one in which the boundary conditions are perfectly absorbing. The connection between the wave interpretation and the steady state modal response comes from the fact that ignoring the reverberant field is equivalent to the log-magnitude average of the structural input mobility, which in turn is the same as assuming that all structural modes are critically damped [65]. The dereverberated mobility is therefore a smooth function that follows the backbone of the log magnitude curve.

The dereverberated mobility Y_B^d for the free-free beam of Example 2 is plotted in Figure 2.26 versus the exact input mobility. The function Y_B^d is obtained by critically damping all flexible modes in the base model, and can be well approximated over the range 0.1 to 50 Hz by a 5th order polynomial of real poles and zeros (not shown).

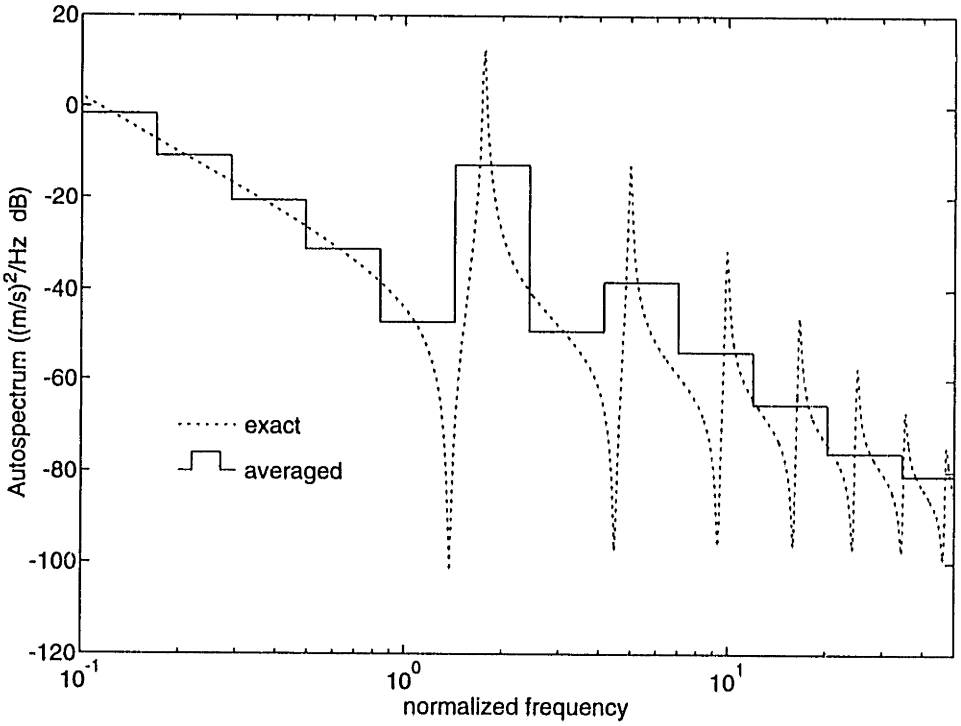

Figure 2.24: Averaged and exact hardmount velocity autospectrum for B-E beam of Example 2.

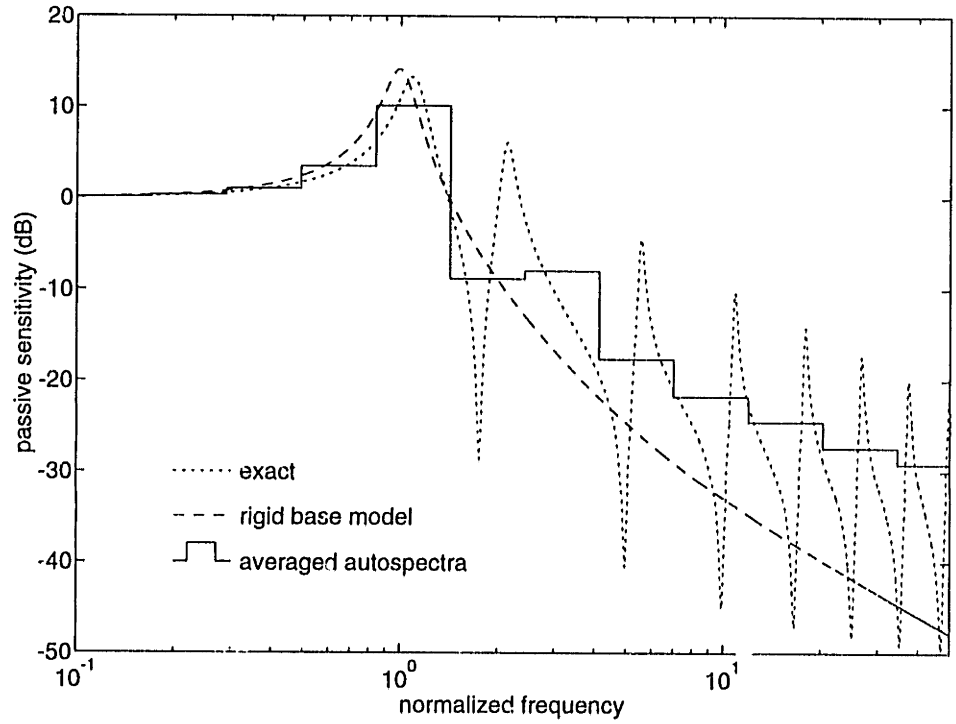

Figure 2.25: Mount passive sensitivity for Example 2: averaged passive sensitivity ratio $\mathcal{P}_a(\bar{s})$ compared to exact $\mathcal{P}(\bar{s})$ and rigid base mode $\mathcal{P}_r(\bar{s})$. The function $\mathcal{P}_a(\bar{s})$ is computed as the ratio of softmount and hardmount averaged autospectra.

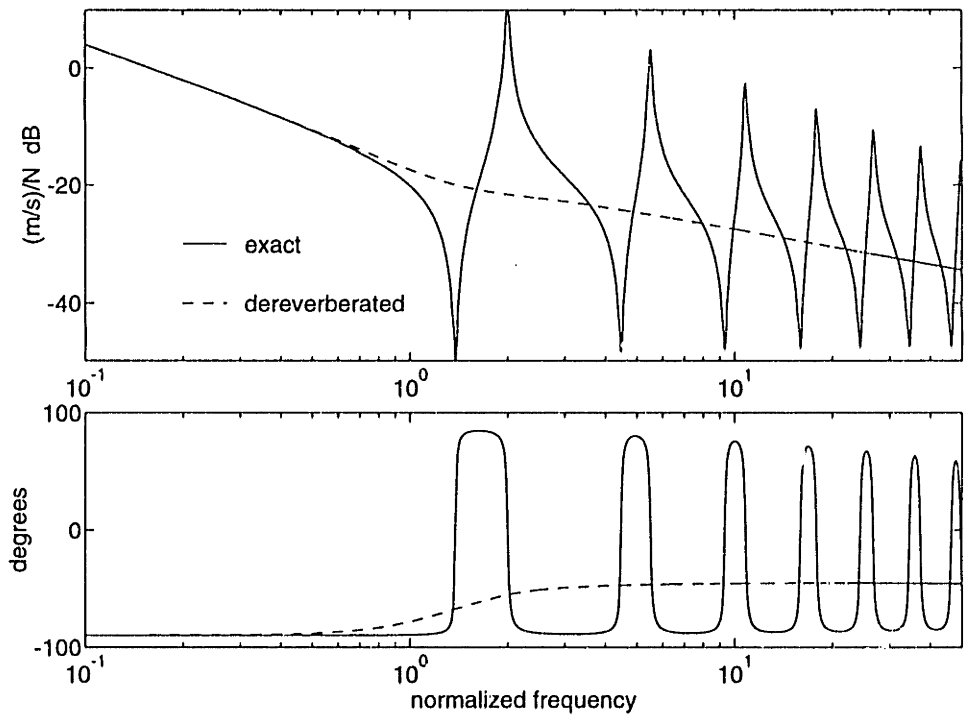

Figure 2.26: Dereverberated mobility $Y_B^d(\bar{s})$ and exact mobility $Y_B(\bar{s})$ at tip of free-free B-E beam.

Observe that Y_B^d follows the "backbone" of the exact mobility, and correctly models the rigid body response. The high frequency asymptote rolls off at $s^{-1/2}$, with phase $-45°$.

Figure 2.27 is a plot of the modified passive sensitivity function $\tilde{\mathcal{P}}$ that is obtained when the dereverberated mobility model $Y_B^d(s)$ is substituted for $\tilde{Y}_B$ in Eq. 2.146. In this simulation the first (uncoupled) beam resonance ω_1 is assumed to occur at $2\omega_o$. The modified passive sensitivity $\tilde{\mathcal{P}}$ can be considered to be an improvement over the rigid base passive sensitivity $\mathcal{P}_r$ for two reasons: the shift in natural frequency of the mount is captured, and the function magnitude is closer to the averaged sensitivity $\mathcal{P}_a$ at high frequencies. However the discrepancy between the modified passive sensitivity $\tilde{\mathcal{P}}$ and the averaged passive sensitivity $\mathcal{P}_\dashv$ is as much as 9 dB at $50\omega_o$.

The discrepancy is even more pronounced in Figure 2.28, in which the first beam natural frequency is set at $0.5\omega_o$. In simulations it was observed that including beam modes with natural frequencies in the range of $0.5\omega_o$ to $2\omega_o$ in the dereverberated model greatly improves the accuracy of the modified passive sensitivity in the vicin-

ity of ω_o. However, in all cases the high frequency magnitude remains in error. This discrepancy arises because the increase in passive sensitivity magnitude at high frequency depends on the magnitude of the base mobility. The dereverberated mobility, based on the log magnitude frequency average, will always underestimate the average linear magnitude, which may be considerably larger than the logarithmic mean when the base is lightly damped.

Passive Sensitivity Based on Linear Magnitude Average of Base Mobility: In light of the previous results, a base mobility model will now be constructed that is based on a linear magnitude average. The input mobility of the beam is again plotted in Figure 2.29, along with a histogram representing an average of the magnitude in each of 12 logarithmically spaced frequency bands. A 7^{th} order function was chosen to approximate the histogram for each of these bands; this function is defined as the *average magnitude* function Y_B^a. In comparison with Figure 2.26, the average magnitude is greater than the dereverberated mobility magnitude, and has asymptotic phase less than -45 degrees, indicating a log magnitude rolloff steeper than $s^{-1/2}$. This is due to the fact that as frequency goes to infinity, the beam mobility exhibits a high degree of modal overlap, and the linear and logarithmic averages of the mobility magnitude converge. Figure 2.30 is a plot of the modified passive sensitivity function $\tilde{\mathcal{P}}$ obtained by substituting the average magnitude model Y_B^a for $\tilde{Y}_b$ in Eq. 2.146. The plot clearly shows that the agreement between the averaged autospectra histogram $\mathcal{P}_a$ and the modified passive sensitivity $\tilde{\mathcal{P}}$ is clearly superior to that obtained for the modified passive sensitivity based on the dereverberated mobility. For the case $\omega_1 = 0.5\omega_o$ shown in Figure 2.31, the results are also good. Of course, the details of the mount passive sensitivity are lost using the averaged method, particularly near ω_o. By simulation is was determined that retaining base modes in the vicinity of $0.5\omega_o$ to $2\omega_o$ – while retaining the averaged magnitude approximation at high frequency – greatly improves the estimate of the mount passive sensitivity function near ω_o.

It is obvious by inspection of Figure 2.29 that if the average modal damping in the base structure were to decrease, then the average magnitude function Y_B^a would

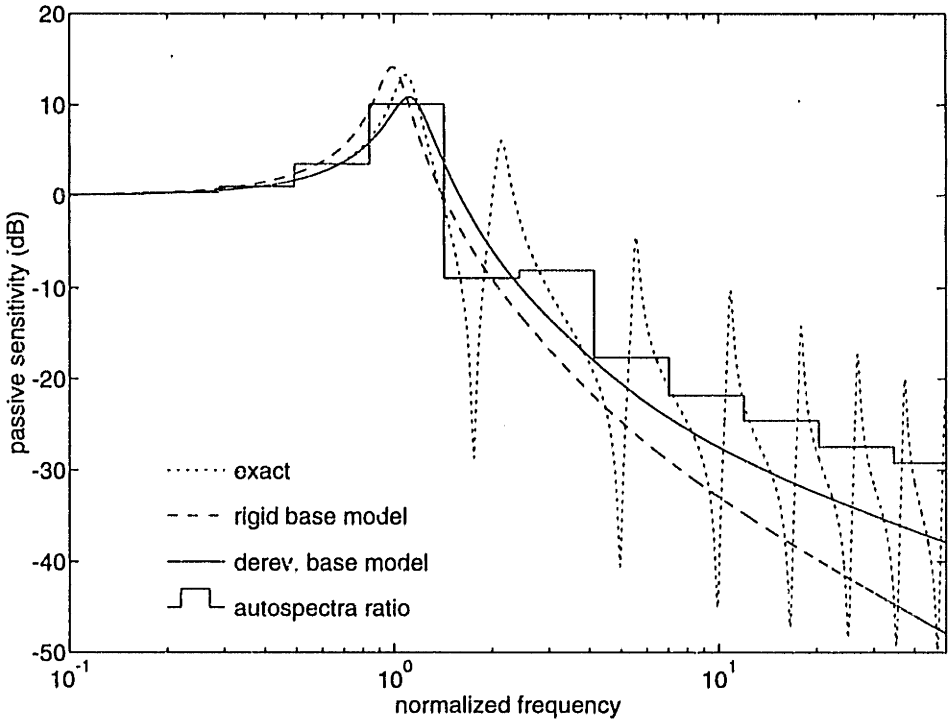

Figure 2.27: Passive sensitivity based on dereverberated base model vs autospectra ratio: Parameters: $m/M_b = 0.1$, $\omega_1/\omega_o = 2$, $\beta_b = 20$. Estimate is improved compared to rigid base passive sensitivity.

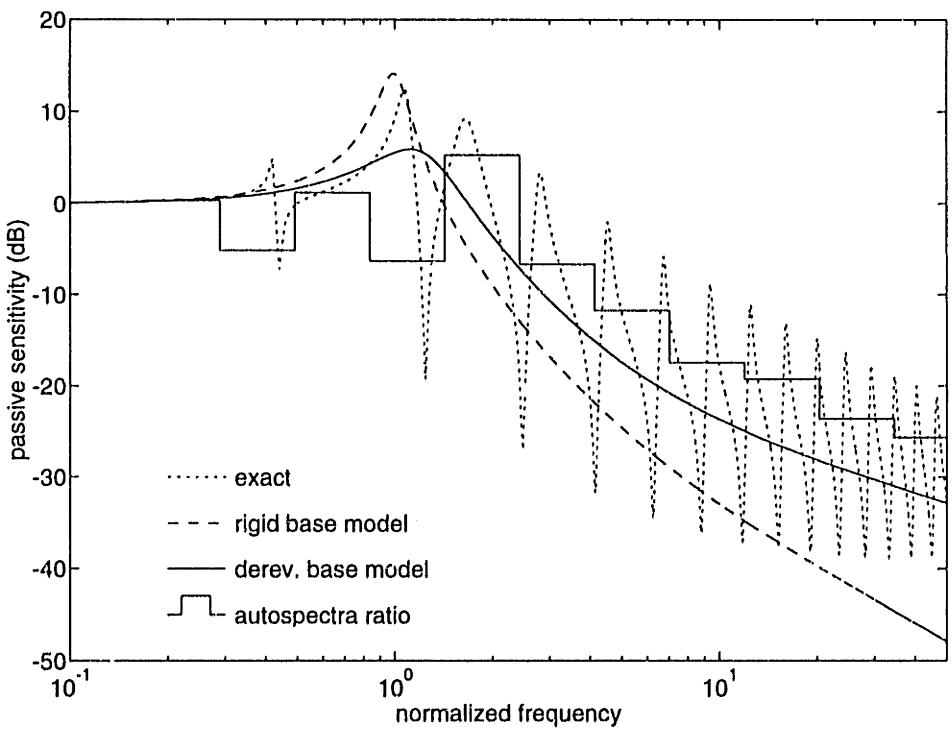

Figure 2.28: Passive sensitivity based on dereverberated base model vs autospectra ratio. Parameters: $m/M_b = 0.1$, $\omega_1/\omega_o = 0.5$, $\beta_b = 20$.

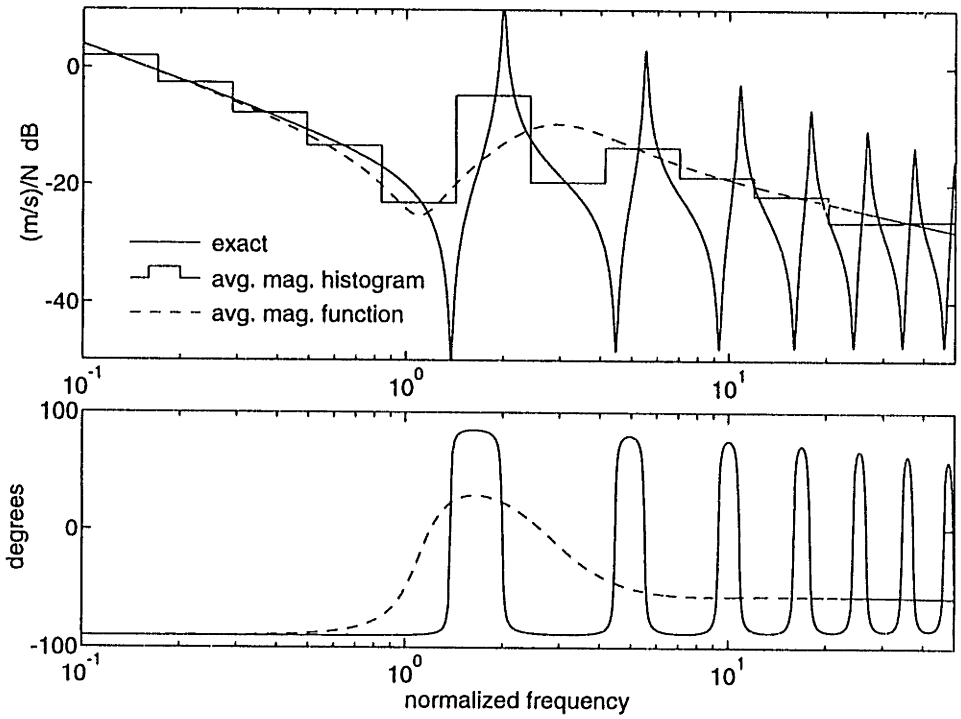

Figure 2.29: Linearly averaged magnitude $Y_B^a(\bar{s})$ and exact mobility at tip of free-free Bernoulli-Euler beam.

necessarily be greater; the dereverberated mobility, on the other hand, would be unchanged. Therefore, the damping of the base structure influences the mount passive sensitivity, in addition to any effect caused by the backbone mobility of the structure. In fact, the individual contributions to the modified passive sensitivity $\tilde{\mathcal{P}}$ of both the backbone and the damping can be identified in Figures 2.27 and 2.30, respectively.

From these examples, it is evident that for moderate or strong modal coupling, the average magnitude response of the base must be considered when evaluating the performance of a passive isolator. However, for low levels of modal coupling – roughly $\beta_b < 1$ – the rigid-base effectiveness $\mathcal{P}_r$ is nearly correct in predicting mount performance.

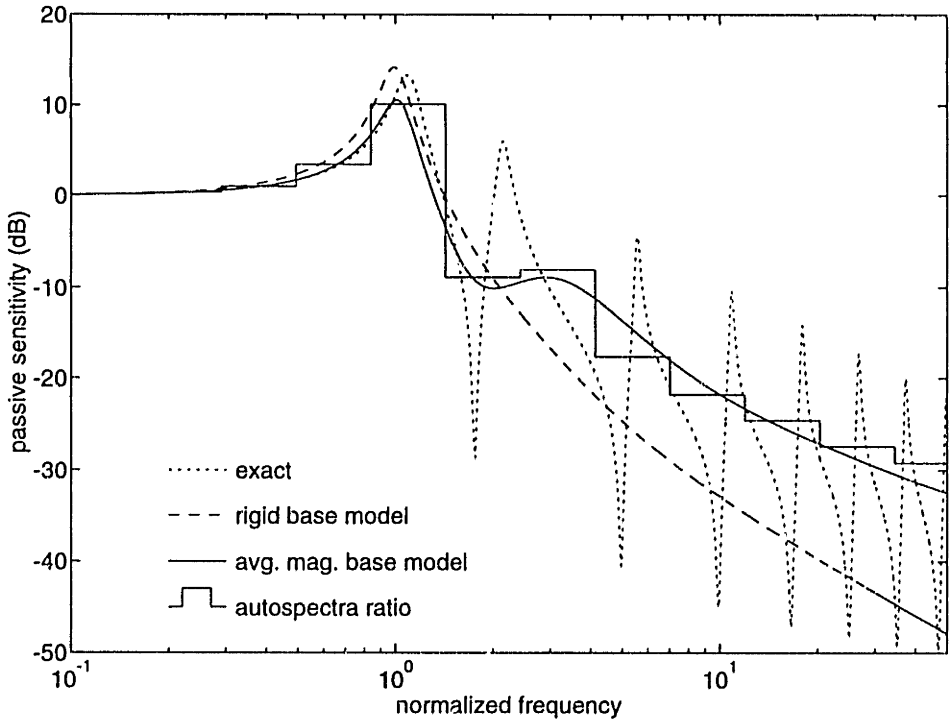

Figure 2.30: Passive sensitivity based on linearly averaged magnitude vs autospectra ratio. Parameters: $m/M_b = 0.1$, $\omega_1/\omega_o = 2$, $\beta_b = 20$. Modified passive sensitivity $\tilde{\mathcal{P}}(\bar{s})$ matches the averaged passive sensitivity $\mathcal{P}_a(\bar{s})$.

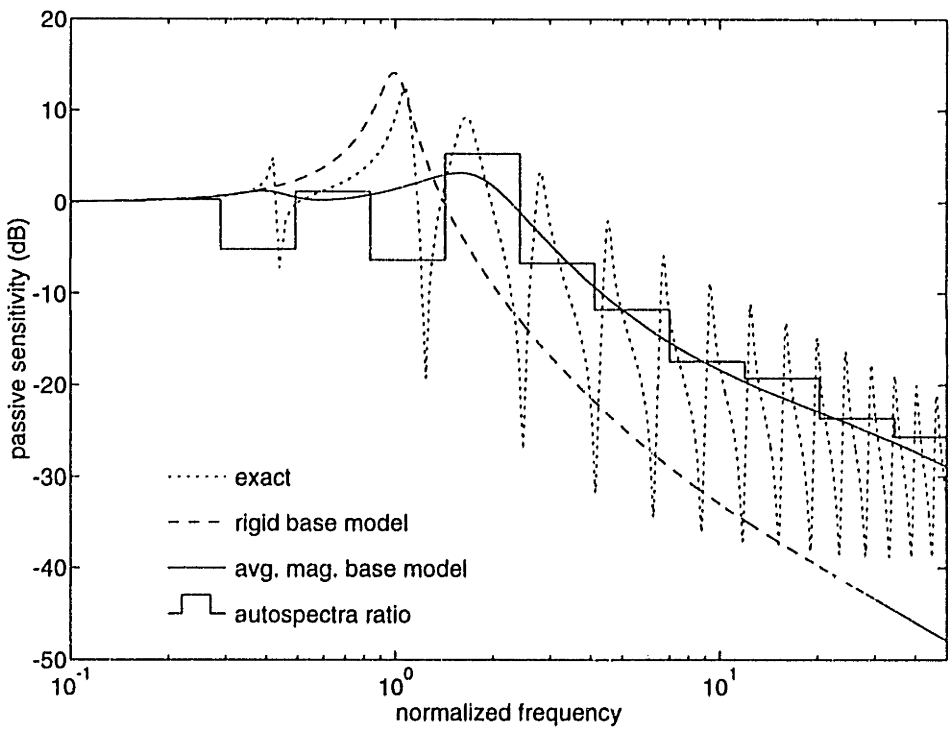

Figure 2.31: Passive sensitivity using linearly averaged magnitude vs autospectra ratio. Parameters: $m/M_b = 0.1$, $\omega_1/\omega_o = 0.5$, $\beta_b = 20$.

2.8 Summary

In this section the concepts of mount transmissibility and passive sensitivity are studied for the general force and isolation problems using four-pole mobility methods. The analysis leads to the important simplification that the single function of mount passive sensitivity $\mathcal{P}$ can be used to describe nearly all the performance functions of interest for both force and velocity isolation; this conclusion is not affected by the presence of base or equipment flexibility. The effect of flexibility on the passive sensitivity function $\mathcal{P}$ is investigated for several simple order models and the impact on mount performance is characterized in terms of simple dimensionless parameters. Flexibility in the base structure and isolated equipment is found to have identical parametric effects on mount passive sensitivity. State models are introduced and used to simulate a velocity isolation problem on a modally rich base structure. Finally, it is shown by example how a low order function that approximates the average linear magnitude of the base input mobility can be used in a modified passive sensitivity function to provide an improved estimate of the energy transmitted by the passive isolation mount.

Chapter 3

Plant Transfer Functions for Active Isolation

3.1 Objectives

The term *active isolation* refers to a feedback control architecture in which sensors and actuators that are local to the isolation mount are connected by feedback for the purpose of actively modifying the mount passive sensitivity $\mathcal{P}$ or transmissibility T. Local sensors include acceleration of the isolated equipment, interface gap or force, and acceleration of the base structure at the isolator interface. In the introduction, four configurations of local actuation are shown in Figure 1.5 for an isolation mount; in each case the force is applied at points that are collocated with the interface terminals of either the equipment or base structure.

Ideally the mount performance and stability are independent of the base to which it is mounted. In Chapter 2 it is shown that when base or equipment flexibility becomes large (in a dimensionless sense) the passive sensitivity $\mathcal{P}$ of the mount is increased, making the mount less effective. Since the performance of the active mount depends upon the compensation of local sensor/actuator transfer functions, the effect of flexibility on these transfer functions must be considered. When the perturbations to the loop gain due to base flexibility are sufficiently small, the performance and stability of the active mount will be similar to that for a rigid base mounting. This

chapter investigates the practical limits of ignoring base flexibility in the active mount compensator design.

To study this problem, general models for active isolation are investigated in the frequency domain using the four-pole mobility analysis for simple lumped parameter models of base flexibility. The analysis is restricted to the parallel actuator configuration of Figure 1.5(a), and to a special case of series isolation illustrated in Figure 1.5(b). Similarities are shown for the effects of base and equipment flexibility on the plant transfer functions, and a parametric multiplicative error model is constructed to account for unmodelled base or equipment modal flexibility. Dereverberated mobility models of the base are shown to improve models of transfer functions in the presence of flexibility. Finally, the results of the analysis are summarized by a discussion of the effects of flexibility on the closed loop mount stability.

Relevant Literature: Several studies and many experimental demonstrations are reported in the literature for broadband active isolation design in which rigid body models are assumed for the base and isolated equipment. Su et al. [75] study the closed loop transmissibility achievable with feedback of absolute and relative position, velocity and acceleration of local mount variables, and the effect of actuator dynamics on mount performance. Sinha and Kao [68] present a direct design approach using equipment acceleration and gap as feedback to obtain a specified closed loop transmissibility. A modern control synthesis for active vehicle suspension is investigated by Thompson [79].

Some recent studies have considered flexibility of the base structure during controller design for an active mount. Spanos *et al.* [71] employ classical control techniques for force feedback for equipment mounted to a flexible structure. Watters *et al.* [82] study feedback sensor selection for the active isolation of machinery disturbances from a modally rich base structure. A thorough review of active isolation research and development prior to 1968 is provided by Ruzicka [60].

This chapter does not include closed loop simulations or provide a tutorial on closed loop design for active mounts. It is assumed that well-known classical or

modern control methods can be used to design compensators based on the nominal model (assumed rigid base and equipment modelled as a mass); typically these models are low-order and do not involve lightly damped modes. What the chapter does discuss, however, is how base or equipment flexibility might impact such control designs, and what the implications are for the choice of feedback sensor and local mount hardware design. The dimensionless analysis presented applies to isolation mounts that are either soft or stiff, and is relevant to control designs that are either broadband or narrowband.

3.2 Parallel Actuator Model

The general parallel active isolation problem is illustrated in Figure 3.1. A passive isolator I is placed between equipment E and base B to attenuate transmission of disturbances across the interface. The mount is made active by the control force f_a applied between terminals 1 and 2 (in parallel with isolator I) in order to modify the passive sensitivity $\mathcal{P}$.

The transfer functions between f_a and local response variables are independent of the disturbance source, and are therefore relevant to either the force or velocity isolation problems introduced in Chapter 2. When $f_a = 0$, Figure 3.1 is identical to the passive isolator models in Figure 2.8 and Figure 2.9. In the following analysis the four-pole mobility method is used to derive system transfer functions from the input force f_a to the local output variables listed in Table 3.1.

The relationship between force F_1 and velocity v_1 at the interface to the base structure from Eq. 2.53, (with base disturbance v_B^f set to zero), is expressed in matrix form as

$$0 = \begin{bmatrix} Y_B & 1 \end{bmatrix} \begin{bmatrix} F_1 \\ v_1 \end{bmatrix} \tag{3.1}$$

In Figure 3.1, the elements between terminals 1 and 2 – a passive isolator in parallel with a pure force actuator – are the same as the actuator model illustrated in Figure 2.4. Using Eq. 2.33, the forces and velocities across the interface are expressed

Table 3.1: Transfer functions for parallel actuator model.

sensor	transfer function	symbol
equipment (output) acceleration	$\frac{a_3}{f_a}$	G_1
equipment (interface) acceleration	$\frac{a_2}{f_a}$	G_2
interface force (2)	$\frac{F_2}{f_a}$	G_3
interface force (1)	$\frac{F_1}{f_a}$	G_4
gap	$\frac{x_2 - x_1}{f_a}$	G_5
base acceleration	$\frac{a_1}{f_a}$	G_6

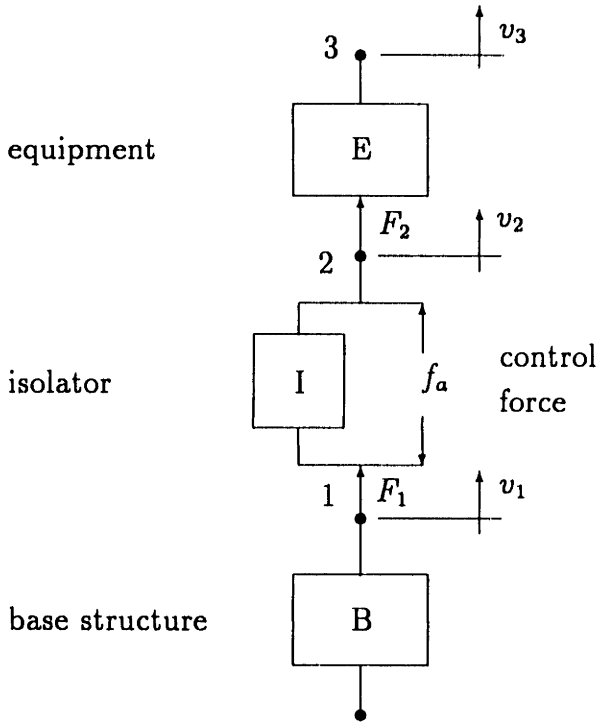

Figure 3.1: The general parallel actuator model. An actuator applies a commanded force in parallel to a passive isolator.

as

$$\begin{bmatrix} F_1 \\ v_1 \end{bmatrix} = \begin{bmatrix} \dfrac{1}{(T_v)_{21}} & \dfrac{1}{Y_{12}^f} \\ Y_{12}^b & \dfrac{1}{(T_v)_{12}} \end{bmatrix} \begin{bmatrix} F_2 \\ v_2 \end{bmatrix} + \begin{bmatrix} 1 - \dfrac{1}{(T_v)_{21}} \\ -Y_{12}^b \end{bmatrix} f_a \tag{3.2}$$

The equipment four-pole model is taken from Eq. 2.40

$$\begin{bmatrix} F_2 \\ v_2 \end{bmatrix} = \begin{bmatrix} \dfrac{1}{Y_{23}^f} \\ \dfrac{1}{(T_v)_{23}} \end{bmatrix} v_3 \tag{3.3}$$

Substitution of Eq. 3.3 and Eq. 3.2 into Eq. 3.1 yields

$$v_3 = \frac{Y_{12}^b + Y_B\left(\dfrac{1}{(T_v)_{21}} - 1\right)}{\dfrac{1}{(T_v)_{12}(T_v)_{23}} + \dfrac{Y_{12}^b}{Y_{23}^f} + Y_B\left(\dfrac{1}{(T_v)_{21}Y_{23}^f} + \dfrac{1}{(T_v)_{23}Y_{12}^f}\right)} f_a \tag{3.4}$$

which upon multiplication of numerator and denominator by $(T_v)_{23}$ and application of Eq. 2.45 leads to

$$v_3 = \frac{N(s)}{D(s)} f_a = \frac{(T_v)_{23}\left[Y_{12}^b + Y_B\left(\dfrac{1}{(T_v)_{21}} - 1\right)\right]}{\dfrac{1}{(T_v)_{12}} + \dfrac{Y_{12}^b}{Y_E} + Y_B\left(\dfrac{1}{(T_v)_{21}Y_E} + \dfrac{1}{Y_{12}^f}\right)} f_a \tag{3.5}$$

As expected, the denominator $D(s)$ is the same as that derived for the general passive isolation model in Eq. 2.46. The transfer functions between commanded force f_a and output variables are found easily by the substitution of Eq. 3.5 into Eq. 3.3 and by the substitution of Eq. 3.3 into Eq. 3.2:

(a) equipment acceleration $a_3 = sv_3$:

$$\frac{a_3}{f_a} = \frac{s(T_v)_{23}\left[Y_{12}^b + Y_B\left(\dfrac{1}{(T_v)_{21}} - 1\right)\right]}{D(s)} \tag{3.6}$$

(b) equipment acceleration $a_2 = sv_2$:

$$\frac{a_2}{f_a} = \frac{s\left[Y_{12}^b + Y_B\left(\frac{1}{(T_v)_{21}} - 1\right)\right]}{D(s)} \tag{3.7}$$

(c) interface force F_2:

$$\frac{F_2}{f_a} = \frac{\frac{Y_{12}^b}{Y_E} + Y_B\left(\frac{1}{(T_v)_{21}} - 1\right)}{D(s)} \tag{3.8}$$

(d) interface force F_1:

$$\frac{F_1}{f_a} = \frac{Y_{12}^b\left(\frac{1}{Y_E} + \frac{1}{Y_{12}^f}\right) + \frac{1}{(T_v)_{12}}\left(1 - \frac{1}{(T_v)_{21}}\right)}{D(s)} \tag{3.9}$$

(e) gap $x_2 - x_1 = (v_2 - v_1)/s$:

$$\frac{x_2 - x_1}{f_a} = \frac{Y_{12}^b\left(1 + \frac{Y_B}{Y_E} + \frac{Y_B}{Y_{12}^f}\right) - Y_B\left(1 + \frac{1 - (T_v)_{12} - (T_v)_{21}}{(T_v)_{12}(T_v)_{21}}\right)}{sD(s)} \tag{3.10}$$

(f) base acceleration $a_1 = sv_1$:

$$\frac{a_1}{f_a} = -sY_B(s)G_4(s) \tag{3.11}$$

Eqs. 3.6 to 3.11 represent the general form of the local actuator-sensor transfer functions for the parallel actuator model, for any equipment, isolator or base mobilities that can be described in four-pole form. Table 3.1 lists the symbols used to represent each transfer function. In the following, each transfer function is investigated for the classical parallel actuator model and for cases in which the base or equipment exhibit flexibility.

3.2.1 Classical Parallel Actuator Model

In Figure 3.2, equipment mass m is passively mounted to a rigid base by a viscously damped spring. A relative control force f_a is applied between terminals 1 and 2. Disturbances may enter the system either as a force disturbance on the mass m or as a velocity disturbance at the base. This model, referred to here as the *classical parallel actuator model*, is based on the following assumptions (of which the first four are identical to those for the classical passive isolation model in Section 2.4):

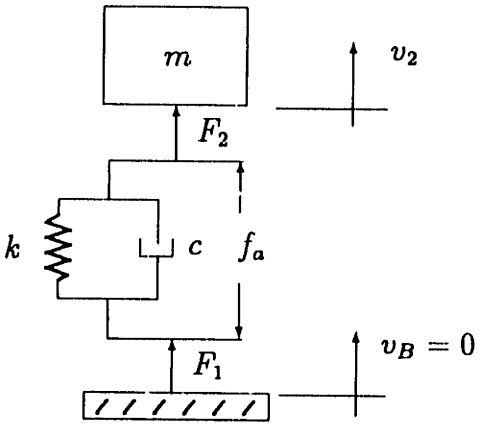

Figure 3.2: Classical parallel actuator model.

(i) base structure B is rigid

(ii) equipment E modelled as a rigid mass m

(iii) passive isolator I is massless

(iv) passive isolator I modelled as a viscously damped spring. The spring and viscous damping constants are frequency independent.

(v) ideal relative force f_a is applied between terminals 1 and 2.

The assumptions greatly simplify the plant transfer functions of Eqs. 3.6 to 3.11. Firstly, the assumption of a rigid base implies zero base mobility, or $Y_B = 0$. Based on the second assumption, the equipment input mobility becomes $Y_E = 1/ms$ and the equipment velocity transmissibility becomes $(T_v)_{23} = 1$. Additionally, terminals 2 and 3 on the equipment condense to the same point. The assumption of a massless isolator leads to $Y_{12}^f = \infty$ and $(T_v)_{12} = (T_v)_{21} = 1$; the physical interpretation is that force $F_2 = F_1$. According to the fourth assumption, the blocked transfer mobility of an isolator modelled as a massless viscously damped spring is given by Eq. 2.78, and is denoted for simplicity as Y_I. With these simplifications, the transfer functions become

$$G_1(s) = \frac{sY_I}{1 + \dfrac{Y_I}{Y_E}} \tag{3.12}$$

$$G_4(s) = \frac{\frac{Y_I}{Y_E}}{1 + \frac{Y_I}{Y_E}} \tag{3.13}$$

$$G_5(s) = \frac{\frac{1}{s}Y_I}{1 + \frac{Y_I}{Y_E}} \tag{3.14}$$

$$G_6(s) = 0 \tag{3.15}$$

where $G_2 = G_1$, and $G_3 = G_4$. Eqs. 3.12 through 3.14 can be expressed in parametric form by substituting $Y_E = 1/ms$ and $Y_I = s/(cs + k)$. In terms of normalized frequency $\bar{s} = s/\omega_o$, the three nonzero functions become

$$G_1(\bar{s}) = \frac{\frac{1}{m}\bar{s}^2}{\bar{s}^2 + 2\zeta_o\bar{s} + 1} \tag{3.16}$$

$$G_4(\bar{s}) = \frac{\bar{s}^2}{\bar{s}^2 + 2\zeta_o\bar{s} + 1} \tag{3.17}$$

$$G_5(\bar{s}) = \frac{\frac{1}{m\omega_o^2}}{\bar{s}^2 + 2\zeta_o\bar{s} + 1} \tag{3.18}$$

These three transfer functions, derived for a rigid base, are compared in the following pages to examples in which the base is modelled as flexible. For example, the transfer functions in Eqs. 3.16 and 3.18 are plotted as dashed lines in Figures 3.3 and 3.4. The parametric models assumed for base flexibility – that of a mass, damper, spring, and single resonant mode – parallel the analysis for the passive isolator in Section 2.5. The first three models of base flexibility are referred to below as *broadband flexibility.*

3.2.2 Effects of Base Flexibility

When the base structure B is not rigid, only the first assumption for the classical parallel isolator is relaxed; otherwise the remaining assumptions hold. Therefore, $G_2 = G_1$ (equipment is a rigid mass m) and $G_3 = G_4$ (isolator is massless). With Y_B retained, the transfer functions of Eqs. 3.6 to 3.11 become

$$G_1(s) = \frac{sY_I}{1 + \frac{Y_I}{Y_E} + \frac{Y_B}{Y_E}} \tag{3.19}$$

$$G_4(s) = \frac{\dfrac{Y_I}{Y_E}}{1 + \dfrac{Y_I}{Y_E} + \dfrac{Y_B}{Y_E}} \tag{3.20}$$

$$G_5(s) = \frac{\frac{1}{s}Y_I\left(1 + \dfrac{Y_B}{Y_E}\right)}{1 + \dfrac{Y_I}{Y_E} + \dfrac{Y_B}{Y_E}} \tag{3.21}$$

$$G_6(s) = \frac{-sY_I\left(\dfrac{Y_B}{Y_E}\right)}{1 + \dfrac{Y_I}{Y_E} + \dfrac{Y_B}{Y_E}} \tag{3.22}$$

When compared to the rigid base transfer functions of Eqs. 3.12 to 3.14, it is evident in the above equations that Y_B/Y_E is a perturbation term. Table 2.2 lists expressions for this term when the base mobility Y_B is modelled as a mass, spring, or damper. Recovery of the rigid base transfer functions in Eqs. 3.12 to 3.14 is expected as the perturbation term goes to zero. Because the perturbation term appears as a factor in the numerator of G_6 in Eq. 3.22, $G_6 \to 0$ as $Y_B/Y_E \to 0$, which is consistent with a base that is rigid.

In all cases in which the equipment E can be modelled as a rigid mass m, the equipment mobility is expressed as $Y_E = 1/ms$ and Eqs. 3.19 and 3.20 only differ by a factor of m, or $G_4 = mG_1$. In order to reduce the number of plots in the following sections, only one plot is used to illustrate both G_1 and G_4/m. Later, modal flexibility is permitted in the equipment and this simplification is no longer valid.

Base Modelled by Broadband Flexibility

Base Modelled as a Mass: The output mobility of the base B is modelled as $Y_B = 1/Ms$ from Table 2.2. Using the definitions of modal parameters ω_o and ζ_o from Eq. 2.80, and substituting the expressions for Y_I and Y_E from above, the transfer functions in Eqs. 3.19 to 3.22 are expressed in terms of dimensionless frequency $\bar{s} = s/\omega_o = j\omega/\omega_o$:

$$G_1(\bar{s}) = \frac{\bar{s}^2/m}{\bar{s}^2 + 2\zeta_o\left(1 + \dfrac{m}{M}\right)\bar{s} + \left(1 + \dfrac{m}{M}\right)} \tag{3.23}$$

$$G_5(\bar{s}) = \frac{\frac{1}{m\omega_o^2}\left(1+\frac{m}{M}\right)}{\bar{s}^2 + 2\zeta_o\left(1+\frac{m}{M}\right)\bar{s} + \left(1+\frac{m}{M}\right)} \tag{3.24}$$

$$G_6(\bar{s}) = \frac{-\bar{s}^2/m\left(\frac{m}{M}\right)}{\bar{s}^2 + 2\zeta_o\left(1+\frac{m}{M}\right)\bar{s} + \left(1+\frac{m}{M}\right)} \tag{3.25}$$

where $G_4 = mG_1$. Transfer functions for G_1, G_5 and G_6 are plotted in Figures 3.3 to 3.5 for different values of the dimensionless parameter m/M. When the base is infinitely massive, or $m/M = 0$, the rigid base (classical parallel actuator) model is recovered, and is represented by a dashed line. However, the base acceleration transfer function G_6 equals zero for $m/M = 0$. The trends exhibited in Figures 3.3 to 3.5 with respect to increasing m/M – increased mount natural frequency and damping – are the same as those for the passive isolator model illustrated in Figure 2.13.

Base Modelled as a Massless Damper: In this case $Y_B = 1/C$ and the mount transfer functions (in terms of normalized frequency) become

$$G_1(\bar{s}) = \frac{\bar{s}^2/m}{\left(1+2\zeta_o\frac{m\omega_o}{C}\right)\bar{s}^2 + \left(2\zeta_o + \frac{m\omega_o}{C}\right)\bar{s} + 1} \tag{3.26}$$

$$G_5(\bar{s}) = \frac{\frac{1}{m\omega_o^2}\left(1+\frac{m\omega_o}{C}\right)}{\left(1+2\zeta_o\frac{m\omega_o}{C}\right)\bar{s}^2 + \left(2\zeta_o + \frac{m\omega_o}{C}\right)\bar{s} + 1} \tag{3.27}$$

$$G_6(\bar{s}) = \frac{-\bar{s}^3/m\left(\frac{m\omega_o}{C}\right)}{\left(1+2\zeta_o\frac{m\omega_o}{C}\right)\bar{s}^2 + \left(2\zeta_o + \frac{m\omega_o}{C}\right)\bar{s} + 1} \tag{3.28}$$

Eqs. 3.26 to 3.28 are plotted in Figures 3.6 to 3.8 for different values of the dimensionless parameter $m\omega_o/C$. The viscous damping coefficient for the isolation mount is $c = 2\zeta_o m\omega_o$. As the base damping C decreases relative to mount damping c, the mount resonance for the coupled system becomes more heavily damped.

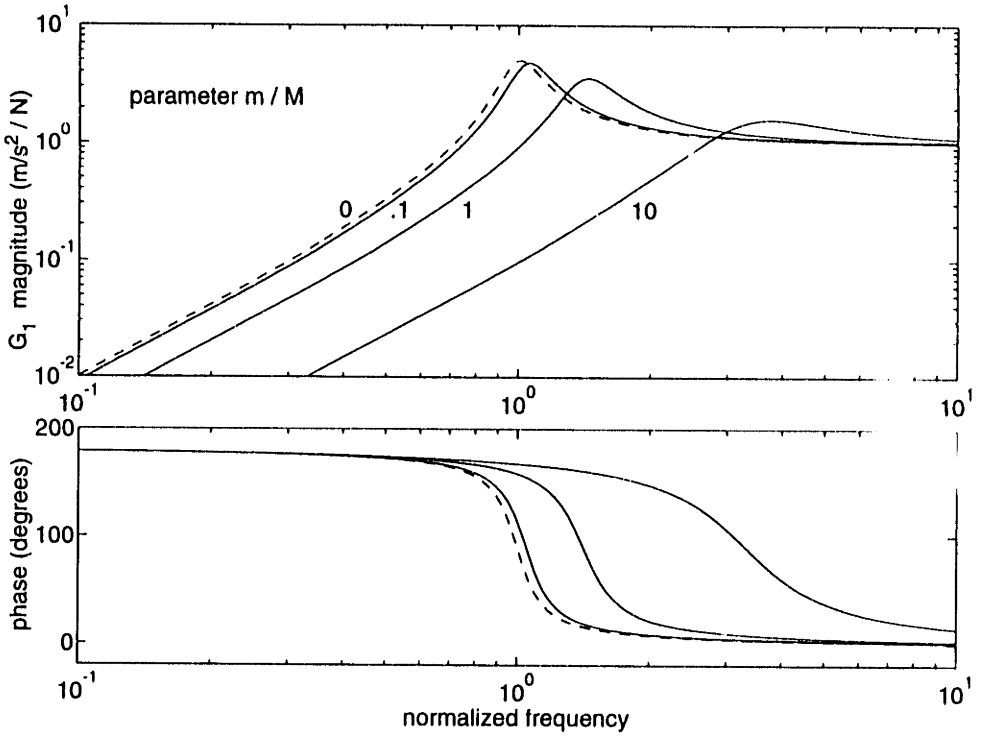

Figure 3.3: Equipment acceleration $G_1(\bar{s}) = a_3/f_a$, and scaled interface force $G_4(\bar{s}) = F_1/f_a = mG_1(\bar{s})$. Base modelled as mass M.

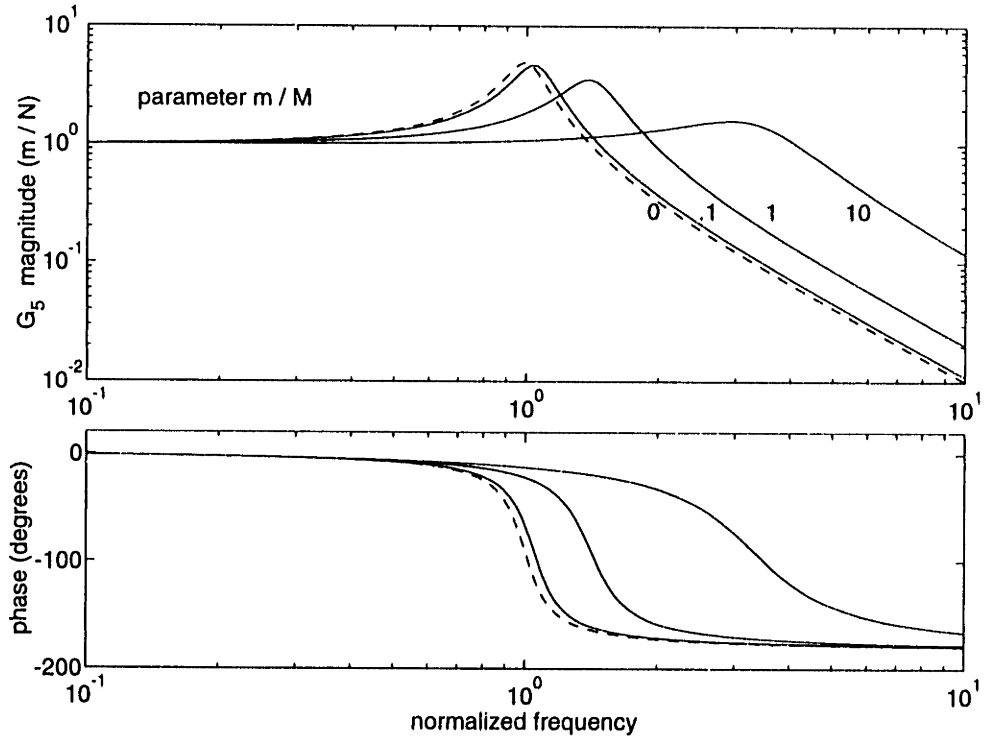

Figure 3.4: Gap $G_5(\bar{s}) = (x_2 - x_1)/f_a$. Base modelled as mass M.

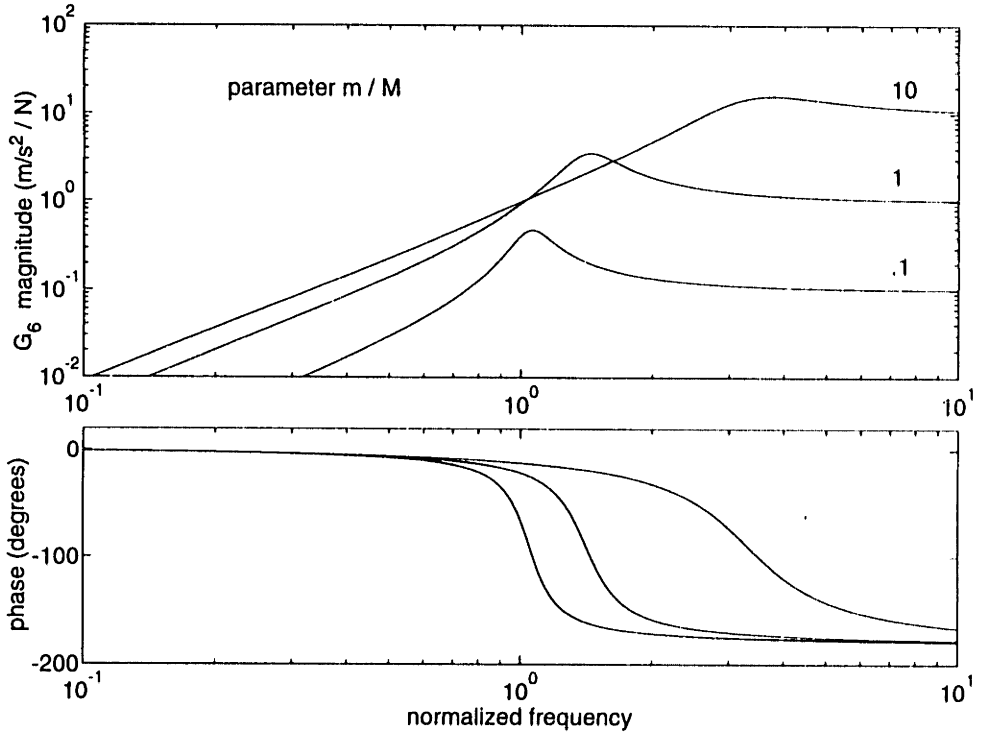

Figure 3.5: Base acceleration $G_6(\bar{s}) = a_1/f_a$. Base modelled as mass M.

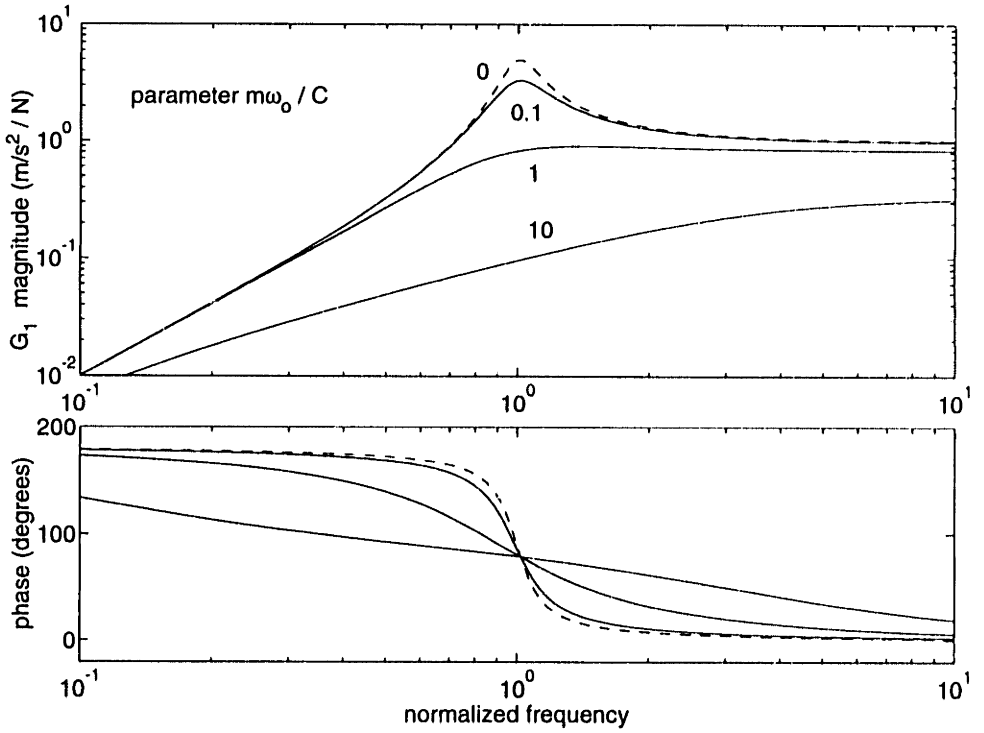

Figure 3.6: Equipment acceleration $G_1(\bar{s}) = a_3/f_a$, and scaled interface force $G_4(\bar{s}) = F_1/f_a = mG_1(\bar{s})$. Base modelled as massless damper C.

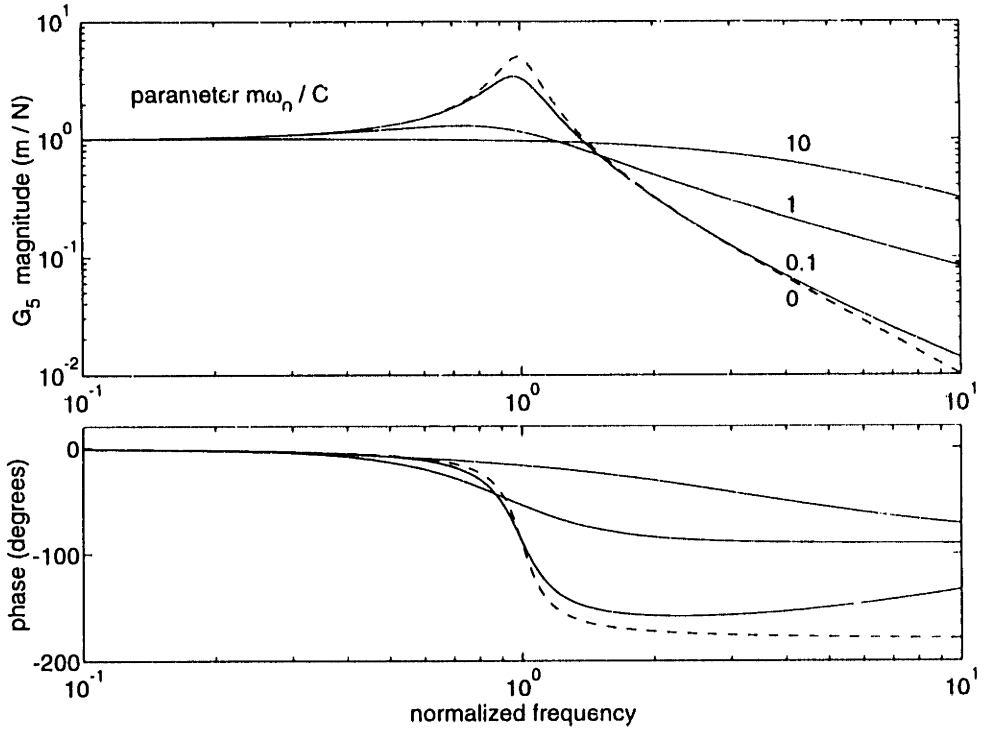

Figure 3.7: Gap $G_5(\bar{s}) = (x_2 - x_1)/f_a$. Base modelled as massless damper C.

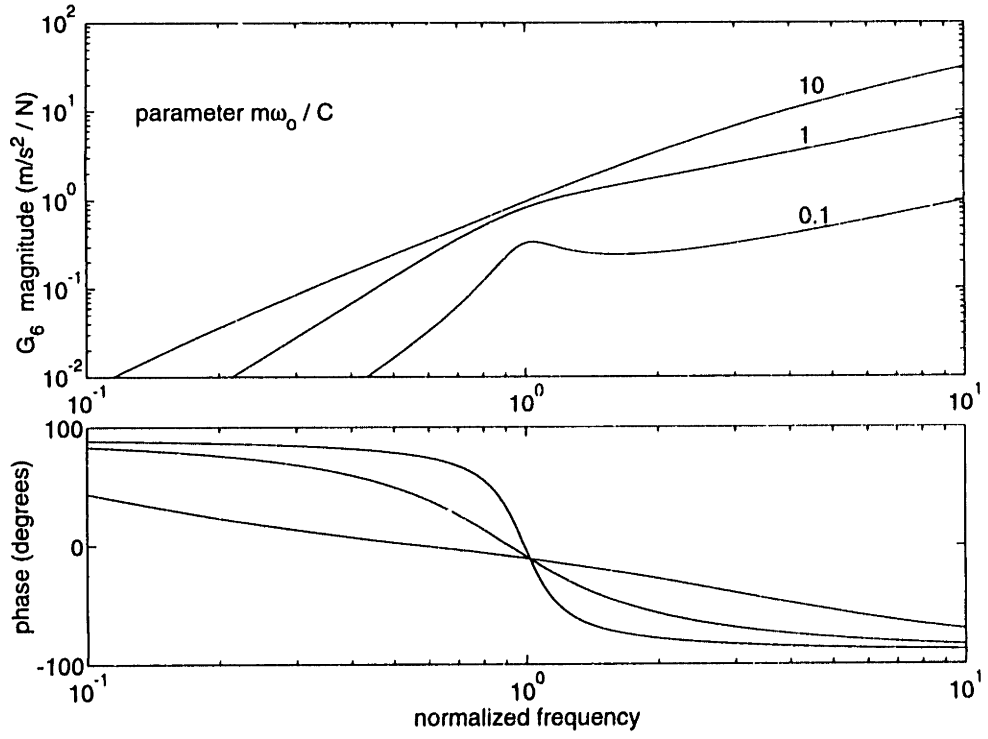

Figure 3.8: Base acceleration $G_6(\bar{s}) = a_1/f_a$. Base modelled as massless damper C.

Base Modelled as a Massless Spring: From Table 2.2 the mobility of the base modelled as a massless undamped spring is $Y_B = s/K$ and the system transfer functions of Eqs. 3.19 to 3.22 become

$$G_1(\bar{s}) = \frac{\bar{s}^2/m}{\left(2\zeta_o\frac{k}{K}\right)\bar{s}^3 + \left(1+\frac{k}{K}\right)\bar{s}^2 + 2\zeta_o\bar{s} + 1} \tag{3.29}$$

$$G_5(\bar{s}) = \frac{\frac{1}{m\omega_o^2}\left(1+\frac{k}{K}\bar{s}^2\right)}{\left(2\zeta_o\frac{k}{K}\right)\bar{s}^3 + \left(1+\frac{k}{K}\right)\bar{s}^2 + 2\zeta_o\bar{s} + 1} \tag{3.30}$$

$$G_6(\bar{s}) = \frac{-\bar{s}^4/m\left(\frac{k}{K}\right)}{\left(2\zeta_o\frac{k}{K}\right)\bar{s}^3 + \left(1+\frac{k}{K}\right)\bar{s}^2 + 2\zeta_o\bar{s} + 1} \tag{3.31}$$

The dimensionless parameter k/K governs the degree of interaction of base spring flexibility with the local mount transfer functions, as illustrated in Figures 3.9, 3.10 and 3.11. The transfer function for equipment acceleration a_3 in Figure 3.9 shows a decrease in mount natural frequency, and a decrease in mount damping ratio, for increasing values of the parameter k/K. An important observation is that the base spring mobility adds a high frequency real pole to the denominators of Eqs. 3.29 to 3.31. The real pole leads to additional phase loss (beyond 180 degrees) for both G_1 and G_6. The gap transfer function G_5 also loses phase due to the real pole, but due to an undamped complex zero pair at $\bar{\omega} = K/k$, remains bounded in phase between 0 and -180 degrees, as is expected for a collocated transfer function. In fact, because the force is applied as a pair in the interface, only gap is a collocated output variable; transfer functions to the acceleration of the equipment or base exhibit collocated characteristics only when the flexibility of equipment or base structure is small.

Base Modelled as a Single Resonant Mode

Transfer Functions for Equipment Acceleration and Force: Consider first the general expression for the acceleration transfer function G_1 in Eq. 3.19 for the

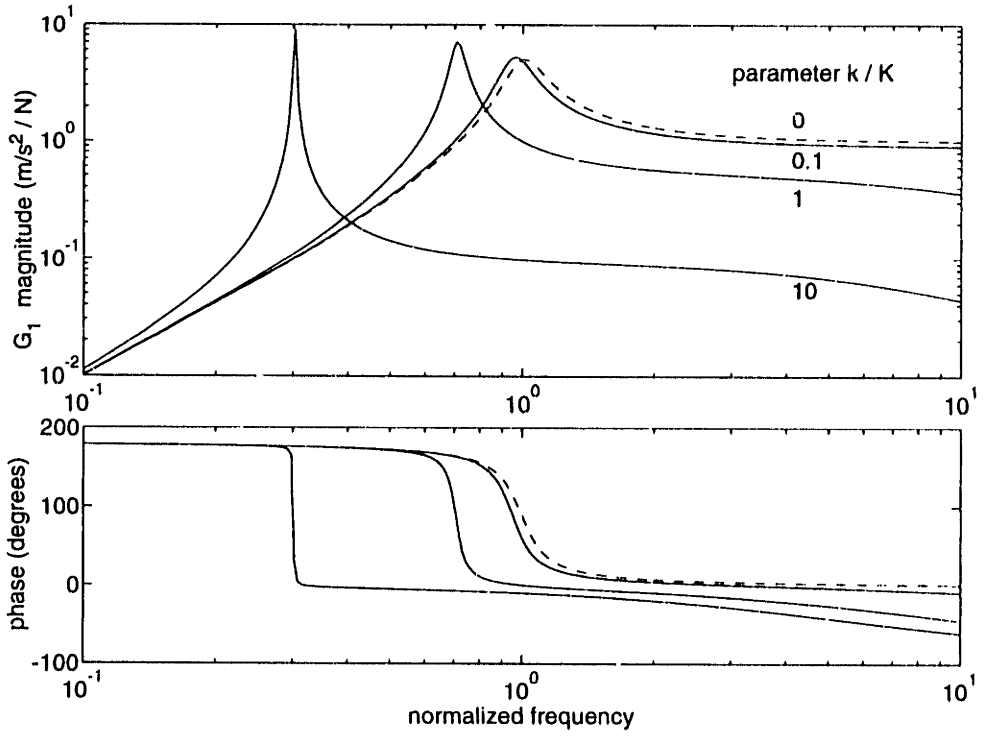

Figure 3.9: Equipment acceleration $G_1(\bar{s}) = a_3/f_a$, and scaled interface force $G_4 = F_1/f_a = mG_1$. Base modelled as massless spring K.

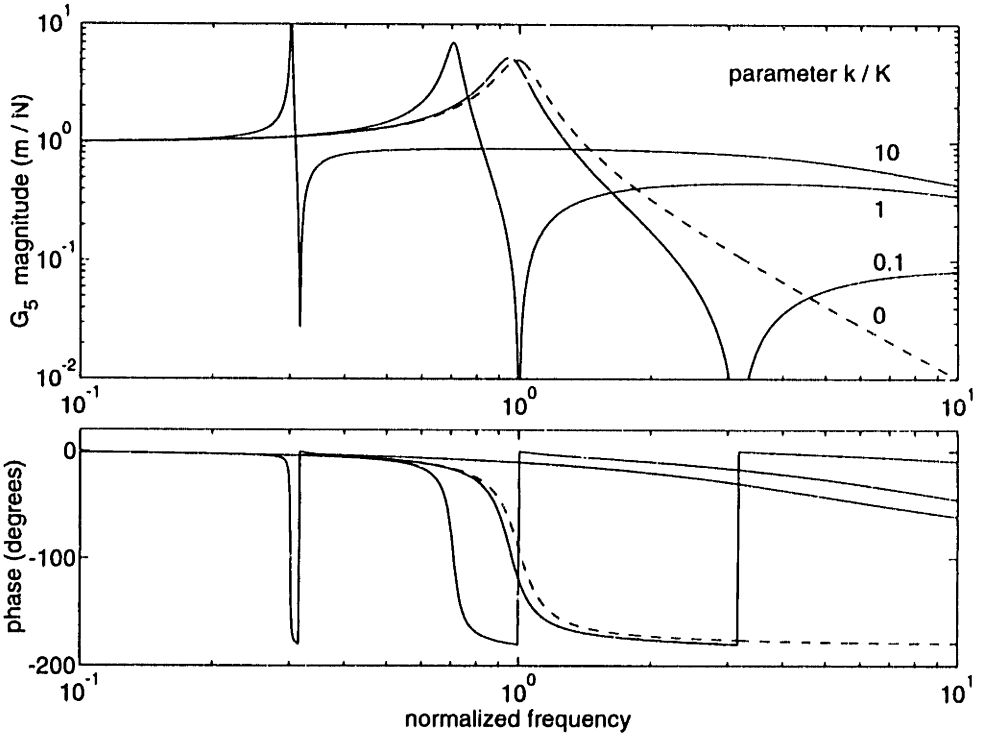

Figure 3.10: Gap $G_5(\bar{s}) = (x_2 - x_1)/f_a$. Base modelled as massless spring K.

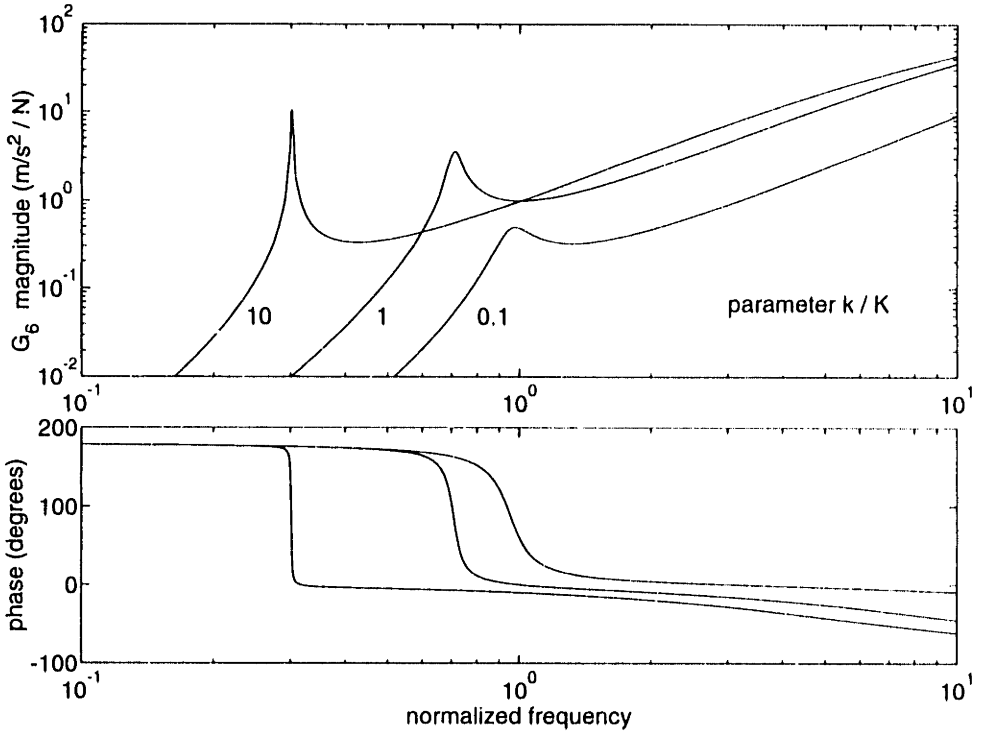

Figure 3.11: Base acceleration $G_6(\bar{s}) = a_1/f_a$. Base modelled as massless spring K.

parallel active isolator mounted to a flexible base:

$$G_1(s) = \frac{sY_I}{1 + \dfrac{Y_I}{Y_E} + \dfrac{Y_B}{Y_E}(s)} \tag{3.32}$$

which also describes the transfer function for interface force F_1 since $G_4 = mG_1$. Substitution of the expressions for $Y_I = s/(cs + k)$ and $Y_E = 1/ms$ leads to

$$G_1(s) = \frac{s^2}{s^2 m + cs + k + (k + cs)\dfrac{Y_B}{Y_E}(s)} \tag{3.33}$$

Using the definitions $k = m\omega_o^2$, $c = 2\zeta_o\omega_o m$, and $\bar{s} = s/\omega_o$, the equipment acceleration in terms of normalized frequency becomes

$$G_1(\bar{s}) = \frac{\dfrac{1}{m}\bar{s}^2}{\bar{s}^2 + 2\zeta_o\bar{s} + 1 + (1 + 2\zeta_o\bar{s})\dfrac{Y_B}{Y_E}(\bar{s})} \tag{3.34}$$

where the perturbation term in the denominator is from Eq. 2.93

$$\frac{Y_B}{Y_E}(\bar{s}) = \frac{\bar{s}^2 m\phi_b^2}{\bar{s}^2 + 2\zeta_b\bar{\omega}_b\bar{s} + \bar{\omega}_b^2} \tag{3.35}$$

The degree of coupling of the base mode into the plant transfer function G_1 depends upon (among other factors) the dimensionless frequency ratio $\bar{\omega}_b = \omega_b/\omega_o$, the ratio of base mode frequency to rigid base mount resonance. The two simplest cases to consider are low frequency ($\bar{\omega}_b \ll 1$) and high frequency ($\bar{\omega}_b \gg 1$).

Pole-Zero Spacing Below ω_o: For the low frequency case, $\bar{s}^2 \ll 1$ and $\bar{\omega}_b \ll 1$, and Eq. 3.34 is approximated by

$$\begin{aligned} G_1(\bar{s}) &= \frac{\frac{1}{m}\bar{s}^2}{1 + \frac{Y_B}{Y_E}(\bar{s})} \qquad\qquad (\bar{s}^2, \bar{\omega}_b^2) \ll 1 \\ &= \frac{\frac{1}{m}\bar{s}^2\left(\bar{s}^2 + 2\zeta_b\bar{\omega}_b\bar{s} + \bar{\omega}_b^2\right)}{\bar{s}^2\left(1 + m\phi_b^2\right) + 2\zeta_b\bar{\omega}_b\bar{s} + \bar{\omega}_b^2} \end{aligned} \tag{3.36}$$

For small base mode damping ζ_b, the base mode creates a complex zero pair in the transfer function at the frequency

$$z_i = \bar{\omega}_b \tag{3.37}$$

and the poles p_i are at the roots of the undamped characteristic equation

$$\bar{s}^2\left(1 + m\phi_b^2\right) + \bar{\omega}_b^2 = 0 \tag{3.38}$$

$$\bar{s} = \pm j\bar{\omega}_b\left(1 + m\phi_b^2\right)^{-\frac{1}{2}} \tag{3.39}$$

For values of $m\phi_b^2 = m/\bar{m}_b$ (the ratio of equipment mass to modal mass) small compared to one, to first order in $m\phi_b^2$ the plant poles p_i are at the frequency

$$p_i = \bar{\omega}_b\left(1 - \frac{m\phi_b^2}{2}\right) \qquad m\phi_b^2 \ll 1 \tag{3.40}$$

leading to a pole-zero spacing of

$$z_i - p_i = \frac{m\phi_b^2}{2}\bar{\omega}_b \tag{3.41}$$

or alternately, relative pole-zero spacing

$$\frac{z_i - p_i}{\bar{\omega}_b} = \frac{m\phi_b^2}{2} \tag{3.42}$$

The pole frequency p_i lies below the zero frequency z_i. For a base mode with large modal mass, $m\phi_b^2 \ll 1$ and the relative pole-zero spacing in Eq. 3.42 is small. The transfer function for G_1 in Eq. 3.36 then looks like the function $\bar{s}^2/m$ perturbed by a closely spaced, lightly damped pole-zero pair. This result agrees with the results of Garcia *et al.* [24], who investigated the coupling of base flexibility into the transfer function G_1 for the frequency range below mount resonance ω_o.

Pole-Zero Spacing Above ω_o: Now consider the case in which the base mode $\bar{\omega}_b$ lies above resonance, where $\bar{\omega}_b^2 \gg 1$ and $\bar{s}^2 \gg 1$ and Eq. 3.34 is approximated by

$$G_1(\bar{s}) = \frac{\frac{1}{m}\bar{s}^2}{\bar{s}^2 + (1 + 2\zeta_o\bar{s})\frac{Y_B}{Y_E}} \qquad (\bar{s}^2, \bar{\omega}_b^2) \gg 1$$

$$= \frac{\frac{1}{m}\left(\bar{s}^2 + 2\zeta_b\bar{\omega}_b\bar{s} + \bar{\omega}_b\right)}{\bar{s}^2 + \bar{s}\left(2\zeta_b\omega_b + \zeta_o m\phi_b^2\right) + \left(\bar{\omega}_b^2 + m\phi_b^2\right)} \tag{3.43}$$

Once again, the base mode creates a complex zero pair at $z_i = \bar{\omega}_b$ but now to first order in $m\phi_b^2$ the pole is at the frequency

$$p_i = \bar{\omega}_b\left(1 + \frac{m\phi_b^2}{2\bar{\omega}_b^2}\right) \qquad m\phi_b^2 \ll 1 \tag{3.44}$$

Here the pole lies above the zero frequency z_i. An important result of Eq. 3.44 is that for a given base modal mass, the relative pole-zero spacing decreases above mount resonance ω_o by the factor $\bar{\omega}_b^2$:

$$\frac{z_i - p_i}{\bar{\omega}_b} = -\frac{m\phi_b^2}{2\bar{\omega}_b^2} \tag{3.45}$$

The effect of the relative pole-zero spacing on the transfer functions can be seen in the frequency domain in the following figures. The transfer function G_1 is plotted in Figure 3.12 for $\bar{\omega}_b = 0.3$ and in Figure 3.13 for $\bar{\omega}_b = 3$. The function is plotted for values of the dimensionless parameter β_b between 0 and 50, where from Eq. 2.94

$$\beta_b = \frac{m\phi_b^2}{2\zeta_b} \tag{3.46}$$

Since the base damping ζ_b is fixed at 1%, the range $0 \leq \beta_b \leq 50$ corresponds to a range of $m\phi_b^2$ between 0 and 1, where $m\phi_b^2 = 1$ corresponds to the case in which the

isolated mass m equals the modal mass, $\bar{m}_b = 1/\phi_b^2$, of the base resonance. In both Figure 3.12 and Figure 3.13 the effect of the flexible base mode is to contribute a pole-zero pair to the rigid base transfer function (plotted as a dashed line, but hidden by the curve for $\beta_b = 0.1$) as well as to shift the mount resonance at $\bar{\omega} = 1$. In Figure 3.12 the perturbation in magnitude and phase is nearly zero for $\beta_b = 0.1$; at higher values of β_b the pole-zero separation increases and the magnitude and phase perturbations also increase. The mount resonance at $\bar{\omega} = 1$ shifts upward in frequency and becomes more heavily damped, which is consistent with Figure 3.3 since above $\bar{\omega}_b$ the base input mobility appears to be that of a mass with magnitude $1/\phi_b^2$.

Figure 3.13 indicates that the pole zero separation for base modes above mount resonance ω_o is much less sensitive to the parameter β_b, as discussed above. In this case, magnitude and phase perturbations are barely noticeable for $\beta_b = 1$. For a given β_b, the pole-zero separation continues to decrease by the factor $1/\bar{\omega}_b^2$ as the base resonance $\bar{\omega}_b$ is moved to higher frequency, until the mode is characterized by a virtual pole-zero cancellation and is effectively decoupled from the plant transfer function. It is worth noting that the while the zero contributed by the base mode remains lightly damped, the pole becomes more heavily damped (as indicated by the additional term in the denominator of Eq. 3.43). Since below base mode resonance $\bar{\omega}_b$ the base output mobility approximates that of a spring with magnitude $\bar{\omega}_b^2\phi_b^2$, high values of β_b force the mount resonance at $\bar{\omega} = 1$ to decrease in frequency and become more lightly damped. The spring-like effect of Y_B below $\bar{\omega}_b$ also contributes to a loss in phase (below 0°), which is consistent with the results shown in Figure 3.9.

Pole-Zero Spacing for Base Modes Near ω_o: Figure 3.14 illustrates the effect that a base resonance at $\bar{\omega}_b = 1$ has on G_1. As in Figure 3.12, the magnitude and phase perturbations are very small for $\beta_b \ll 1$. The base mode introduces a zero at $\bar{\omega} = 1$ but the modal separation no longer follows a first order perturbation. To investigate this, an approximation for the imaginary part of the system poles of the characteristic equation of G_1 is determined. The perturbation term Y_B/Y_E of Eq. 3.35 is substituted into Eq. 3.34 and the (undamped) fourth-order characteristic equation

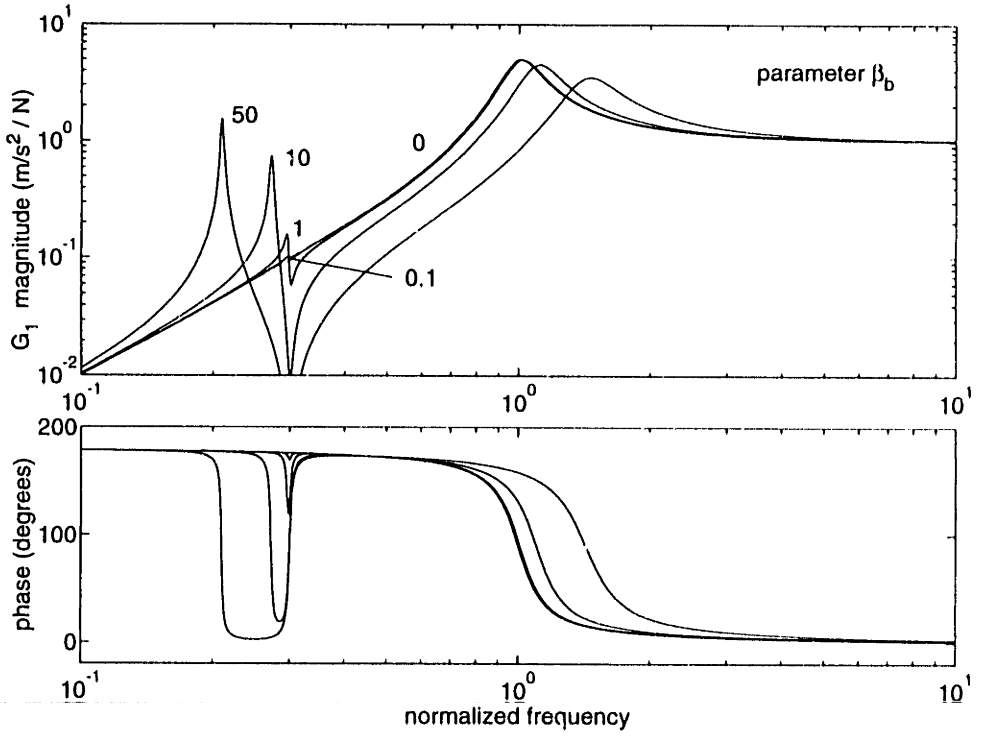

Figure 3.12: Equipment acceleration $G_1(\bar{s}) = a_3/f_a$, and scaled interface force $G_4(\bar{s}) = F_1/f_a = mG_1(\bar{s})$. Base resonant mode: $\bar{\omega}_b = 0.3, \zeta_b = 0.01$.

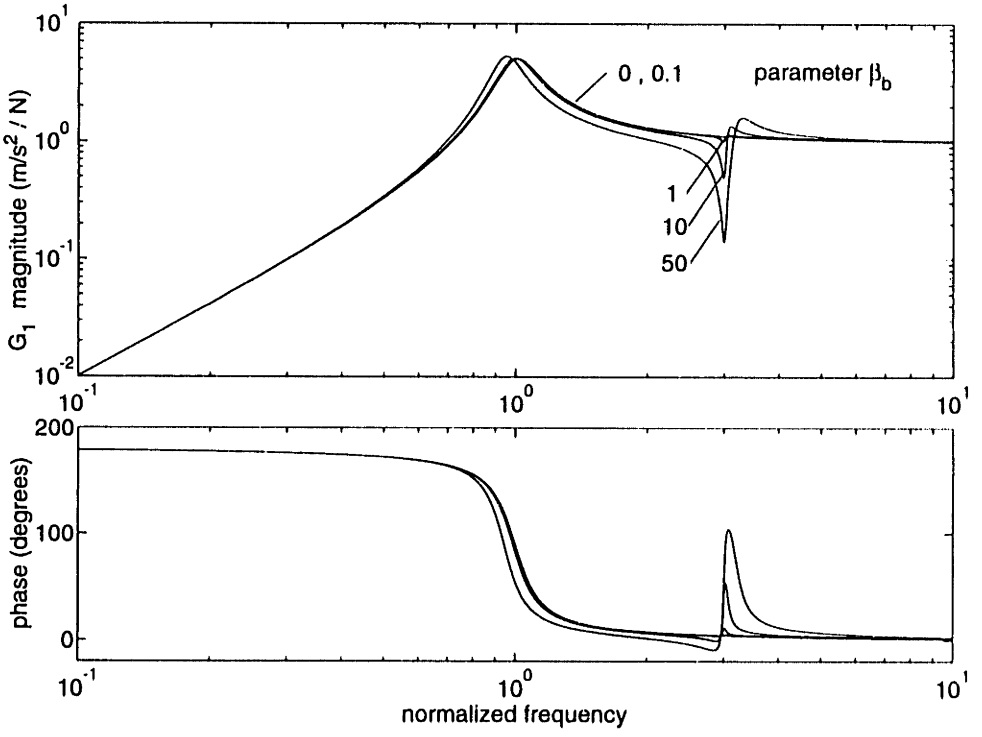

Figure 3.13: Equipment acceleration $G_1(\bar{s}) = a_3/f_a$, and scaled interface force $G_4(\bar{s}) = F_1/f_a = mG_1(\bar{s})$. Base resonant mode: $\bar{\omega}_b = 3, \zeta_b = 0.01$.

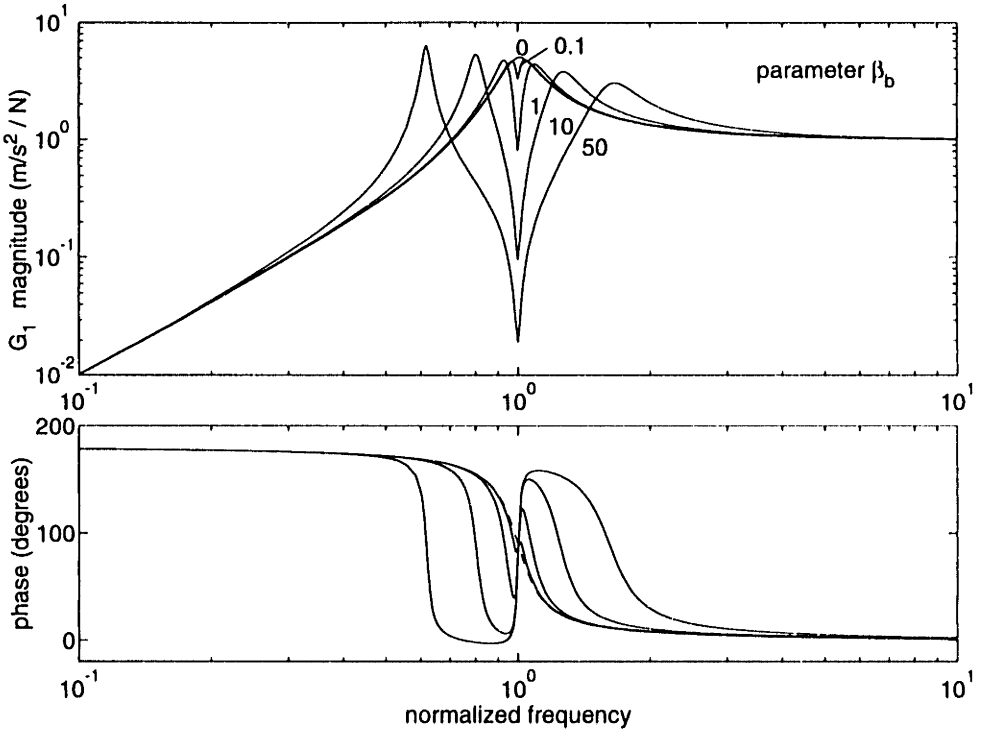

Figure 3.14: Equipment acceleration $G_1(\bar{s}) = a_3/f_a$, and scaled interface force $G_4(\bar{s}) = F_1/f_a = mG_1(\bar{s})$. Base resonant mode: $\bar{\omega}_b = 1, \zeta_b = 0.01$.

of G_1 becomes:

$$\bar{s}^4 + \bar{s}^2\left(1 + \bar{\omega}_b^2 + m\phi_b^2\right) + \bar{\omega}_b^2 = 0 \tag{3.47}$$

Since the uncoupled plant poles are at $\bar{s} = 1j$ and $\bar{s} = j\bar{\omega}_b$, the perturbed roots of Eq. 3.47 are expressed as

$$\bar{s}_1 = j(1 + \varepsilon) \tag{3.48}$$

$$\bar{s}_2 = j\bar{\omega}_b(1 + \gamma) \tag{3.49}$$

Roots $\bar{s}_1$ and $\bar{s}_2$ are substituted into the characteristic equation in Eq. 3.47 separately, and after expansion, terms up to second order in ε and γ are retained. Solving for ε and γ:

$$\varepsilon = \frac{\bar{\omega}_b^2 - 1 + m\phi_b^2 \pm \sqrt{(1 - \bar{\omega}_b^2)^2 + m\phi_b^2(3 + \bar{\omega}_b^2)}}{5 - \bar{\omega}_b^2 - m\phi_b^2} \tag{3.50}$$

$$\gamma = \frac{-\bar{\omega}_b^2 + 1 + m\phi_b^2 \pm \sqrt{(1 - \bar{\omega}_b^2)^2 + m\phi_b^2(1 + 3\bar{\omega}_b^2)}}{-1 + 5\bar{\omega}_b^2 - m\phi_b^2} \tag{3.51}$$

Table 3.2 lists approximate values for ε and γ based on Eqs. 3.50 and 3.51 for three frequency ranges, along with an estimate of the error of the approximation. It can

Table 3.2: Approximations for pole perturbations.

parameter	$\bar{\omega}_b = 1$	$\bar{\omega}_b \ll 1$	$\bar{\omega}_b \gg 1$
ε	$\sqrt{\frac{m\phi_b^2}{2}}$	$\frac{m\phi_b^2}{2}$	$-\frac{m\phi_b^2}{2\bar{\omega}_b^2}$
γ	$-\sqrt{\frac{m\phi_b^2}{2}}$	$-\frac{m\phi_b^2}{2}$	$\frac{m\phi_b^2}{2\bar{\omega}_b^2}$
Bounds for 2% error	$m\phi_b^2 \leq 0.1$	$m\phi_b^2 \leq 0.1$ $\bar{\omega}_b \leq 0.6$	$m\phi_b^2 \leq 0.1$ $\bar{\omega}_b \geq 2$

be seen that the pole perturbation for $\bar{\omega}_b = 1$ is quadratic, and that the first order expressions for the coupled system poles in Eqs. 3.40 and 3.44 are approximately recovered for $\bar{\omega}_b < 0.6$ and $\bar{\omega}_b > 2$.

Transfer Function for Gap: The gap transfer function G_5 is now investigated. Consider the general expression for G_5 on a flexible base in Eq. 3.21

$$G_5(s) = \frac{\frac{1}{s}Y_I\left(1 + \frac{Y_B}{Y_E}\right)}{1 + \frac{Y_I}{Y_E} + \frac{Y_B}{Y_E}} \tag{3.52}$$

Substituting for $Y_I = s/(cs + k)$ and $Y_E = 1/ms$

$$G_5(s) = \frac{1 + \frac{Y_B}{Y_E}(s)}{ms^2 + cs + k + (k + cs)\frac{Y_B}{Y_E}(s)} \tag{3.53}$$

In terms of modal parameters $k = m\omega_o^2$ and $c = 2\zeta_o\omega_o m$, and normalized frequency $\bar{s} = s/\omega_o$, the gap transfer function becomes

$$G_5(\bar{s}) = \frac{\frac{1}{m\omega_o^2}\left(1 + \frac{Y_B}{Y_E}(\bar{s})\right)}{\bar{s}^2 + 2\zeta_o\bar{s} + 1 + (1 + 2\zeta_o\bar{s})\frac{Y_B}{Y_E}(\bar{s})} \tag{3.54}$$

where the perturbation term Y_B/Y_E is given by Eq. 3.35. Naturally, the poles of G_5 are the same as those of G_1 in Eqs. 3.40 and 3.44

$$p_i = \bar{\omega}_b \left(1 - \frac{m\phi_b^2}{2}\right) \qquad (m\phi_b^2, \bar{\omega}_b^2) \ll 1 \tag{3.55}$$

$$p_i = \bar{\omega}_b \left(1 + \frac{m\phi_b^2}{2\bar{\omega}_b^2}\right) \qquad m\phi_b^2 \ll 1, \ \bar{\omega}_b^2 \gg 1 \tag{3.56}$$

but due to the presence of the term Y_B/Y_E in the numerator, the zeros are different. For any value of $\bar{\omega}_b$ and small ζ_b, the zeros of G_5 are approximately the roots of

$$\bar{s}^2(1 + m\phi_b^2) + \bar{\omega}_b^2 = 0 \tag{3.57}$$

or to first order in $m\phi_b^2$,

$$z_i = \bar{\omega}_b(1 - \frac{m\phi_b^2}{2}) \qquad m\phi_b^2 \ll 1 \tag{3.58}$$

which together with Eqs. 3.55 and 3.56 leads to a relative pole-zero spacing of

$$\frac{z_i - p_i}{\bar{\omega}_b} = 0 \qquad \bar{\omega}_b^2 \ll 1 \tag{3.59}$$

$$\frac{z_i - p_i}{\bar{\omega}_b} = -\frac{m\phi_b^2}{2} \qquad \bar{\omega}_b^2 \gg 1 \tag{3.60}$$

Thus for the gap transfer function G_5, the pole-zero spacing is a constant above mount resonance, unlike the behavior for the acceleration transfer function G_1, in which the pole-zero spacing decreases to zero above mount resonance by the ratio $1/\bar{\omega}_b^2$. The first order analysis indicates pole-zero cancellation for base modes $\bar{\omega}_b \ll 1$, however, as shown in Table 3.2, the first order approximation of pole perturbation is in error above 2% for $\bar{\omega}_b >= 0.6$. It is expected that the cancellation will not be exact for frequencies near mount resonance $\bar{\omega} = 1$, as is shown in the following plots. Table 3.3 summarizes the relative pole-zero spacing for the acceleration (or force) and gap transfer functions.

Figures 3.15 and 3.16 illustrate the effects of base resonances on G_5 for different values of the parameter β_b. The base resonance is most strongly coupled *above* mount resonance ω_o at $\bar{\omega} = 1$, and nearly decoupled *below* $\bar{\omega} = 1$. Again, this behavior is opposite to the trend observed for the acceleration and force transfer functions G_1

Table 3.3: Relative pole-zero spacing $(z_i - p_i)/\bar{\omega}_b$ for parallel actuator model due to resonant mode in base structure.

transfer function	symbol	frequency range	
		$\bar{\omega}_b \ll 1$	$\bar{\omega}_b \gg 1$
equipment acceleration	G_1	$\frac{m\phi_b^2}{2}$	$-\frac{m\phi_b^2}{2\bar{\omega}_b^2}$
interface force	G_4	$\frac{m\phi_b^2}{2}$	$-\frac{m\phi_b^2}{2\bar{\omega}_b^2}$
gap	G_5	0	$-\frac{m\phi_b^2}{2}$

in Figures 3.12 and 3.13. Shifts in mount resonance and additional damping in base resonance for $\bar{\omega}_b = 3$ at high levels of β_b are consistent with the plots for G_1.

Figures 3.18 and 3.17 illustrate the base acceleration transfer function G_6 for the two cases of $\bar{\omega}_b$ considered. Unlike the transfer functions for equipment acceleration, interface force or gap, the base flexibility does not perturb a nominal transfer function, but rather is responsible for making the measurement nonzero in the first place. Examination of Eq. 3.22 indicates that the perturbation term Y_B/Y_E is a factor in the numerator of G_6. Thus, the base acceleration transfer function is roughly proportional to the base output mobility Y_B, which for a general structure may be a highly complex function of frequency. This phenomenon is illustrated below with an example from the literature.

Comparison of Results to Watters *et al.* (1989): The parallel actuator model of Figure 3.1 was considered in a previous study by Watters *et al.* [82] for a diesel engine mounted on a modally rich base structure. Figure 3.19, from this reference, is a comparison of the transfer function from commanded force f_a (current in the actuator) to measured force F_1 and measured base acceleration a_1, which correspond to transfer functions G_4 and G_6 respectively. The mount resonance for this example

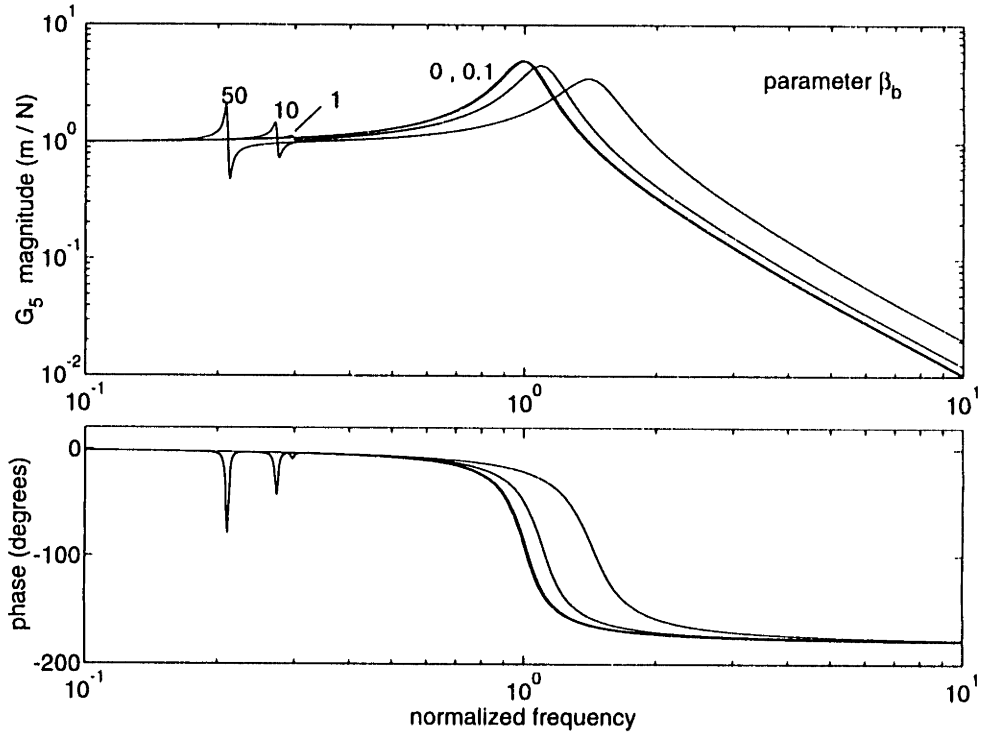

Figure 3.15: Gap $G_5(\bar{s}) = (x_2 - x_1)/f_a$. Base modelled as resonant mode: $\bar{\omega}_b = 0.3, \zeta_b = 0.01$.

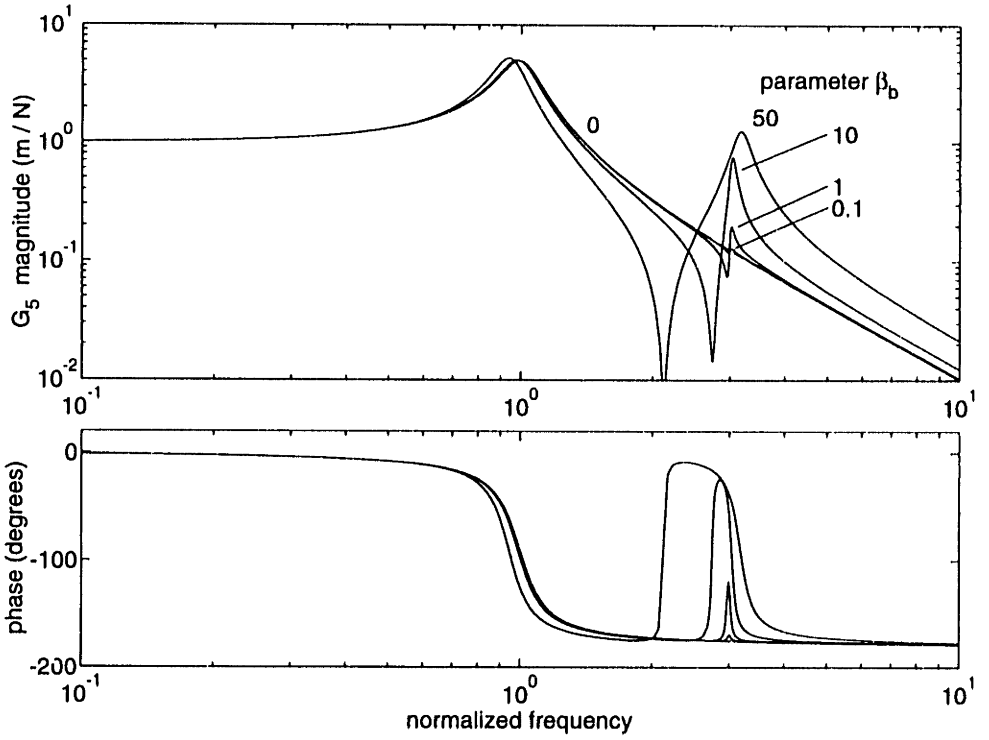

Figure 3.16: Gap $G_5(\bar{s}) = (x_2 - x_1)/f_a$. Base modelled as resonant mode: $\bar{\omega}_b = 3, \zeta_b = 0.01$.

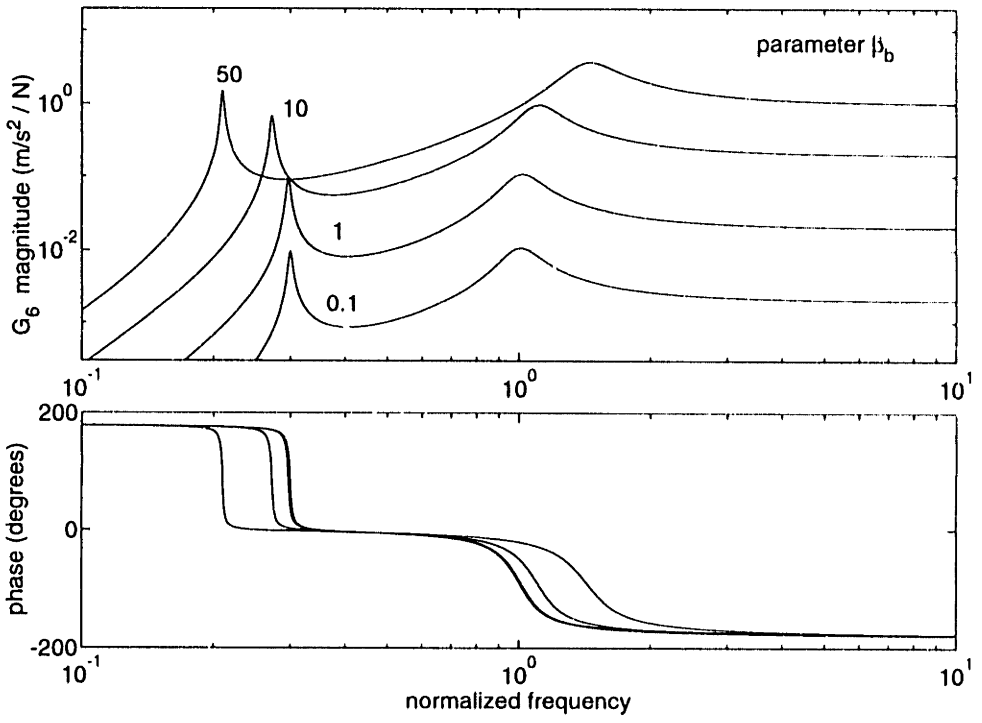

Figure 3.17: Base acceleration $G_6(\bar{s}) = a_1/f_a$. Base modelled as resonant mode: $\bar{\omega}_b = 0.3, \zeta_b = 0.01$.

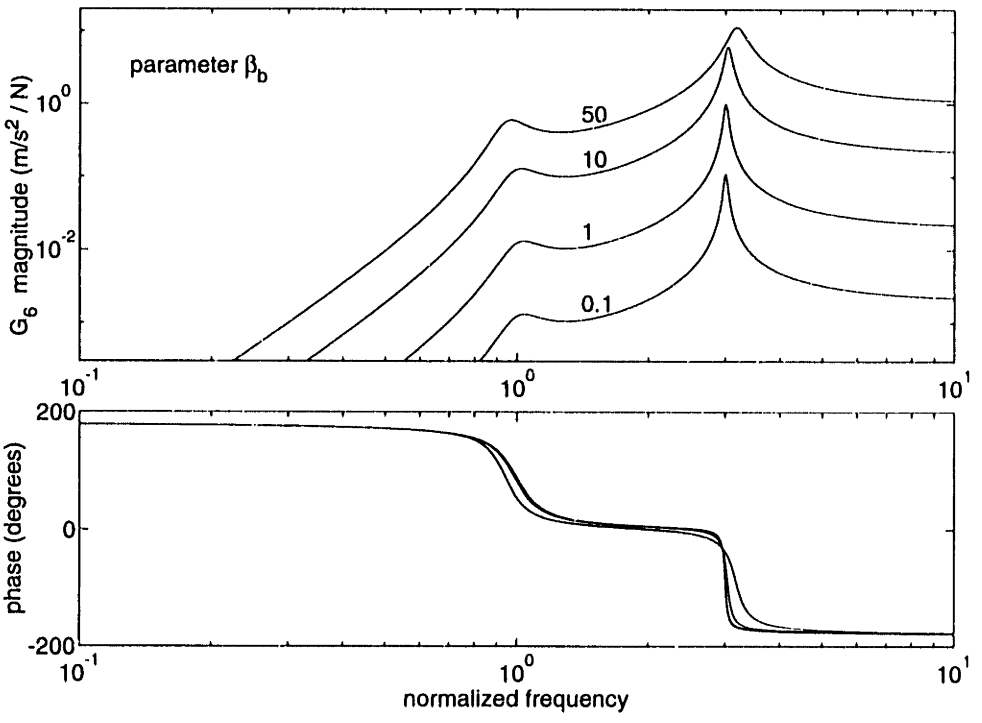

Figure 3.18: Base acceleration $G_6(\bar{s}) = a_1/f_a$. Base modelled as resonant mode: $\bar{\omega}_b = 3, \zeta_b = 0.01$.

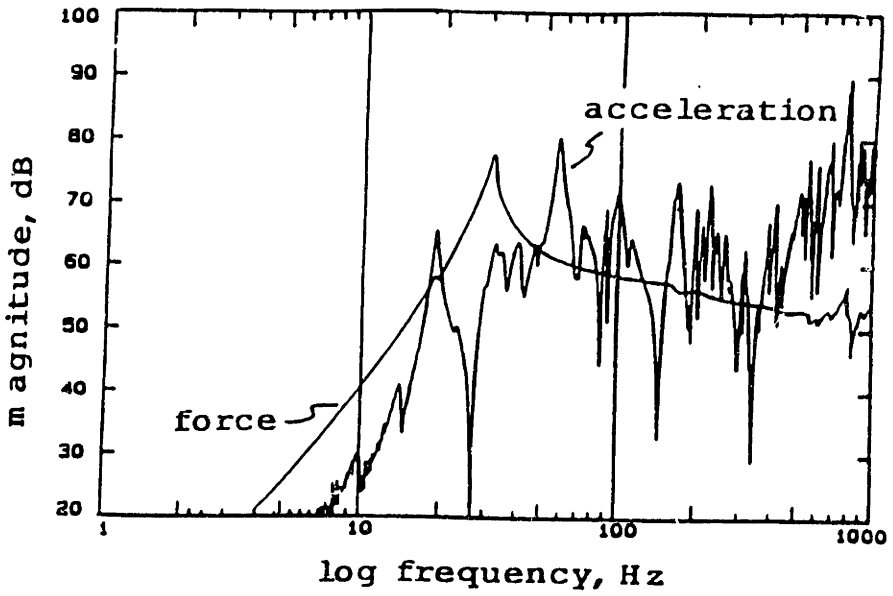

Figure 3.19: Interface force F_1 and base acceleration a_1 due to commanded force f_a, from Watters *et al.* (1989).

is at approximately 30 Hz. Figure 3.19 shows that there is no coupling of base modes with the force output above 30 Hz, and little below 30 Hz – thus the dimensionless parameter $\beta_b = m\phi_b^2/(2\zeta_b)$ and the perturbation Y_B/Y_E for the base modes must be small. Even for low values of the base mode perturbation, however, the base acceleration shows a high degree of modal coupling. From Eq. 3.22, for small Y_B/Y_E the function G_6 is approximated by

$$G_6(s) \approx -sY_B(s) \qquad \bar{s}^2 \ll 1 \tag{3.61}$$

$$G_6(s) \approx -\frac{s^3}{\omega_o^2}Y_B(s) \qquad \bar{s}^2 \gg 1 \tag{3.62}$$

If the base mobility Y_B exhibits many lightly damped flexible modes, then the resulting transfer function will be like that shown in Figure 3.19, even for small Y_B/Y_E or small β_b.

Transfer Function Insights of Pole-Zero Spacing: Figure 3.20 illustrates the effect that a change in base mode damping ζ_b, for a constant $\beta_b = 1$, has on the transfer function for G_1 in Figure 3.12. Since β_b is constant, as damping is increased from zero to 10% the mass ratio $m\phi_b^2$ takes on the ratios 0, 0.002, 0.02, 0.1, and 0.2 respectively. The magnitude perturbation induced by the base resonance – defined

as the ratio of the perturbed to nominal (dashed) transfer function at the frequency of base resonance – remains nearly constant for a given value of β_b, regardless of the (finite) value of damping. The perturbation is approximately 4.35 dB, or a factor of 1.65, for $\zeta_b \leq 1\%$. Similarly for the phase: the maximum phase excursion remains nearly constant at approximately -64 degrees (-1.12 radians). The pole-zero separation widens according to Eq. 3.41.

$\bar{s}$-plane Insights of Relative Pole-Zero Spacing: An $\bar{s}$-plane investigation of the relative pole-zero spacing is approached by expressing $\beta_b = 1$

$$\frac{m\phi_b^2}{2\zeta_b} = 1 \tag{3.63}$$

and multiplying each side by the factor $\zeta_b\bar{\omega}_b$:

$$\frac{m\phi_b^2}{2}\bar{\omega}_b = \zeta_b\bar{\omega}_b \tag{3.64}$$

The left hand side of Eq. 3.64 is just the first order approximation for pole-zero spacing below mount resonance from Eq. 3.41, and the right hand side is the distance of the plant pole from the $j\bar{\omega}$ axis, as shown in Figure 3.21. Therefore, maintaining β_b equal to 1 is equivalent to maintaining the pole-zero frequency separation equal to the distance from the $j\bar{\omega}$ axis.

3.2.3 Effects of Equipment Flexibility

In order to study the effect of equipment flexibility, the base mobility is first assumed rigid ($Y_B = 0$). Assumptions (i) and (iii) through (v) of the classical parallel actuator are retained; only assumption (ii) is relaxed to permit an equipment mobility that is different from a rigid mass. The assumed equipment model is the same as that assumed for the passive isolation investigation of Section 2.5.2.

Consider first the acceleration transfer function G_1 of Eq. 3.6, which relates the acceleration a_3 at equipment output terminal 3 to the input force f_a. Using assumptions (i), (iii) and (iv) of the classical parallel actuator, the transfer function becomes

$$G_1(s) = \frac{s(T_v)_{23}Y_I}{1 + \dfrac{Y_{12}^b}{Y_E}} \tag{3.65}$$

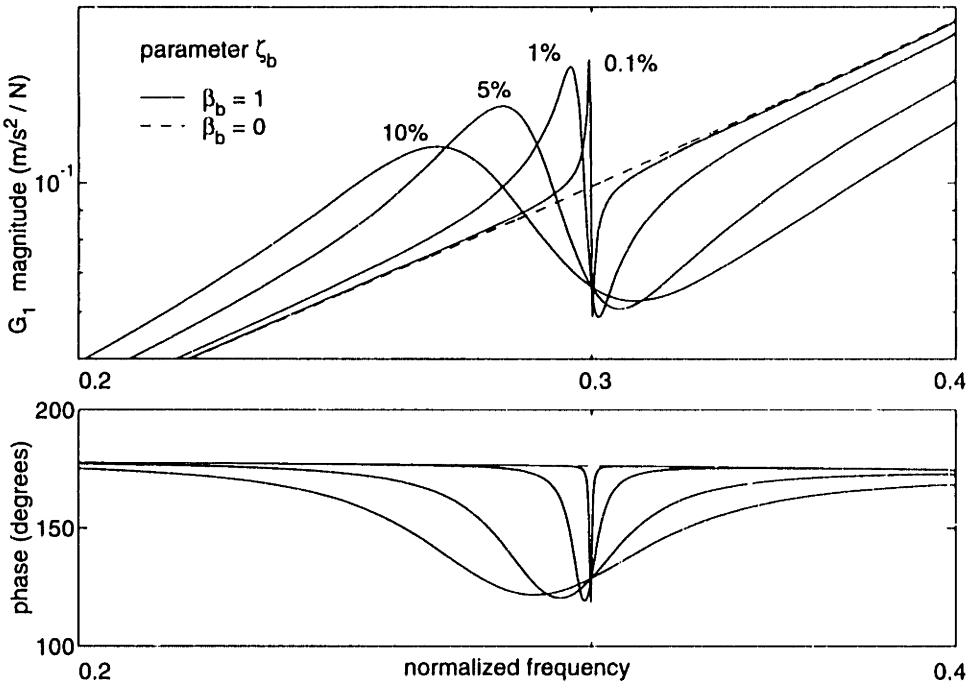

Figure 3.20: Effect of base mode damping ζ_b (at constant $\beta_b = 1$) on pole-zero spacing for equipment acceleration $G_1(\bar{s}) = a_3/f_a$.

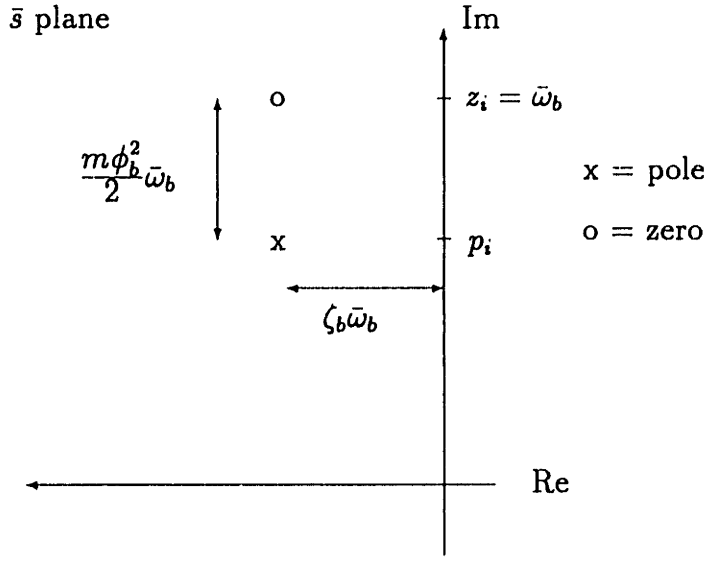

Figure 3.21: For $\beta_b = 1$, the pole-zero separation in $G_1(\bar{s})$ for $\bar{s} << 1$ equals the horizontal distance of the pole from the $j\bar{\omega}$ axis.

The expression for $(T_v)_{23}$ in Eq. 2.45 – representing the velocity transmissibility between terminals 2 and 3 of the equipment – is substituted into Eq. 3.65, and numerator and denominator are multiplied through by Y_E

$$G_1(s) = \frac{sY_{23}^f Y_I}{Y_I + Y_E} \tag{3.66}$$

where Y_E is the equipment input mobility at terminal 2, and Y_{23}^f is the equipment transfer mobility (from input force F_2 at terminal 2 to velocity v_3 at equipment output terminal 3). These functions are modelled as the mobility of a single equipment rigid body mode plus the mobility of a single resonator:

$$Y_E = \bar{Y}_E + Y_{e2} \tag{3.67}$$

$$Y_{23}^f = \bar{Y}_E + Y_{e3} \tag{3.68}$$

where the rigid body mode is from Eq. 2.97

$$\bar{Y}_E = \frac{1}{ms} \tag{3.69}$$

and the resonant mode expressions are based on Eq. 2.96

$$Y_{e2} = \frac{s\phi_{e2}^2}{s^2 + 2\zeta_e\omega_e s + \omega_e^2} \tag{3.70}$$

$$Y_{e3} = \frac{s\phi_{e2}\phi_{e3}}{s^2 + 2\zeta_e\omega_e s + \omega_e^2} \tag{3.71}$$

where ω_e and ζ_e are the base mode frequency and damping, and ϕ_{e2} and ϕ_{e3} are mass normalized eigenvectors of the equipment mode at the input and output terminals 2 and 3, respectively. No further restrictions are placed on the eigenvectors at this time; ϕ_{e2} and ϕ_{e3} are allowed to differ in magnitude and sign. The expressions for Y_E and Y_{23}^f are substituted into Eq. 3.66 to yield

$$G_1(s) = \frac{sY_I\left(\bar{Y}_E + Y_{e3}\right)}{Y_I + \bar{Y}_E + Y_{e2}} \tag{3.72}$$

$$= \frac{sY_I\left(1 + \dfrac{Y_{e3}}{\bar{Y}_E}\right)}{1 + \dfrac{Y_I}{\bar{Y}_E} + \dfrac{Y_{e2}}{\bar{Y}_E}} \tag{3.73}$$

The perturbation term in the denominator, $Y_{e2}/\bar{Y}_E$, is the same as that in Eq. 2.99 introduced for the passive isolation problem. For small damping ζ_e, from Eq. 2.100 this perturbation term has maximum gain (from Eq. 2.100)

$$\beta_{e2} = \frac{m\phi_{e2}^2}{2\zeta_e} \tag{3.74}$$

at $\omega = \omega_e$. Similarly, the perturbation term in the numerator is $Y_{e3}/\bar{Y}_E$, with maximum gain

$$\beta_{e3} = \frac{m\phi_{e2}\phi_{e3}}{2\zeta_e} \tag{3.75}$$

at $\omega = \omega_e$. Because β_{e2} is expressed in terms of the square of ϕ_{e2}, the parameter β_{e2} will always be positive. If however the eigenvectors ϕ_{e2} and ϕ_{e3} at terminals 2 and 3 are out of phase, then β_{e3} will be negative. The relative magnitudes of these two dimensionless parameters will depend on the particular mode shape.

Expressions for the six transfer functions in Table 3.2 in the presence of equipment modal flexibility are derived in a similar manner, and are tabulated in Table 3.4 next to those derived previously for base resonances. The structure of the equations indicates that the perturbation terms Y_B/Y_E and $Y_{e2}/\bar{Y}_E$ affect the denominators of both columns in the same manner: as the perturbation terms go to zero, the rigid base transfer functions are recovered. The perturbation terms are compared in Table 3.5.

Transfer Functions for Force and Gap: By comparing the transfer functions G_4 and G_5 in both columns of Table 3.4, it is obvious that the parametric effect of equipment and base flexibility are the same, with the substitutions

$$\bar{Y}_E \rightarrow Y_E \tag{3.76}$$

$$Y_{e2} \rightarrow Y_B \tag{3.77}$$

where $Y_E = \bar{Y}_E = 1/ms$. Therefore the plots of the effect of base flexibility on the force and gap transfer functions in Figures 3.13 to 3.16 also describe the effect of base flexibility with β_{e2} substituted for β_b, and with the substitutions

$$\begin{aligned} \phi_{e2} &\rightarrow \phi_b \\ \zeta_e &\rightarrow \zeta_b \\ \bar{\omega}_e &\rightarrow \bar{\omega}_b \end{aligned} \tag{3.78}$$

Table 3.4: Comparison of parametric transfer functions for cases in which either the base or equipment exhibit modal flexibility.

transfer function	base flexibility	equipment flexibility
$G_1(s) = \dfrac{a_3}{f_a}$	$\dfrac{sY_I}{1 + \dfrac{Y_I}{Y_E} + \dfrac{Y_B}{Y_E}}$	$\dfrac{sY_I\left(1 + \dfrac{Y_{e3}}{\bar{Y}_E}\right)}{1 + \dfrac{Y_I}{\bar{Y}_E} + \dfrac{Y_{e2}}{\bar{Y}_E}}$
$G_2(s) = \dfrac{a_2}{f_a}$	$\dfrac{sY_I}{1 + \dfrac{Y_I}{Y_E} + \dfrac{Y_B}{Y_E}}$	$\dfrac{sY_I\left(1 + \dfrac{Y_{e2}}{\bar{Y}_E}\right)}{1 + \dfrac{Y_I}{\bar{Y}_E} + \dfrac{Y_{e2}}{\bar{Y}_E}}$
$G_4(s) = \dfrac{F_1}{f_a}$	$\dfrac{\dfrac{Y_I}{Y_E}}{1 + \dfrac{Y_I}{Y_E} + \dfrac{Y_B}{Y_E}}$	$\dfrac{\dfrac{Y_I}{\bar{Y}_E}}{1 + \dfrac{Y_I}{\bar{Y}_E} + \dfrac{Y_{e2}}{\bar{Y}_E}}$
$G_5(s) = \dfrac{x_2 - x_1}{f_a}$	$\dfrac{\dfrac{1}{s}Y_I\left(1 + \dfrac{Y_B}{Y_E}\right)}{1 + \dfrac{Y_I}{Y_E} + \dfrac{Y_B}{Y_E}}$	$\dfrac{\dfrac{1}{s}Y_I\left(1 + \dfrac{Y_{e2}}{\bar{Y}_E}\right)}{1 + \dfrac{Y_I}{\bar{Y}_E} + \dfrac{Y_{e2}}{\bar{Y}_E}}$
$G_6(s) = \dfrac{a_1}{f_a}$	$\dfrac{sY_B\dfrac{Y_B}{Y_E}}{1 + \dfrac{Y_I}{Y_E} + \dfrac{Y_B}{Y_E}}$	0

Transfer Function for Equipment Acceleration a_2: Only the plots for equipment velocities G_1 and G_2 are different (in a dimensionless sense) from the cases considered for base flexibility. Because of flexibility between equipment terminals 2 and 3, the transfer function G_1 does not equal G_2. Transfer function G_2 of column 2 in Table 3.4 is plotted in Figures 3.22 and 3.23 for equipment resonance $\bar{\omega}_e$ at 0.3 and 3, respectively. Each plot is parameterized in terms of the dimensionless quantity β_{e2}. It is worthwhile to compare these plots to the case involving base flexibility in Figures 3.12 and 3.13, which are parameterized by β_b. In contrast to base modes,

Table 3.5: Dimensionless perturbation terms for base and equipment flexibility.

	base flexibility	equipment flexibility	
		interface terminal 2	output terminal 3
perturbation term	$\frac{Y_B}{Y_E}$	$\frac{Y_{e2}}{Y_E}$	$\frac{Y_{e3}}{Y_E}$
maximum gain	$\frac{m\phi_b^2}{2\zeta_b}$	$\frac{m\phi_{e2}^2}{2\zeta_e}$	$\frac{m\phi_{e2}\phi_{e3}}{2\zeta_e}$
symbol for max gain	β_b	β_{e2}	β_{e3}

equipment modes are strongly coupled *above* mount resonance $\bar{\omega} = 1$, and nearly pole-zero canceled *below* $\bar{\omega} = 1$. The effect on mount damping due to equipment modes is opposite to that caused by base modes.

Transfer Function for Equipment Acceleration a_3: The most interesting output variable when equipment flexibility is present is the acceleration a_3 at the equipment output terminal 3, as illustrated in Figures 3.24 and 3.25 for equipment resonance $\bar{\omega}_e$ at 0.3 and 3, respectively. The function is plotted for negative β_{e3} corresponding to the case in which eigenvectors ϕ_{e2} and ϕ_{e3} are of opposite sign. Here the equipment mode is strongly coupled both *below* and *above* mount resonance. Note that when $\phi_{e2} = \phi_{e3}$ the transfer function reverts to G_2 illustrated in Figures 3.22 and 3.23. A surprising result is that for $\phi_{e2} > \phi_{e3}$ the pole and zero at $\bar{\omega}_e = 0.3$ flip and the phase excursion is positive; this result is predicted by the relative pole zero spacing for G_1 in Table 3.6.

Figure 3.25 is plotted for $\beta_{e3} < 0$ and for $\bar{\omega}_e = 3$, and the pole-zero pair has flipped relative to the same case for G_2 in Figure 3.23. However, the 180 degree loss in phase is recovered for all values of β_{e3} greater than -50, which for $\zeta_e = 0.01$ corresponds to a ratio of 1 between equipment rigid body mass and equipment modal mass. The case $\beta_{e3} = -50$ is the familiar one: two equal masses connected by a parallel spring

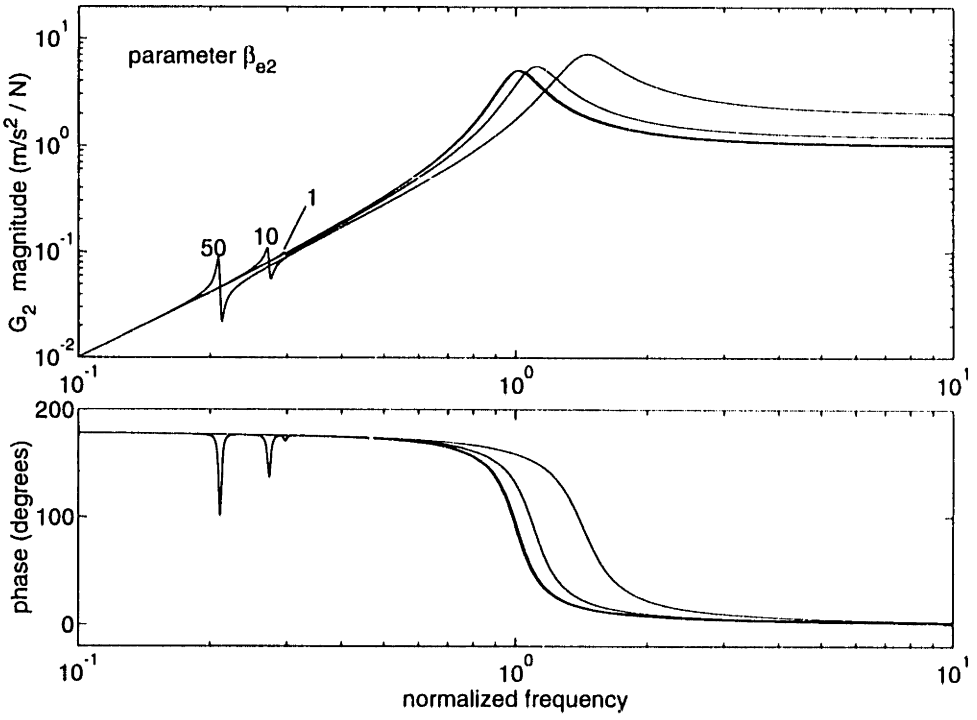

Figure 3.22: Equipment acceleration $G_2(\bar{s}) = a_2/f_a$ due to equipment resonance. Parameters: $\beta_{e2} = m\phi_{e2}^2/(2\zeta_e)$, $\bar{\omega}_e = 0.3$, $\zeta_e = 0.01$.

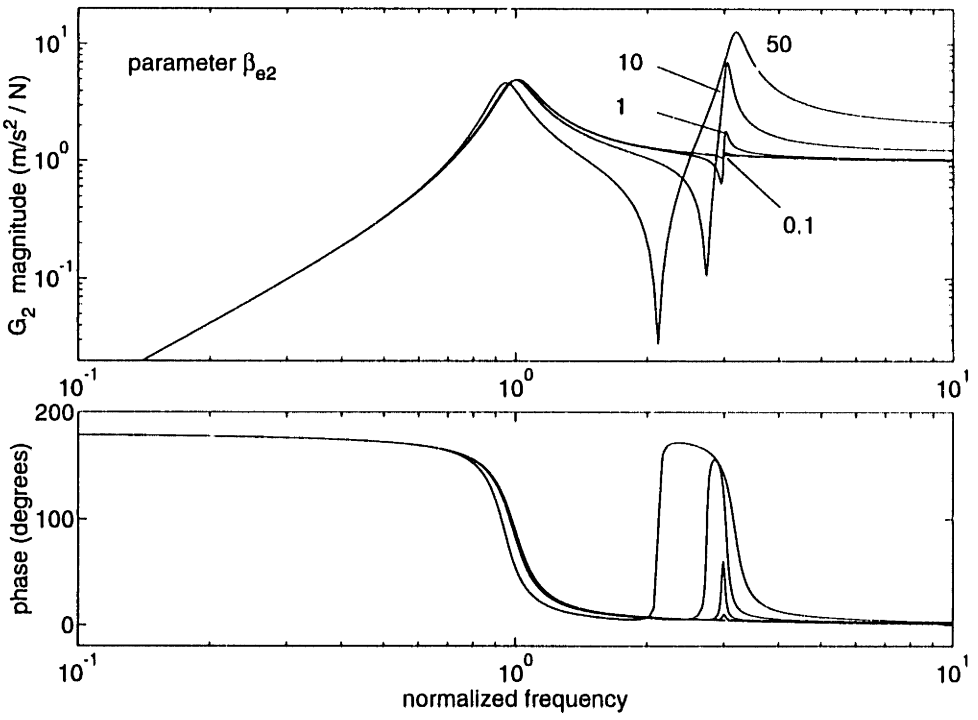

Figure 3.23: Equipment acceleration $G_2(\bar{s}) = a_2/f_a$ due to equipment resonance. Parameters: $\beta_{e2} = m\phi_{e2}^2/(2\zeta_e)$, $\bar{\omega}_e = 3$, $\zeta_e = 0.01$.

Table 3.6: First order approximation (in $m\phi_{e2}^2$) for relative pole-zero spacing for actuator model due to resonant mode in equipment.

transfer function	symbol	frequency range	
		$\bar{\omega}_e \ll 1$	$\bar{\omega}_e \gg 1$
equipment output acceleration	$G_1(s)$	$\frac{m\phi_{e2}^2}{2}\left(1-\frac{\phi_{e3}}{\phi_{e2}}\right)$	$-\frac{m\phi_{e2}^2}{2}\left(\frac{\phi_{e3}}{\phi_{e2}}\right)$
equipment interface acceleration	$G_2(s)$	0	$-\frac{m\phi_{e2}^2}{2}$
interface force	$G_4(s)$	$\frac{m\phi_{e2}^2}{2}$	$-\frac{m\phi_{e2}^2}{2\bar{\omega}_e^2}$
gap	$G_5(s)$	0	$-\frac{m\phi_{e2}^2}{2}$

and damper; in which case the resonant modal mass equals the rigid body mass and the transfer function assumes the noncollocated form of the curve parameterized by $\beta_{e3} = -50$. For $\beta_{e3} > -50$, however, the rigid body mobility overcomes the flexible mode mobility at a sufficiently high frequency above $\bar{\omega}_e$, resulting in a plant zero and a recovery of 180 degrees of phase. Finally, the acceleration transfer function behavior for the case $\bar{\omega}_e = 1$ is illustrated in Figure 3.26.

Table 3.6 summarizes the relative pole-zero spacing due to equipment modes for each transfer function. Table 3.6 can be compared to Table 3.3 which lists the pole-zero spacing due to a mode in the base structure.

3.3 Series Actuator Model

For the parallel actuator model illustrated in Figure 3.2 the interface spring constant k is determined by the sum of the passive isolator stiffness plus any internal impedance of the physical force actuator. In some situations the internal actuator impedance is too high to provide any passive isolation for the equipment (for example, a stiff

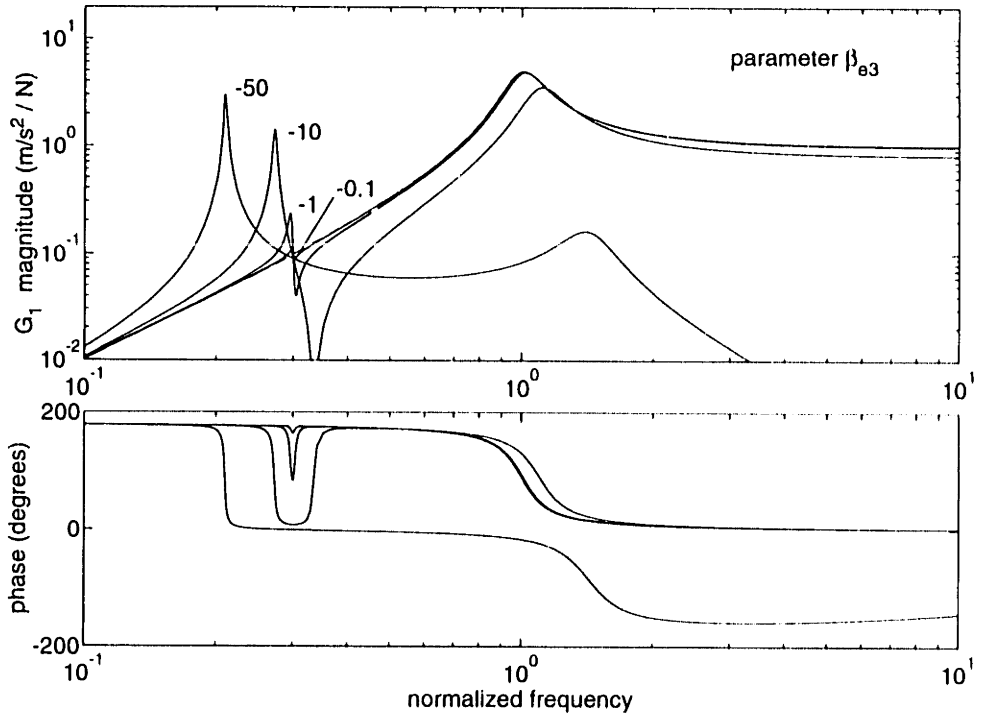

Figure 3.24: Equipment acceleration $G_1(\bar{s}) = a_3/f_a$ due to equipment resonance. Parameters: $\beta_{e3} = m\phi_{e2}\phi_{e3}/(2\zeta_e)$, $\bar{\omega}_e = 0.3$, $\zeta_e = 0.01$. $\beta_{e3} = 50$ represents a massive equipment mode.

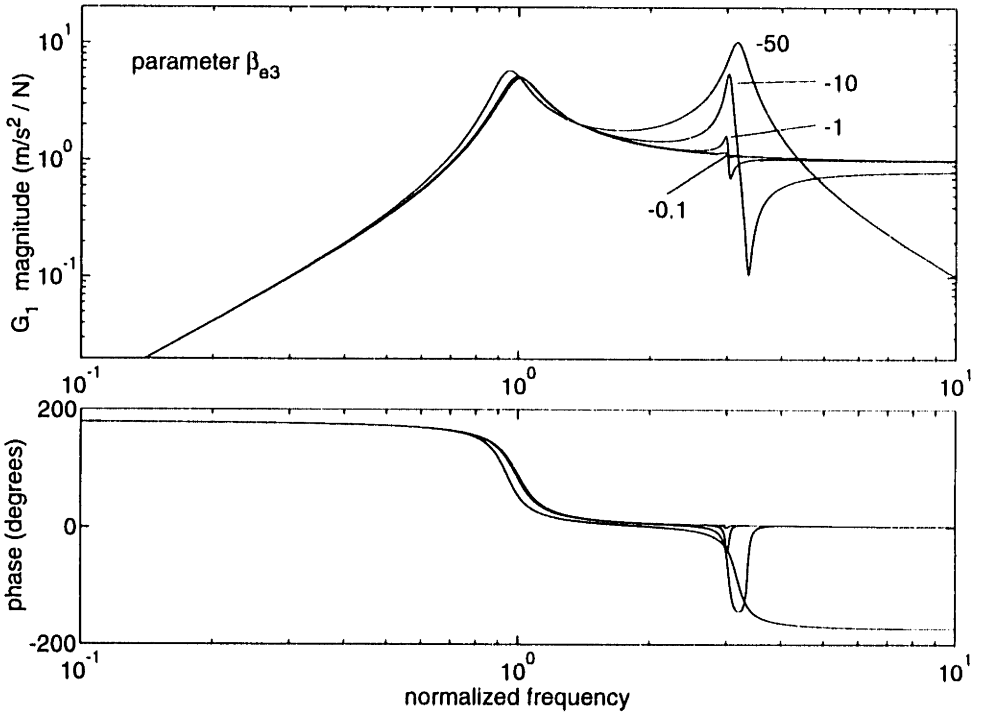

Figure 3.25: Equipment acceleration $G_1(\bar{s}) = a_3/f_a$ due to equipment resonance. Parameters: $\beta_{e3} = m\phi_{e2}\phi_{e3}/(2\zeta_e)$, $\bar{\omega}_e = 3$, $\zeta_e = 0.01$. $\beta_{e3} = 50$ represents a massive equipment mode.

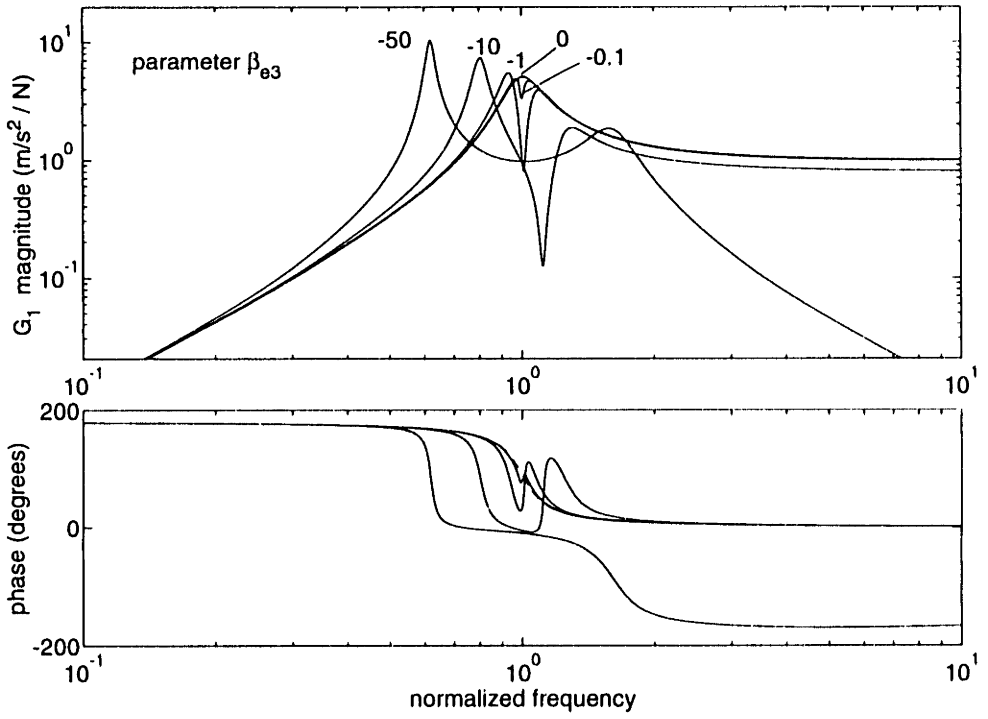

Figure 3.26: Equipment acceleration $G_1(\bar{s}) = a_3/f_a$ due to equipment resonance. Parameters: $\beta_{e3} = m\phi_{e2}\phi_{e3}/(2\zeta_e)$, $\bar{\omega}_e = 1$, $\zeta_e = 0.01$.

piezoelectric actuator) and series actuation becomes necessary. Figure 3.27 illustrates a simple representation of series actuation for a vibrating base. A series isolator (typically a low impedance element such as a viscously damped spring) lowers the effective interface spring constant in order to provide the required passive isolation corner frequency. A lower mount resonance provides decoupling of disturbances from the output (reducing demands on the active control) and leads to modal decoupling from loop transfer functions when base or equipment flexibility are present. These advantages come at a cost, however: increased complexity and isolator mass, and reduced actuator control authority at high frequency.

Series isolation may be used for either the force or velocity isolation problems. Figure 3.28 illustrates two possible series isolation configurations for the velocity isolation (vibrating base) problem; in each case the performance variable is the velocity v_2 at the equipment interface. In Figure 3.28(a), a series isolator is placed between the actuator and the base structure (the vibration source). The actuator is modelled as a pure force applied in parallel with a viscously damped spring which represents

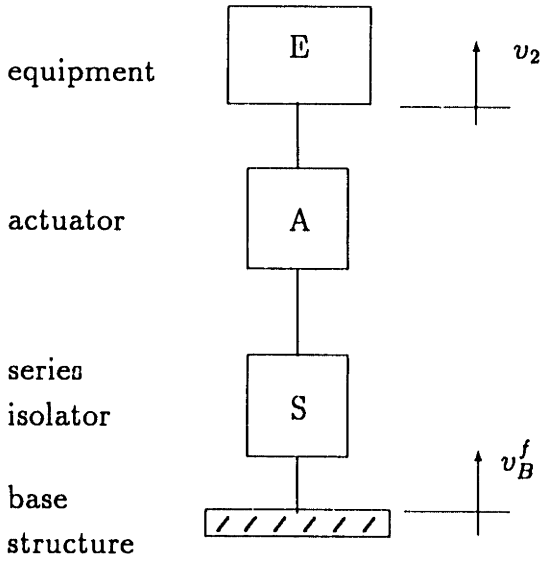

Figure 3.27: Series actuation model for velocity isolation problem. A soft isolator S is installed in series with the actuator A.

the internal impedance of the actuator (refer to Figure 2.4), and is considered here to be much stiffer than the series spring k_2.

The series isolator in Figure 3.28(a) is itself comprised of two elements: a soft viscously damped spring that provides the desired mount passive resonance, and a reaction mass which both preserves high frequency actuator authority over v_2 and decouples any base dynamics from the loop transfer function v_2/f_a. As such, the mount can be used to regulate v_2 whether the disturbances originate from the base structure (v_B^f) or impact the equipment mass directly (vibration receiver). Figure 3.28(a) can also be interpreted as an active mirror positioning device, in which the receiver is a mirror and the error signal is an external measurement of v_2.

The configuration of Figure 3.28(a) has been proposed for a payload pointing system [84] in which a stiff gimbal is attached to flexible base. This configuration is also used to model active vehicle suspension for road vehicles [79], in which the mass m_2 and spring k_2 represent the tire mass and stiffness, and the mass m_1 and spring k_1 represent the "sprung mass" (quarter-car mass) and the body spring stiffness. A force actuator in parallel with the body spring k_1 is used to modify the passive transmissibility to improve handling and rider comfort. The parameter values for a conventional automobile front suspension from reference [79] are $m_2 = 28$ kg, $k_2 =$

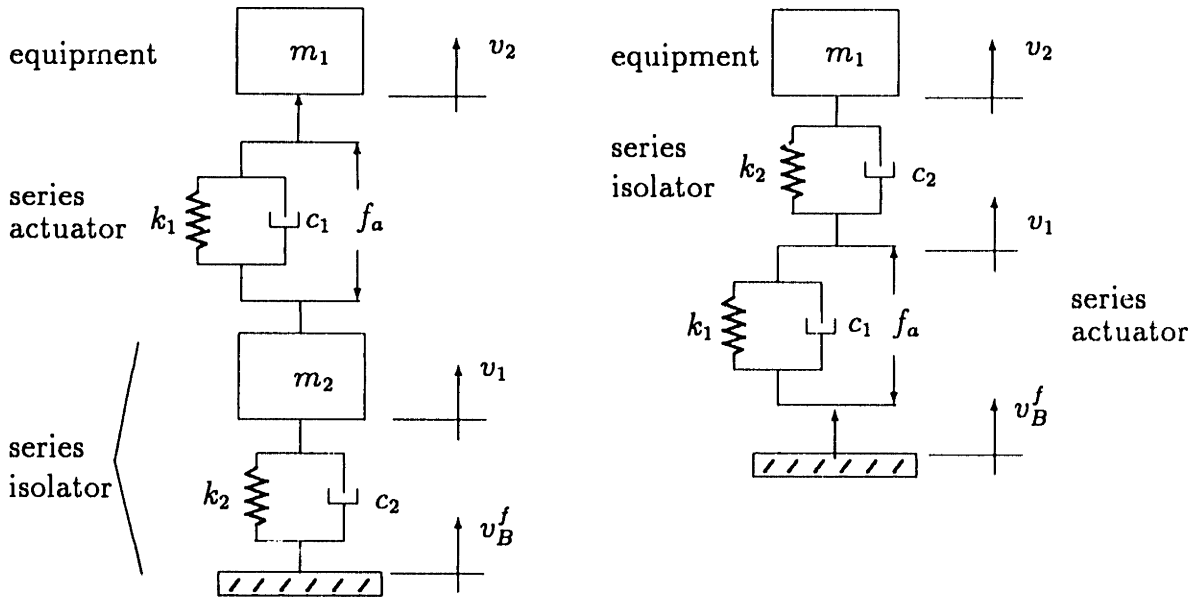

Figure 3.28: Two examples of active isolators in series with softmount. Configuration (a) permits actuation authority over v_2 even to high frequency but couples strongly with equipment (receiver) flexibility. Configuration (b) rejects only disturbances originating in the source but couples weakly with both base (source) and equipment (receiver) flexibility.

0.16 N/μm, and $m_1/m_2 \simeq 10$ and $k_1/k_2 \simeq 0.13$.

In Figure 3.28(b) the series isolator is a soft spring installed between the active stage and the equipment. If the only disturbance to the mount were due to v_B^f, then the mass velocity v_2 could be regulated by feedback of velocity v_1 (or acceleration a_1) to the force actuator. The sensor-actuator pair remains collocated, but cannot reject disturbances at v_2 that originate from sources other than the base. Because of the location of the soft spring, Figure 3.28(b) is superior to Figure 3.28(a) in terms of decoupling unmodelled equipment flexibility from the loop transfer function, as is described below.

In this section only the velocity actuation problem are studied for the series isolation model, although the analysis can easily be extended to the force isolation problem. Secondly, only variations of the configuration in Figure 3.28(a) is studied in detail, since this configuration is the one used for active isolation and active mirror positioning in the experimental chapters of this thesis.

3.3.1 General Model for Series Actuator

A general model for the configuration of Figure 3.28(a) is illustrated in Figure 3.29 in which the series isolator is modelled as a general mobility element S between the actuator and the base structure. For this model the transfer function G_{S1} from control force f_a to equipment acceleration $a_3 = sv_3$ can be derived using four-pole mobility methods. For simplicity the actuator stage is assumed massless. From Eq. 3.2 the four-pole model of the actuator stage is simply

$$\begin{bmatrix} F_1 \\ v_1 \end{bmatrix} = \begin{bmatrix} 1 & 0 \\ Y_I & 1 \end{bmatrix} \begin{bmatrix} F_2 \\ v_2 \end{bmatrix} + \begin{bmatrix} 0 \\ -Y_I \end{bmatrix} f_a \tag{3.79}$$

where $Y_I = s/(c_1 s + k_1)$. The four-pole equipment model is given by Eq. 3.3, and the base structure four-pole model at output terminal 0 is adapted from Eq. 2.42

$$v_B^f = \begin{bmatrix} Y_B & 1 \end{bmatrix} \begin{bmatrix} F_0 \\ v_0 \end{bmatrix} \tag{3.80}$$

The passive series element S is modelled as a general four-pole system based on Eq. 2.17 (to permit later substitution of different models for S into the final result)

$$\begin{bmatrix} F_0 \\ v_0 \end{bmatrix} = \begin{bmatrix} \dfrac{1}{(T_v)_{10}} & \dfrac{1}{Y_{01}^f} \\ Y_{01}^b & \dfrac{1}{(T_v)_{01}} \end{bmatrix} \begin{bmatrix} F_1 \\ v_1 \end{bmatrix} \tag{3.81}$$

By assembling the four-pole matrices for each element in the system, the mount transmissibility T_{v3} and plant transfer function G_{S1} can be determined for the general case:

$$T_{v3}(s) = \frac{v_3}{v_B^f} = \frac{(T_v)_{01}(T_v)_{23}}{1 + \dfrac{Y_I}{Y_E} + \dfrac{(T_v)_{01}Y_{01}^b}{Y_E} + Y_B(T_v)_{01}\left[\dfrac{1}{Y_E(T_v)_{10}} + \dfrac{1}{Y_{01}^f}\left(1 + \dfrac{Y_I}{Y_E}\right)\right]} \tag{3.82}$$

$$G_{S1}(s) = \frac{a_3}{f_a} = \frac{s(T_v)_{23}Y_I\left[1 + Y_B\dfrac{(T_v)_{01}}{Y_{01}^f}\right]}{1 + \dfrac{Y_I}{Y_E} + \dfrac{(T_v)_{01}Y_{01}^b}{Y_E} + Y_B(T_v)_{01}\left[\dfrac{1}{Y_E(T_v)_{10}} + \dfrac{1}{Y_{01}^f}\left(1 + \dfrac{Y_I}{Y_E}\right)\right]} \tag{3.83}$$

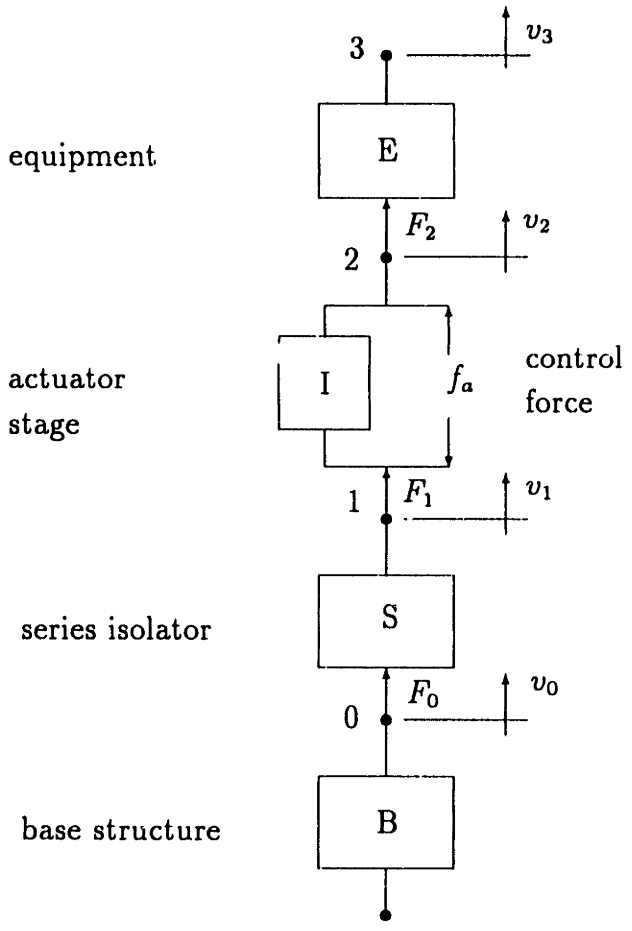

Figure 3.29: General model for series isolator on vibrating flexible base structure.

These two functions are investigated first for the situation in which the base is rigid, and then for a base modelled as a single resonant mode.

3.3.2 Rigid Base Models

A rigid base implies zero base mobility ($Y_B = 0$). In order to simplify the following analysis, the equipment E is modelled as a rigid mass m_1, although the effect of equipment flexibility can easily be treated by returning to Eqs. 3.82 and 3.83 and applying the analysis of Section 2.5.2 and 3.2.3. With this assumption for the equipment, $Y_E = 1/m_1 s$ and $(T_v)_{23} = 1$. The series isolator S will first be modelled as a rigid element (in order to characterize the mount transmissibility T_{v3} and transfer function G_{S1} before the series isolator S is applied) and then by two flexible elements that are illustrated in Figure 3.30.

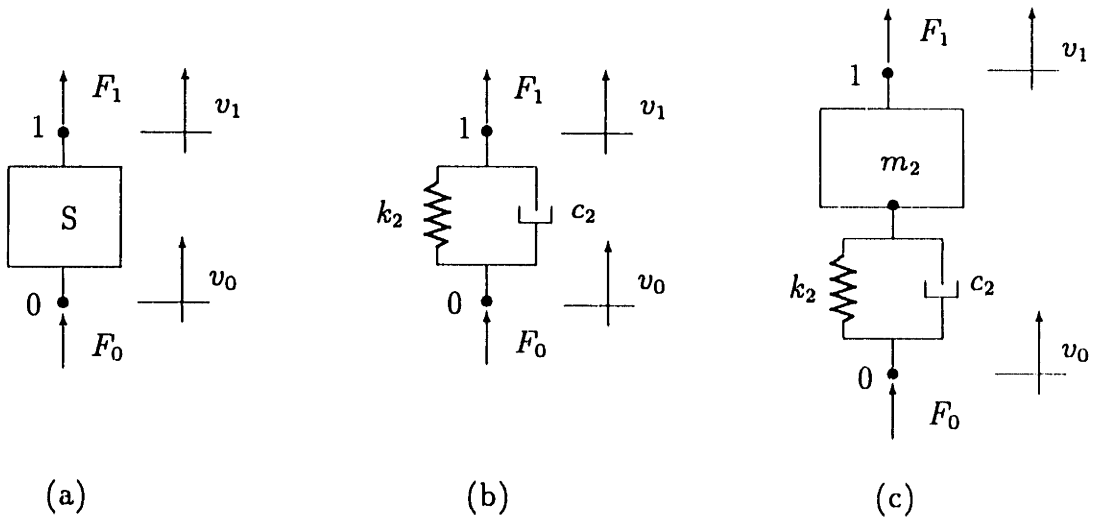

Figure 3.30: Series isolator models: (a) general representation, (b) massless viscously damped spring, and (c) softmounted reaction mass.

Series Isolator Modelled as Rigid, Massless Element: A rigid, massless element S implies that $(T_v)_{10} = (T_v)_{01} = 1$ (velocity and force constant across the element) and that $Y_{01}^b = 0$ and $Y_{01}^f = \infty$. Substitution of these expressions into Eqs. 3.82 and 3.83 leads to the following simple expressions for the mount transmissibility and acceleration transfer function:

$$T_{v3}(s) = \frac{1}{1 + \dfrac{Y_I}{Y_E}} \tag{3.84}$$

$$G_{S1}(s) = \frac{sY_I}{1 + \dfrac{Y_I}{Y_E}} \tag{3.85}$$

These functions are identical to those derived for the classical passive isolator and the parallel actuator model in Eqs. 2.79 and 3.12, as is expected since Figure 3.29 reverts to the parallel actuator general model in Figure 3.1 when the series element is both massless and rigid. The transmissibility of Eq. 3.84 is plotted as the solid line in Figure 3.31 in terms of normalized frequency $\bar{\omega} = \omega/\omega_o$, where ω_o is the frequency at which the equipment resonate on the stiff actuator. In this example, the resonance at ω_o is assumed to be lightly damped ($\zeta_o = 0.02$). Further, it is assumed that the mount resonance at $\bar{\omega} = 1$ is too high to provide a desired level of passive isolation in the frequency range below $\bar{\omega} = 1$, requiring the addition of a series isolator.

The acceleration transfer function G_{S1} of Eq. 3.85 is plotted in Figure 3.32 and is identical to G_1 plotted as the dashed line in Figure 3.3 for the classical parallel isolator, with the exception that the damping at resonance $\bar{\omega} = 1$ in the current example is assumed to be much lower than in Figure 3.3.

Series Isolator Modelled as Viscously Damped Spring: Let the series isolator in Figure 3.29 be the massless viscously damped spring illustrated in Figure 3.30(b). Using Eq. 2.21 the four-pole mobility of the isolator S becomes

$$\begin{bmatrix} F_1 \\ v_1 \end{bmatrix} = \begin{bmatrix} 1 & 0 \\ Y_S & 1 \end{bmatrix} \begin{bmatrix} F_2 \\ v_2 \end{bmatrix} + \begin{bmatrix} 0 \\ -Y_S \end{bmatrix} f_a \tag{3.86}$$

where the blocked mobility of the series spring is $Y_S = s/(c_2 s + k_2)$. From Eq. 3.86 the velocity transmissibilities $(T_v)_{01}$ and $(T_v)_{10}$ are equal to unity, and $Y_{01}^f = \infty$. Given these assumptions, the functions in Eqs. 3.82 and 3.83 become

$$T_{v3}(s) = \frac{1}{1 + \left(\dfrac{Y_I + Y_S}{Y_E}\right)} \tag{3.87}$$

$$G_{S1}(s) = \frac{sY_I}{1 + \left(\dfrac{Y_I + Y_S}{Y_E}\right)} \tag{3.88}$$

The effect of the series spring, therefore, is to create an effective mount isolator mobility of $Y_I + Y_S$. When the actuator spring mobility Y_I is much stiffer than the series isolator Y_S, then $Y_S \gg Y_I$ and the mount corner frequency ω_2 and damping ζ_2 are set primarily by the resonance of the mass m on the series isolator. Given this assumption, two new modal parameters are introduced:

$$\omega_2^2 = \frac{k_2}{m_1} \qquad \zeta_2 = \frac{c_2}{2\omega_2 m_1} \tag{3.89}$$

In Figure 3.31 the transmissibility T_{v3} of Eq. 3.87 is plotted versus the rigid element transmissibility, in which it is assumed that $\bar{\omega}_2 = \omega_2/\omega_o = 0.04$ and $\zeta_2 = 0.1$. These values are selected because they are representative of experimental parameters encountered in Chapter 5. Since $Y_S \gg Y_I$, the transmissibility is essentially identical

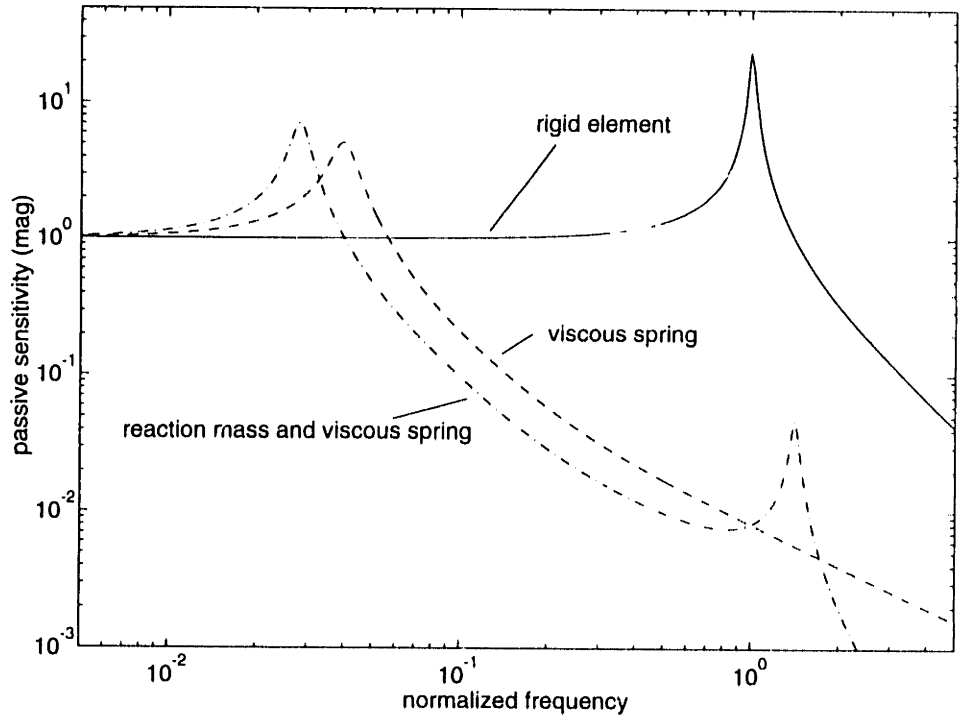

Figure 3.31: Mount passive sensitivity $\mathcal{P}(\bar{s})$ for three models. Parameters: $\omega_2/\omega_o = 0.04$, $\zeta_o = 0.02$, $\zeta_2 = 0.1$, $m_2/m_1 = 1$.

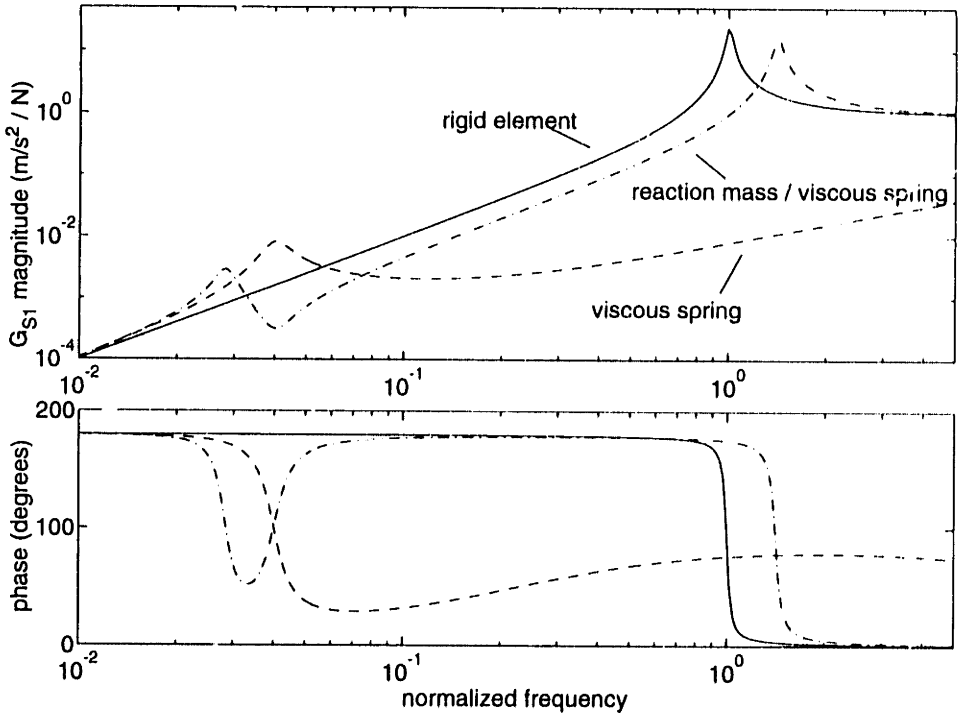

Figure 3.32: Equipment acceleration $G_1(\bar{s}) = a_3/f_a$ on rigid base. Parameters: $\omega_2/\omega_o = 0.04$, $\zeta_o = 0.02$, $\zeta_2 = 0.1$, $m_2/m_1 = 1$.

to the curve parameterized by $\zeta_o = 0.1$ in Figure 2.11 for the classic parallel actuator model, with the mount resonance shifted from $\bar{\omega} = 1$ to $\bar{\omega} = 0.04$.

The transfer function G_{S1} is plotted in Figure 3.32 versus the rigid series element transfer function. At low frequencies the plot resembles that for the classic parallel actuator model in Figure 3.3, but at high frequencies G_{S1} in Figure 3.32 exhibits an increase in gain due to the presence of damping in the series isolator. By comparing Eqs. 3.88 and 3.12, it can be seen that while the series isolator modifies the denominator of Eq. 3.88, the numerator remains unchanged, leading to a real pole-zero pair that increases actuator gain in the frequency range between $\bar{\omega} = 0.04$ and $\bar{\omega} = 1$.

Series Isolator Modelled as Softmounted Reaction Mass: In Figure 3.30(c) a reaction mass m_2 is added to the viscously damped spring, resulting in an isolator S with internal dynamics. The four-pole expression for this combined system is found by assembling the models in Eqs. 2.18 and 2.21 in series

$$\begin{bmatrix} F_0 \\ v_0 \end{bmatrix} = \begin{bmatrix} 1 & m_2 s \\ \dfrac{s}{c_2 s + k_2} & \dfrac{1}{(T_v)_{01}} \end{bmatrix} \begin{bmatrix} F_1 \\ v_1 \end{bmatrix} \tag{3.90}$$

where the velocity transmissibility from terminal 0 to terminal 1 is

$$(T_v)_{01} = \frac{c_2 s + k_2}{m_2 s^2 + c_2 s + k_2} \tag{3.91}$$

Eq. 3.91 can be recognized as transmissibility function with corner frequency $\omega = \sqrt{k_2/m_2}$. Above this corner frequency, velocity disturbances between terminal 0 and terminal 1 are attenuated. Likewise, force disturbances applied to the mass m_2 (due to the force actuation f_a, for example) are also attenuated before being transmitted to the base structure. Using the four-pole parameters given by Eq. 3.90, the transmissibility T_{v3} and acceleration transfer function G_{S1} become

$$T_{v3}(s) = \frac{(T_v)_{01}}{1 + \dfrac{Y_I}{Y_E} + \dfrac{Y_S}{Y_E}(T_v)_{01}} \tag{3.92}$$

$$G_{S1}(s) = \frac{sY_I}{1 + \dfrac{Y_I}{Y_E} + \dfrac{Y_S}{Y_E}(T_v)_{01}} \tag{3.93}$$

The transmissibility T_{v3} of Eq. 3.92 is plotted in Figure 3.31 for the same set of parameters used for the viscous spring series isolator, with the additional parameter $m_2/m_1 = 1$. Due to the addition of mass m_2 the passive mount resonance now occurs at $\bar{\omega} = \bar{\omega}_2/\sqrt{2} = 0.028$, and the former hardmount resonance at $\bar{\omega} = 1$ increases to $\bar{\omega} = \sqrt{2}$. For frequencies below $\bar{\omega} = 1$, the transmissibility resembles that of the classic passive actuator model with corner frequency at $\bar{\omega} = 0.028$.

The transfer function G_{S1} plotted in Figure 3.32, however, is much different from the previous two models of series isolators. Above mount resonance at $\bar{\omega} = 0.028$, the transfer function magnitude is recovered to one-half of the value below mount resonance, since the actuator reacts against the inertia of mass m_2 at all frequencies instead of reacting against the soft series spring. The phase loss at passive mount resonance is also recovered in this frequency range.

3.3.3 Effect of Base Flexibility

The acceleration transfer function $G_{S1} = a_3/f_a$ is investigated for the case that $Y_B \neq 0$. The pole-zero spacing in G_{S1} due to a base resonant mode is determined for a base mobility modelled as in Eq. 2.91, for the two frequency ranges $\bar{\omega} \ll \bar{\omega}_2$ and $\bar{\omega}_2 \ll \bar{\omega} \ll 1$ illustrated in Figure 3.32.

Series Isolator Modelled as Rigid, Massless Element: When Y_B is retained Eq. 3.85 becomes

$$G_{S1}(s) = \frac{sY_I}{1 + \dfrac{Y_I}{Y_E} + \dfrac{Y_B}{Y_E}} \tag{3.94}$$

Eq. 3.94 is identical to Eq. 3.19 derived for parallel isolator model. Therefore the relative pole-zero spacing for $\bar{\omega} \ll 1$ is given by Eq. 3.42

$$\frac{z_i - p_i}{\bar{\omega}_b} = \frac{m_1 \phi_b^2}{2} \tag{3.95}$$

Series Isolator Modelled as a Viscously Damped Spring: With Y_B retained, Eq. 3.88 becomes

$$G_{S1}(s) = \frac{sY_I}{1 + \dfrac{Y_I + Y_S}{Y_E} + \dfrac{Y_B}{Y_E}} \tag{3.96}$$

For frequencies well below series spring resonance ($\bar{\omega} \ll \bar{\omega}_2$) the series mount appears rigid and the pole-zero spacing for base modes occurring in this frequency range is the same as Eq. 3.95. Above resonance $\bar{\omega}_2$, $Y_S/Y_E \gg 1$ and $Y_S/Y_E \gg Y_I/Y_E$, and Eq. 3.96 is approximated by

$$G_{S1}(s) = \frac{sY_I}{\dfrac{Y_S}{Y_E} + \dfrac{Y_B}{Y_E}} \tag{3.97}$$

By substituting the expression Y_B/Y_E of Eq. 3.35 into Eq. 3.97, and by repeating the analysis of Eqs. 3.43 to 3.44, the relative pole-zero spacing is determined to be

$$\frac{z_i - p_i}{\bar{\omega}_b} = -\frac{m\phi_b^2}{2(\bar{\omega}_b/\bar{\omega}_2)^2} \tag{3.98}$$

which is identical to the relative pole-zero spacing for the parallel actuator model above mount resonance ω_o, only here the base mode coupling is attenuated by $\bar{\omega}^2$ above series mount corner frequency ω_2 instead of above softmount corner frequency ω_o.

Series Isolator Modelled as a Softmounted Reaction Mass: The relative pole-zero spacing for the frequency range $\bar{\omega} \ll \bar{\omega}_2$ can be found by considering the general form for G_{S1} in Eq. 3.83. In this frequency range $(T_v)_{01} \approx 1$ and $Y_S/Y_E \ll Y_I/Y_E \ll 1$, and G_{S1} is approximately

$$G_{S1}(s) = \frac{a_3}{f_a} = \frac{sY_I\left(1 + \dfrac{Y_B}{Y_M}\right)}{1 + Y_B\left(\dfrac{1}{Y_E} + \dfrac{1}{Y_M}\right)} \tag{3.99}$$

Using $Y_M = 1/sm_2$ and $Y_E = 1/sm_1$,

$$G_{S1}(s) = \frac{sY_I(1 + sm_1Y_B)}{1 + s(m_1 + m_2)Y_B} \tag{3.100}$$

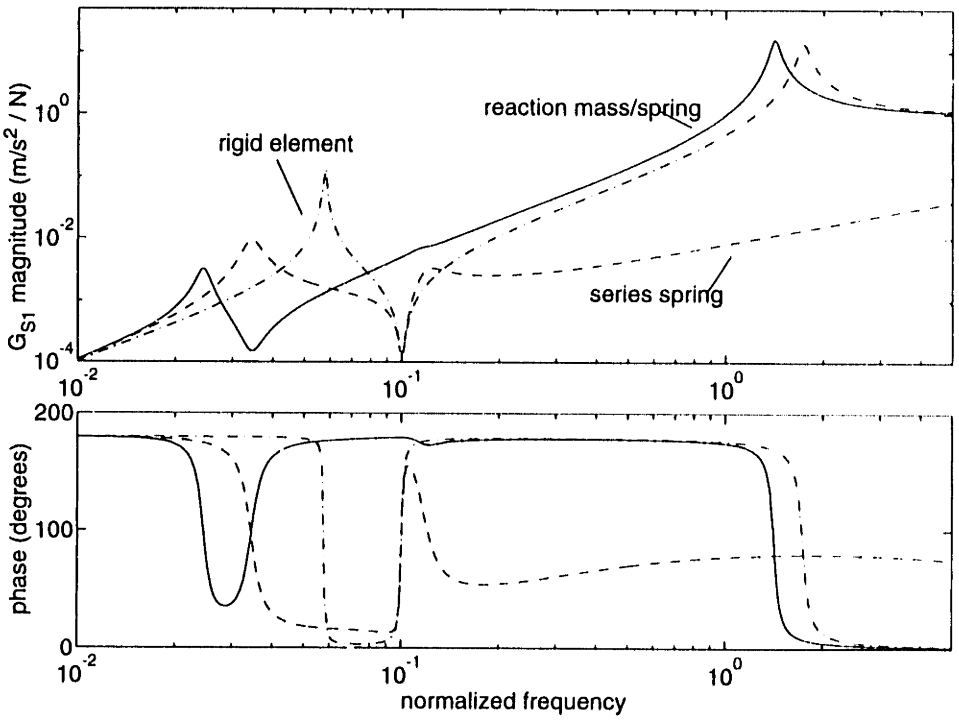

Figure 3.33: Equipment acceleration $G_{S1}(\bar{s}) = a_3/f_a$ on flexible base. Parameters: $\beta_b = 100$, $\omega_2/\omega_o = 0.04$, $\zeta_o = 0.02$, $\zeta_2 = 0.1$, $m_2/m_1 = 1$

Substitution of Y_B from Eq. 2.91 leads to

$$G_{S1}(s) = \frac{sY_I\left[s^2(1+m_2\phi_b^2) + 2\zeta_b\omega_b s + \omega_b^2\right]}{s^2\left[1+(m_1+m_2)\phi_b^2\right] + 2\zeta_b\omega_b s + \omega_b^2} \tag{3.101}$$

For small ζ_b, zeros and poles of G_{S1} are at

$$z_i = \bar{\omega}_b\left(1 - \frac{m_2\phi_b^2}{2}\right)^{-1/2} \tag{3.102}$$

$$p_i = \bar{\omega}_b\left(1 - \frac{(m_1+m_2)\phi_b^2}{2}\right)^{-1/2} \tag{3.103}$$

where $\bar{\omega}_b = \omega_b/\omega_o$. Eqs. 3.102 and 3.103 indicate that both the zero and pole are shifted, but the relative pole zero spacing, to first order in $m_1\phi_b^2$, remains the same as that for the previous two models studied for series isolators:

$$\frac{z_i - p_i}{\bar{\omega}_b} = \frac{m_1\phi_b^2}{2} \tag{3.104}$$

Therefore, the presence of the additional reaction mass does not increase the pole-zero spacing (or the degree of modal coupling) in the frequency region below $\bar{\omega}_2$.

Consider now the frequency range above $\bar{\omega}_2$ but below the actuator resonance at $\bar{\omega} = 1$. In this frequency range, $Y_I/Y_E \ll 1$ and Eq. 3.83 becomes

$$G_{S1}(s) = \frac{sY_I\left(1 + \frac{Y_B}{Y_M}(T_v)_{01}\right)}{1 + \frac{Y_S}{Y_E}(T_v)_{01} + Y_B(T_v)_{01}\left(\frac{1}{Y_E} + \frac{1}{Y_E}\right)} \tag{3.105}$$

The second term in the denominator can be simplified to

$$\begin{aligned} \frac{Y_S}{Y_E}(T_v)_{01} &= \left(\frac{s^2 m_1}{sc_2 + k_2}\right)\left(\frac{sc_2 + k_2}{s^2 m_2 + c_2 s + k_2}\right) \\ &\approx \frac{sm_1}{sm_2} = \frac{Y_M}{Y_E} \qquad\qquad s \gg \omega_2 \end{aligned} \tag{3.106}$$

Substitution of Eq. 3.106 into Eq. 3.105 and rearranging terms leads to the following expression for G_{S1}:

$$\begin{aligned} G_{S1}(s) &= sY_I\left(\frac{Y_E}{Y_E + Y_M}\right)\frac{\left[1 + \frac{Y_B}{Y_M}(T_v)_{01}\right]}{\left[1 + \frac{Y_B}{Y_M}(T_v)_{01}\right]} \\ &= sY_I\left(\frac{Y_E}{Y_E + Y_M}\right) \end{aligned} \tag{3.107}$$

Eq. 3.107 indicates that there is perfect pole-zero cancellation in the frequency region between $\bar{\omega}_2$ and $\bar{\omega} = 1$. There is no restriction that $m_1\phi_b^2$ or $m_2\phi_b^2$ be small compared to one, only that the base mode frequency $\bar{\omega}_b$ be well above $\bar{\omega}_2$ and well below $\bar{\omega} = 1$. Effects of a mismatch between the masses of m_1 and m_2 are illustrated in the multiplicative error analysis of Section 3.5. Table 3.7 summarizes the relative pole-zero separation for each of the series isolator configurations.

Transfer functions for the three series isolator configurations are compared in Figure 3.33 for an assumed base mode occurring at $\bar{\omega}_b = 0.1$ with damping $\zeta_b = 1\%$ and parameter $\beta_b = 100$ – a strongly coupled mode that corresponds to a base modal mass only one-half of the equipment mass. The mode is strongly coupled into G_{S1} when S is rigid, but is significantly decoupled from the transfer function when S is a viscous spring. There is almost no coupling of the base mode when the series isolator is modelled as the softmounted reaction mass.

Table 3.7: First order coupling (in $m_1\phi_b^2$) of base resonance at $\bar{\omega}_b = 0.1$ into acceleration transfer function $G_{S1}(\bar{s}) = a_1/f_a$ for series isolator with $\bar{\omega}_2 = 0.04$.

series isolator configuration	frequency range	
	$\bar{\omega}_b \ll \bar{\omega}_2$	$\bar{\omega}_2 \ll \bar{\omega}_b \ll 1$
rigid, massless element	$\frac{m_1\phi_b^2}{2}$	$\frac{m_1\phi_b^2}{2}$
viscously damped spring	$\frac{m_1\phi_b^2}{2}$	$-\frac{m_1\phi_b^2}{2(\bar{\omega}_b/\bar{\omega}_2)^2}$
softmount reaction mass	$\frac{m_1\phi_b^2}{2}$	0

The two series isolators studied decouple base modes from the loop transfer function, due to the presence of a soft spring between the actuator and the base structure. Modal resonances in the equipment, however, will be strongly coupled into the loop transfer functions unless the series configuration of Figure 3.28 is used, in which the soft spring is located between the actuator and isolated equipment.

Reactionless Actuator: The softmounted reaction mass isolator can be designed so that it is completely reactionless at all frequencies, not just above softmount resonance. A single-axis reactionless isolator is illustrated in Figure 3.34. A command f_a moves both equipment and reaction masses the same distance but in opposite directions, leading to equal and opposite reaction forces applied to the the base structure. The actuator transfer function is independent of the dynamics of the base, and the soft series isolator provides passive vibration isolation of base motion. The benefits of reactionless actuation have been shown for gimballed systems [38], and have been manufactured as actuators for optical systems [48].

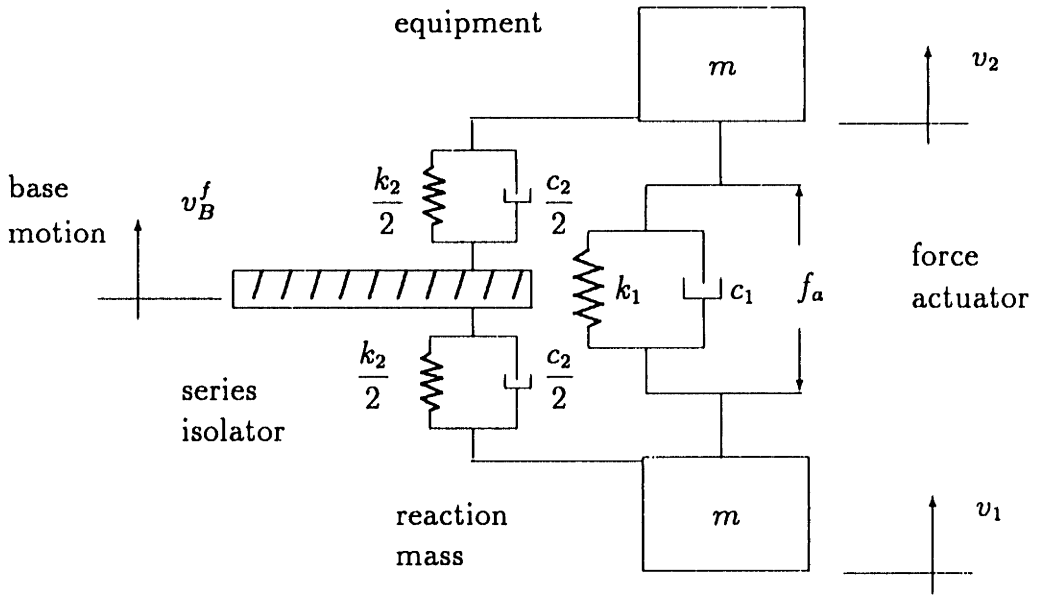

Figure 3.34: Reactionless actuator model.

3.4 Multiplicative Error Models

The objective of this section is to develop parametric models for the multiplicative error introduced to a nominal plant model by the presence of a resonance in the base or isolated equipment. In the last section the degree to which these modes are coupled (or uncoupled) into the local isolator transfer functions is explained in terms of relative pole-zero spacing; here the degree of coupling is quantified in terms of a multiplicative error and perturbations in gain and phase due to the base or equipment mode.

The *nominal* plant G_o is defined as a transfer function measured for the classic parallel actuator model of Section 3.2.1, in which the base is assumed rigid and the equipment is modelled as a rigid mass. The *actual* plant G_a includes the effects of base or equipment flexibility. As illustrated in Figure 3.35, the actual plant G_a is related to the nominal plant by

$$G_a(s) = G_o(s)L(s) \tag{3.108}$$

$$= G_o(s)\left[1 + e(s)\right] \tag{3.109}$$

$$= G_o(s) + G_o(s)e(s) \tag{3.110}$$

where $e(s)$ is termed the *multiplicative error*. The Nyquist plane interpretation of

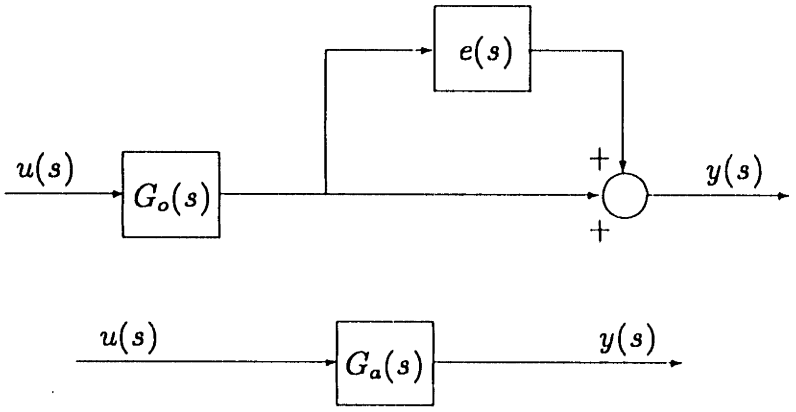

Figure 3.35: Unstructured uncertainty modelled as multiplicative error $e(s)$.

Eq. 3.110 is illustrated in Figure 3.36 for the plant transfer function evaluated at the frequency $s = j\omega_i$. If the complex perturbation $e(j\omega_i)$ is known, then the vector $G_o(j\omega_i)e(j\omega_i)$ and thus the position of $G_a(j\omega_i)$ are known. If, however, only the magnitude $|e(j\omega_i)|$ is known, then the actual plant $G_a(j\omega_i)$ can only be assumed to lie somewhere within the circle of radius $r = |G_o(j\omega_i)e(j\omega_i)|$ that is centered on the point $G_o(j\omega_i)$.

In a control design $e(s)$ might be treated as unstructured uncertainty (only the magnitude is known, not the phase). In the following analysis the true structure of $e(s)$ is investigated since analytical expressions are available for the nominal and actual plants. It is assumed that some knowledge of the base dynamics is available to create an estimate of the magnitude of the perturbation: specifically, it is assumed that estimates (or bounds) are available of the mode frequency, damping and modal mass as seen from the isolator attach point. With this information, estimates for the dimensionless parameters $\beta_b = (m\phi_b^2)/(2\zeta_b)$ or $\beta_{e2} = (m\phi_{e2}^2)/(2\zeta_e)$ can be made for each mode of the base or equipment, based on experimental data or an analytical model.

3.4.1 Parallel Actuator Model

Consider the acceleration transfer function G_1 for the case of base flexibility. From Table 3.4, the actual transfer function G_{a1} – which includes the effect of the single

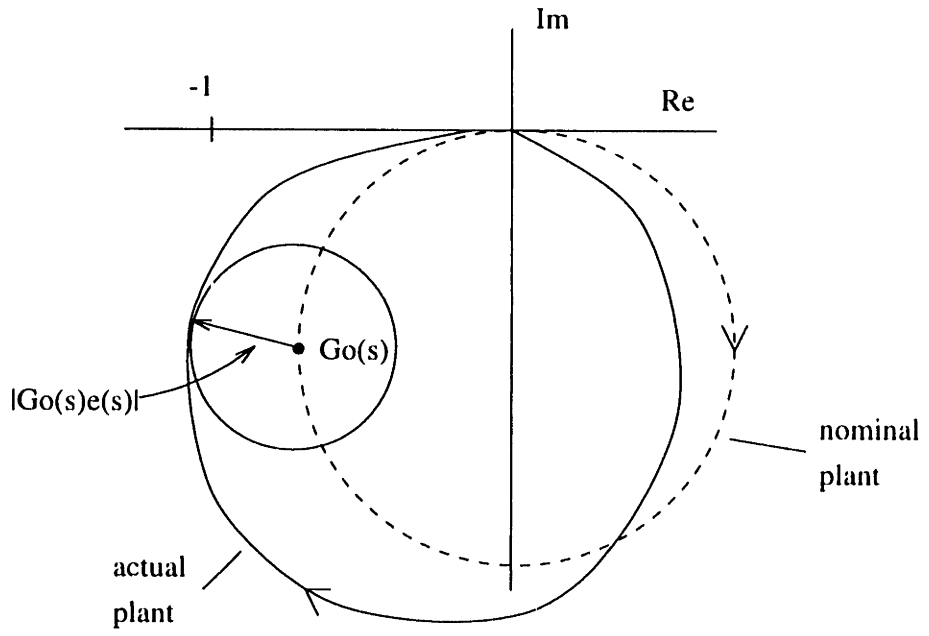

Figure 3.36: Illustration of multiplicative error $e(s)$ in the Nyquist plane. The error radius is $|G_o(s)e(s)|$ at each frequency, $s = j\omega$.

base mode – is given by

$$G_{a1}(s) = \frac{sY_I}{1 + \frac{Y_I}{Y_E} + \frac{Y_B}{Y_E}} \tag{3.111}$$

The nominal transfer function G_{o1}, defined as that measured on a rigid base, is simply

$$G_{o1}(s) = \frac{sY_I}{1 + \frac{Y_I}{Y_E}} \tag{3.112}$$

An expression for the multiplicative error can be calculated using Eq. 3.110:

$$\begin{aligned} G_{a1}(s) - G_{o1}(s) &= \frac{Y_I\left(1 + \frac{Y_I}{Y_E} + \frac{Y_B}{Y_E}\right) - sY_I\left(1 + \frac{Y_I}{Y_E}\right)}{\left(1 + \frac{Y_I}{Y_E}\right)\left(1 + \frac{Y_I}{Y_E} + \frac{Y_B}{Y_E}\right)} \\ &= G_{o1}(s)\left[\frac{-\frac{Y_B}{Y_E}}{1 + \frac{Y_I}{Y_E} + \frac{Y_B}{Y_E}}\right] \end{aligned} \tag{3.113}$$

Therefore the multiplicative error itself is

$$e(s) = \frac{-\dfrac{Y_B}{Y_E}}{1 + \dfrac{Y_I}{Y_E} + \dfrac{Y_B}{Y_E}} \tag{3.114}$$

The multiplicative error for each transfer function of the active parallel isolator tabulated in Table 3.4 can be calculated in this manner, and the results are listed in Table 3.8. A surprising result of Table 3.8 is that only three functions – represented as $e_{\rm I}$, $e_{\rm II}$, and $e_{\rm III}$ respectively – describe the multiplicative error for the eight transfer functions. A further simplification is that the function $e_{\rm III}$ reduces to variations of $e_{\rm II}$ for most cases of interest. Therefore, the multiplicative error can be characterized by studying the behavior of the functions $e_{\rm I}$ and $e_{\rm II}$. The asymptotic behavior of these functions – well above and below mount resonance ω_o – is investigated first in order to provide insight.

The multiplicative error $e(s)$ reaches a maximum at the roots of its characteristic equation, which is the same as that for the transfer functions determined for base and equipment flexibility, listed in Table 3.4. Therefore the roots of $e(s)$ are at the poles p_i from Eq. 3.55 and Eq. 3.56. Using the definition of β_b in Eq. 2.94, the pole locations are written as

$$p_i = \bar{\omega}_b \left(1 - \frac{m\phi_b^2}{2}\right) = \bar{\omega}_b \left(1 - \zeta\beta_b\right) \qquad (m\phi_b^2, \bar{\omega}_b^2) \ll 1 \tag{3.115}$$

$$p_i = \bar{\omega}_b \left(1 + \frac{m\phi_b^2}{2\bar{\omega}_b^2}\right) = \bar{\omega}_b \left(1 + \frac{\zeta\beta_b}{\bar{\omega}_b^2}\right) \qquad m\phi_b^2 \ll 1,\ \bar{\omega}_b^2 \gg 1 \tag{3.116}$$

The subscript $(\cdot)_b$ is used for the parameter β_b for the remainder of this section for clarity, although the derivation applies equally well to equipment modes described by the parameter β_{e2}. The maximum value of $e_{\rm I}$ and $e_{\rm II}$ are determined by evaluating the functions in Table 3.8 at $\bar{\omega} = p_i$, and are listed in Table 3.9 for frequency ranges well above and below mount resonance ω_o. In the derivation, the approximations $Y_I/Y_E \ll 1$ for $\omega \ll \omega_o$ and $Y_I/Y_E \gg 1$ for $\omega \gg \omega_o$ are used to simplify the expressions for $e_{\rm I}$ and $e_{\rm II}$ in Table 3.8. The only assumption placed on the magnitude of β_b is that $\zeta_b\beta_b = m\phi_b^2 \ll 1$, which is not overly restrictive. For damping of 1%, a strongly coupled mode of $\beta_b = 10$ easily meets this restriction. The peak magnitude

Table 3.8: Form of the multiplicative error for active parallel isolator.

function	base flexibility	equipment flexibility
$G_1 = \dfrac{a_3}{f_a}$	e_{I}	e_{III}
$G_2 = \dfrac{a_2}{f_a}$	e_{I}	e_{II}
$G_4 = \dfrac{F_1}{f_a}$	e_{I}	e_{I}
$G_5 = \dfrac{x_2 - x_1}{f_a}$	e_{II}	e_{II}
e_{I}	$\dfrac{-\dfrac{Y_B}{Y_E}}{\left[1 + \dfrac{Y_I}{Y_E} + \dfrac{Y_B}{Y_E}\right]}$ or	$\dfrac{-\dfrac{Y_{e2}}{\bar{Y}_E}}{\left[1 + \dfrac{Y_I}{\bar{Y}_E} + \dfrac{Y_{e2}}{\bar{Y}_E}\right]}$
e_{II}	$\dfrac{\dfrac{Y_B}{Y_E}\left(\dfrac{Y_I}{Y_E}\right)}{\left[1 + \dfrac{Y_I}{Y_E} + \dfrac{Y_B}{Y_E}\right]}$ or	$\dfrac{\dfrac{Y_{e2}}{\bar{Y}_E}\left(\dfrac{Y_I}{\bar{Y}_E}\right)}{\left[1 + \dfrac{Y_I}{\bar{Y}_E} + \dfrac{Y_{e2}}{\bar{Y}_E}\right]}$
e_{III}	$\dfrac{\dfrac{Y_{e3}}{\bar{Y}_E}\left[\dfrac{Y_I}{\bar{Y}_E} + 1 - \dfrac{Y_{e2}}{Y_{e3}}\right]}{\left[1 + \dfrac{Y_I}{\bar{Y}_E} + \dfrac{Y_{e2}}{\bar{Y}_E}\right]}$	

of the multiplicative error is purely imaginary in this analysis, which is correct to first order in $m\phi_b^2$.

Gain Perturbation: The multiplicative error $e(s)$ is used to calculate the magnitude perturbation to G_o from Eq. 3.108

$$\begin{aligned} |G_a(s)| &= |G_o(s)||L(s)| \\ &= |G_o(s)||1 + e(s)| \end{aligned} \tag{3.117}$$

Table 3.9: Maximum value of multiplicative error for parallel actuator model, evaluated at pole frequency $\bar{\omega} = p_i$.

error type	frequency range	
	$\bar{\omega}_b \ll 1$	$\bar{\omega}_b \gg 1$
e_I	$-j\beta$	$\frac{j\beta}{\bar{\omega}_b^2}$
e_{II}	$-j\beta\bar{\omega}_b^2$	$j\beta$

The function L reaches a maximum at the frequency $\bar{\omega} = p_i$ for which the multiplicative error $e(s)$ reaches a maximum. Since $e(jp_i)$ is purely imaginary, the maximum magnitude perturbation is simply

$$|L(s)|_{max} = |L(jp_i)| = (1 + |e(jp_i)|^2)^{1/2} \tag{3.118}$$

The maximum values of the magnitude perturbations are listed in Table 3.10. The entry for e_I for $\bar{\omega}_b \ll 1$ agrees with the results of Garcia *et al.* [24], although the authors assumed that the result was valid only for $\beta_b \ll 1$. However, only the assumption $\zeta_b\beta_b \ll 1$ is required to derive the simple expressions in Table 3.10, which is far less restrictive.

Phase Perturbation: The maximum phase perturbation to the nominal transfer functions due to base or equipment modes occurs not at the pole frequency p_i, but rather at a frequency ω_ϕ halfway between the transfer function pole and zero caused by the base or equipment resonance (refer to Figure 3.12 or Figure 3.13). Zeros for the acceleration and gap transfer functions are given by Eq. 3.37 and Eq. 3.57. The maximum phase perturbation due to each multiplicative error type is determined by evaluating the function $L(s) = 1 + e(s)$ at the frequency $\bar{\omega}_b = \omega_\phi$, and the results are listed in Table 3.11 for the frequency ranges well above and below resonance. Again, the analysis only requires that $\zeta_b\beta_b \ll 1$. The result for e_I below resonance correctly

Table 3.10: Maximum value for gain perturbation for parallel actuator model, evaluated at pole frequency $\bar{\omega} = p_i$.

error type	frequency range	
	$\bar{\omega}_b \ll 1$	$\bar{\omega}_b \gg 1$
e_{I}	$(1+\beta^2)^{1/2}$	$\left(1+\dfrac{\beta^2}{\bar{\omega}_b^4}\right)^{1/2}$
e_{II}	$\left(1+\bar{\omega}_b^4\beta^2\right)^{1/2}$	$(1+\beta^2)^{1/2}$

Table 3.11: Asymptotic values for phase perturbation (in radians) for parallel actuator model.

error type	frequency range	
	$\bar{\omega}_b \ll 1$	$\bar{\omega}_b \gg 1$
e_{I}	$\mathrm{atan}\left(\dfrac{-4\beta}{4-\beta^2}\right)$	$\mathrm{atan}\left(\dfrac{\beta}{\bar{\omega}_b^2}\right)$
e_{II}	$\mathrm{atan}\left(-\bar{\omega}_b^2\beta\right)$	$\mathrm{atan}\left(\dfrac{4\beta}{4-\beta^2}\right)$

predicts that the phase loss for $\beta_b = 2$ is $-90°$, and that the phase loss for $\beta_b \to \infty$ is $-180°$. When $\beta_b \ll 1$, the phase perturbation is approximately $(-\ \mathrm{atan}(\beta_b))$, which agrees with the results of Garcia *et al.* [24].

Multiplicative Error Near ω_o: The value of the maximum multiplicative error for base or equipment resonances near ω_o is more difficult to determine analytically since the function characteristic equation is fourth order. However, for small values

of the parameter β_b the functions $e_{\rm I}$ and $e_{\rm II}$ are approximately

$$e_{\rm I}(s) \approx \frac{-\dfrac{Y_B}{Y_E}}{1+\dfrac{Y_I}{Y_E}} \tag{3.119}$$

$$e_{\rm II}(s) \approx \frac{\left(\dfrac{Y_I}{Y_E}\right)\dfrac{Y_B}{Y_E}}{1+\dfrac{Y_I}{Y_E}} \tag{3.120}$$

which when evaluated at $\bar{\omega}_b = 1$ lead to

$$e_{\rm I}(j\omega_o) \approx \left(\frac{1+2\zeta_o}{2\zeta_o}\right)\beta \tag{3.121}$$

$$e_{\rm II}(j\omega_o) \approx \frac{1}{2\zeta_o}\beta \tag{3.122}$$

Eqs. 3.121 and 3.122 predict that the degree of moda' coupling (in terms of magnitude and phase perturbations) will become stronger near the resonance $s = j\omega_o$. This effect can be seen in Figure 3.37 and Figure 3.38, which are plots of the inverse (maximum) magnitude of the multiplicative error $e_{\rm I}$ and $e_{\rm II}$ as a function of base mode frequency $\bar{\omega}_b$, based on the full order function from Table 3.8. A mount damping ratio of $\zeta_o = 0.1$ is assumed, and for small β_b, the coupling is increased by roughly a factor of 4, with smaller increases for large values of β_b. For base modes well above and below $\bar{\omega} = 1$, the curves assume asymptotic values predicted by Table 3.9. The form of $1/|e|$ is shown since this establishes a stability boundary commonly used for control design.

Multiplicative Error for Equipment Output Acceleration a_3: The behavior of the multiplicative error type $e_{\rm III}$ governs the perturbations to the acceleration transfer function G_{o1} when the output terminal 3 of the equipment is not collocated with the isolator interface terminal 2. When the transfer mobility Y_{e3} is equal to Y_{e2}, then $e_{\rm III} = e_{\rm II}$. However, when $Y_{e3} = -Y_{e2}$, corresponding to a mode shape at terminals 2 and 3 that are mutually 180 degree out of phase, then $e_{\rm III}$ becomes

$$e_{\rm III} = \frac{\dfrac{-Y_{e2}}{\bar{Y}_E}\left(\dfrac{Y_I}{\bar{Y}_E}+2\right)}{1+\dfrac{Y_I}{\bar{Y}_E}+\dfrac{Y_{e2}}{\bar{Y}_E}} \tag{3.123}$$

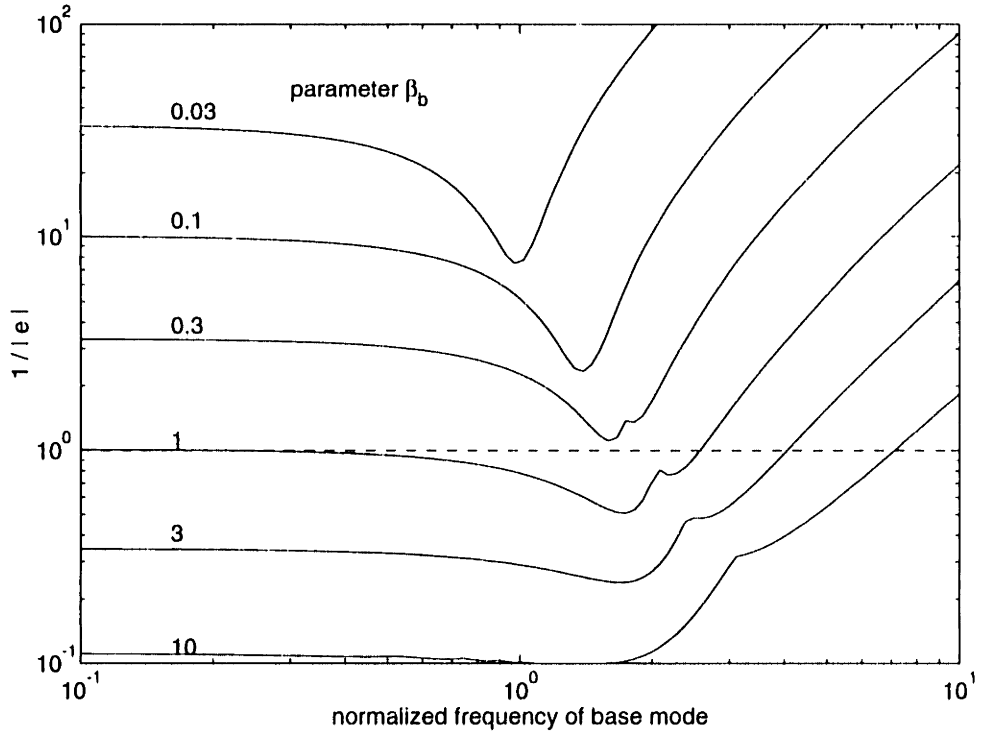

Figure 3.37: Multiplicative error type I as a function of base mode frequency $\bar{\omega}_b$. Curves parameterized by $\beta_b = m\phi_b^2/(2\zeta_b)$.

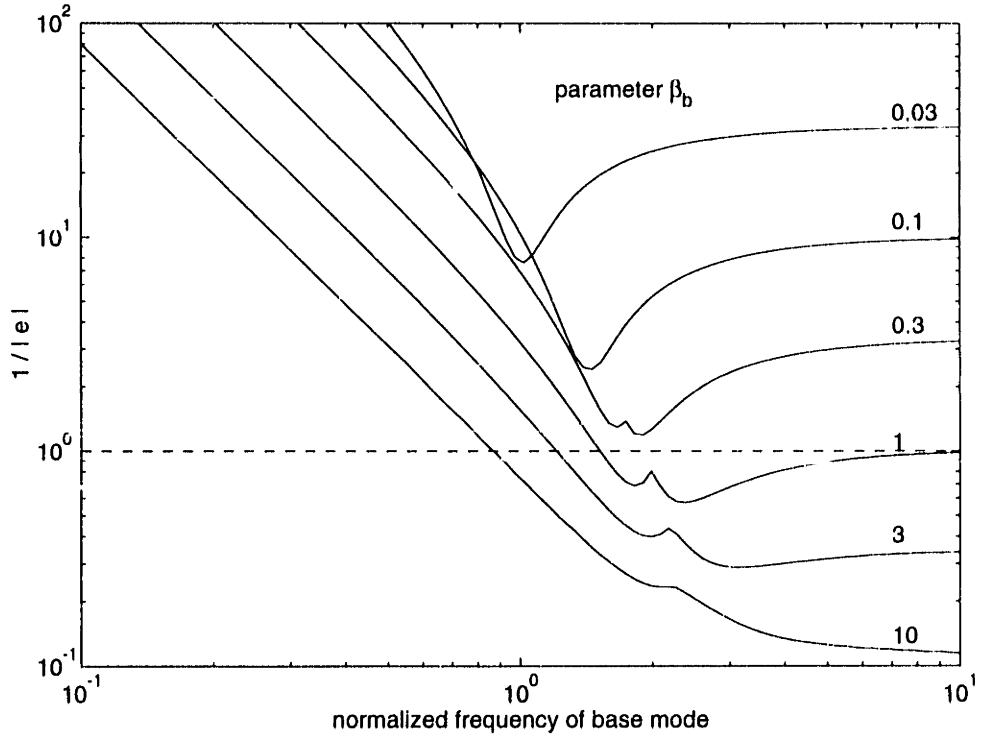

Figure 3.38: Multiplicative error type II as a function of base mode frequency $\bar{\omega}_b$. Curves parameterized by $\beta_b = m\phi_b^2/(2\zeta_b)$.

which for frequencies well above and below mount resonance becomes

$$e_{III} \approx 2e_I \qquad (\bar{s}^2, \bar{\omega}_b \ll 1) \tag{3.124}$$

$$e_{III} \approx -e_{II} \qquad (\bar{s}^2, \bar{\omega}_b \gg 1) \tag{3.125}$$

Eq. 3.124 predicts that below ω_o the equipment resonance will be coupled twice as strongly into the acceleration output a_3 compared to the acceleration a_2 (with the same phase perturbation). Eq. 3.125 predicts that above ω_o the equipment mode remains coupled in the output a_3, but with a phase perturbation that is still negative. These predictions are observed in Figures 3.22 to 3.26.

3.4.2 Series Isolation Model

The pole-zero separation for the case in which the series isolator is a softmounted reaction mass is shown in Section 3.3 to be zero for the frequency range above softmount frequency $\bar{\omega}_2$. Thus, it is expected that the multiplicative error will also be zero in this frequency range. This can be shown by considering the transfer function G_o from Eq. 3.93 (evaluated on a rigid base) and the transfer function G_a in Eq. 3.105 evaluated on a base with a single flexible mode. Substitution of these functions into Eq. 3.110 leads to the following complicated expression for the multiplicative error:

$$e(s) = \frac{\frac{Y_B}{Y_E}\left[\frac{Y_I}{Y_E} + \frac{Y_S}{Y_E}(T_v)_{01} - \frac{Y_E}{Y_M} - \frac{Y_I}{Y_M}\right]}{1 + \frac{Y_I}{Y_E} + \frac{Y_S}{Y_E}(T_v)_{01} + \frac{Y_B}{Y_E}(T_v)_{01}\left[1 + \frac{Y_E}{Y_M} + \frac{Y_I}{Y_M}\right]} \tag{3.126}$$

This function can be simplified by using Eq. 3.106 and that for frequencies below $\bar{\omega} = 1$, $Y_I/Y_E \ll 1$ and $Y_I/Y_M \ll 1$. After substitution and some algebra the multiplicative error is simplified to

$$e(s) = \frac{\frac{Y_B}{Y_M}(T_v)_{01}\left(\frac{Y_M}{Y_E} - 1\right)}{1 + \frac{Y_B}{Y_M}(T_v)_{01}} \qquad \bar{\omega}_2^2 \ll \bar{\omega} \ll 1 \tag{3.127}$$

Eq. 3.127 indicates that for a reaction mass m_2 that is equal to the isolated equipment mass m_1, or $Y_M = Y_E$, the multiplicative error will be zero above the softmount

frequency $\bar{\omega}_2$. However, even for mismatches between m_2 and m_1, the resulting multiplicative error is highly attenuated by the low-pass filter $(T_v)_{01}$ factor in the numerator.

3.5 Use of Dereverberated Mobility

Based on simulations in previous sections, it is observed that base or equipment flexibility affect the isolator transfer functions in two ways: 1) in a broadband sense, based on the general mass, spring, or damping qualities of the base, and 2) over narrow frequency ranges due to the resonant behavior of individual modes of the base. In this section a procedure is proposed using dereverberated mobility that incorporates both of these effects, and provides a means to approximately capture the modal coupling when the base or equipment mobility is represented by the response of several modes.

Consider a general representation for the base mode input mobility, in which the response is due to an infinite sum of modes

$$Y_B(s) = \sum_{i=1}^{\infty} \frac{s\phi_{bi}^2}{s^2 + 2\zeta_{bi}\omega_{bi}s + \omega_{bi}^2} \tag{3.128}$$

In a narrow frequency range near the r^{th} mode, the beam mobility is approximated by the modal response of the r^{th} mode plus residual terms representing the truncated modes at low and high frequency

$$Y_B(s) \approx \frac{1}{R_1 s} + \frac{s\phi_{br}^2}{s^2 + 2\zeta_{br}\omega_{br}s + \omega_{br}^2} + \frac{s}{R_2} \tag{3.129}$$

The dereverberated mobility of the base structure is introduced in Section 2.7, and is used here to approximate the residual terms due to the truncated modes

$$\begin{aligned} Y_B(s) &\approx Y_B^d + \frac{s\phi_{br}^2}{s^2 + 2\zeta_{br}\omega_{br}s + \omega_{br}^2} \\ &\approx Y_B^d + Y_r \end{aligned} \tag{3.130}$$

The term Y_r in Eq. 3.130 can be recognized as simply the single-mode base mobility introduced in Eq. 2.91 for the single mode analysis. Because the dereverberated mobility Y_B^d represents the average, or broadband response of the base input mobility,

it is assumed that this term can be modelled and incorporated into the nominal plant transfer function. For example, consider the acceleration transfer function $G_1 = G_2$ from column 1 of Table 3.4. When the term Y_B^d is substituted for Y_B, the new nominal plant $\tilde{G}_{o1}$ becomes

$$\tilde{G}_{o1}(s) = \frac{sY_I}{1 + \dfrac{Y_I}{Y_E} + \dfrac{Y_B^d}{Y_E}} \tag{3.131}$$

In the vicinity of the r^{th} base mode, the base mobility includes both terms in Eq. 3.130 and the actual transfer function becomes

$$\tilde{G}_{a1}(s) \approx \frac{sY_I}{1 + \dfrac{Y_I}{Y_E} + \dfrac{Y_B^d}{Y_E} + \dfrac{Y_r}{Y_E}} \tag{3.132}$$

Using Eqs. 3.113 to 3.114, the new multiplicative error is

$$\tilde{e}(s) = \frac{-\dfrac{Y_r}{Y_E}}{1 + \dfrac{Y_I}{Y_E} + \dfrac{Y_B^d}{Y_E}} \tag{3.133}$$

Since well above or below mount resonance ω_o the term Y_B^d/Y_E is small compared to either 1 or Y_I/Y_E, then a reasonable approximation is that $\tilde{e}(s) \approx e(s)$ from Eq. 3.114, which allows the multiplicative error results from Section 3.4 to be used. In summary, when the base is characterized by a multiple mode response, then the multiplicative error analysis of Section 3.6 best describes perturbations in magnitude and phase to the (new) nominal transfer function function $\tilde{G}_{o1}$ of Eq. 3.131

$$G_{a1} = \tilde{G}_{o1}\,[1 + e(s)] \tag{3.134}$$

Examples are shown below which illustrate these effects.

Dereverberated Models for Base Flexibility: Figure 3.39 is a plot of the acceleration transfer function G_1 in which the equipment is assumed to be a rigid mass m and the base structure is modelled as the free-free Bernoulli-Euler beam model introduced in Section 2.7. The first beam resonance is assumed to occur at $\omega = 0.5\omega_o$, where ω_o is the passive mount resonance. The beam mass is 10 times the equipment mass, or $m/M_b = 0.1$. Damping in all beam modes are assumed to be 1%, corresponding to a dimensionless coupling parameter $\beta_b = 20$ for each mode.

The exact transfer function G_1 is plotted versus the rigid base model G_{o1} and versus $\tilde{G}_{o1}$ which incorporates the dereverberated base model from Figure 2.26. The degree of modal coupling for the exact transfer function G_{a1} in Figure 3.39 is typical of that for error type e_I - strong coupling below ω_o, and coupling attenuated by $(\omega/\omega_o)^2$ above mount resonance. The function $\tilde{G}_{o1}$ is better than G_{o1} at capturing the reduction in gain at low frequencies and in capturing the backbone shape throughout the mount resonance region. It also appears that the resonant mode near $\bar{\omega} = 0.4$ is a perturbation about the backbone curve $\tilde{G}_{o1}$ instead of about G_{o1}. Because of the modal decoupling above mount resonance, $\tilde{G}_{o1}$ and G_{o1} overlay for $\omega \gg \omega_o$.

Dereverberated Models for Equipment Flexibility: A very different behavior is shown for the acceleration transfer function G_1 plotted in Figure 3.40, in which the base is assumed rigid but the equipment mobility is instead modelled as that of the free-free Bernoulli-Euler beam described above. The modal coupling is that of error type e_{II}: decoupling below mount resonance, and strong coupling above. In this case, the function $\tilde{G}_{o1}$ best captures the backbone trend at high frequencies. Clearly, the magnitude perturbations are about this backbone and not about the simpler model G_{o1}. The new nominal plant $\tilde{G}_{o1}$ also approximates the average phase.

In summary, the dereverberated mobility model of the base or equipment can be used to incorporate averaged, broadband knowledge of the flexible components into the nominal transfer function. The dereverberated model provides information about gradual changes in the plant transfer function gain, and captures the shift in frequency and damping of the mount resonance ω_o. The multiplicative error for the transfer function magnitude best describes perturbations about the nominal transfer function $\tilde{G}_{o1}$ which incorporates the dereverberated information.

3.6 Effects of Flexibility on Loop Stability

This section discusses the stability risks encountered when a compensator is designed for an active isolation mount that ignores the presence of base or equipment dynamics.

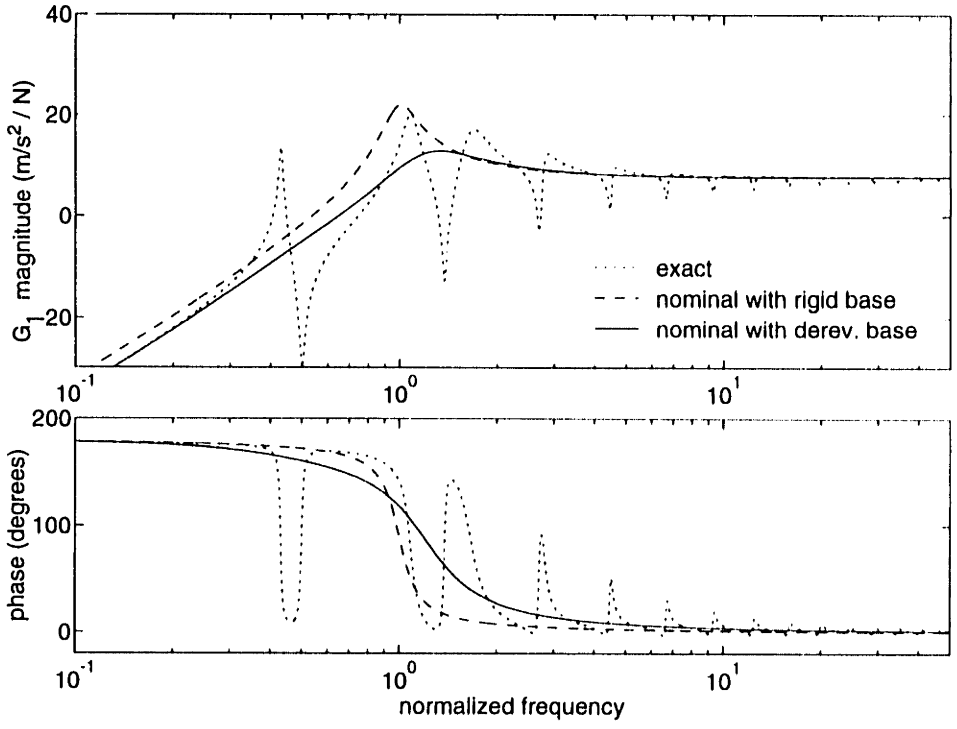

Figure 3.39: Acceleration transfer function $G_1(\bar{s}) = a_3/f_a$ for isolator on a B-E beam. Parameters: $m/M_b = 0.1$, $\omega_1/\omega_o = 0.5$, $\beta_b = 20$.

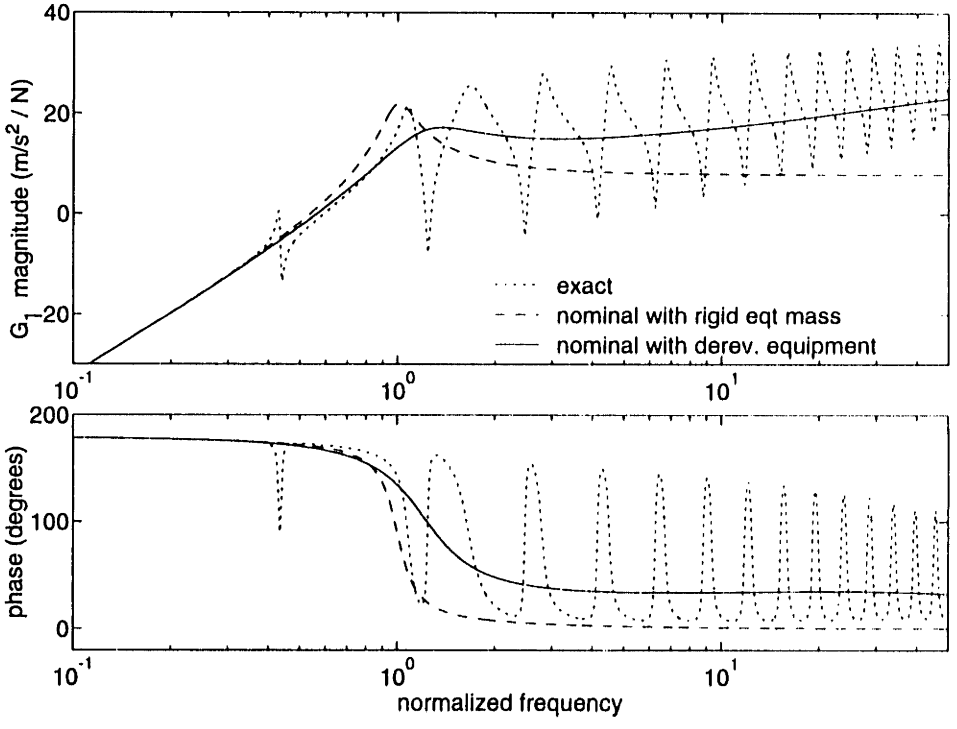

Figure 3.40: Acceleration transfer function $G_1(\bar{s}) = a_3/f_a$, rigid base, equipment modelled as B-E beam. Parameters: $m/M_b = 0.1$, $\omega_1/\omega_o = 2$, $\beta_b = 20$.

This situation may arise if the mount is designed and tested on a rigid test stand before installation on a flexible base, or if the isolated equipment is not well modelled during the control design. The discussion is restricted to the single-input single-output (SISO) case.

Table 3.4 summarizes the actuator-sensor transfer functions used for control design for the parallel actuator model of Figure 3.1. The compensator design is assumed to be based on the nominal plant G_o – that is, base or equipment flexibility are not present in the transfer functions – and that the compensator will be implemented on the actual plant G_a which includes the additional flexibility. The additional flexibility falls into two categories: broadband flexibility of the base, with effects that are like that of a mass, spring, or damper; and modal flexibility of the base or equipment, which impacts the transfer functions over a more narrow frequency range.

3.6.1 Broadband Flexibility

Figures 3.3 to 3.11 illustrate the changes to mount transfer functions due to base flexibility – modelled as a mass, spring, or damper – in terms of the dimensionless parameters listed in Table 2.2. The general effect is to shift the frequency and damping of the mount mode at ω_o, leading to changes in the transfer function gain and phase at low and high frequency. It is concluded that effects on the transfer functions are negligible for $Y_B/Y_E < 0.1$ from Table 2.2 (for example, $m/M < 0.1$). Because the mount mode is moderately damped, it is not very sensitive to the perturbation. The base acceleration, however, shows strong sensitivity to changes in the base mobility

Figures 3.3 to 3.8 show that increases in transfer function gain due to mass or damper base flexibilities are accompanied by stabilizing changes in phase – that is, away from ± 180. Compensators designed for the single-mode nominal plant model will be a low order lag-lead filter for acceleration or force feedback, or lead-lag for gap feedback [68]. Therefore, it is concluded that mass and damper flexibility pose little stability risk (except for base acceleration feedback), and primarily act to change the loop bandwidth.

Base mobility modelled as that of a spring K has a destabilizing effect on the loop

transfer functions. For equipment acceleration or force feedback, spring flexibility contributes to a loss in phase at high frequency; below resonance, to an increase in gain while the phase remains near 180 degrees. Spring flexibility also contributes to a significant increase in the magnitude of the gap transfer function at high frequency, even for small values of k/K. Therefore, spring flexibility of the base leads to a reduction in gain or phase margin.

Many structures at high frequency appear to have input mobilities like that of a damper, a result predicted by Statistical Energy Analysis when modal density is great [44]. In this case the base flexibility will not have a destabilizing effect on active isolation using force, equipment acceleration or gap feedback. It is shown in the previous section how a dereverberated mobility model of the base can be used to incorporate the effects of broadband base flexibility into the nominal transfer function. If this step is taken, only modal flexibility of the equipment or base remains as a threat to loop stability when these modes are ignored in the compensator design.

3.6.2 Modal Flexibility

In Section 3.4 the multiplicative error $e(s)$ is derived for a single mode in the base or equipment. Assume that the nominal plant G_o is used as the plant model for a regulator design which generates the compensator is K. When K is applied to the actual plant as shown in Figure 3.41, closed loop stability is guaranteed for [19, 74]

$$|C(s)| = \frac{|K(s)G_o(s)|}{|1 + K(s)G_o(s)|} < \left|\frac{1}{e(s)}\right| \tag{3.135}$$

The stability bound of Eq. 3.135 is conservative since it does not contain any information about the location of G_a within the error circle in Figure 3.36. Whether the mode is destabilizing depends on the magnitude of $e(s)$, its direction in the complex plane, and the proximity to loop crossover frequency where gain and phase margins are low.

In Sections 3.2.2 and 3.2.3, the perturbations to the transfer function G_1 through G_5 are parameterized in terms of the dimensionless parameter β_b and β_{e2}, which are always nonnegative, and in terms of β_{e3}, which may be either positive or negative.

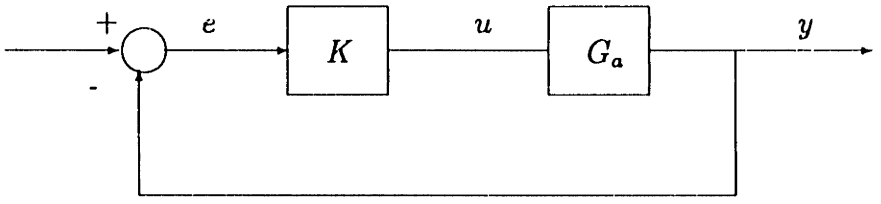

Figure 3.41: Regulator closed loop block diagram.

From inspection of these transfer functions, it is evident that for all cases in which the dimensionless term is nonnegative the effect of the resonant mode is stabilizing: the phase perturbation is away from ± 180 degrees and remains essentially bounded within a 180 degree envelope. The magnitude plots all retain the alternating pole-zero pattern characteristic of a collocated transfer function (the acceleration and force transfer functions, which are not true collocated outputs do show a slight trespass outside the 180 envelope in Figure 3.13, due to spring-like effects of base mode). Base acceleration, however, shows a destabilizing effect of the base mode: a 180 degree loss in phase at the frequency of the base mode, indicating a poor choice for feedback.

Nyquist Plots Assuming No Other Lags in Plant: Figure 3.42 illustrates the Nyquist plot of either the force or acceleration transfer functions when there are no sensor dynamics or other lags in the system. The large (major) loop corresponds to the mount mode ω_o for the nominal transfer function G_o on a rigid base. The full loop transfer function G_oK, of course, will also include at least one additional real pole to roll off the loop gain, in which case the Nyquist plot will approach the origin from -90 degrees at high frequencies.

In Figure 3.42, mode A represents a base resonance with $\omega_b < \omega_o$ and $\beta > 0$, and it creates a minor loop that is inside G_oK and away from the critical point. The multiplicative error bound, shown by a dashed line, is overly conservative. If the base mode is above resonance, then it is strongly attenuated and appears as a smaller loop as shown at mode B, also within the outer Nyquist loop. Base modes that occur near or at ω_o simply lead to larger loops within the nominal loop for G_oK and do not approach the critical point. Therefore, it is concluded that for perfect sensors, base resonances are not destabilizing: minimum phase compensators designed to stabilize

G_o will also stabilize G_a.

Equipment modes, however, are coupled differently into the force and equipment acceleration transfer functions. The effect of equipment modes on the force transfer function G_4 is the same as that for modes A and B in Figure 3.42: high coupling below mount resonance, and decoupling above mount resonance. In all cases, $\beta_{e2} > 0$ for G_4.

The acceleration transfer function, however, exhibits strong coupling of equipment modes *above* mount resonance. For equipment modes with $\beta_{e2} > 0$, the mode creates an internal minor loop like that of Mode B in Figure 3.42, and does not pose a stability risk. The equipment mode may have a coupling parameter $\beta_{e3} < 0$ if the acceleration is measured at output terminal 3 and the the mode eigenvectors at terminals 2 and 3 are of different signs. Mode C shown in Figure 3.42 illustrates an equipment mode with $\beta_{e3} < 0$, and in this case the minor loop is outside of the loop for G_oK. If the compensator or other elements contribute additional phase loss to the loop, then the minor loop will approach the critical point and the multiplicative error bound will not be conservative. Also, the equipment mode could create a minor loop outside of the major loop at mode A if $\phi_{e3} > \phi_{e2}$, as discussed in Section 3.3.2.

The gap transfer function G_5 always exhibits minor loops that are interior to the major Nyquist loop, for both base and equipment modes. Positive gap feedback is used to destiffen the mount passive spring; the feedback is typically rolled off at low frequencies to preserve the static stiffness of the mount. This rolloff adds phase lead to the plant which could possibly destabilize modes (of type A) that are lightly coupled in this frequency range. Because gap feedback is used to actively soften the passive spring over some frequency range, the feedback must be positive to allow the vibrating base or equipment to achieve its full free velocity v_B^f. The loop gain must be approximately $(1 - \epsilon)$, where $\epsilon \ll 1$, in order to significantly soften the passive spring. The gain perturbations due to unmodelled flexible modes can destabilize this compensation scheme.

Nyquist Loops Assuming Lags in Plant: The presence of additional phase lags – due to sensor dynamics, actuator dynamics, or pure time delays – will shift the Nyquist plot as shown in Figure 3.43. In this case, even stabilizing modes can lead to instabilities, as was shown by Spanos [70]. Mode D shown in Figure 3.43 is typical of an equipment mode with $\beta_{e2} > 0$, which no longer creates a minor loop interior to the major loop, but instead draws near to the critical point. This behavior would also occur for strongly coupled base modes (strong enough to counteract the decoupling effect of mount resonance). In these cases the multiplicative error is again nonconservative.

Importance of the size of β: When the coupling parameter β (representing either β_b, β_{e2}, or β_{e3}) is small, the effects on the transfer function magnitude and phase are also small. For instance, $\beta = 1$ corresponds to a magnitude perturbation of

$$\begin{aligned} |L(s)| &= (1+\beta^2)^{1/2} \\ &= \sqrt{2} \end{aligned} \tag{3.136}$$

which is a perturbation of 3 dB. Similarly, the phase perturbation is

$$\begin{aligned} \angle L(s) &= -\text{atan}(\beta) \\ &= -45^\circ \end{aligned} \tag{3.137}$$

For $\beta = 0.35$, these values fall to 0.5 dB and 20 degrees, respectively. Thus, for values of β small compared to one, multiplicative error due to base or equipment modes will be small compared to phase margins typically included in control designs.

For the force transfer function G_4, all modes (base and equipment) are decoupled above mount resonance by $(\omega_o/\omega_b)^2$. Assuming that loop crossover occurs at 5 times the frequency of mount resonance, then each base or equipment mode is decoupled by a factor of 25. For this reason a soft passive isolation corner frequency helps to condition the plant, by diminishing the importance of poorly known base or equipment modes from the loop transfer function. Since the force output decouples both base and equipment modes above mount resonance ω_o, this sensor appears to be the most attractive choice for feedback.

Series Isolator Modelled as Softmounted Reaction Mass: It was shown in Section 3.4 that a softmounted reaction mass used as a series isolator for a stiff actuator stage can perfectly decouple base dynamics from the loop transfer function $G_{S1} = a_3/f_a$, as shown in Figure 3.33. Since at frequencies at or below mount resonance ω_o the transfer function G_{S1} resembles that for the parallel actuator model, it is expected that base or equipment resonances (with $\beta > 0$) would affect the loop in the same stable manner. Because base modes are decoupled from the loop at high frequencies they do not interact unstably near crossover. Thus, minimum phase compensators designed for the nominal plant will be robust with respect to base modes occurring at resonance or near high frequency crossover. Modes on the equipment side, however, will remain strongly coupled and could provide a stability risk unless modelled.

3.7 Summary

In Chapter 3, the effects of equipment and base structure modal flexibility on the plant transfer functions used for active isolation are investigated. Models for both parallel and series force actuation are studied. It is shown that the effect of flexibility can be captured by a dimensionless coupling parameter β, based on the modal damping and simple impedance ratios. The flexibility perturbation is modelled as a multiplicative error to the nominal (rigid base, rigid equipment) transfer functions, and it is shown that only three functions are needed to describe the multiplicative error for the entire set of transfer functions and modal flexibilities. Dereverberated mobility models of the base or equipment are shown to account for broadband changes in the transfer function magnitude, phase and mount resonance ω_o, and lead to the correct backbone model for the modal perturbations.

An important conclusion is that above the mount resonance ω_o, base modes are strongly decoupled from the force and equipment acceleration outputs, but strongly coupled to the gap and base acceleration outputs. Secondly, equipment modes are strongly coupled to the equipment acceleration and gap outputs above mount res-

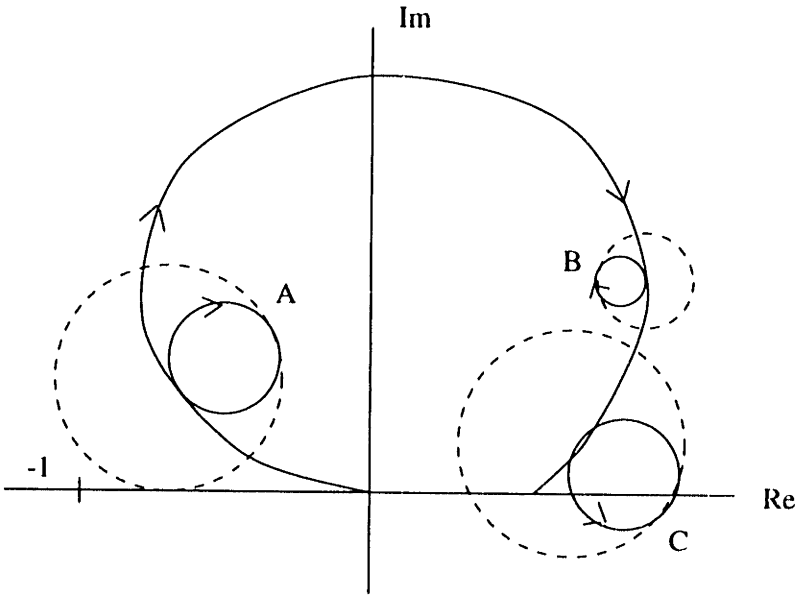

Figure 3.42: Nyquist plot for G_1K or G_4K, showing the effects of modal flexibility. Multiplicative error bound plotted as dashed line.

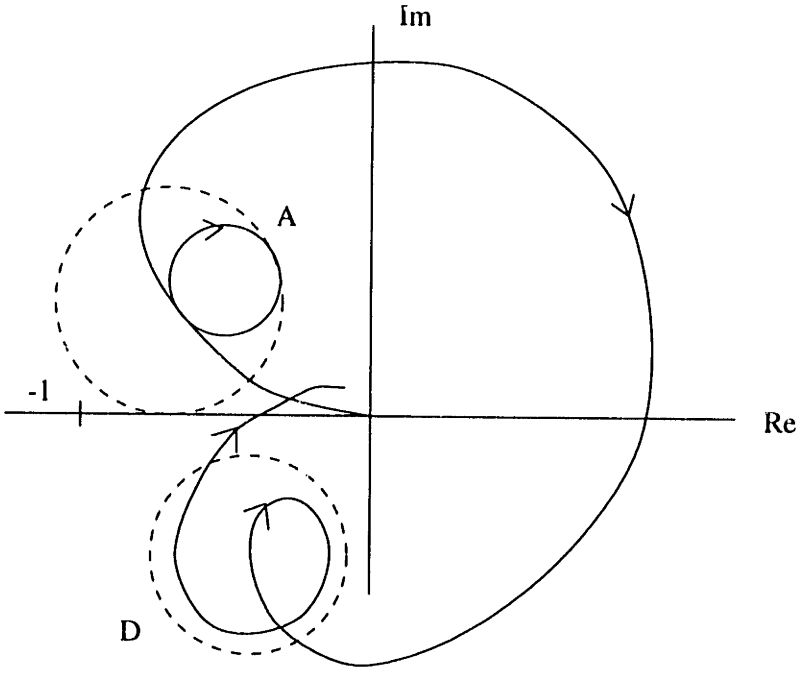

Figure 3.43: Nyquist plot for G_1K or G_4K which includes additional lags in the plant. Mode D that was formerly stabilizing now approaches the critical point.

onance ω_o yet are again decoupled from the force output. Thus, when using force feedback or equipment acceleration feedback (in the absence of equipment modes), it is practical to ignore base flexible modes in the control design and to base the compensator on the rigid base model. Finally, a softmounted reaction mass series isolator is shown to completely decouple base resonances from the loop transfer function above the softmount resonant mode.

Chapter 4

Interferometer Testbed

4.1 Objectives

This chapter describes the SERC Interferometer Testbed used for demonstration of active isolation and pathlength control in this thesis. The testbed design and performance metric are introduced in relation to scientific requirements for an interferometer spacecraft, and it is shown how the laboratory testbed incorporates a relevant subset of the technical issues involved with a full spacecraft mission. Measurements of the performance metric of the nominal truss configuration are shown, and the input mobility of the component test stand is presented and shown to be effectively rigid.

4.2 Testbed Description

The MIT SERC Interferometer Testbed is designed to be relevant to a class of space-based optical astronomy missions, as well as to provide a versatile laboratory for experimental structural control research. After a number of candidate missions that would benefit from CST were evaluated, it was determined that a broad class of large-baseline interferometers pose the most stringent pathlength and pointing stability constraints, as well as generate significant interest in the scientific community. A model of a proposed space-based optical interferometer with nanometer-level pathlength stability requirements was selected as a mission focus for an experimental

testbed structure [20]. The laboratory testbed is intended to capture the essential configuration, physics, and performance metric of an actual observatory spacecraft [10].

4.2.1 Science Motivation

The next generation of NASA's orbiting stellar observatories identified in the Bahcall Report [6] will require high angular resolution to meet their scientific objectives: extrasolar planet detection, resolution of close binaries, imaging the cores of active galactic nuclei, and direct measurement of the parallax of extra-galactic objects. By spatially separating smaller but discrete apertures, interferometric telescopes provide the angular resolution of a comparable filled aperture telescope of the same diameter, while avoiding the problems associated with fabricating and launching large-diameter filled aperture telescopes. Optical and ultraviolet space-based interferometers, in the 2 to 10 meter baseline range, are under consideration for high resolution astrometry and planetary detection (OSI, POINTS, etc.) [66]. Space-based measurement of ultraviolet light (λ = 100 to 300 nm) is particularly desirable since these wavelengths are blocked by the earth's atmosphere.

Figure 4.1 is used to illustrate both the testbed configuration as well as the principle of operation of an actual interferometer. A planar wavefront of light from a star is shown striking siderostats (three are shown) that reflect the light into the optical train of the interferometer. The light is steered to an intensity detector where light from any two of the siderostats is combined (interfered) to generate an intensity fringe pattern from which scientific measurements are extracted. A clear interference pattern is formed only when the optical paths traveled in each leg of the interferometer are the same to within fractions of a wavelength of light; alignment to within $\lambda/20$ is a typical design target for alignment. To accomplish this, an adjustable length segment called an optical delay line (or ODL, not shown) is introduced in each leg. On the Mark III Interferometer on Mt. Wilson in California, the ODL consists of three stages: a movable trolley for large motion, a voice-coil actuator for coarse adjustment, and a piezoelectric actuator for fine motion control [64].

Successful measurement of the stellar fringe pattern requires the performance of

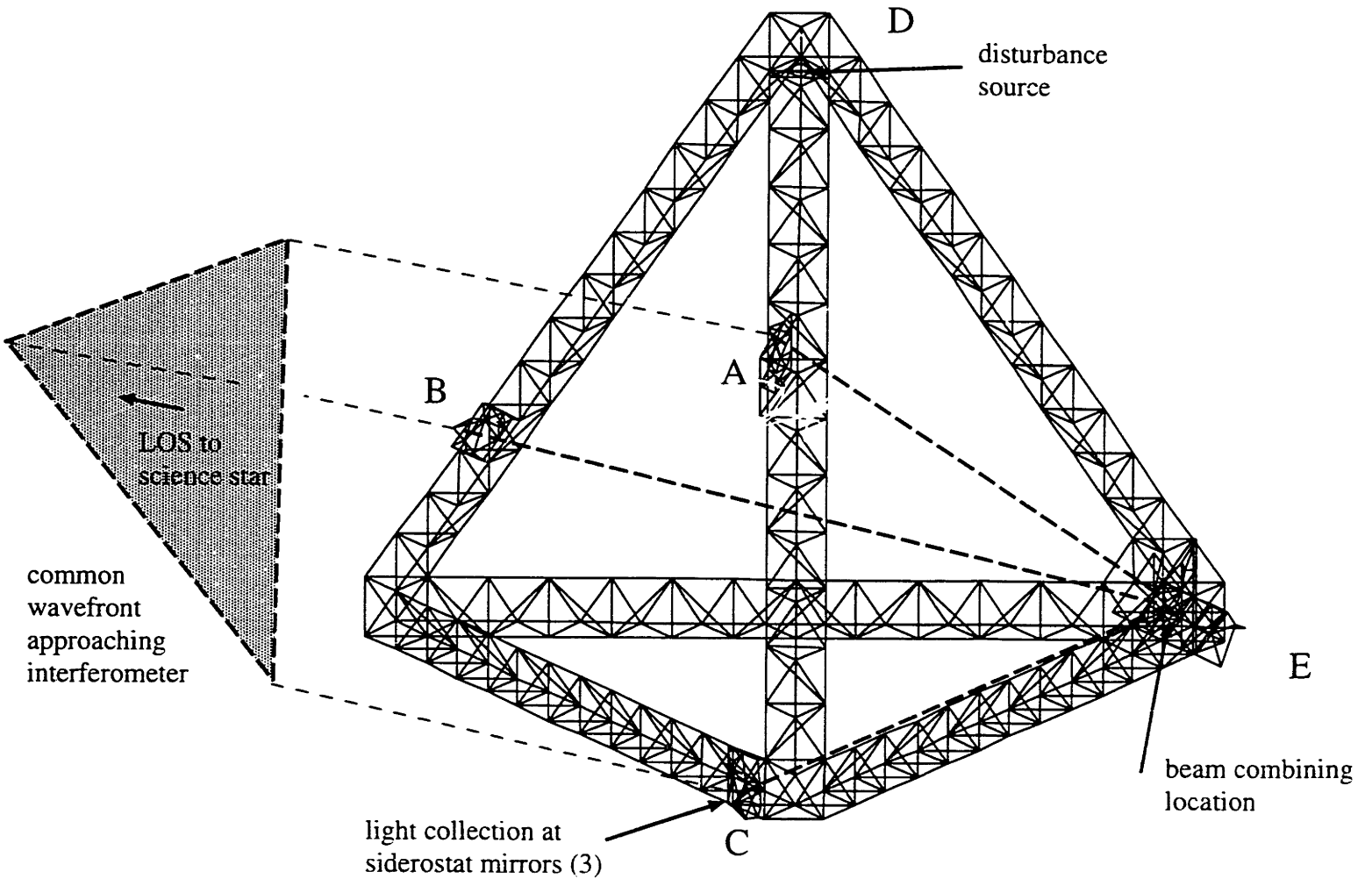

Figure 4.1: Illustration of laboratory testbed and its relation to the operation of the focus mission spacecraft.

three technical functions within the instrument, of which only the first is retained in the laboratory testbed. First, an ODL must reject disturbances which introduce differential pathlength error (DPL) in each pair of optical paths between points on the common wavefront and the detector. The requirement is that DPL disturbances must be maintained below $\lambda/20$, which for light in the center of the visible spectrum (500 nm) is 25 nm; an on-board laser metrology system measures the internal DPL error for feedback to the ODL. Secondly, coarse and fine steering mirrors must maintain parallel wavefronts at the detector plane, which places a requirement on wavefront tilt jitter of 0.5 arcsec. Third, the pathlength difference in each leg of the interferometer must be slowly varied in order to locate, capture and track the central fringe of the interference pattern, and to scan the range around the central fringe in order to record the fringe intensity. It is expected that a combination of disturbance rejection, vibration isolation and optical pathlength control technologies will be required to produce the quiet vibration environment in the presence of on-board disturbances due to attitude control hardware, machinery disturbances or thermal distortions [11].

4.2.2 The Laboratory Testbed

The laboratory testbed design and performance metric capture the problem of control of differential pathlengths between widely separated siderostats and a common beam combining location. External pathlength error, beam tilt, and low-frequency optical delay line control are not incorporated into the problem. Also, no science light or reference star is used in the testbed; only pathlength error that is internal to the truss is measured by a set of on-board lasers.

The testbed configuration is illustrated in Figure 4.1. Six triangular truss beams form a tetrahedron measuring 3.5 meters on a side. A laser mounted to the structure at the vertex point E is used to measure the pathlength changes between point E and each mock siderostat located at points A, B, and C. Three positions for the siderostats were chosen to create different baselines, as well as to simulate stiff mounting locations (point C at the vertex) and progressively more flexible locations at the midpoints of the truss legs (points B and A). At each mock siderostat location is an articulated

Table 4.1: Testbed parameters.

Description	Value	Description	Value
testbed mass	36 kg (bare truss)	*diagonal struts*	
	68 kg (testbed)	number	72
baseline	3.5 meter	mass	50.15 g
cat's eye mass	516 g (3)	stiffness	7.77 N/μm
fundamental mode	34.5 Hz (bare truss)	length	32.33 cm
	24.9 Hz (testbed)	*nodes*	
longerons and battens		number	229
number	641	mass	34.45 g
mass	39.5 g	stiffness	265 N/μm
stiffness	11.2 N/μm	diameter	3.02 cm
length	21.97 cm		

mirror assembly containing a common endpoint retro-reflector, or cat's eye optics. The structural control problem is to minimize structural deformations due to vibration in the three pathlengths defined by points A, B, and C and the fourth vertex point E.

Table 4.1 summarizes important testbed parameters. The statically determinate truss lattice is constructed from aluminum tubes of 3/8 inch outer diameter and 0.058 inch wall thickness, bolted tightly to 229 aluminum nodes. The struts are designed to have local bending resonances near 230 Hz, well above the fundamental structural modes beginning at 24.9 Hz. The 68 kg testbed is suspended in the laboratory from soft springs, resulting in suspension modes from 0.3 Hz (pendulum) to 2.5 Hz (bounce). The structural dynamic response of the truss is characterized by a high modal density due to the near symmetry of the six truss legs; roughly three dozen structural modes occur below 100 Hz, with modal damping ratios in the range of 0.4% to 0.8%. Appendix A lists the modes predicted by a finite element model of the testbed [7].

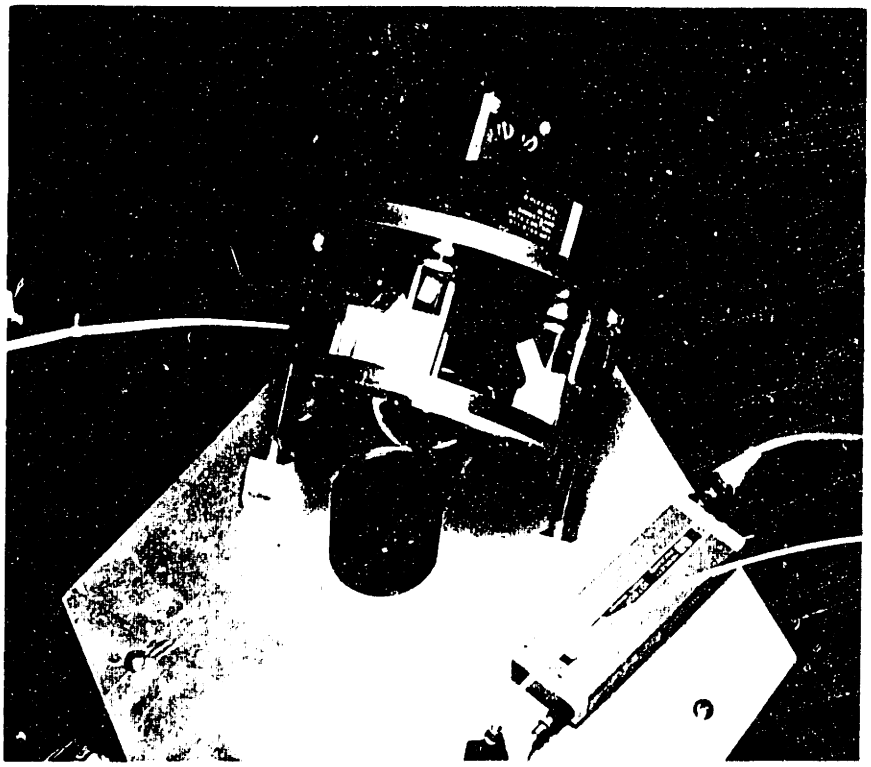

Figure 4.2: Photograph of original hardmounted cat's eye optics at plate C. A rigid fixture orients the cat's eye assembly at 60 degree angle to the base plate. A triax of Sunstrand QA1400 accelerometers is mounted to the back of the rigid fixture.

Figure 4.2 is a photograph of the original configuration of the articulated mirror and optics mounting plate at point C. The base plate is 1/8 inch aluminum that is connected by short mounting brackets to the nodes of the truss. Angled at 60 degrees to the base plate is a smaller mounting plate which positions the articulated mirror so that its field of view contains the line of sight to each of the three other cat's eye optics. The cat's eye is mounted to an aluminum annular ring, which in turn is connected to the small mounting plate by three stiff 1.8 cm piezoelectric multilayer actuators. A triax mounting of Sunstrand QA1400 accelerometers is bolted to the back of the small mounting plate. Similar configurations exist at plates A and B, except that at plate A a less expensive retro-reflector was initially used in place of the glass cat's eye for many early experiments. The bare truss mass is 36 kg, and each siderostat plate and mirror assembly has a mass of 4.8 kg. The fourth vertex optics assembly has a mass of 13.5 kg.

A disturbance source is located at the top vertex of the truss, at point D in Figure 4.1. Three axes of piezoelectric multilayer actuators and 494 gram reaction masses generate a disturbance force input to the truss structure. The actuators are driven by a white noise signal that is passed through a 4^{th} order Bessel filter with 70 Hz corner frequency; this signal is the invariant disturbance input to the truss for the performance metric defined below, and is referred to below as the *standard disturbance source.*

Passive Damping Hardware: Two hardware components have been developed for passive damping implementation on the testbed [4]. The first is a constrained layer viscoelastic treatment for the testbed longerons: struts are wrapped with 30 mils of 3M 110 viscoelastic layer, which is constrained by 35 mil thickness aluminum tubing. Up to 50 of these struts (labeled J-struts) can be substituted for the original truss longerons in order to add a small amount of "broadband" damping to most of the structural modes. Each strut has a loss factor of $\eta = 0.07$. Also available are five Honeywell D-struts, derived from the viscous dampers used in the HST reaction wheel isolation assembly. The D-strut loss factor is high ($\eta = 1.5$) and can be placed to add a large amount of "target" damping in selected structural modes [4]. In Chapter 6, five D-struts are used with three active pathlength control loops in a layered control design.

Support Equipment: The internal pathlengths are measured in realtime to 10 nm resolution using a 1 milliwatt dual-frequency laser interferometer manufactured by Hewlett Packard. The measurement beams terminate at a fiber optic feed to a receiver mounted to the truss; the outputs are then digitally fed into the VME bus of the realtime computer for measurement and feedback. The realtime computer consists of a 68030 microprocessor and CSPI vector processor with 16 A/D channels and 8 D/A channels. Other amplifier and sensor equipment that directly pertain to the isolation experiments is described in Chapter 5.

4.3 Performance Metric

The standard testbed performance metric is used as a common measure of performance improvement due to any passive or active modification to the testbed. In Figure 4.1, let the 3 absolute pathlengths (APL) between the siderostat plates and the fourth vertex at point E be denoted by the letters A, B and C. The three differential pathlengths (DPL) are defined as the difference between the absolute pathlength measurements, or A - B, B - C and C - A, respectively.

The testbed performance metric to be minimized is DPL error between the frequencies of 10 and 500 Hz. For example, the variance in DPL A - B that contributes to the metric is calculated by

$$\sigma^2_{AB} = \int_{10}^{500} \Phi_{AB}(f)df \tag{4.1}$$

where $\Phi_{AB}(f)$ is the measured autospectrum of DPL A - B in units of nm^2/Hz. The upper limit of integration is chosen to overbound the frequency range of significant structural response to the disturbance source, while the lower limit falls midway between the suspension modes and the first structural dynamic mode. This definition is consistent with that for an actual interferometer mission, in which dynamic DPL errors must be rejected for all frequencies above the sampling frequency of the detector, which typically is on the order of several Hz, well above the frequency crossover of the spacecraft rigid body controller. The goal is to reduce the performance metric to 50 nm RMS or less in each of the three differential pathlength measurements (the scientific requirement of 25 nm RMS is relaxed due to the 10 nm resolution limit of the laser metrology).

4.3.1 Measured Open Loop Disturbances

The performance metric results (both APL and DPL) for the *original hardmount* configuration of the truss are listed in the first row of Table B.1 in Appendix B. The term *original hardmount* refers to the initial configuration in which the cat's eye optics are mounted to the plates via the stiff piezoelectric actuators; a second

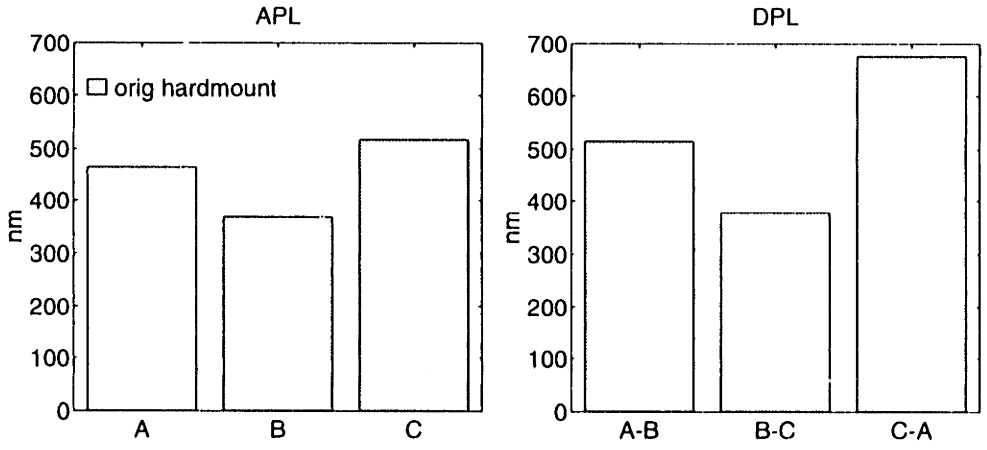

Figure 4.3: Testbed performance metric (RMS 10 - 500 Hz) for original hardmount configuration. Data are shown for RMS motion in the absolute pathlength (APL) and differential pathlength (DPL) measurements.

design is later used to further stiffen these mounts to reduce local dynamics. A Tektronix Fourier analyzer was used to measure the output of the realtime computer running at 4100 Hz with the standard disturbance source running on the truss. The pathlength measurements are in the range of 368 nm to 676 nm RMS, and are plotted for comparison in Figure 4.3.

Figure 4.4 illustrates the measured autospectrum of APL B for the original hardmount configuration. The data represents 30 averages of time blocks of 4096 points, leading to 1600 spectral lines linearly spaced between 0 and 500 Hz. At least one spectral line occurs in the half power bandwidth of each of the lower modes (more points would have been desirable, but the measurement of a single spectrum for the metric was found to be fast and convenient, given the number of tests conducted). The energy content of the spectrum remains correct despite the frequency spacing. Overplotted on the autospectrum is the average autospectrum in each of 17 third-octave bands (commonly used in acoustic measurement [55]) along with the RMS level of the disturbance energy in each frequency band. The majority of the energy is concentrated below 200 Hz, and is highest at frequencies near 100 Hz. A distinct clump of modes between 20 and 40 Hz corresponds to first bending modes of each of the six truss beams.

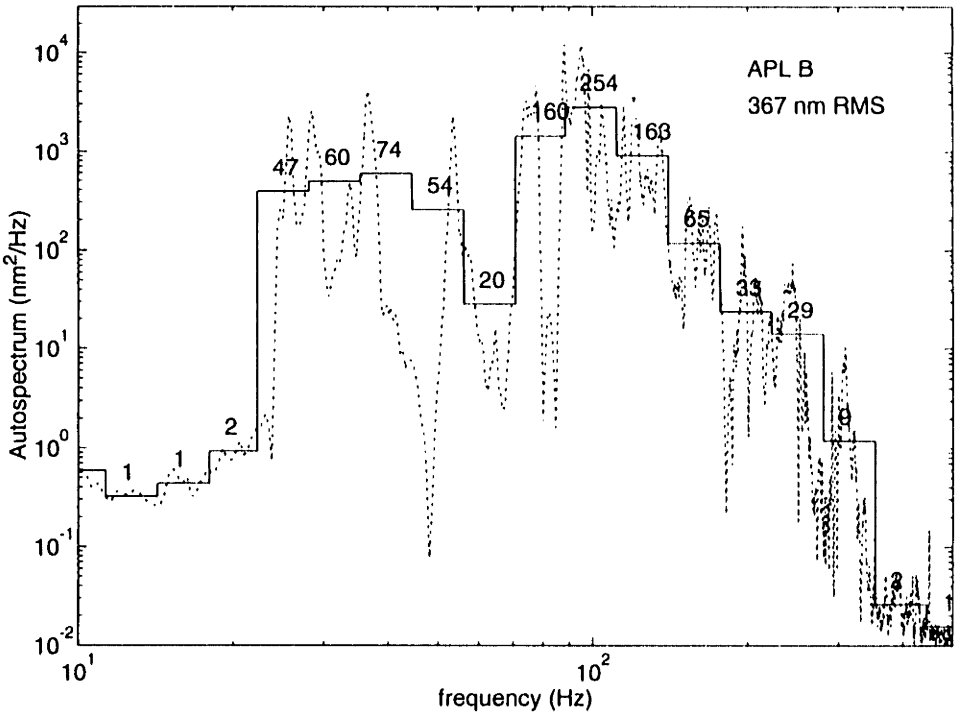

Figure 4.4: Absolute pathlength B, original hardmount configuration. Measured autospectrum (dotted) potted vs 1/3 octave band average autospectrum (solid) with RMS in each band.

The output spectrum reflects the spectrum of the disturbance input force: a white noise spectrum drives the piezoelectric actuators up to a corner frequency of 70 Hz, generating a reaction force input to the truss which increases proportionally to ω^2. The force-to-displacement transfer function of a lightly damped general structure is proportional to $1/\omega^2$, resulting in an APL disturbance spectrum that is roughly flat up to 100 Hz. At high frequencies, the voltage input to the piezoelectric actuators rolls off at a log slope of -4, leading to a rolloff in the output spectrum of -8, given the autospectrum units of nm^2/Hz.

4.4 Proposed Isolation and Pathlength Control

The subset of the testbed CST design addressed in this thesis is *vibration isolation* and direct *pathlength control* of each of the optical legs. Initial accelerometer tests indicated that most of the motion in the DPL error was due to motion at the three siderostat plates, and that the motion of point E in Figure 4.1 was small due to the

stiffness and inertia of the fourth vertex hardware. The cat's eye optics at plates A, B, and C were targeted for passive and active isolation from the vibrating truss structure; isolation of the disturbance source at point D was not addressed in the experiment. Since the testbed performance metric was originally planned to include laser pathlength measurement *between* the three siderostat plates, isolation in three translational axes at each mirror location was required, in order to "lock down" points A, B, and C in inertial space.

The active mount design for the cat's eye optics was required to function either as an isolator (using local error sensors for feedback) or as an active mirror positioner (using the absolute laser measurements for feedback). It is expected that pathlength control will improve the performance metric (a relative measurement) more than active isolation (using local feedback), since some motion does occur at the fourth vertex cat's eye, which is not isolated from structural vibrations. However, the standard testbed metric represents only one measure of performance. The attractiveness of the active isolation configuration is to validate the design approach in which the active mount is first tested and controlled on a rigid base, and is then mounted directly to an uncertain flexible base structure using the same compensator.

4.5 Rigid Block for Component Tests

Open and closed loop tests of the isolation mount were conducted on a test block that was designed to appear rigid to the test article. The anticipated mass of the test article was 1 kg with a softmount corner frequency of 20 Hz, leading to an isolator spring stiffness of $k = m\omega_o^2 = 0.025\text{N}/\mu\text{m}$. Figure 4.5 illustrates the test block, which measures 26 inches wide and is constructed of concrete with embedded steel. An optics jig plate was anchored by aluminum bolts into the wet concrete and the entire block was isolated from the floor by four inflatable rubber isolators. The vertical bounce mode of the block was measured at 5.4 Hz with a modal damping of 4%; the isolators had been expected to provide higher damping according to the manufacturers specification sheets. Two rocking modes of the test stand occur at 4.4

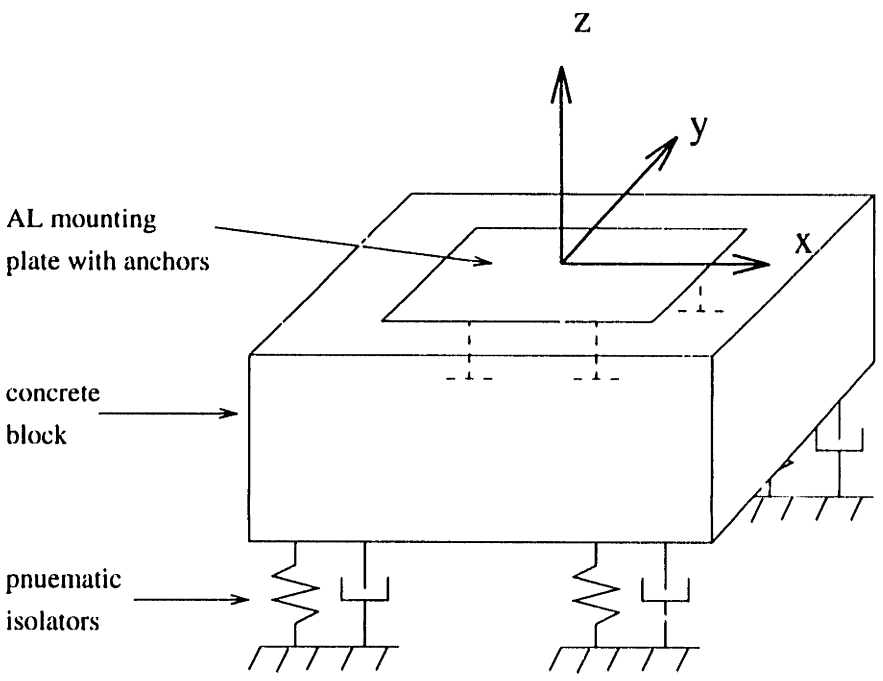

Figure 4.5: Concrete test block used for component tests. Mass = 230 kg; above 100 Hz the test block exhibits 153 N/μm spring stiffness in z direction due to flexibility in the aluminum mounting plate.

and 8.3 Hz, respectively, with 5% measured damping. The frequency difference in the rocking modes is due to asymmetries in the inflation pressure in each of the four mounts; the frequency difference would not occur if only 3 mounts had been used.

The input mobility of the test block in the z direction was measured by a shaker connected by a flexible stinger to a collocated accelerometer and load cell attached to the aluminum mounting plate. The plot shows dashed lines which represent three simple mobility models of the base. Above 5.5 Hz the testbed input mobility looks like that of a 230 kg mass, while below 5.5 Hz it appears to be a spring with stiffness k_1 = 0.265N/μm, corresponding to the stiffness of the pneumatic isolators. An unexpected result of the measurement is that the base input mobility is that of a stiff spring above 100 Hz: the measured stiffness of k_2 = 153N/μm corresponds to the stiffness of the 1 dozen steel anchors used to hold in the plate. Thus, the plate is not clamped by the cement around its edges as had been originally thought. The first resonance of the plate occurs at 1 kHz.

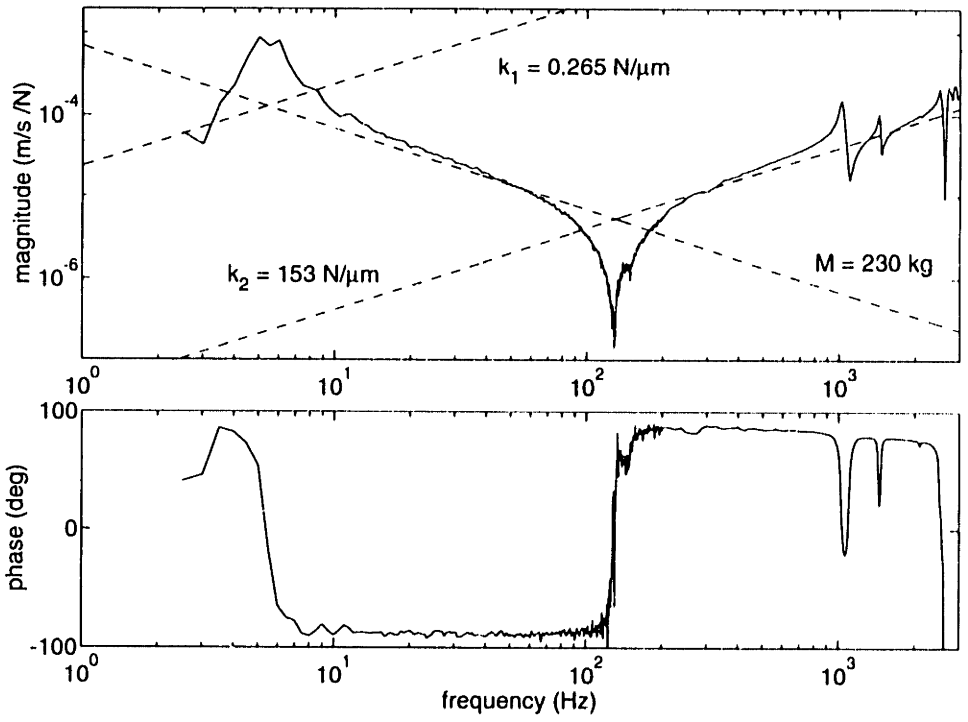

Figure 4.6: Input mobility of test block used for component tests. Solid line shows transfer function measured at center along z direction. Block mobility is much smaller than mobility for test articles, and is considered rigid for the proposed component tests.

The measured base mobility supports the assumption that the test block is a rigid test stand. The block suspension modes occur well below the 25 Hz corner frequency of the test article, and no other modal dynamics of the base appear below 1 kHz. The ratio of test mass to block mass is $m/M = 0.004$, and the ratio of softmount spring stiffness to base stiffness is $k/k_1 = 0.094$ and $k/k_2 = 0.0002$. In Chapters 2 and 3, the passive isolator sensitivity $\mathcal{P}$ and loop transfer functions were shown to be insensitive to base impedance ratios of these magnitudes; the case $k/k_1 = 0.09$ only becomes important well above the 25 Hz mount resonance, at which point the base input mobility is dominated instead by the large mass and stiff anchor stiffness k_2. Based on these results the test block will be treated as rigid for the proposed isolator component tests.

4.6 Summary

In this chapter, the SERC Interferometer Testbed is motivated by the scientific and vibration performance requirements of proposed orbiting stellar interferometer telescopes. The laboratory testbed captures a subset of the engineering problem, that of maintaining constant differential pathlengths between widely separated apertures on a flexible truss structure. It is proposed that passive and active isolation of the cat's eye optics at the three siderostat plates can provide a moderate amount of improvement to the performance metric, although the primary objective is to demonstrate active isolation both on a rigid base and a flexible base. A greater performance improvement is expected for active pathlength control using the same actuators in the active mount with absolute pathlength measurements as the feedback variable. Finally, the dynamic response of the test block is measured and shown to be effectively rigid for the testing of the passive and active isolators.

Chapter 5

Open Loop Tests of the Active Mounts

5.1 Objectives

The objective of this chapter is to present the design of an active mount developed for isolation and pathlength control and to demonstrate its experimental performance. The passive isolation performance and open loop transfer functions are presented for both rigid base and flexible testbed mountings. Functional requirements for the active mount are derived based on the testbed performance metric data, and are used to motivate the design of the hardware. Open loop transfer functions measured on the testbed data clearly indicate the advantages of using a soft isolation stage for modal decoupling, both for SISO (single-input, single-output) and MIMO (multiple-input, multiple-output) plant models. An experimental verification of the modified passive sensitivity model $\tilde{\mathcal{P}}$ is shown using an averaged model of the testbed input mobility based on the measured mobiity. The testbed performance metric, as well as local acceleration measurements at the isolation mounts, are shown to improve when the softmount actuators are installed on the truss. Models based on these open loop measurements are used in Chapter 6 for model based compensator designs.

5.2 Active Mount Hardware

5.2.1 Functional Requirements

Three identical active mounts were constructed for each of the three cat's eye retro-reflectors at points A, B and C in the testbed experiment, illustrated in Figure 4.1. Functional requirements for the mounts are listed in Table 5.1. The primary function of the mount is to provide articulation of the cat's eye along three translational axes defined by the lines of sight to each of the other three cat's eyes: for instance, one mount must move point B in the three directions formed by the lines of sight from B to points A, C and E. Rotations of the cat's eye optics are unobservable by the laser metrology system. Each cat's eye retro-reflector has a mass of 520 grams and an outer diameter of 7.5 cm.

The stroke magnitude and bandwidth requirements listed in Table 5.1 were based on measurements taken in the presence of the standard testbed disturbance source. Variations in absolute pathlength (defined in Chapter 4) were measured to be below 500 nm RMS in the 10-500 Hz range. Accelerations on the rigid mounting plates for each cat's eye, as recorded by triaxial mounts of Sunstrand QA1400 accelerometers, produced estimates of local linear displacements that were below 325 nm RMS at each mirror, in any direction. To overbound these disturbances a stroke requirement of $\pm 3\mu m$ was imposed.

Each mount was required to stiffly mount the cat's eye to the siderostat plates for the nominal testbed configuration; a second softmount design was required to provide sufficiently small static deflection to maintain optical alignment of the laser beams, which have 5 mm beam width. A local sensor suite was needed for local feedback for active isolation, in addition to the laser measurement for direct pathlength control. Also, each mount was required to orient the optics so that the other 3 cat's eyes were within the 120° cone angle of the optics.

The reactuation requirement was added after preliminary tests showed that interaction between the three hardmount isolators was strong enough to prohibit robust, decoupled control loop design. A softmount or reaction stage was needed to isolate the

Table 5.1: Active mount functional requirements.

stroke	• $\geq 3\mu$m in three translational axes • fine motion control to 10 nm • bandwidth 10 to 500 Hz
stiffness	• static stiffness to maintain optical alignment • local structural resonances $\geq$ 500 Hz
local sensor	• measure 3 axis linear motion of point M • bandwidth 10 to 500 Hz • noise $\ll$ 50 nm RMS over 10-500 Hz
field of view	• 3 other cat's eyes within 120° cone angle
reactuation	• isolate piston and rotational actuation • decouple base modes near loop crossover

base structure from reaction forces generated by actuation of the mirror. Examples of this interaction are shown below in Sections 5.4 and 5.5.

5.2.2 Hardware Description

Piezoelectric multilayer ceramics were selected as actuators for the active mount for several reasons: the piezoelectrics provide high stiffness and fine motion control, were readily available, and had been used in previous SERC laboratory experiments. A number of configurations were considered, and the final design described below represents the best choice based on the criteria of stiffness, fewest actuators for 3 axis control, and geometric simplicity for design, machining and assembly. Three prototype actuators were built (the "old hardmount" design illustrated in Figure 4.2) and were used as cat's eye mounts for initial performance metric tests. These early tests indicated that the local mount design was insufficiently stiff – local shear modes of the actuator occurred below 200 Hz – and that coupling between the 3 hardmount actuators was strong enough to require a softmounted reaction stage to permit inde-

Table 5.2: Mass of each isolator assembly.

component	mass (kg)	
	hardmount	softmount
active stage	1.050	1.050
reaction mass	n.a.	1.050
collar assy.	1.135	0.640
total	2.185	2.740

pendent control design for the three active mounts. The second and final actuator design incorporates changes for reactuation and increased stiffening, and is presented below along with a discussion of the important trades considered in the design.

The softmount and hardmount actuators are illustrated in the scale drawings in Figures 5.2 and 5.1, and are shown in three photographs (Figures 5.5 to 5.7). The mount is comprised of three primary components, as illustrated in Figure 5.2. The first is a stiff outer *collar* which orients the entire assembly and acts as a stiff interface to the siderostat plate; this mount is considered to be part of the unisolated base structure (the vibration source) and is represented by the dark shading. The second component is the *reaction stage* (lighter shade) which is softly suspended from the collar by damped blade flexures. The *active stage* (unshaded) is the third component, and is comprised of the cat's eye, accelerometers, and piezoelectric actuators with wire flexures.

The active mount can be used either with or without the reaction stage and flexures, by replacing the first collar with one that provides a rigid mounting for the active stage, as illustrated in Figure 5.1. A flexure locking mechanism was dismissed in favor of the replaceable collar, based on tests which indicated that a prototype flexure lock was not completely effective in enforcing a hardmount boundary condition. A list of the isolator component masses in Table 5.2 shows that the hardmount configuration is lighter than the softmount configuration by 555 grams. The total testbed mass is 68 kg with the new hardmounts installed.

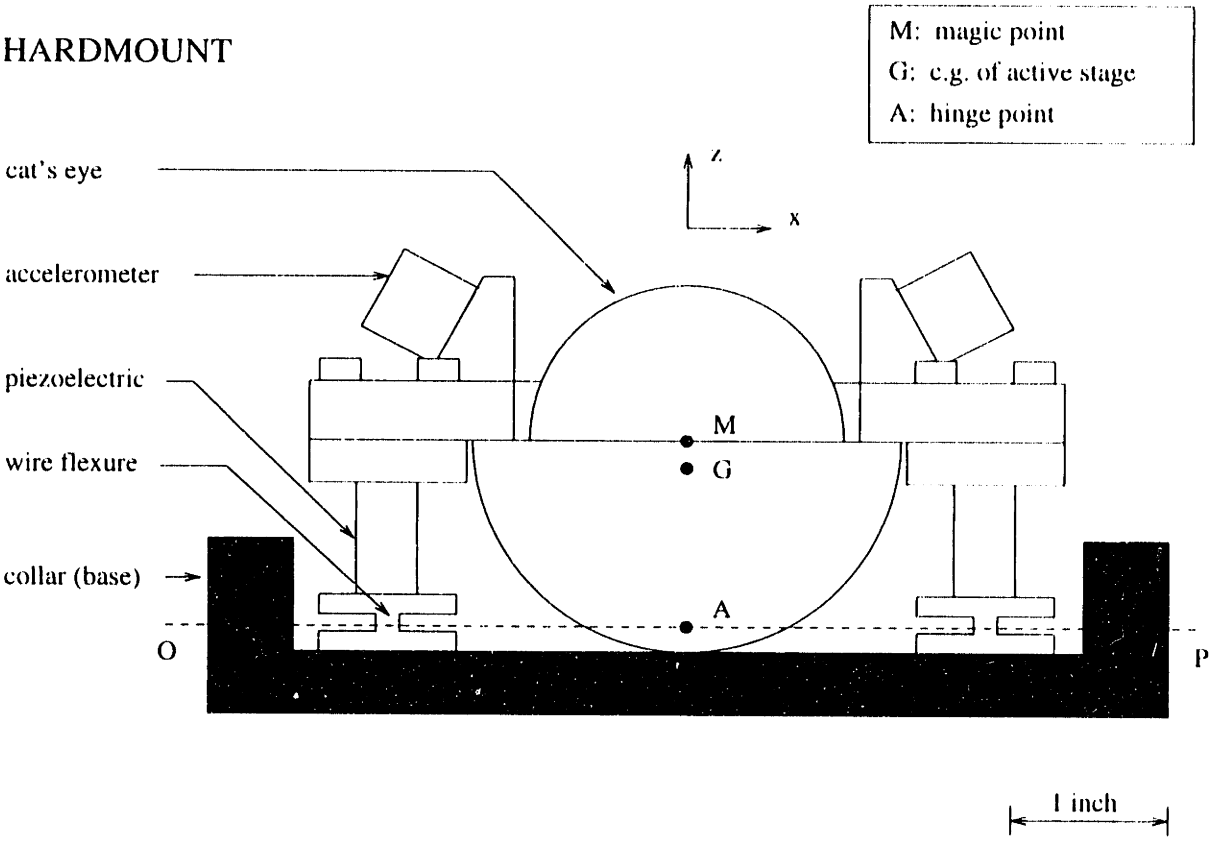

Figure 5.1: Scale drawing of the active hardmount isolator. Area in white is the active stage, dark shade represents ground. Accelerometer triax measures the linear motion of point M. Wire flexures permit stictionless rotation about point A when the actuators are operated in differential mode, but are otherwise stiff.

Hardmount Actuation Design: Three piezoelectric multilayer actuators provide articulation of the active stage in five axes (three translation, two rotation), only three of which are independent. The actuators are model no. NLA-10x10x18 from Piezo Electric Products Inc., have a stroke of 13.5 μm at 150 volts, capacitance of 6500 nF, and axial stiffness of 350 N/μm. The piezoelectric stacks are bonded between wire flexures and steel spacers by Hysol EA 9394 structural adhesive, which was determined in a destructive test to be stronger than the actuators themselves. Two nylon bolts hold the actuator in 20 N of tension during epoxy cure and in case of breakage. The actuators are biased at 75 volts in order to provide $\pm 6.75 \mu m$ of stroke.

When the actuators are operated in common mode, the cat's eye is moved in the

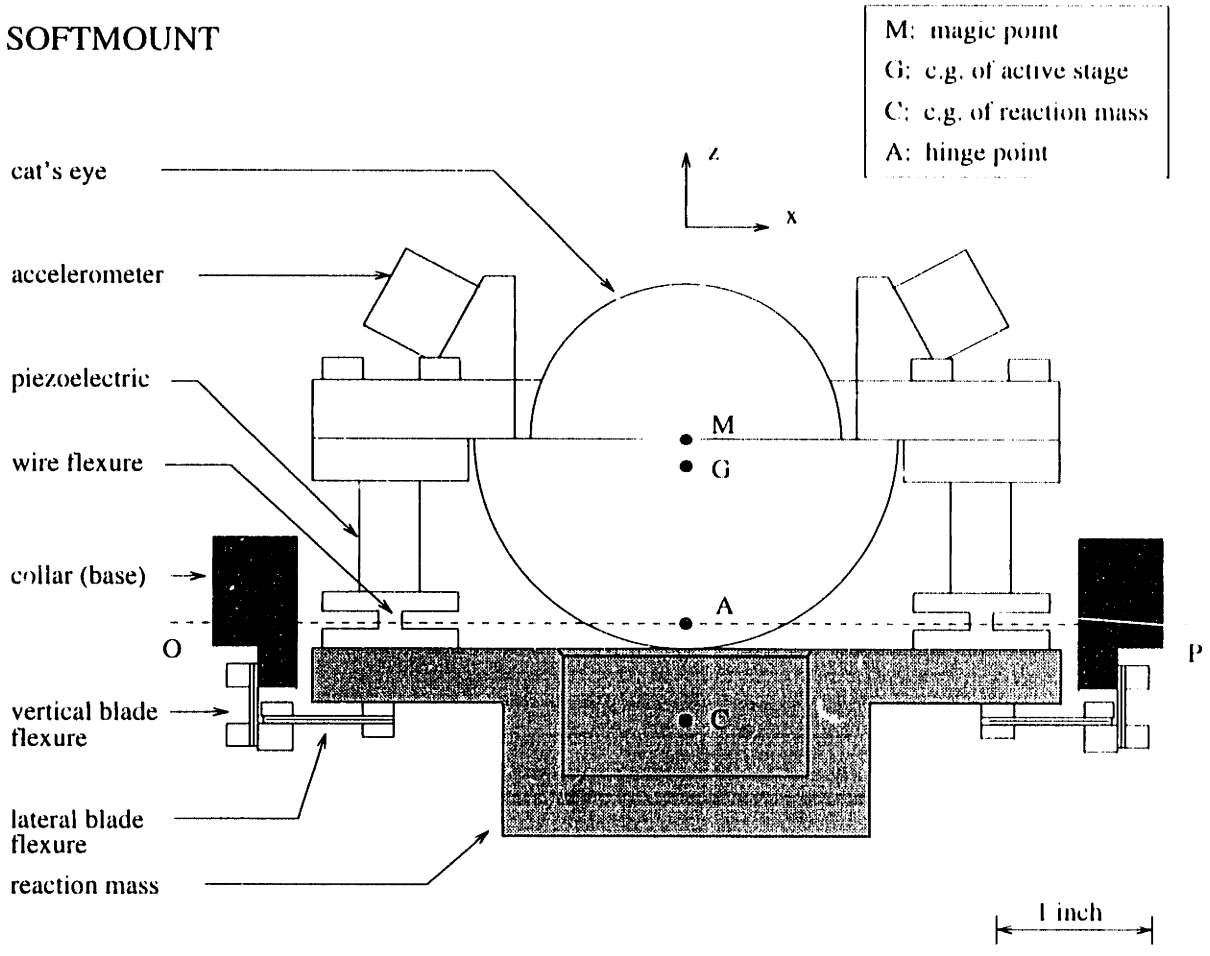

Figure 5.2: Scale drawing of the active softmount isolator. Active stage (white) is mounted to reaction stage (medium shade) which enables high frequency dynamic decoupling from base (dark shade) due to soft damped blade flexures.

z (piston) direction; when operated differentially, the active stage rotates about the hinge point A defined by the bending axis OP of the soft wire flexures, as shown in Figure 5.1. Because of the lever arm AM, the cat's eye magic point M (the point measured by the external laser) is articulated laterally by $\pm 4.2 \mu m$. Rotations of the cat's eye about point M are unobservable in the linear laser pathlength measurement due to the symmetry of the cat's eye optics.

An illustration of the hardmount displacement mechanism is provided in Figure 5.3(a) and Figure 5.4(a), in which the reaction mass is considered for the present to be a rigid base. The actuation command is modelled as a force f applied across

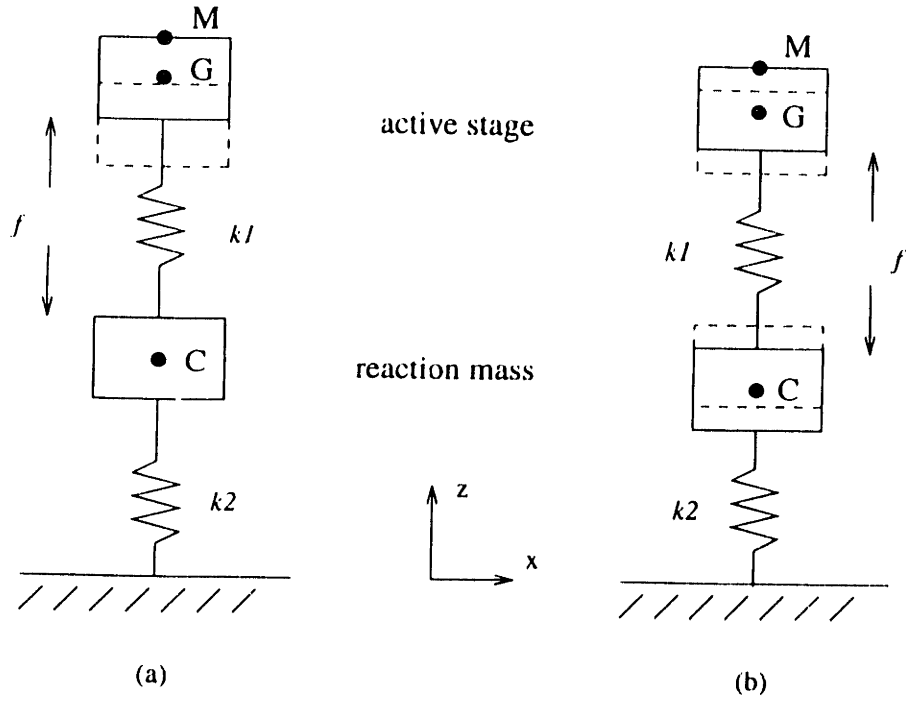

Figure 5.3: Vertical actuation model of the actuator. At low frequency (a) lower spring is rigid and point M moves full commanded stroke $\delta = f/k1$. At high frequency (b) lower spring is soft and point M moves $\delta/2$. A hardmounted active stage is also represented by (a).

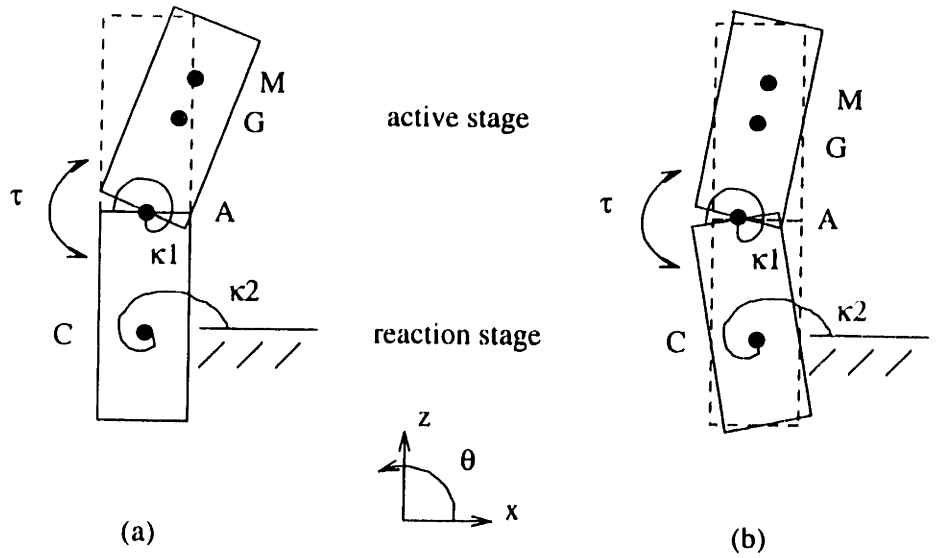

Figure 5.4: Transverse actuation model of the actuator. Piezoelectric actuators produce torque which pivots active stage about point A. At low frequency (a) reaction stage spring is rigid; at high frequency (b) both active stage and reaction mass pivot about their respective centers of gravity (points G and C). High frequency stroke is reduced by $\frac{1}{2} \cdot |MG|/|MA|$ compared to low frequency.

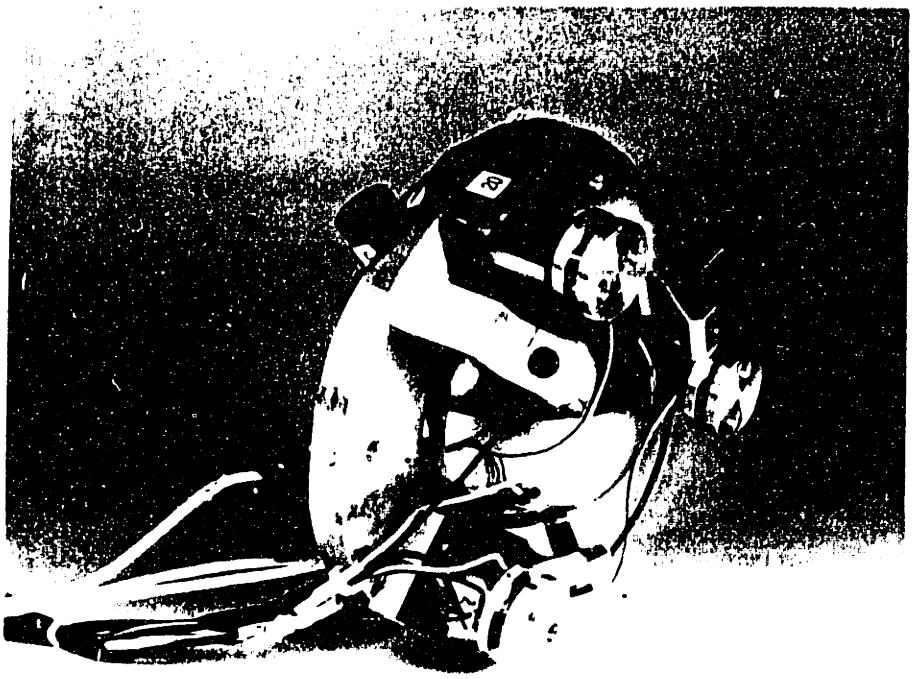

Figure 5.5: Rear view of active stage. Cat's eye retro-reflector is held in place by three plastic-tipped set screws. Three piezoelectric actuators are arranged symmetrically around the cat's eyes, and are bonded to wire flexures which interface to the reaction mass.

the lumped axial piezoelectric stiffness $k1$, producing (unconstrained) static deflection $\delta = f/k1$. Similarly, $\theta = \tau/\kappa 1$ describes the commanded rotation.

The wire flexures were designed to be soft enough in bending such that 95% of active stage rotation occurs within the flexures. The lowest structural resonance of the active stage is a lateral shear mode, in which the combined assembly of wire flexures, actuators and spacers act as a shear spring, permitting vibration of the cat's eye mass in the x and y directions. The height of the actuator/flexure assembly was chosen to set the shear modes at 550 Hz, above the testbed disturbance bandwidth. Vertical bounce and rotational modes about the active stage center of gravity (point G) were calculated to occur above 1 kHz, governed by the flexibility in the wire flexures.

Softmount Reactuation Design: The reaction stage mass and inertia were selected to be identical to that of the active stage. As demonstrated in Figure 3.33 for the series isolator in Chapter 3, the frequency at which high base modal decoupling

Figure 5.6: Front view of softmount actuator. The large outer ring is rigidly bolted to the vibrating base structure by two struts and a rear brace. Smaller circular plate is active stage which contains cat's eye optics. Three Kistler PiezoBeam accelerometers measure three axis translation of cat's eye magic point M.

occurs is $\sqrt{2}\omega_o$, for equal active stage and reaction stage masses. For lighter reaction masses, the decoupling begins at a higher frequency, and also results in lower actuator stroke at high frequency.

In Figure 5.2 the reaction mass is suspended from the collar by three damped blade flexures which were designed to provide a suspension mode in the z direction of 25 Hz. Each flexure is comprised of a lateral component and a smaller vertical component; the latter provides stress relaxation in the flexure and prevents nonlinear "snap through" buckling observed when the vertical flexure is omitted. The lateral flexure is 2.5 cm wide and 1 cm in length, and is constructed of 3 layers of steel shim (4 mil thickness) and 3M ISD 112 viscoelastic material (13 mil thickness). A detailed analysis using an assumed modes energy method was used to select the flexure geometry, number of layers, and type of viscoelastic necessary to provide both

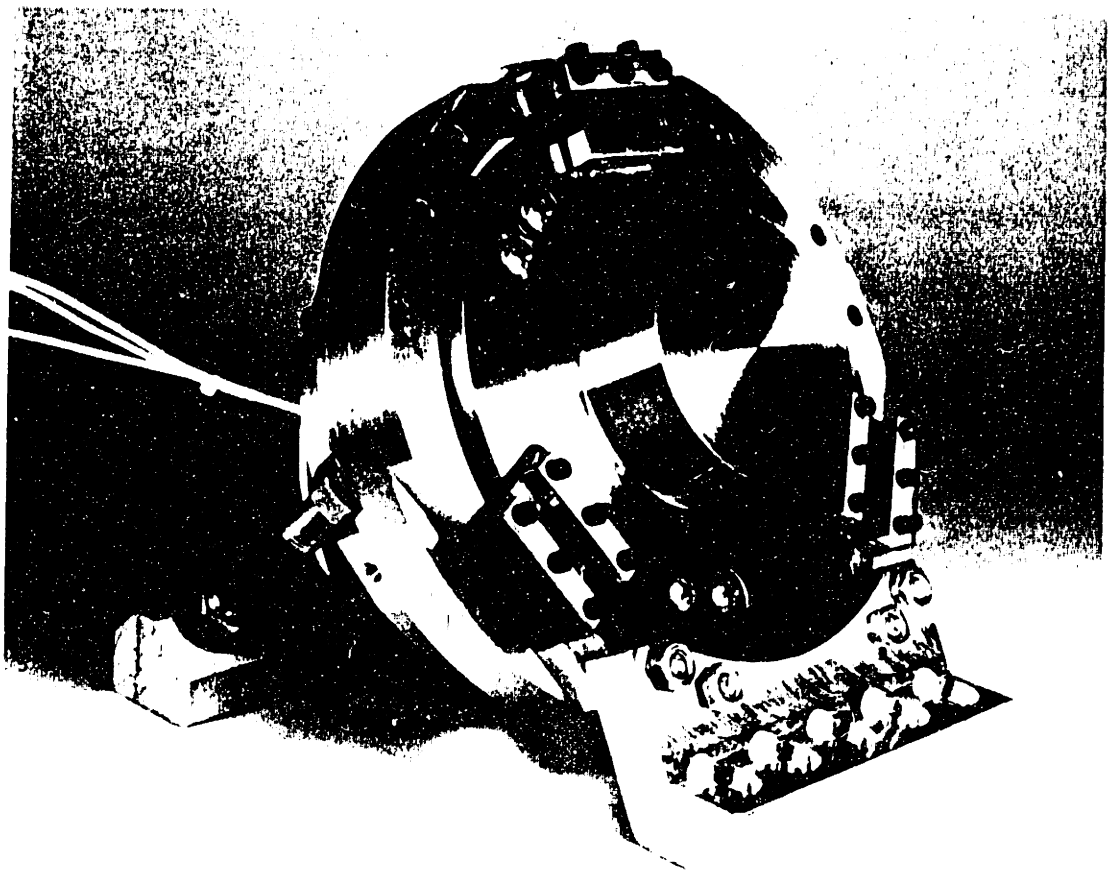

Figure 5.7: Rear view of softmount actuator. Inner reaction mass is suspended from outer support ring by three damped blade flexures. Bolts in reaction mass show attachment location of active stage to opposite side.

high stiffness and high loss factor. The side flexures are one half of the length of the lateral flexures and are comprised of two layers of 7 mil steel shim and one layer of ISD 112.

Table 5.3 lists the predicted and measured natural frequency and damping of the bounce and rotational modes of the combined active/reaction mass (2.10 kg) on the soft flexures. A higher mount damping ratio was desired, but was limited by the required flexure stiffness and by a constraint on flexure width. The mount natural frequency of 25 Hz was selected to provide less than 1 mm of static deflection of the cat's eye optics when installed in various configurations on the testbed.

The actuation mechanism involving the reaction mass is illustrated in Figure 5.3 and Figure 5.4. Well below softmount resonance, the active stage articulates as if the reaction mass was rigidly connected to the collar (ground). Well above softmount

Table 5.3: Predicted and measured softmount frequency and damping, measured on rigid test stand.

	predicted	measured			
		mirror C		mirror B	
	vertical	vertical	rotational	vertical	rotational
frequency (Hz)	25	28.1	33.1	33.1	38.6
damping (%)	8	10.0	5.7	5.7	5.3

resonance, the lower flexure spring $k2$ or $\kappa 2$ can be ignored and only the inertia of the reaction mass need be considered. The vertical actuation mode is straightforward: the actuator stroke is equally divided between positive vertical displacement of the cat's eye (point M) and the negative vertical displacement of the reaction mass. Rotational actuation of point M occurs by a commanded angular deflection by the piezoelectric, which is divided between rotation of the active and reaction stages about their respective c.g. locations (points G and C). Point A remains as the hinge point. The bending axis of the soft blade flexure was designed to coincide with the reaction mass c.g. point C, to prevent any lateral reaction forces from being transmitted to the base structure. The models in Figures 5.3 and 5.4 indicate that well above softmount resonance, no reaction forces due to actuation are transmitted to the base structure.

The penalty for using the reaction mass, however, is an increase in weight and a loss of actuator stroke at high frequency. For vertical displacement, 50% of the high frequency stroke is retained, while for transverse actuation the figure is only 10%, due to the proximity of the c.g. points G and output point M. In the testbed closed loop experiments, the actuators are articulated along lines of sight that form angles of less than 40 degrees with the mount z direction, thus the isolators maintain a significant amount of high frequency stroke, as is shown below in Section 5.4.

Sensor Selection: A triax of Kistler PiezoBeam accelerometers measure the three-axis linear acceleration of the cat's eye magic point M. The accelerometers provide

1 volt/g sensitivity over a 3 Hz to 3kHz frequency range. Load cells located in the load path of the actuators were an alternate choice, but were not selected since five sensors would have been needed to measure all base disturbances (two rotation and three translation) capable of disturbing point M in translation. Load cells with a resolution of 0.5 volt/N are commercially available and provide displacement resolution comparable to the Kistler PiezoBeam accelerometers given the active stage mass of 1 kg.

The Kistler PiezoBeam accelerometers were selected based on sensitivity, size, and availability. The acceleration noise spectrum was originally expected to provide less than 20 nm RMS equivalent displacement noise between 10 and 500 Hz. A comparison between the measured noise spectra of Kistler PiezoBeam and Sunstrand QA1400 accelerometers is provided in Appendix C. It was discovered during closed loop tests, however, that due to an error in measurement scale factor the noise content over the 10 to 500 Hz ranges is closer to 200 nm RMS, which does not meet the functional requirements listed in Table 5.1. Sunstrand QA1400 accelerometers were considered as a retrofit, but the 400 g combined mass of the Sunstrand accelerometers proved too great to preserve a c.g. location of the active stage mass below the magic point M, required for minimum phase lateral articulation of the active stage. The Kistler PiezoBeam accelerometers were retained and used for acceleration feedback control designs in Chapter 6. The results indicate the expected performance that would be obtained for noiseless sensors. Appendix C also lists the noise spectrum of a new lightweight accelerometer introduced shortly before the time of this writing. The sensor exhibits a lower noise spectrum and higher sensitivity than the PiezoBeam accelerometers used in the following experiments.

5.2.3 Passive Isolation Description

Although the soft blade flexures were designed to attenuate actuator reaction forces from being transmitted to the base structure, a side benefit of the flexures is passive isolation of the cat's eye from base disturbances. Figure 5.8 illustrates the mechanism of passive isolation for the softmount actuator design. Because the reaction mass

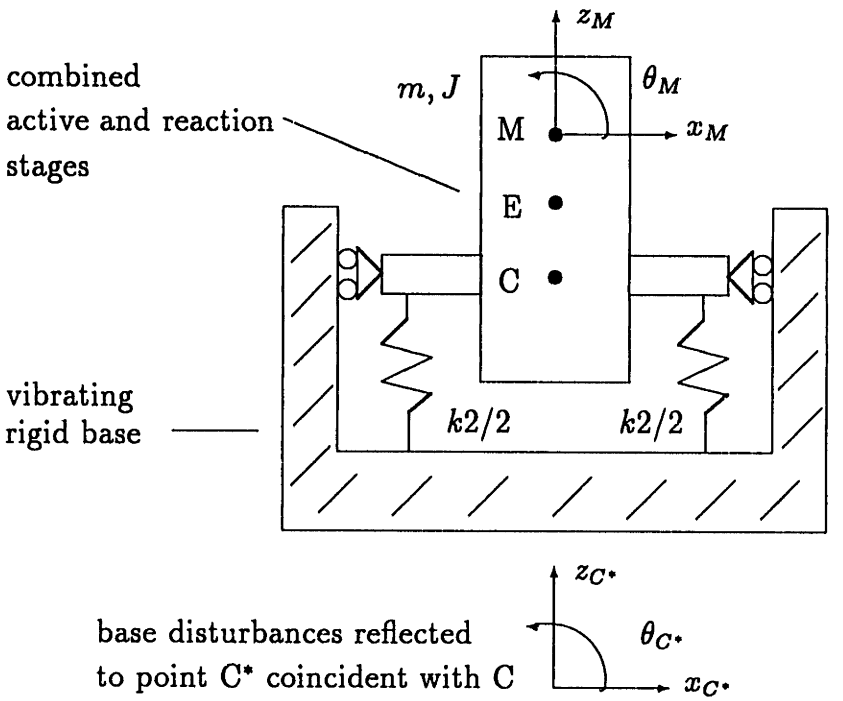

Figure 5.8: Model to illustrate five-axis passive isolation of the mount. Base disturbance represented as rotational and two translational disturbances, referenced to point C* coincident with C.

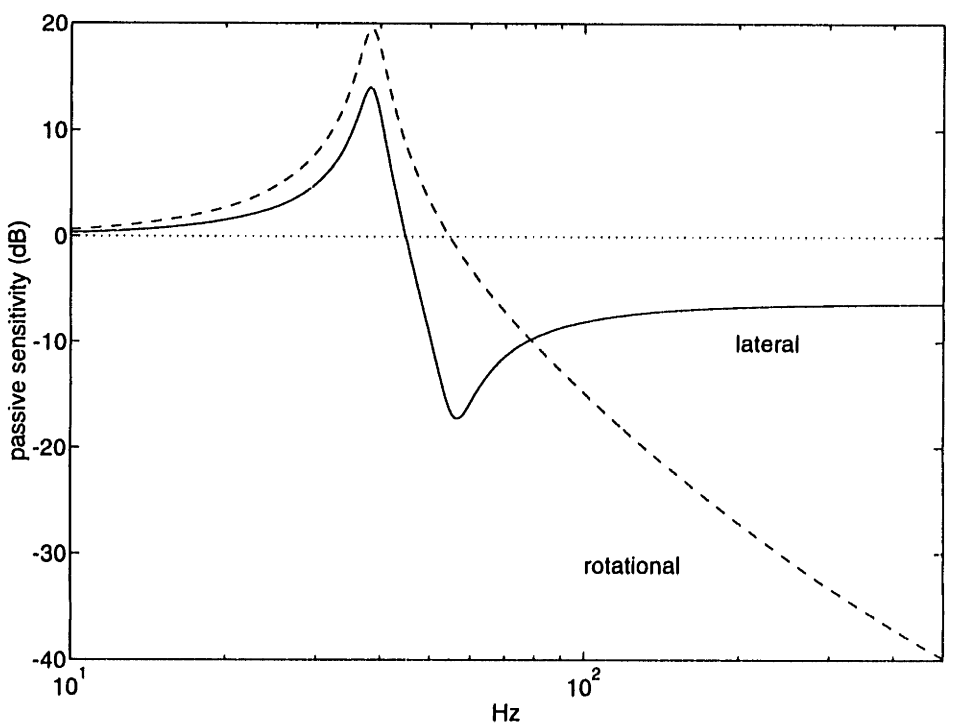

Figure 5.9: Comparison of passive sensitivity $\mathcal{P}_r(s)$ for rotational and lateral degrees of freedom. Actual mount performance will depend on output direction and the directional content of base disturbance.

Table 5.4: Comparison of hardmount and softmount local displacement spectrum measured along the laser lines of sight, in the presence of the standard disturbance source. Isolation performance degrades as the angle between the local z axis and the line of sight increases.

mirror	angle between l.o.s. and mirror z axis	nm RMS 10-500 Hz		dB improvement
		hardmount	softmount	
A	40°	195	145	2.6
B	35°	220	103	6.5
C	20°	302	109	8.0

were also recorded. An electronic circuit was used to perform the necessary 1×3 matrix multiplication to transform the three triax measurements to the acceleration along each laser line of sight to the fourth vertex.

5.3.1 Local Acceleration Results

Acceleration and absolute pathlength measurements for mirror B are used to illustrate the performance improvement due to passive isolation. The improvement due to passive isolation is represented by the change in local acceleration between the *new hardmount* and the *softmount* configurations (the old hardmount data only serve as a reference to the nominal configuration). Figure 5.10 is a comparison of these autospectra (converted to displacement) measured in the presence of the standard disturbance. The softmount attenuates vibration in frequencies above 50 Hz, and amplifies disturbances below. Above 50 Hz, the effect of the mount is a simple downward shift of the autospectrum, without addition of passive damping to the truss modes. The mount modes near 25-40 Hz are coupled to the base modes.

The improvement in broadband displacement at mirror B is 6.5 dB. Results for the other mirrors are listed in Table 5.4. The mirror performance is correlated with the degree of alignment between the individual mirror lines of sight and the mirror piston (z) direction, in which the isolation effectiveness is highest.

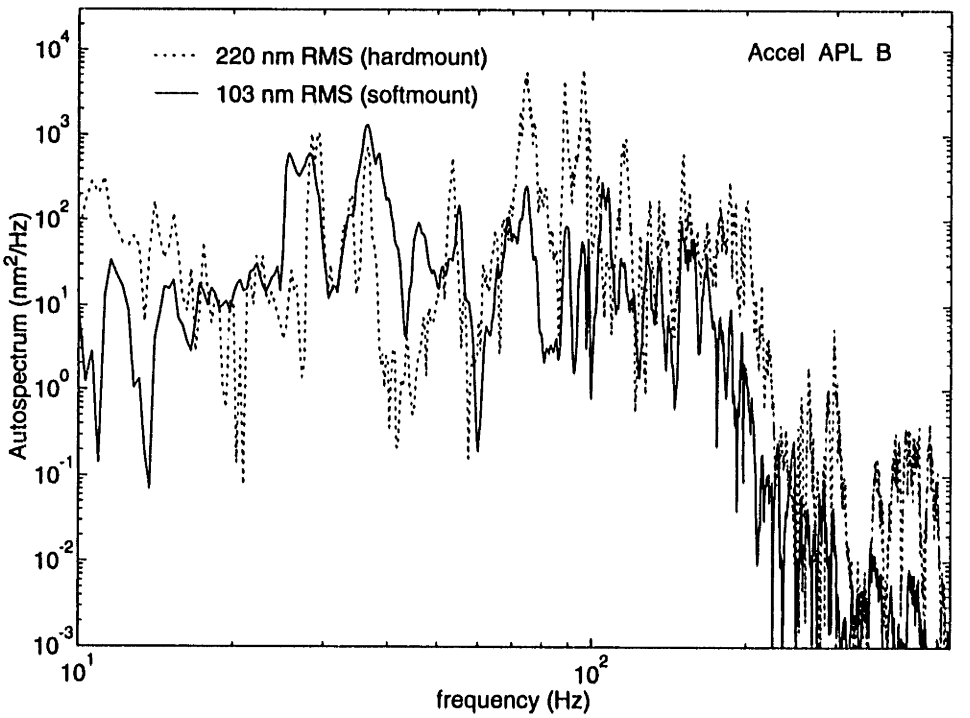

Figure 5.10: Improvement in local acceleration along laser B line of sight due to passive isolation at mirror B.

Figure 5.11 is a plot of the mirror B averaged passive sensitivity $\mathcal{P}_a$, calculated from Figure 5.10 by taking the ratio of the averaged autospectrum in each third octave frequency band over the performance metric bandwidth. Regions of amplification and attenuation are clearly visible. Below 20 Hz this function is not well defined, since in this range there is little vibration energy in the truss, and the sensor noise is high. High frequency attenuation is somewhat degraded for two reasons: first, the line of sight direction for laser B is 35 degrees off-axis from the mount piston (z) direction, and the mount is not as effective in attenuating transverse disturbances. Secondly, the flexibility of the base leads to some increase in the transmitted vibration at high frequencies, as described in Chapter 2. The effect is shown experimentally for mirror C below, since an experimental measurement of the truss input mobility at mirror C was available.

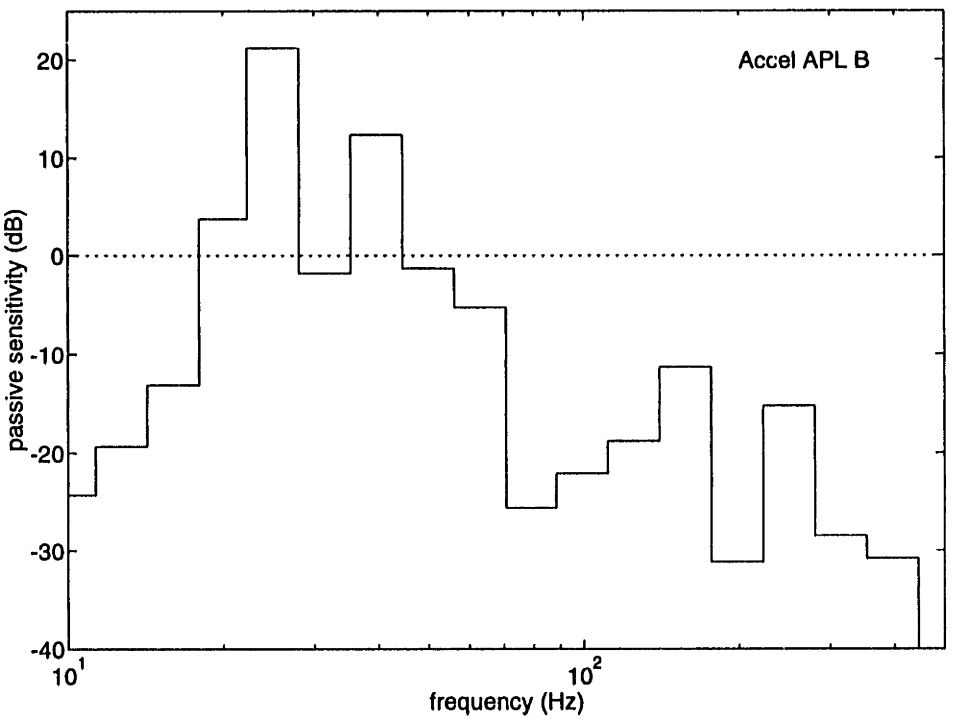

Figure 5.11: Computed average passive sensitivity $\mathcal{P}_a(s)$ along laser B line of sight at mirror B for each third octave band.

5.3.2 Comparison to Theory

The effect of base flexibility on passive isolation at mirror C is shown for the piston (z) direction. The acceleration autospectra for both the new hardmount and softmount configurations were measured at mirror C, converted to displacement and averaged into third octave bands. Using Eq. 2.148, the ratio of the autospectra defines the averaged passive sensitivity $\mathcal{P}_a$ and is plotted as a histogram in Figure 5.12. The rigid base sensitivity $\mathcal{P}_r$, based on the rigid base data in Table 5.3, is overplotted as a dotted line. The isolated mass is 2.1 kg. The data indicates a downward shift in natural frequency and an increase in $\mathcal{P}_a$ above 200 Hz not predicted by the rigid base model $\mathcal{P}_r$.

These effects can be modelled using the modified sensitivity analysis introduced in Chapter 2. An averaged magnitude model of the base mobility $\tilde{Y}_B$ is used to calculate

the modified passive sensitivity $\tilde{\mathcal{P}}$ repeated from Eq. 2.146

$$\tilde{\mathcal{P}}(s) = \frac{1 + \dfrac{\tilde{Y}_B}{Y_E}}{1 + \dfrac{Y_I}{Y_E} + \dfrac{\tilde{Y}_B}{Y_E}} \tag{5.2}$$

The frequency-averaged magnitude base mobility model $\tilde{Y}_B$ is based on the measured mobility of the testbed at the isolator interface, shown in Figure 5.13. The data were measured by exciting the hardmount collar using an external shaker with a flexible stinger and collocated accelerometer and load cell. The data show a dense modal response above 25 Hz, which up to 300 Hz follows a general +1 log magnitude slope, representing the effective spring mobility of the base plate. A three mode model plus inertia term is used to approximate the *linear* magnitude of the base mobility over this frequency range, and is plotted as a solid line in Figure 5.13.

The averaged mobility $\tilde{Y}_B^a$ is substituted for $\tilde{Y}_B$ in Eq. 5.2 and the resulting expression for $\tilde{\mathcal{P}}$ is overplotted in Figure 5.12 as a solid line. The modified sensitivity function $\tilde{\mathcal{P}}$ captures the downward shift in mount natural frequency, as well as the magnitude perturbations in the averaged sensitivity function near 40 Hz and 100 Hz. The model correctly predicts the large increase in sensitivity $\mathcal{P}_a$ at high frequency, which is as much as 10 dB compared to $\mathcal{P}_r$.

5.3.3 Performance Metric Improvement

Figures 5.14 illustrates the performance metric improvement due to the replacement of the original hardmounts by the new hardmount isolators at each mirror location. The change also includes the replacement of the corner cube at mirror A by a cat's eye retro-reflector. The improvement in absolute and differential pathlengths is due almost entirely to a decrease in modal energy in the frequency range above 100 Hz. The stiffer design resulted in local mount dynamics that were outside the frequency range of significant disturbance energy. In addition, a strong resonance at 240 Hz (not shown) due to motion of the original retro-reflector at mirror A completely disappeared, leading to a significant reduction in RMS level in pathlength A.

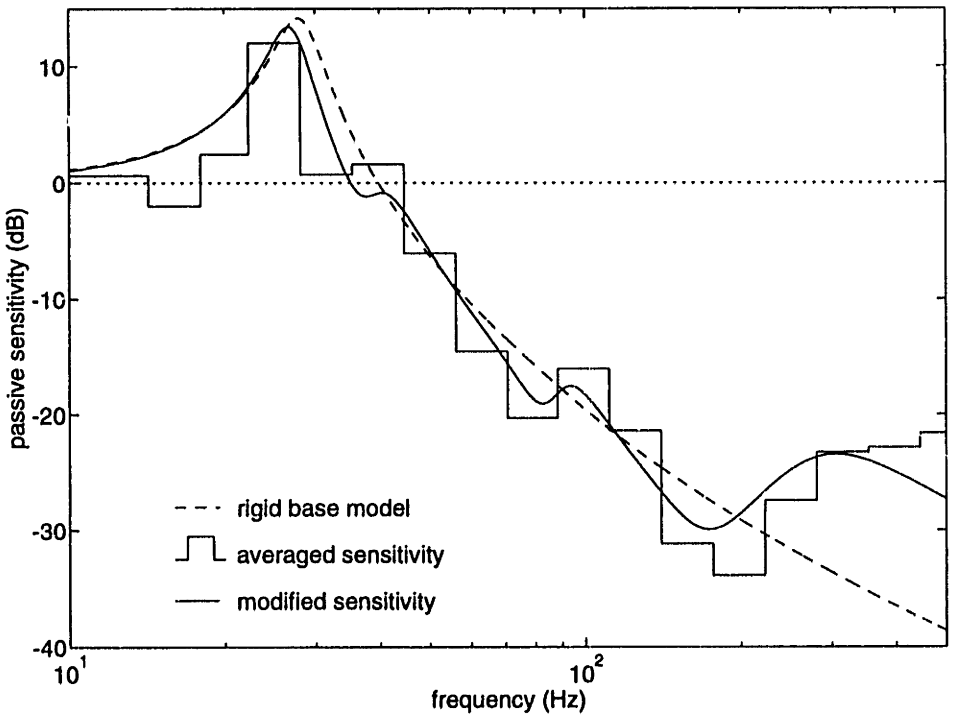

Figure 5.12: Measured passive sensitivity $\mathcal{P}_a(s)$ (histogram) at mirror C compared to rigid base sensitivity $\mathcal{P}_r(s)$ (dotted) and modified sensitivity $\tilde{\mathcal{P}}(s)$ (solid) which accounts for base flexibility.

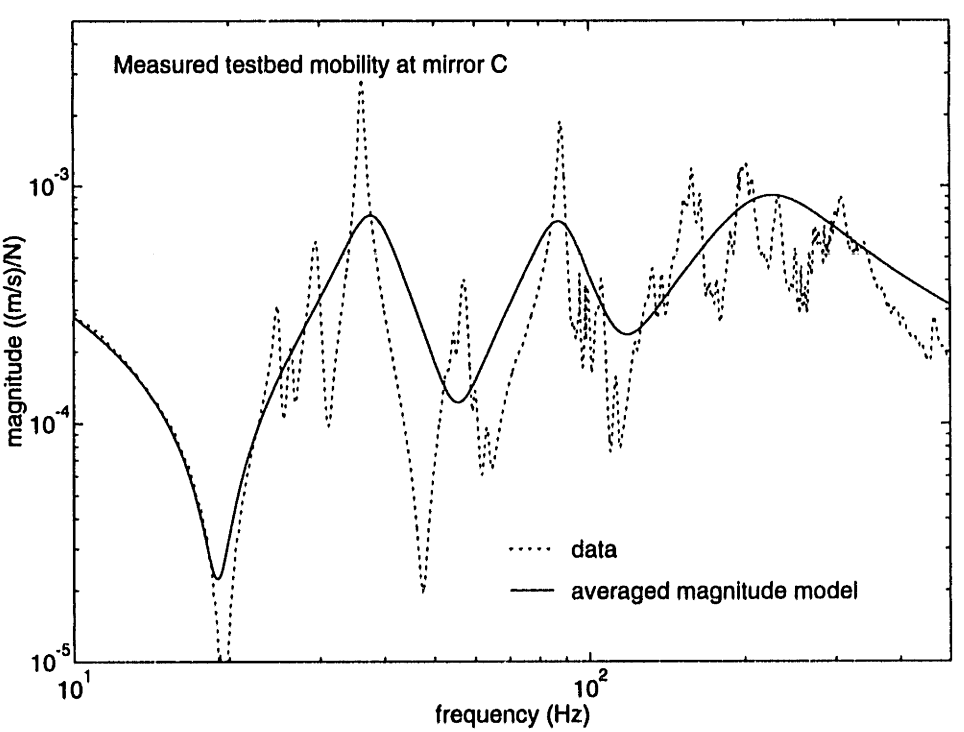

Figure 5.13: Input mobility of testbed in piston (z) direction at mirror C location. The *linear* average magnitude mobility $\tilde{Y}_B^a(s)$ is based on a 3 mode model plus rigid body inertia.

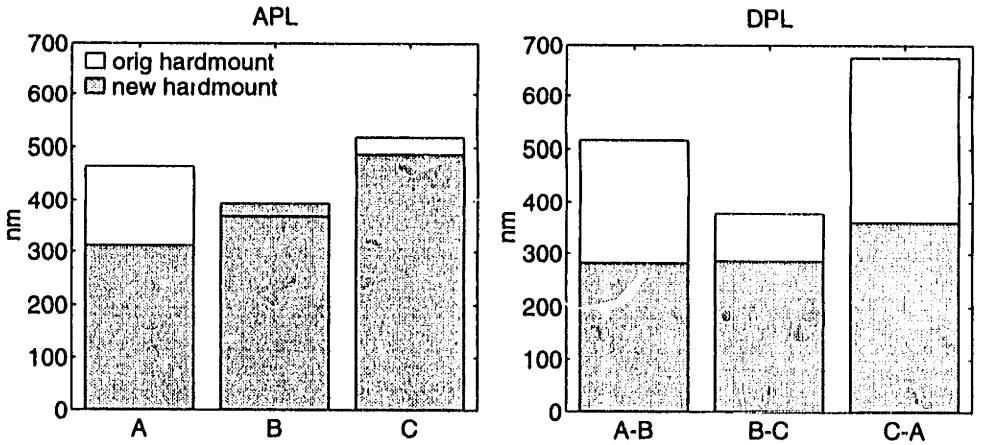

Figure 5.14: Testbed performance metric (RMS 10 - 500 Hz) showing improvement due to new hardmount design. Absolute pathlength B exhibits a small increase due to the new hardmounts.

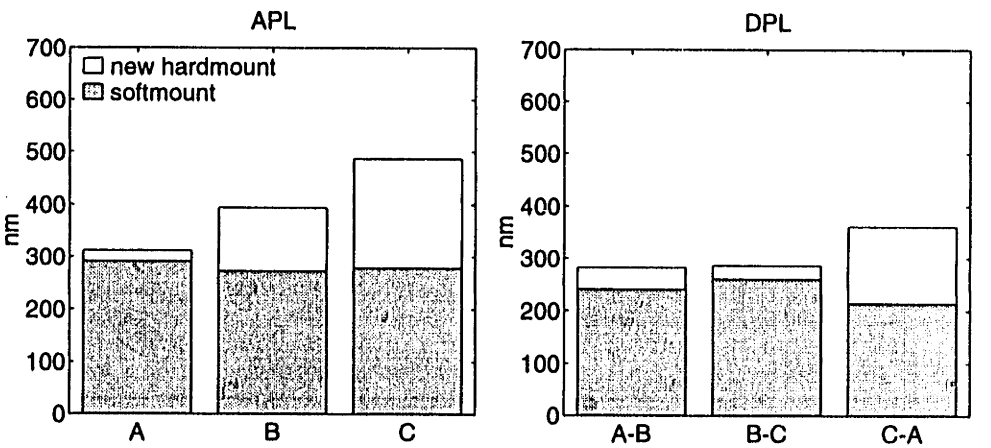

Figure 5.15: Testbed performance metric (RMS 10 - 500 Hz) showing the improvement due to passive isolation. The improvement is not very dramatic since the isolation only affects one end of the relative pathlength measurements between each mirror and the unisolated fourth vertex.

The performance metric improvement due to the passive isolation of the softmounts is illustrated in Figure 5.15. Absolute pathlength C demonstrates the largest improvement, since this mounting location is stiffest and the laser line of sight is most closely aligned with the mount piston direction at mirror C. In all, the improvement in the absolute pathlength measurements is small compared to the local acceleration results, since the isolation affects only one end of the relative pathlength measurement. This point is highlighted by Figure 5.16, in which the hardmount laser pathlength B

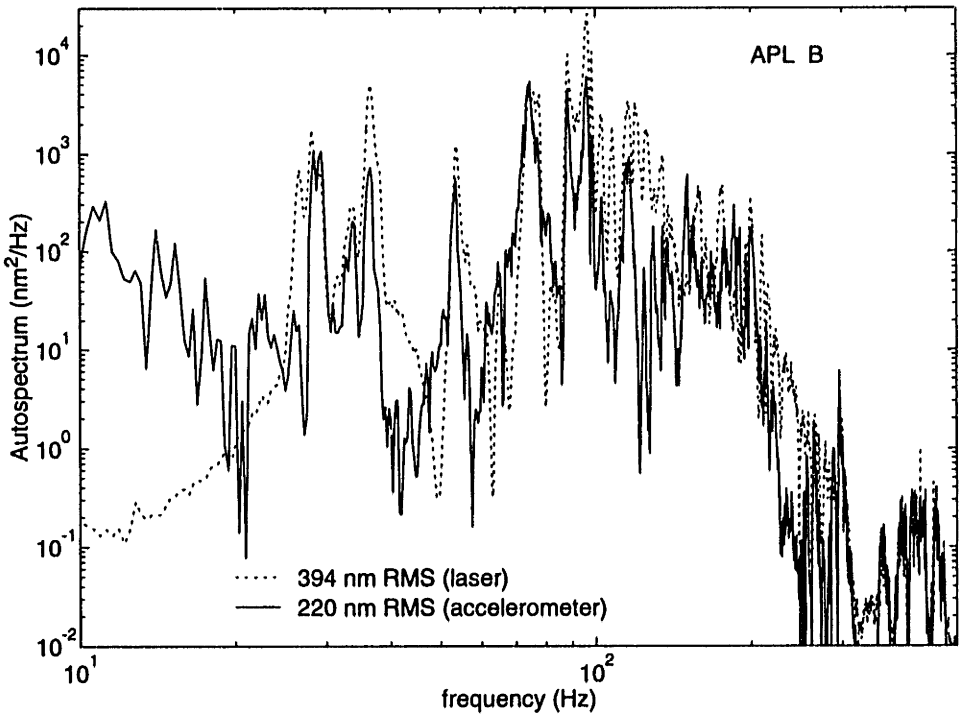

Figure 5.16: Only the component of APL B (dotted) which is due to motion at B (solid) can be improved by isolation at B. Fourth vertex cat's eye vibrates more than had originally been predicted.

is compared with local motion at mirror B along the line of sight, as measured by the accelerometers. The data show that a significant amount of energy in APL B is due to motion at the fourth vertex. Modes in APL B that lack significant motion at mirror B – notably at 46 and 100-120 Hz – are not well attenuated by the passive isolation, as illustrated in Figure 5.17.

5.4 Active Isolator Transfer Functions

The hardmount and softmount isolators were tested on the rigid test block and at their respective mounting locations on the testbed, as listed in Table 5.5. Transfer functions were recorded using a Tektronix 2630 Fourier analyzer using broadband random excitation in four frequency ranges up to 10 kHz. The excitation signal was input to an amplifier that provided a gain of 20 as well as a bias voltage of 75 volts to each of the three actuators in the mount. Electronic circuits were used to transform both the input voltage and triax acceleration measurements such that

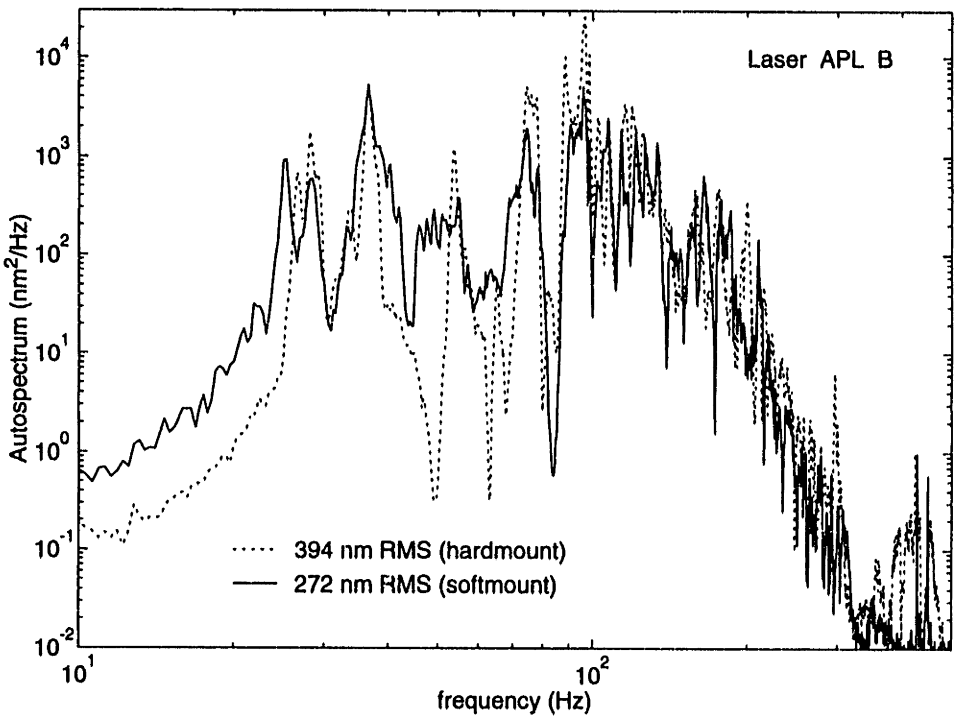

Figure 5.17: Effect of passive isolation on absolute laser pathlength B. Attenuation is much less than for local acceleration at mirror B.

transfer functions could be measured for the (x, y, z) coordinate system in Figure 5.2, or for the directions of the individual laser lines of sight.

The data presented below illustrate the directionality of the mounts and the degree to which the reaction stage decouples the base dynamics. The hardmount and softmount actuators were tested on the rigid block in order to determine the component structural dynamics, as well as to create an open loop transfer function model for line of sight actuation on the block and on the truss. Mirror C was the first actuator built, and was most extensively tested: an external shaker was used in a modal test to determine component mode shapes, and the mount transfer function from actuator voltage to output acceleration was measured for both hardmount and softmount configurations. Mirrors A and B were built as a set, and when tested were found to be dynamically nearly identical to one another and to mirror C, except that mirrors A and B are somewhat stiffer and less damped at the 30 Hz softmount resonances.

Table 5.5: Test matrix of active isolation mounts. HM = hardmount, SM = softmount. Solid bullet (•) indicates test was performed.

Test configuration	Mirror A		Mirror B		Mirror C	
	HM	SM	HM	SM	HM	SM
Rigid Block (Accel)	o	•	o	•	•	•
Testbed (Accel)	•	•	•	•	•	•
Testbed (Laser)	•	•	•	•	•	•

5.4.1 Rigid Block Mounting

Mirror C Accelerometer Tests

Figure 5.18 is a comparison of the piston (z) and transverse (x) transfer functions for mirror C hardmount, as defined in Figure 5.1. The input voltages to the individual piezoelectric actuators for independent actuation of point M in x, y and z were determined by calibration of the mount at 15 Hz. When actuated along one of these axes, there is some motion in the other axes (not shown here) due to imperfect decoupling. The z transfer function in Figure 5.18 exhibits a slope of 40 dB/decade up to a resonance at 1.2 kHz, which corresponds to the axial bounce of the active stage on the wire flexures. The transfer function in x exhibits a 600 Hz shear mode (actually two closely spaced modes), unobservable in z, due to flexibility in the piezoelectric actuators and wire flexures. A real pole at 3 kHz due to the RC time constant of the piezoelectrics (C = 6500 nF) and the output impedance of the amplifiers ($R = 8\Omega$) leads to a gradual loss in phase at high frequency.

The modes in Figure 5.18 for the hardmounted active stage shift to higher frequencies when the 1 kg reaction stage is installed between the active stage and the rigid test block, as shown in Figure 5.19. The reaction stage introduces damped softmount resonances in piston and rotation at 27 and 40 Hz, respectively. The phase indicates that the modes are stabilizing. Above 100 Hz, the transfer functions show a decrease in gain, which is more pronounced for the x direction due to the proximity of points

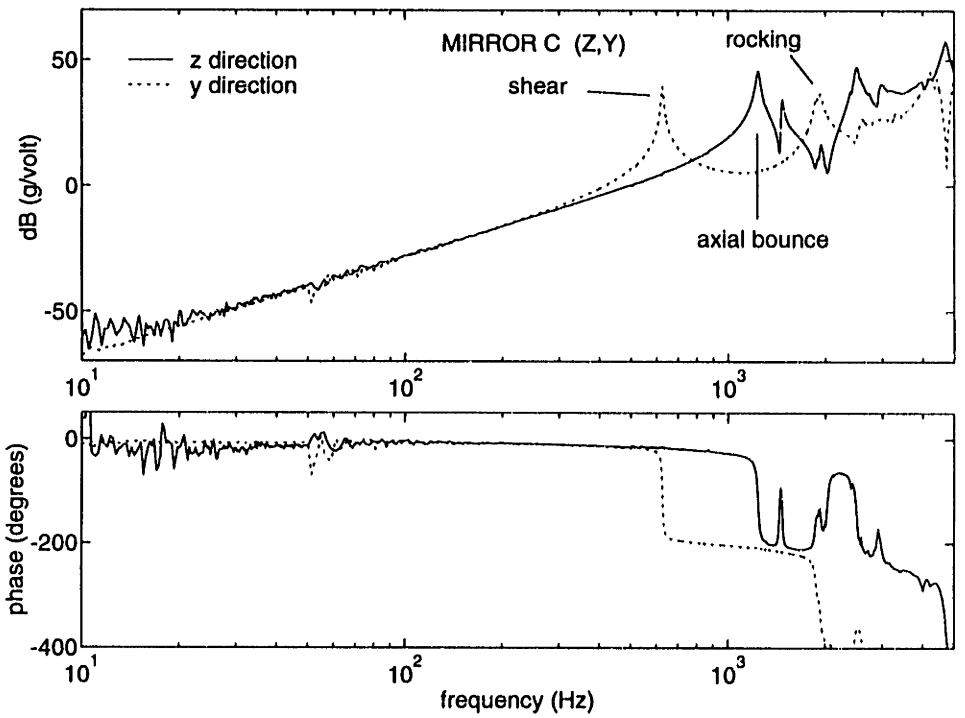

Figure 5.18: Mirror C hardmount transfer functions in two axes, measured on rigid block. Vertical actuator/flexure assembly leads to 600 Hz shear mode.

M and G in Figure 5.4. An unexpected lightly damped pair of modes occurred 440 Hz, which is due to lateral spring flexibility of the vertical blade flexures. Viscoelastic material had been added to the flexures, but unfortunately did not damp these modes. These modes were expected to create some stability problems given their proximity to the anticipated 300 Hz crossover frequency, but another mechanical redesign was dismissed in favor of active compensation of these modes, in order to complete testing within the available time.

5.4.2 Testbed Mounting

Mirror C Accelerometer Tests (z)

When the hardmount mirror C is mounted to the testbed at point C in Figure 4.1, the new transfer function in z exhibits base modal coupling as illustrated in Figure 5.20. The magnitude and phase perturbations – closely spaced pole-zero pairs with poles below the zeros in frequency – are characteristic of base mode interaction below mount

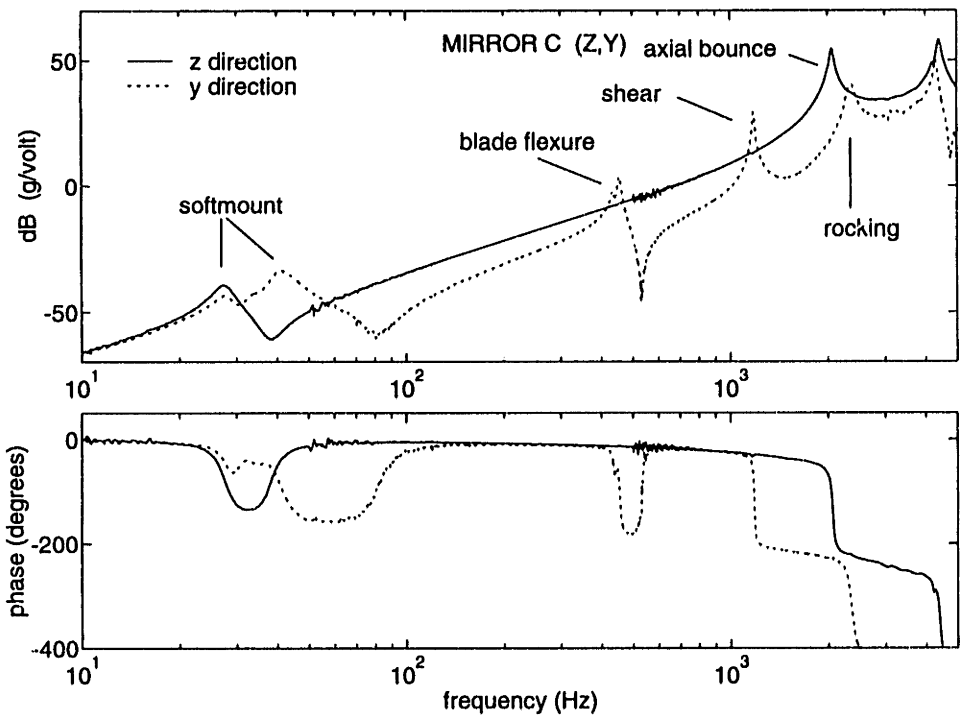

Figure 5.19: Mirror C softmount transfer functions measured on rigid block. Active stage modes increase in frequency; blade flexures add 3 modes at low frequency and also contribute two lightly damped, closely spaced pole-zero pairs at 550 Hz due to a transverse resonance in the blade flexures.

resonance ω_o studied in Chapter 3. Here, the hardmount resonance ω_o is at 1.2 kHz. Above 250 Hz, the 1/4 inch aluminum base plate to which the mount is attached acts as a soft spring which decouples truss modes from the loop (and leads to a reduction in gain of about 6 dB). Modes in this base plate appear above 1 kHz and "wash out" the strong active stage modes. The observation that the phase remains bounded between 0 and -180 degrees in this frequency range is predicted by Figure 3.14 in Chapter 3. Thus, while the base modes strongly modify the gain and phase of the transfer function, they are not destabilizing.

The perturbations for mirror C for the strongly coupled modes near 200 Hz are 6 dB in magnitude and 75 degrees in phase, consistent with a coupling parameter of $\beta_b \approx 1.7$, from Table 3.10. Given an expected controller bandwidth of 300 Hz, the modes in the the 100 - 300 Hz frequency range lead to a significant loss in phase margin, when compared to the measured rigid base transfer function plotted as a

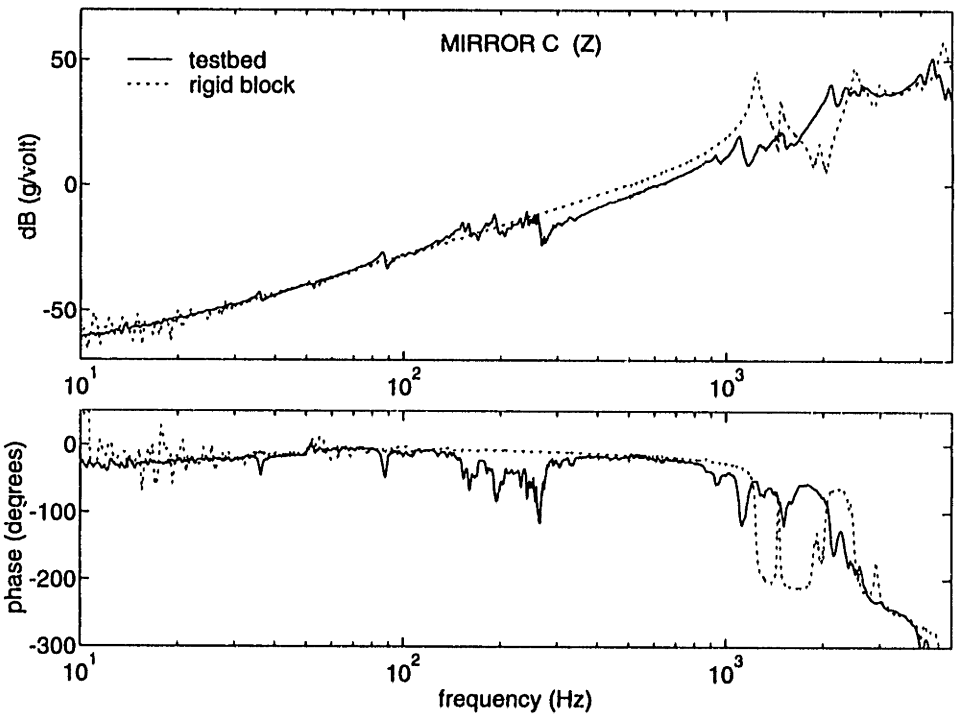

Figure 5.20: Comparison of mirror C hardmount: testbed vs rigid block. Base modes appear strongly coupled 100-300 Hz, and couple with active stage resonances above 1 kHz.

dotted line.

When the softmount isolator transfer function for mirror C is compared for both testbed and rigid block mountings in Figure 5.21, it is evident that the reaction stage strongly decouples any base modes above 40 Hz. The softmount amplifies the coupling of base modes near mount resonance, which had otherwise been nearly unobservable in the hardmount transfer function. A major advantage of the reaction stage is that at high frequency, the plant transfer function is identical to that measured on the rigid block, which is highly advantageous for control designs based on the rigid block component data.

Mirror B Accelerometer Tests (Line of Sight)

Transfer functions for mirror B are presented for the direction defined by the laser line of sight from point B to point E in Figure 4.1. The line of sight forms an angle of 35 degrees with the isolator z direction in Figure 5.1; therefore, it is expected that the

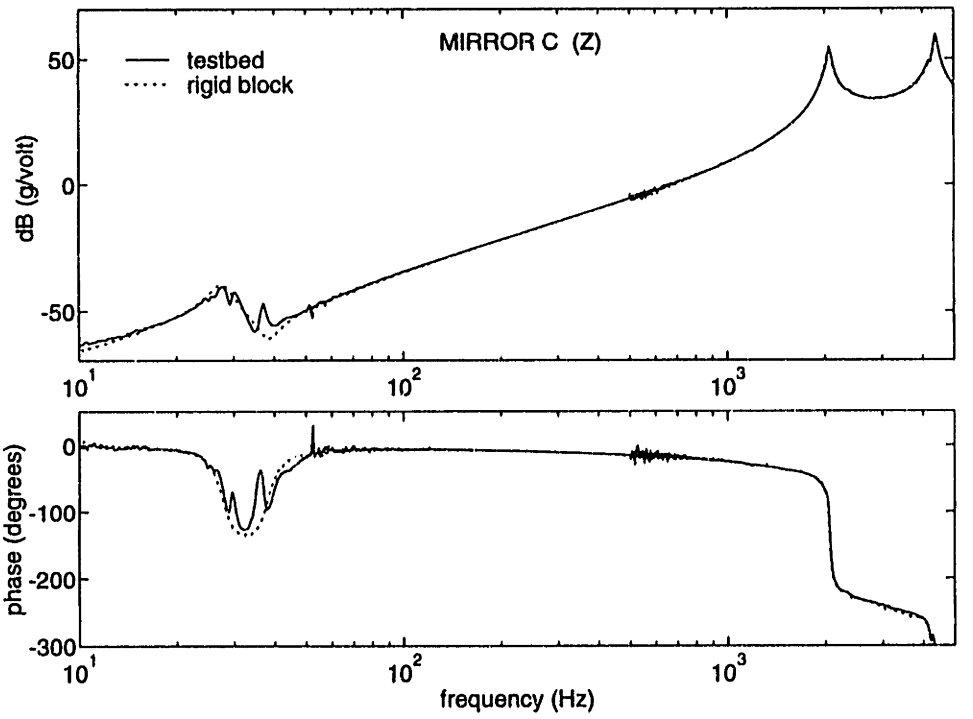

Figure 5.21: Reaction stage of softmount decouples base modes from transfer function above 40 Hz in z direction. Transfer functions overlay perfectly above 40 Hz up to 5 kHz.

transverse blade flexure and active stage shear modes will be observable/controllable in the line of sight transfer function, denoted as H_{BB}.

Figure 5.22 compares the transfer function H_{BB} on the rigid block and the testbed. Both softmount modes (33 and 38 Hz) are visible, as are the transverse blade flexure and wire flexure shear modes at 550 and 1200 Hz, respectively. A testbed mode at 24 Hz is strongly observable at the mirror B mounting location and corresponds to the first beam bending mode in the testbed truss leg. Since the mode frequency occurs below the 33 Hz softmount resonance for mirror B, the coupling in magnitude and phase is strong as predicted in Chapter 3. High frequency base modes are decoupled by the reaction stage.

Some interesting effects occur at high frequency: modes above 1 kHz are unchanged from the rigid block test because these modes (corresponding to resonances of the active stage) are isolated from the base by the reaction mass (an exception is one of the two shear modes at 1200 Hz which appears to have shifted slightly, believed

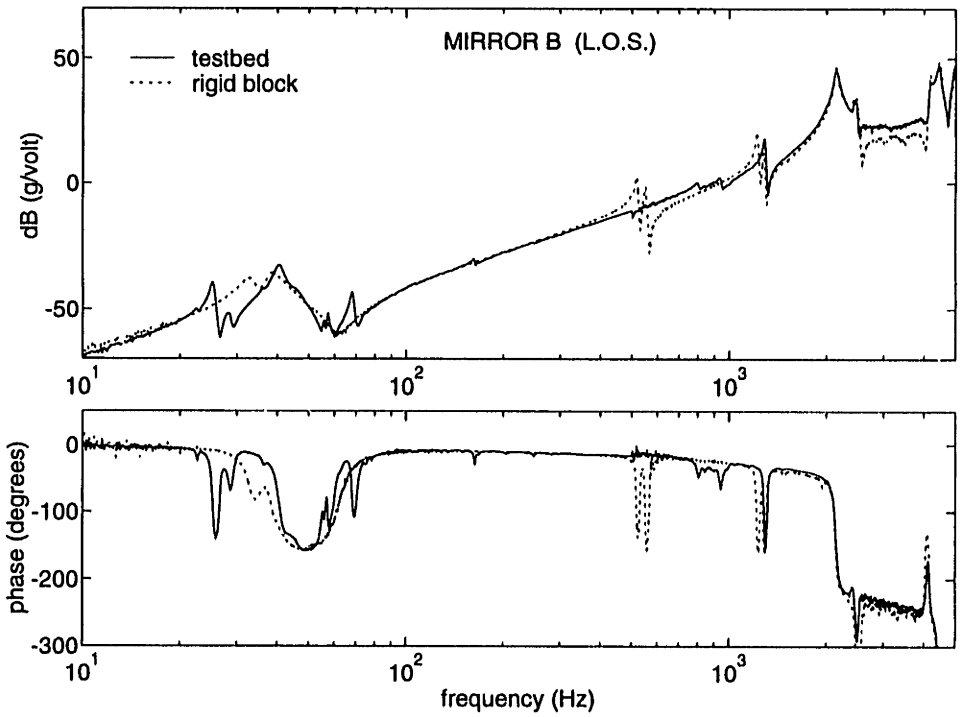

Figure 5.22: Mirror B line of sight transfer function on rigid block and testbed. Blade flexure and shear resonances appear in measurement; flexure modes at 550 Hz are damped via coupling with the testbed flexibility.

due to mechanical handling and mounting on the truss). The blade flexure modes at 550 Hz, however, have become well damped and shifted to 800 Hz and 900 Hz. These blade flexure modes are affected because the flexures are connected to the base, which is modally dense near 550 Hz and has an input mobility somewhat between that of a mass or damper, as illustrated in Figure 5.13. In Figures 3.3 and 3.6 it is shown that this type of base mobility would increase the frequency and damp mount interface modes in the acceleration transfer function.

Figure 5.23 illustrates the advantages of a softmount at mirror B when compared to a hardmount, when each are mounted to the flexible testbed. Base modal coupling is strong for the hardmount throughout the frequency range (and particularly near anticipated crossover), while the softmount decouples these modes and recovers the loss in phase.

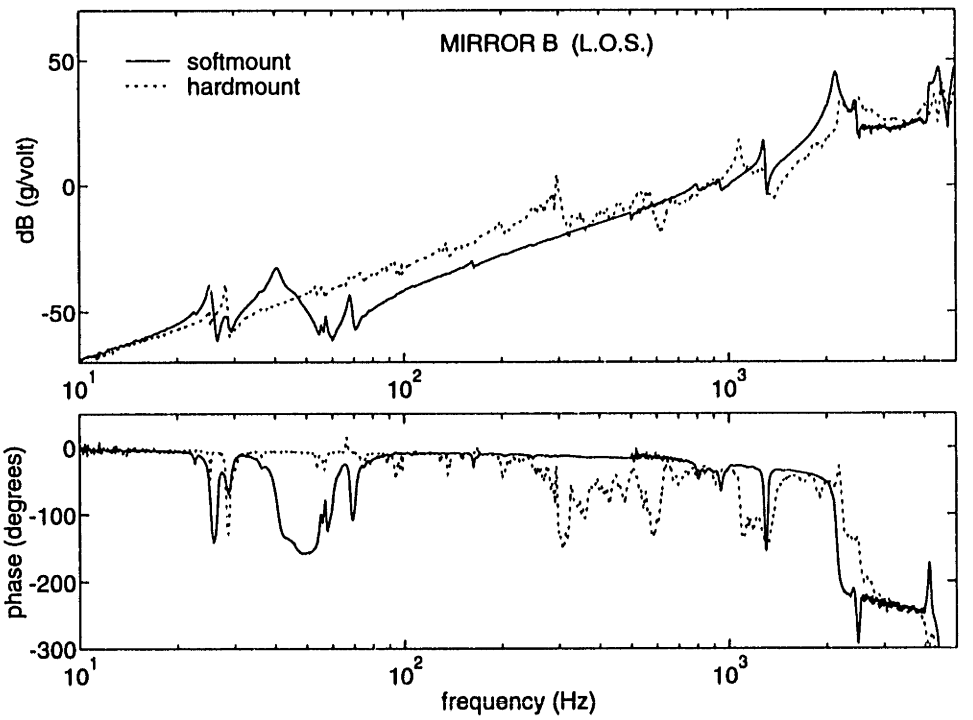

Figure 5.23: Comparison of mirror B line of sight acceleration on testbed: hardmount vs softmount. Reaction stage decouples base resonances and leads to π recovery in phase near anticipated crossover frequency of 300 Hz.

Mirror B Laser Tests

The hardmount/softmount actuation of mirror B was repeated, with the output instead measured by the absolute laser pathlength B. The comparison plotted in Figure 5.24 clearly shows the decoupling due to the reaction stage. Due to the laser sampling rate of 4500 Hz, data were only recorded to 2 kHz. Figure 5.25 compares the softmount laser and acceleration transfer functions (converted to displacement), showing close agreement. It is concluded that motion at the fourth vertex point E contributes little to the base modes which are coupled into the transfer function below 80 Hz. Above this frequency, point E is undisturbed by reaction forces generated by the isolator due to the decoupling effect of the series softmount. Based on this agreement, it is considered possible to design compensators for laser feedback based only on acceleration transfer functions measured on the rigid test block.

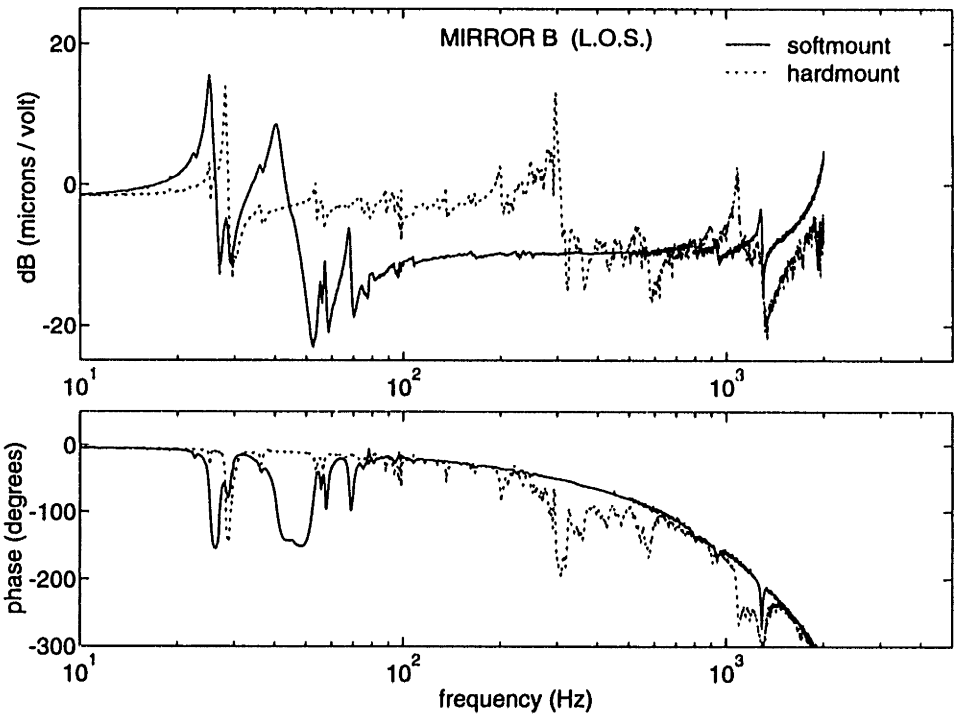

Figure 5.24: Comparison of laser transfer function for mirror B, both hardmount and softmount, showing improvement due to reaction stage. Gradual phase loss is due to 4500 Hz sample rate.

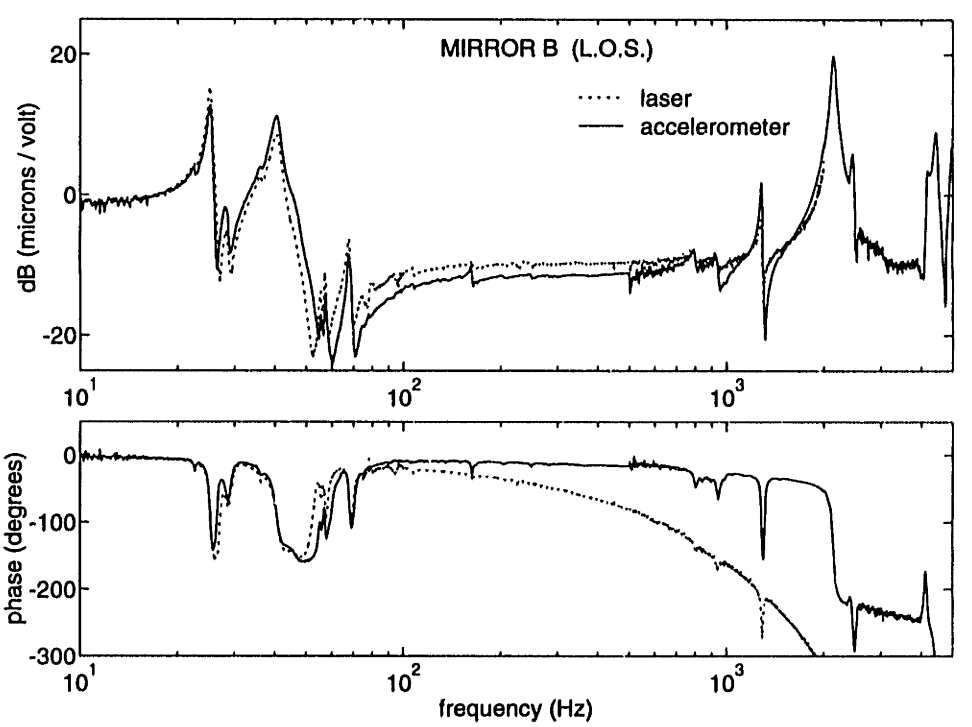

Figure 5.25: Comparison of laser and accelerometer measurements of mirror B actuation on truss, showing excellent agreement. Laser exhibits phase loss due to 4500 Hz sample rate.

5.5 MIMO Isolator Transfer Functions

5.5.1 MIMO Acceleration Data

Figure 5.26 is a plot of the 3×3 transfer function matrix of the three hardmount isolators mounted to the truss structure. The input voltage V to each mount directs the mirror along the laser line of sight, and the outputs u are the accelerations measured in the direction of each mirror line of sight. The transfer function matrix equation is

$$\begin{bmatrix} u_A \\ u_B \\ u_C \end{bmatrix} = \begin{bmatrix} H_{AA} & H_{AB} & H_{AC} \\ H_{BA} & H_{BB} & H_{BC} \\ H_{CA} & H_{CB} & H_{CC} \end{bmatrix} \begin{bmatrix} V_A \\ V_B \\ V_C \end{bmatrix} \tag{5.3}$$

The data show that the diagonal transfer functions contain a large feedthrough term that is perturbed by resonant modes of the structure. The off-diagonal transfer functions exhibit the modal coupling between the actuation point and the other accelerations along the lines of sight, but without the feedthrough term. The off-diagonal transfer functions are of comparable magnitude to the diagonal transfer functions at strongly coupled modes, up to 300 Hz.

The level of coupling for the hardmounts, particularly near the anticipated crossover frequency of 300 Hz, would make independent SISO compensation of each of the isolators difficult. For this reason, the reaction stage was added to the isolator, and the new transfer function matrix is plotted in Figure 5.27. The coupling near crossover is now low, but strong coupling near the mount resonances at 30-60 Hz remains. The remaining low frequency coupling is judged not to be detrimental to stability, since it occurs in a region of high phase margin in each of the loops, as will be seen in Chapter 6. The MIMO transfer function matrix for the laser outputs is presented in Appendix D, and exhibits slightly higher levels of coupling for both the hardmount and softmount configurations.

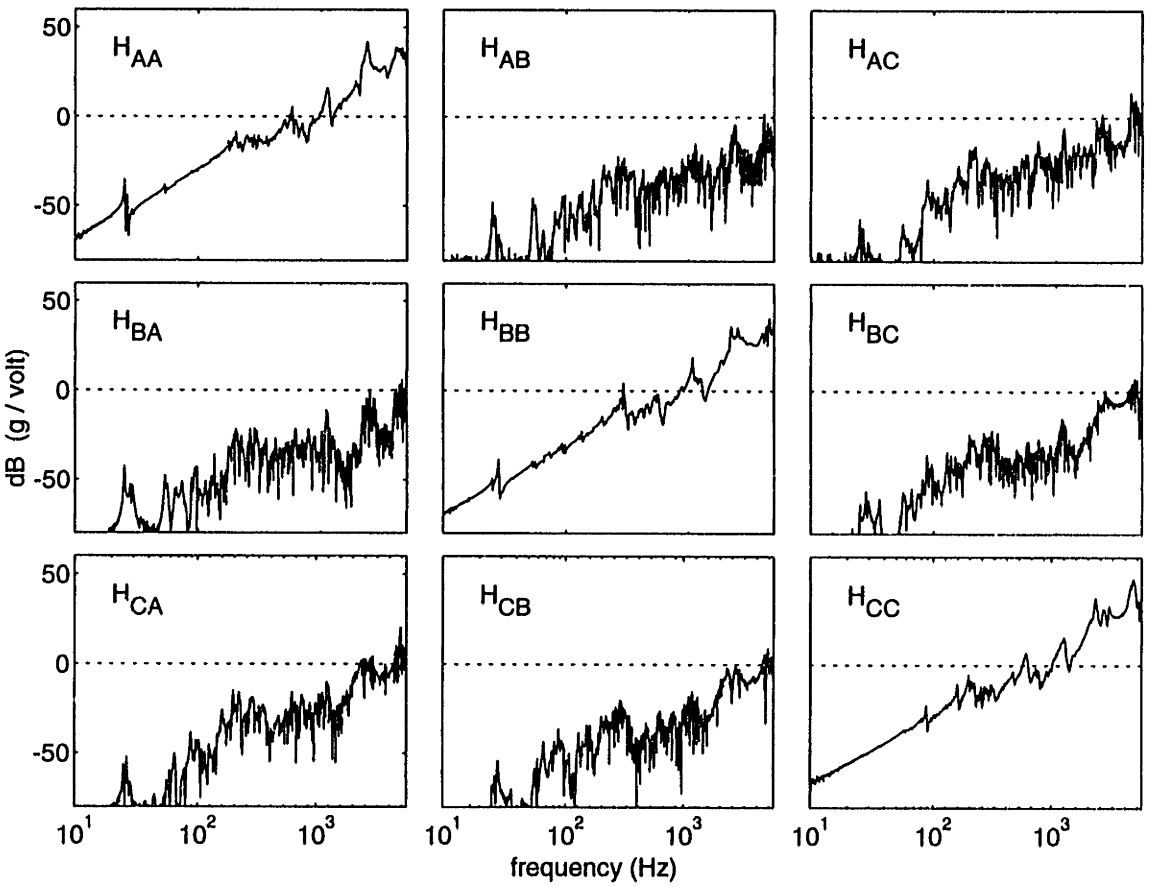

Figure 5.26: Hardmount acceleration transfer function matrix for 3 mirrors actuated along lines of sight. Modal coupling leads to large off-diagonal transfer functions and to large perturbations in the diagonal functions.

5.5.2 Diagonal Dominance of Transfer Functions

The Direct Nyquist Array technique [81] is used to investigate multivariable closed loop stability in Chapter 6. The technique requires that the return matrix $[I + G_{OL}K]$ be diagonally dominant, where K is the compensator matrix and G_{OL} is the open loop plant transfer function matrix. If K is diagonal, then the only off-diagonal coupling introduced in the return matrix is due to G_{OL}. Prior the the design of the compensator K, the anticipated coupling off-diagonal coupling in the return matrix can be investigating by considering the diagonal dominance of the plant G_{OL}, given by the plant transfer function matrix H in Eq. 5.3. From Reference [81] an $m \times m$ matrix $H(s) = \{h_{ij}(s)\}$ is diagonally dominant on the Nyquist contour D if for all s

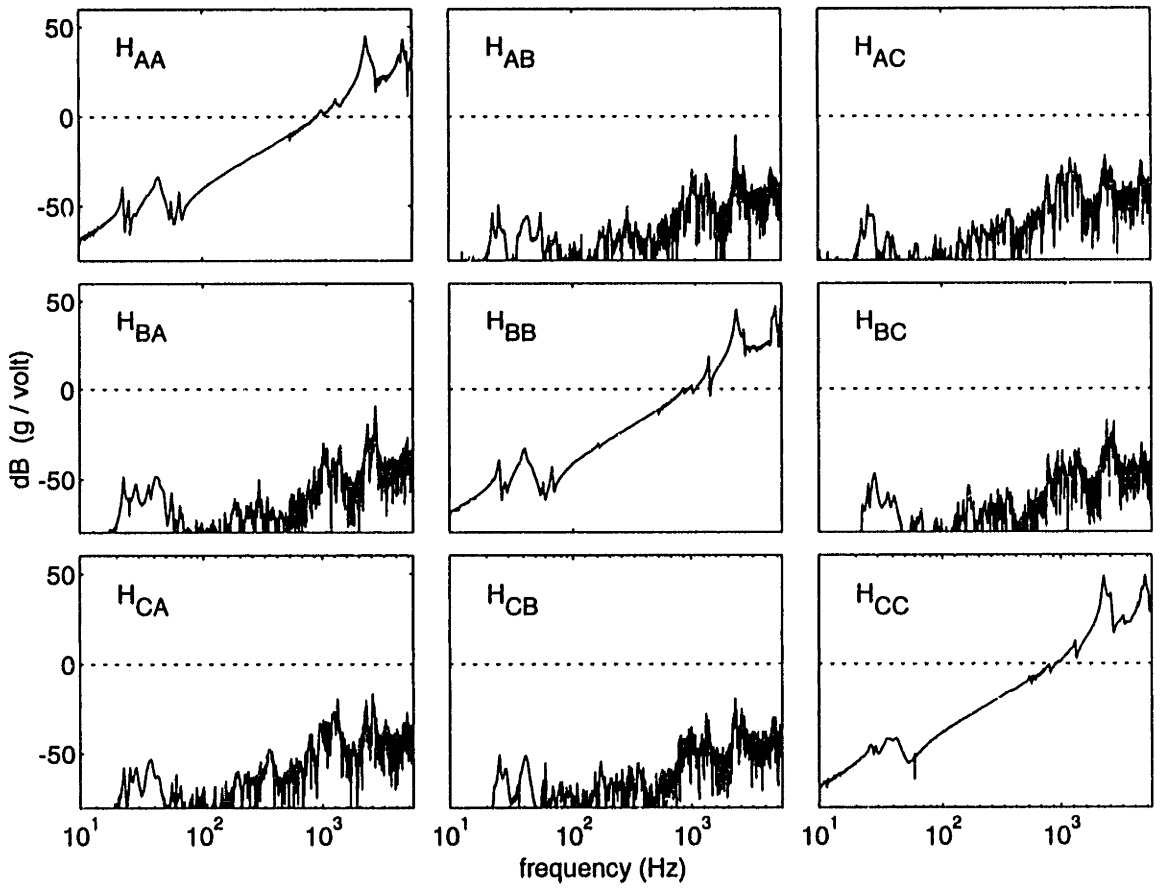

Figure 5.27: Softmount acceleration transfer function matrix for 3 mirrors actuated along lines of sight. The improvement due to the softmount is twofold: coupling is decreased in the off-diagonal functions, and modal perturbations in the diagonal functions is attenuated above 50 Hz.

on D and for all i either

$$|h_{ii}(s)| > d_{ir}(s) = \sum_{j=1,\neq i}^{m} |h_{ij}(s)| \qquad \text{(row dominance)} \tag{5.4}$$

or

$$|h_{ii}(s)| > d_{ic}(s) = \sum_{j=1,\neq i}^{m} |h_{ji}(s)| \qquad \text{(column dominance)} \tag{5.5}$$

which implies that the magnitude of the diagonal element must be greater than the sum of the magnitudes of the off-diagonal row or column elements. Defining the *dominance ratio* $d_i(s)$ as

$$d_i(s) = \max\left\{\frac{d_{ic}(s)}{h_{ii}(s)}, \frac{d_{ir}(s)}{h_{ii}(s)}\right\} \tag{5.6}$$

then only three plots are required to describe the diagonal dominance of the 3×3 transfer function H from Eq. 5.3. A dominance ratio $d_i(s)$ less than one for each diagonal transfer function implies diagonal dominance of the matrix. The dominance ratio $d_i(s)$ is plotted in Figures 5.28 and 5.29 for the hardmount and softmount MIMO acceleration transfer functions. The high frequency decoupling of the softmount is clearly evident, leading to dominance ratios that are well below one, indicating a strong diagonal dominance of the transfer function matrix. At low frequencies, the softmount dominance ratio remains above one, and is increased slightly by the softmount in comparison to the hardmount data. Thus the MIMO plant is strongly diagonally dominant at frequencies near crossover, but not in the 30 to 60 Hz range. The implications of this fact will be investigated in Chapter 6.

5.6 Summary

In this chapter the design and open loop performance of the active mounts is presented. The mount design permits both hard and soft mounting of the cat's eye optics to the testbed, and for both configurations allows three-axis linear articulation of the optics up to $\pm 6\mu$m in stroke. The softmount reaction stage is shown to both provide passive isolation performance (up to 9 dB of displacement RMS at each mirror) as well as to condition each of the open loop transfer functions, by decoupling base mode dynamics from the plant model. The importance of this decoupling is illustrated for the 3×3 transfer function matrix for the three isolators mounted on the truss, for both acceleration as well as laser output. Thus, the softmount design both improves passive performance and improves robustness to the presence of unmodelled base modal flexibility. The active softmount transfer functions presented in this chapter are used as the basis actuator control designs in Chapter 6.

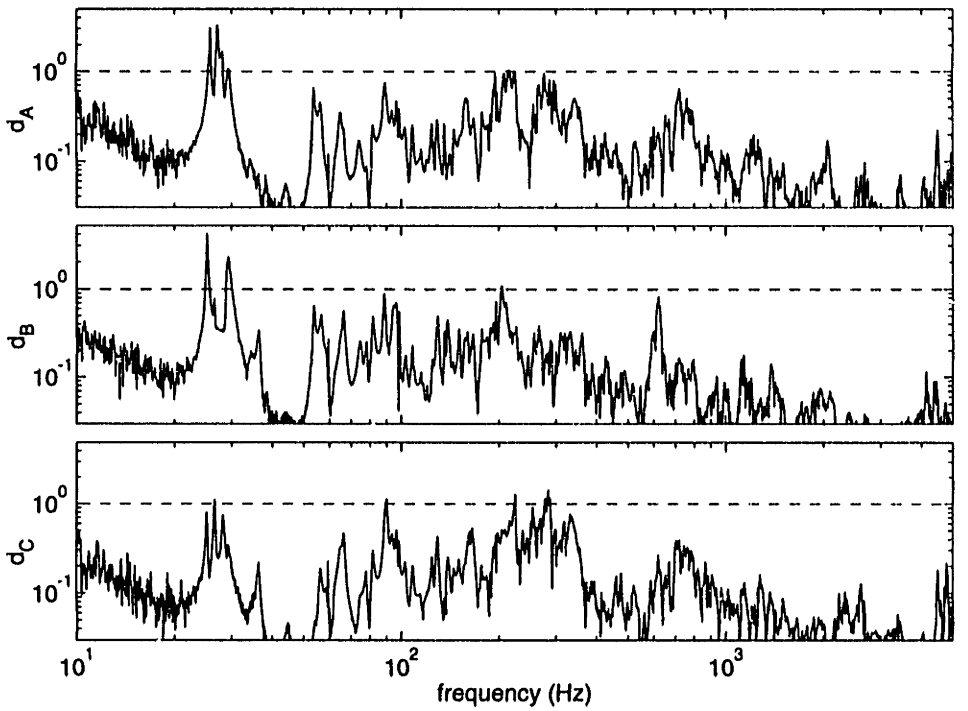

Figure 5.28: Diagonal dominance ratios for hardmount isolators (acceleration output) on the testbed. Dominance ratios near one imply a high level of coupling.

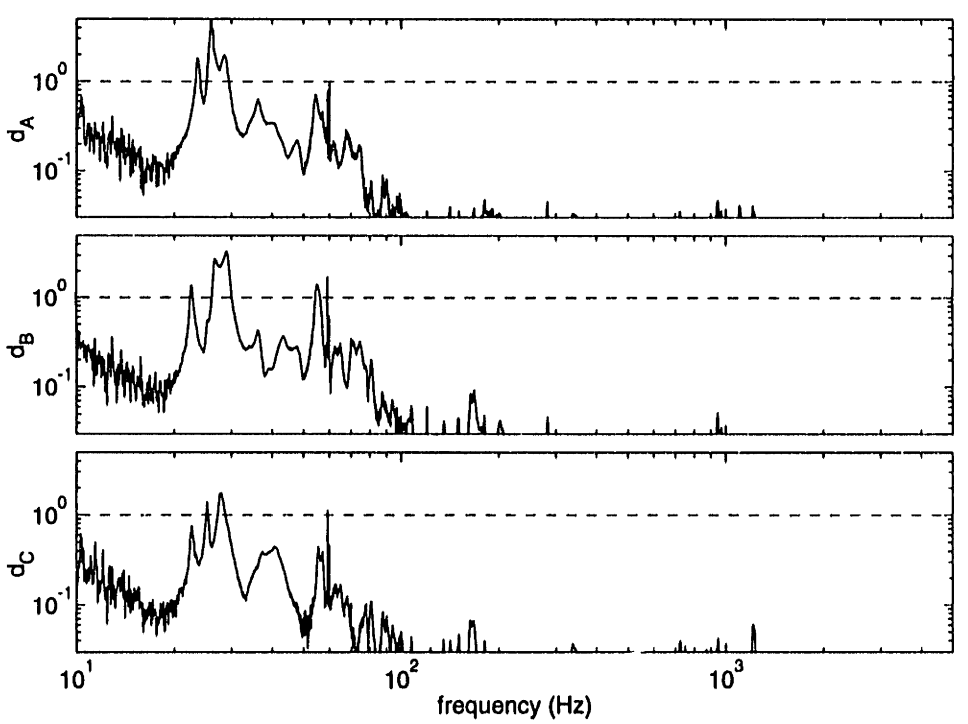

Figure 5.29: Diagonal dominance ratios for softmount isolator (acceleration output) on testbed, showing improvement due to reaction mass. Frequency range near 30–70 Hz is not diagonally dominant.

Chapter 6

Closed Loop Design and Implementation

6.1 Objectives

This chapter presents the compensator design and closed loop results of active isolation and active pathlength control for the three active mounts. The design approach is motivated by the desire to implement low order, high gain compensators that are based only on plant transfer functions measured on a rigid test stand, and are insensitive to the presence of unmodelled modal flexibility in the base structure to which the isolators are mounted. The disturbance is modelled as a filtered white noise signal added to the output of the plant, and LQG (Linear Quadratic Gaussian) methods are used to design compensators based on the full order model. The compensator order is reduced using balancing methods, permitting laboratory implementation of discrete compensators at sample rates up to 6700 Hz. Active mount stability and performance are demonstrated for a rigid test block mounting, and are again demonstrated when the isolator is mounted to the SERC Interferometer Testbed. Simultaneous, independent implementation of two actuators, using acceleration feedback, and of three mounts, using laser feedback, demonstrate significant performance improvement on the testbed, with only minimal interaction between the three mirrors.

6.2 Discussion of Design Approach

The purpose of active control for vibration isolation is to modify the open loop transmissibility T_{OL} of the mount. Figure 6.1 illustrates one model which describes how the open loop disturbance and control affect the output acceleration $\ddot{y}_2$, corresponding to the motion of sensitive equipment on a vibrating base. Base (free) acceleration $\ddot{y}_B^f$ is attenuated by the passive mount transmissibility T_{OL} and appears at the plant output as open loop disturbance $d = \ddot{y}_2^{OL}$. When the feedback loop is closed around the loop transfer function $G_{OL} = G_p K$, the closed loop output acceleration becomes

$$\begin{aligned} \ddot{y}_2^{CL} &= \left(\frac{1}{1+G_{OL}}\right)(T_{OL})\,\ddot{y}_B^f \\ &= (S_{CL}T_{OL})\,\ddot{y}_B^f \\ &= (T_{CL})\,\ddot{y}_B^f \end{aligned} \tag{6.1}$$

where S_{CL} is the closed loop sensitivity function. Thus, the closed loop mount transmissibility T_{CL} is the product of the open loop transmissibility and the closed loop sensitivity function. The preceding model can be recast, as illustrated in Figure 6.2, in terms of the mount passive sensitivity function $\mathcal{P}$ introduced in Chapter 2, in which the exogenous input is assumed to be the *unisolated* acceleration $\ddot{y}_2^{(u)}$ measured at the plant output. The mount sensitivity $\mathcal{P}$ attenuates this input producing *isolated* acceleration $\ddot{y}_2^{(i)}$ (assumed to be the same signal as d in Figure 6.1) which is then regulated by active control:

$$\begin{aligned} \ddot{y}_2^{CL} &= \left(\frac{1}{1+G_{OL}}\right)(\mathcal{P})\,\ddot{y}_2^{(u)} \\ &= (S_{CL}\mathcal{P})\,\ddot{y}_2^{(u)} \\ &= (\mathcal{P}_{CL})\,\ddot{y}_2^{(u)} \end{aligned} \tag{6.2}$$

where $\mathcal{P}_{CL}$ is termed the *closed loop mount sensitivity*, which reflects both active and passive compensation.

The philosophy followed in the design and laboratory implementation of compensators is based on the desire to avoid direct modelling and compensation of poorly known, lightly coupled modes of the testbed structure. Accordingly, compensators

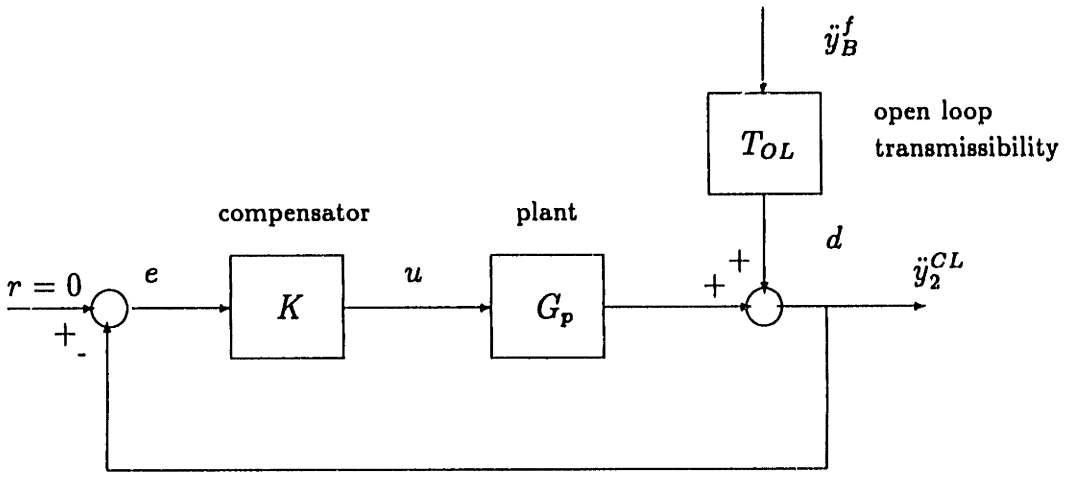

Figure 6.1: Block diagram for output feedback for active isolation. The base disturbance $\ddot{y}_B^f$, filtered by the passive mount transmissibility T_{OL}, produces the open loop acceleration $d = \ddot{y}_2^{(i)}$ at the output.

were designed and implemented first for the active mounts on a rigid test block, a step which built confidence in the models of open and closed loop performance. The mounts, in most cases with the same compensators, were re-implemented on the testbed structure. Table 6.1 lists the tests conducted for each mount. Mirror B was tested most extensively, in order to demonstrate performance at the maximum sample rate (6700 Hz) as well as at sample rates allowing simultaneous implementation with mirror C on the testbed. Mirror A was controlled only for laser feedback experiments on the truss.

Because the accelerometer sensors were determined late in the design process to have excessive sensor noise, accelerometer designs and experiments were conducted assuming that these sensors are noiseless. Open and closed loop autospectra were calculated from transfer function data, which averages out the sensor noise (but results in poor transfer function coherence in frequency ranges where sensor noise is high). The "noise free" experiments illustrate the effects of structural flexibility central to this thesis, and are representative of performance for low noise sensors (measured autospectra from two lower noise models are presented in Appendix C). Laser path-length feedback was used in a final set of experiments to significantly improve the performance metric.

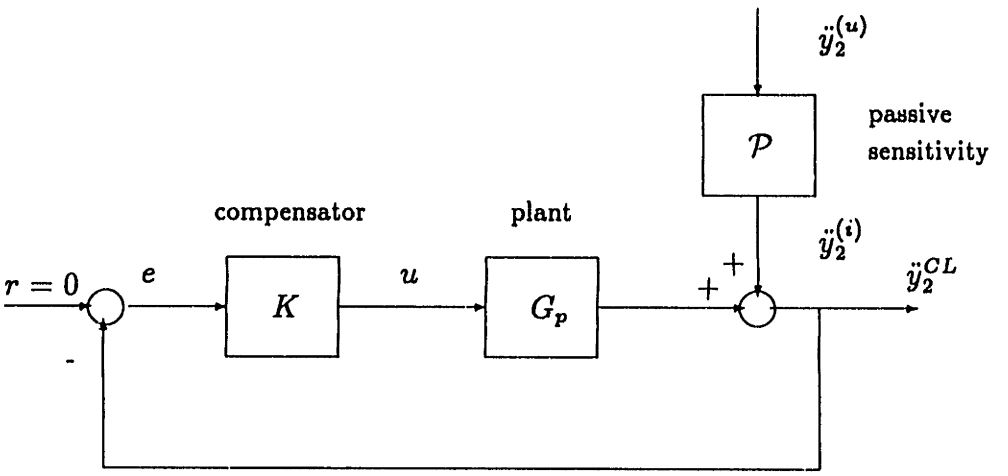

Figure 6.2: Block diagram for active isolation, where the output disturbance $d = \ddot{y}_2^{(i)}$ is the same in the previous figure, but is instead represented as the output of the mount passive sensitivity $\mathcal{P}$ driven by the unisolated acceleration $\ddot{y}_2^{(u)}$.

Table 6.1: Test matrix for closed loop tests. [1]Same compensators implemented as on rigid block. [2]Redesign avoids compensation of 550 Hz modes.

Closed Loop Test		Actuator		
Mounting	Sample Rate	B	C	A
Rigid Block (accel)	6700 Hz	•	o	o
	3100 Hz	•	o	o
Testbed (accel)	6700 Hz[1]	•	o	o
	3100 Hz[1]	•	o	o
	6700 Hz (Redesign)[2]	•	•	o
	3100 Hz (Redesign)[2]	•	•	o
Testbed (laser)	4000 Hz	•	•	•

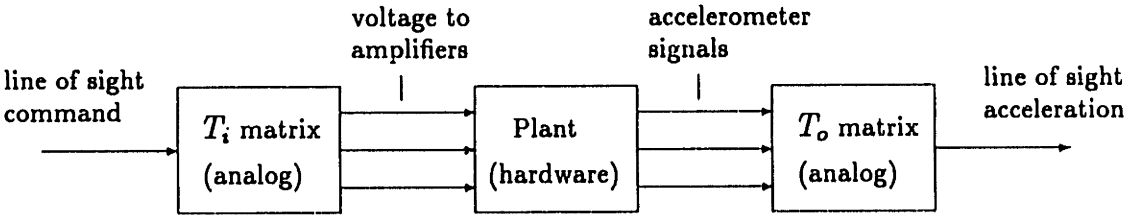

Figure 6.3: Analog constant gain circuits were used for each mount to transform the input command into three voltages to the actuators, and to determine line of sight acceleration from the three sensor outputs.

The Linear Quadratic Gaussian (LQG) method was used to design compensators for this thesis. The method was selected because the LQG design minimizes a quadratic cost function of the defined performance variables, a minimization which correctly captures the Interferometer Testbed performance metric: rejection of disturbance energy for all frequencies between 10 and 500 Hz. The LQG method facilitates the design of stable, model based compensators in state space form, and easily accommodates frequency-weighted loopshaping in the compensator design process. However, since the disturbance filter and sensor noise are used as design tools, it must be stated that the LQG method is used here as a design tool, rather than as a formal minimization of a cost function. The minimization occurs iteratively, as different compensators are evaluated on the design plant and disturbance model, as described below.

Discrete implementation of the compensators was chosen for flexibility. However, it was necessary to implement some elements of the compensators in analog, in order to off-load the burden of the realtime computer for high gain, high dynamic range, and high frequency compensator dynamics. Additionally, two analog constant gain circuits were built to decouple the actuator input command (to the three piezoelectric actuators) and output motion (from the three accelerometers) along the laser line of sight, reducing the number of I/O channels required for the realtime computer. Thus, each actuator is a single-input, single-output plant, as illustrated in Figure 6.3.

The next two sections present the modelling, design choices, and control design for a typical high gain compensator for mirror B. Experimental results for individual

mount control on the test block are compared to the model and to a testbed mounting of the actuator. Simultaneous, independent actuator control using accelerometer or laser feedback is shown in Sections 6.5 and 6.6.

6.3 Loop Transfer Function Modelling

6.3.1 State Space Model of Isolator Plant

Identification software developed by Balmes [7], [8] was used to create state space models of the softmount transfer functions presented in Chapter 5. The software uses frequency domain data, and iteratively updates both frequencies and complex mode shapes. It was necessary to convert plant transfer functions from acceleration to displacement for the identification step, in order to reduce the dynamic range of the plant. The softmount transfer function for mirrors B and C, along their respective lines of sight, are plotted in Figures 6.4 and 6.5 versus the identified state space models. State orders are 24 and 20, respectively. The plants represent the isolator hardware, the voltage amplifiers (gain of 20), and input and output analog transformation matrices. The only dynamics added by the amplifier is a real pole at 3 kHz, contributing to some phase loss at high frequency. The low frequency mount modes have identified damping between 5 and 10 percent, while high frequency modes are lightly damped, between 0.7 and 2.3 percent.

The output of the identification procedure is a state space model of the form

$$\begin{aligned} \dot{x}_1 &= A_1 x + B_1 u \\ y_1 &= C_1 x_1 \end{aligned} \tag{6.3}$$

where y_1 is output displacement and u is voltage input to the transformation circuit. Two modifications were made to this model. A constant term was added to the plant at high frequency to approximately overbound modes above 5 kHz. The term was implemented as a second order high pass filter (with 8 kHz corner) in parallel with the original plant. Secondly, the output of this augmented plant was placed in series with a second order differentiator (with rolloff at 100 kHz) such that for frequencies

below 5 kHz, the plant output is that of acceleration. This step adds a feedthrough term to the modified isolator model:

$$\begin{aligned} \dot{x}_2 &= A_2 x_2 + B_2 u \\ y_2 &= C_2 x_2 + D_2 u \end{aligned} \tag{6.4}$$

where y_2 is acceleration of the cat's eye optics point M (in Figure 5.2) along the line of sight. The modifications add four states to the model. After each augmentation, the new state model was tri-diagonalized in order to preserve numerical conditioning, given the large frequency separation of the modes in the model.

6.3.2 Models of Loop Components

Components of the loop transfer function for the active mount are illustrated in Figure 6.6. The loop is loosely grouped into *Plant*, *Realtime Computer* and *Analog Circuit*, corresponding to the physical arrangement in the laboratory. To be precise for the discussion of the control design, several transfer functions are defined based on the elements in Figure 6.6. The *actuator plant* G_m, for which the identification was performed and defined by the state model in Eq. 6.4, includes the input/output transformation circuits, amplifier and the isolator mount:

$$G_m = T_o H_9 H_7 T_i \tag{6.5}$$

The *hardware plant* G_h includes G_m, as well as the time delay and zero order hold of the realtime computer, and represents the "given" plant for which compensation must be designed:

$$G_h = H_5 H_4 G_m \tag{6.6}$$

The *analog circuit plant* includes all filters and gains added for anti-aliasing, smoothing, and notching:

$$G_a = k_1 k_3 H_8 H_6 H_3 H_2 H_1 \tag{6.7}$$

The complete loop gain is the product of the hardware plant, analog circuit plant and compensator K

$$G_{ol} = G_h G_a K \tag{6.8}$$

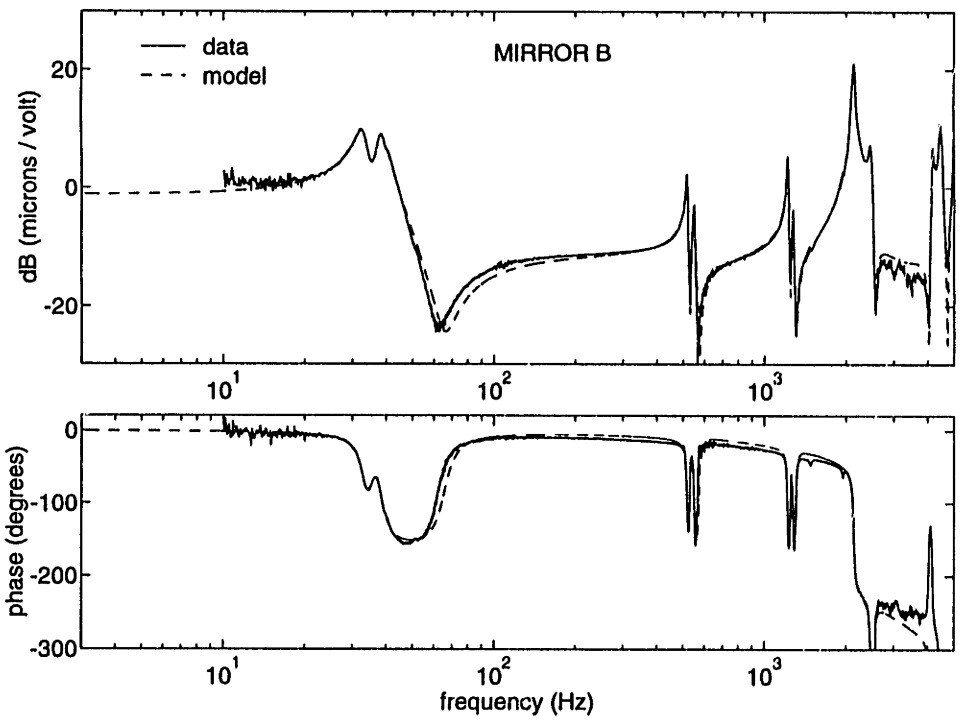

Figure 6.4: 12 mode curve fit of mirror B line of sight transfer function, in microns per volt, defining the actuator plant G_m.

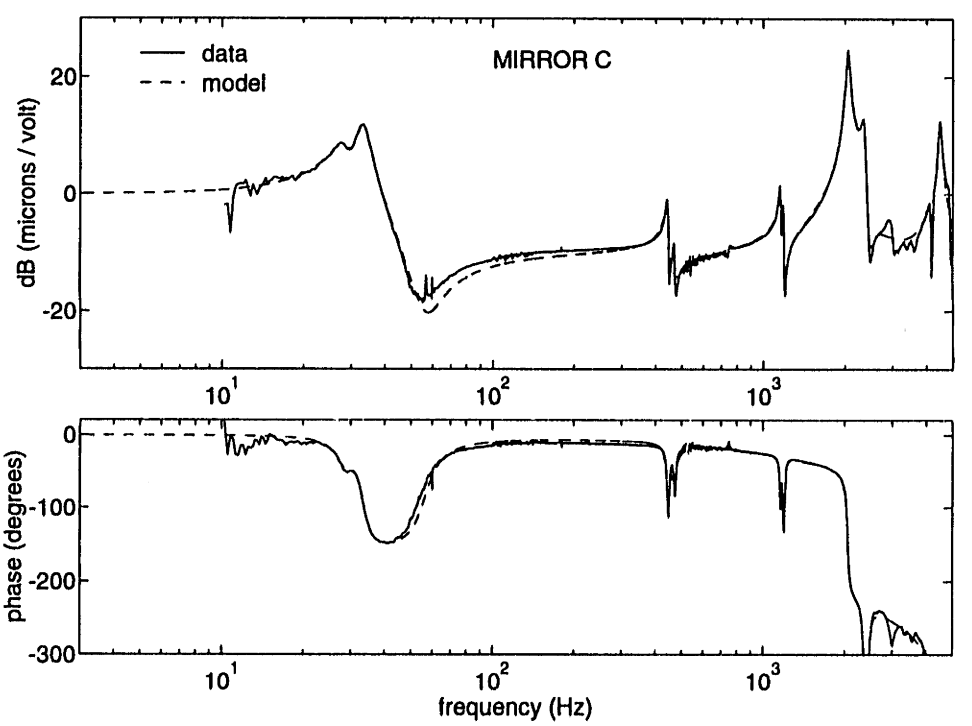

Figure 6.5: 10 mode curve fit of mirror C line of sight transfer function, in microns per volt. Transverse shear modes are much less strongly coupled than for mirror B, since the laser line of sight more closely aligns with the z axis of mirror C.

Based on these definitions, two models are now defined for use in design and performance evaluation of the compensators. The *design model* G_D is simply the full order system based on state space models of each element in the loop gain (except the compensator K)

$$G_D = G_h G_a = H_5 H_4 G_m G_a \tag{6.9}$$

The *evaluation model* G_E uses the measured actuator plant transfer function in place of G_m, and substitutes the exact expressions for the zero order hold and time delay (described below)

$$G_E = (H_5 H_4)_{exact} (G_m)_{msrd} G_a \tag{6.10}$$

Time Delay and ZOH: The time delay through the realtime computer was measured to be $1.6T_S$, where $T_S = 1/F_S$ is the sample period of the realtime computer. Of this, $T_S/2$ is due to the zero order hold on the plant output, and $\tau = (1.1)T_S$ is due to a pure time delay within the realtime computer. These two elements are modelled in the evaluation model G_E by their exact functions [23]

$$H_4 = e^{-s\tau} \qquad \text{(delay)} \tag{6.11}$$

$$H_5 = \frac{1}{T_S}\left[\frac{1 - e^{-sT_S}}{s}\right] \qquad \text{(ZOH)} \tag{6.12}$$

and in the design model G_D as first order systems using the Pade approximation

$$H_4 = \frac{1 - s\tau/2}{1 + s\tau/2} \qquad \text{(delay)} \tag{6.13}$$

$$H_5 = \frac{1}{1 + sT_S/2} \qquad \text{(ZOH)} \tag{6.14}$$

For mirror C, a second order Pade approximation for the time delay was used to improve phase of the model near the 1.2 kHz and 2.1 kHz modes.

Analog Filter Elements: The analog circuit elements consist of three low pass filters, one high pass filter, two gains and one second order notch filter. The analog circuit elements were modelled using simple first and second order state models for each component; Figure 6.7 is a plot of the analog circuit model G_a. The first order high pass filter H_1 has a corner frequency of 5 Hz, and attenuates DC and low

frequency drift of the accelerometers, which respond to subtle temperature variations induced by air currents. Line filter H_3 is an anti-alias filter with corner frequency of 165 Hz, placed at the input to the realtime computer A/D. Line filters H_6 and H_7 are smoothing filters at 31 and 34 Hz, respectively, placed at the input to the $\times 20$ amplifier and at the input to the piezoelectric actuators. These filters attenuate high frequency noise on the line introduced by the D/A of the realtime computer or by other electrical noise sources in the room. These filters were essential to improving the signal to noise ratio at the plant output. The choices of corner frequencies and gains of these elements was based on an iterative design of the LQG compensator, described in Section 6.4. The actual locations of the filters and gains in the loop were chosen to best improve the signal to noise ratio at the sensor output.

Design and Evaluation Models: The full order design model G_D is plotted in Figure 6.8 in comparison to the evaluation model G_E, showing excellent agreement. The mismatch below 10 Hz is due to extremely poor coherence in the transfer function because of low accelerometer signal and high sensor noise, but is also due to the damped modes of the test block that occur between 4.4 and 8.3 Hz. Zoomed transfer functions in this frequency range show reasonably close agreement between the two models. Table 6.2 summarizes the two models and their uses for control design and evaluation.

6.3.3 Disturbance Modelling

The disturbance model is based on open loop autospectra of the acceleration at the individual mirror locations. An 8^{th} order filter driven by white noise, as illustrated in Figure 6.9 for displacement and Figure 6.10 for acceleration, approximates the measured autospectrum. The model is expressed in state space as

$$\begin{aligned} \dot{x}_f &= A_f x_f + L_f \xi \\ y_f &= C_f x_f \end{aligned} \tag{6.15}$$

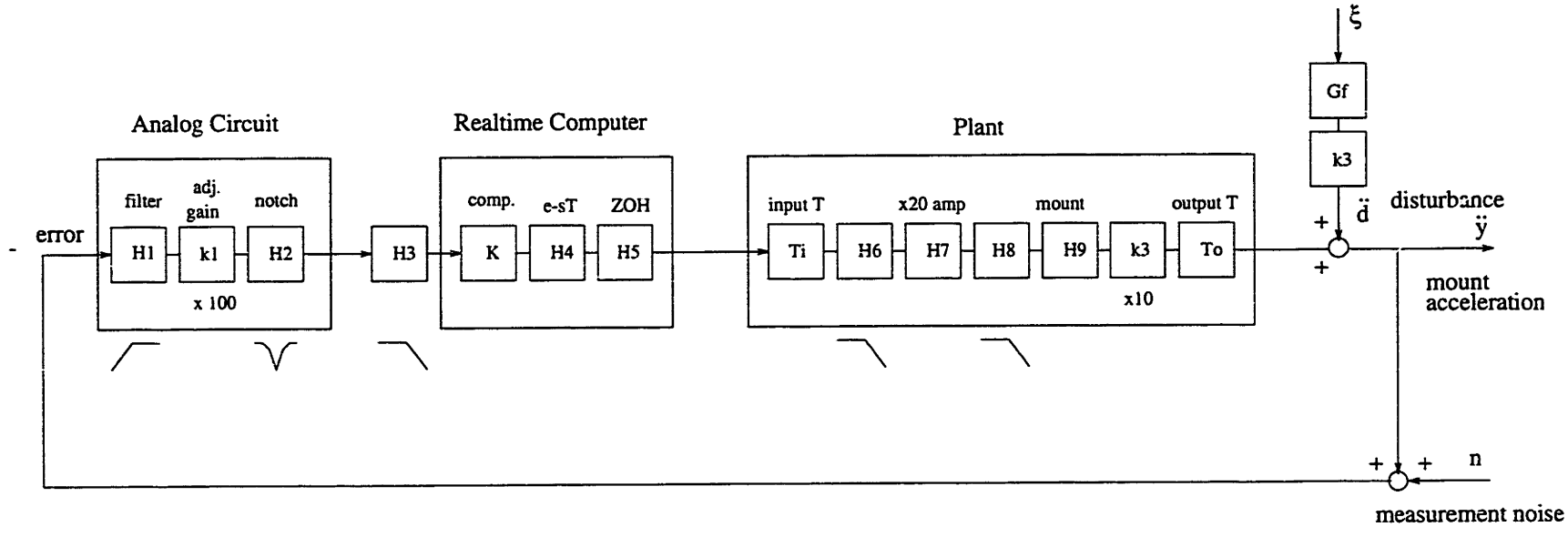

Figure 6.6: Block diagram for acceleration feedback for active isolation.

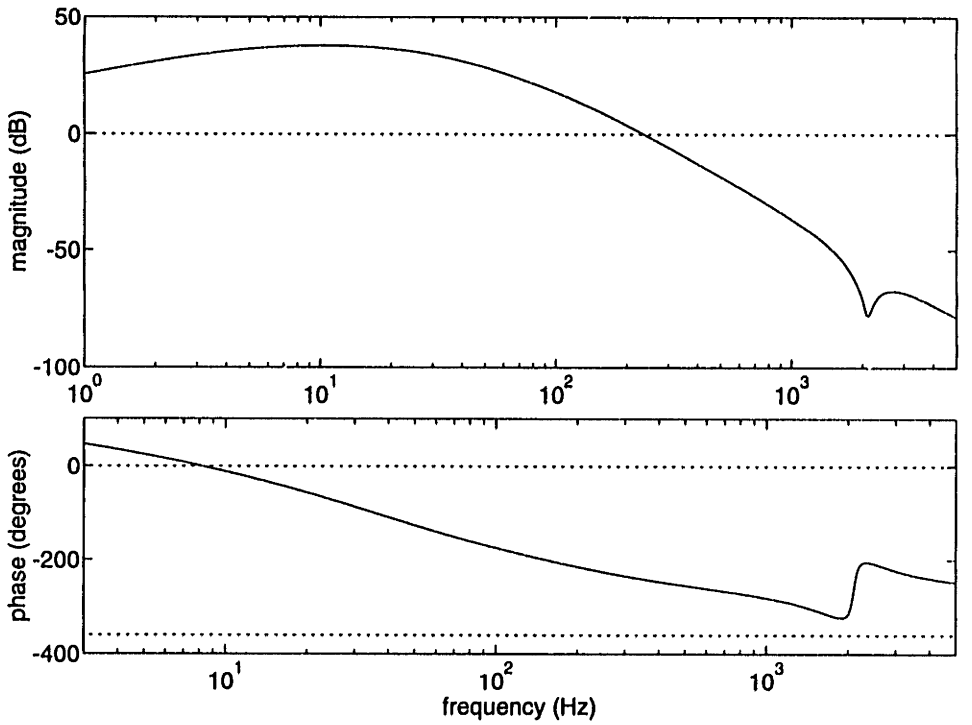

Figure 6.7: Analog circuit elements G_a remove burden of large dynamic range, high gain and high frequency notch from realtime computer. Transfer function G_a implemented using RC and op-amp circuits.

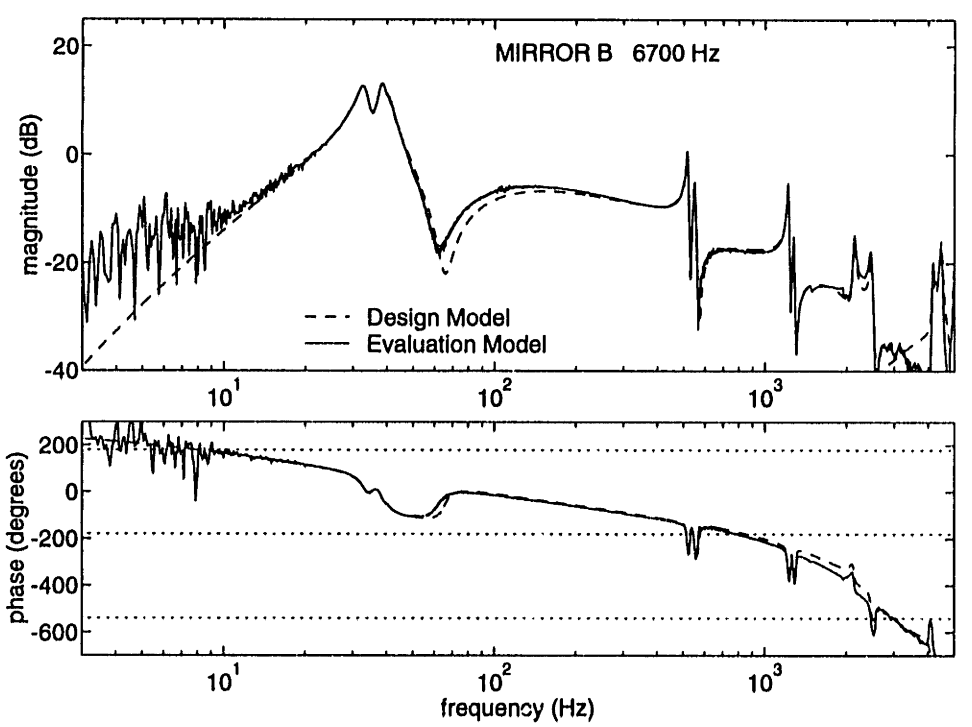

Figure 6.8: Comparison of full order design model G_D and the evaluation model G_E, which is based on the experimental measurement of the isolator plant model and exact functions of ZOH and time delay.

Table 6.2: Definitions and uses of the design and evaluation models.

Model	Description	Use
Design Model G_D	46 state model of all elements in Figure 6.2	to design compensator K and to evaluate reduced order compensator performance.
Evaluation Model G_E	exact function of ZOH and time delay, and measured actuator plant model G_m. Analog circuit model G_a same as design model.	to evaluate compensator K on the experimental plant before implementation; to asses model error.

where it is assumed that $E[\xi(t)\xi(\tau)] = \delta(t-\tau)$, and that the output matrix C_f can be chosen for output of displacement $y_f = d$ or acceleration $y_f = \ddot{d}$. Neither the acceleration nor the displacement model exhibits a feedthrough term. The disturbance transfer function G_f is shown in the block diagram of Figure 6.6, where the disturbance $\ddot{d}$ is modelled as a process noise that enters at the plant output. The model autospectra from Eq. 6.15, plotted in Figures 6.9 and 6.10, are scaled to match the disturbance energy in the data in the frequency range of 10 to 500 Hz.

Weighted Disturbance Filter: Overplotted in Figure 6.10 is a weighted filter model used for loopshaping of the model based compensator in the LQG design. The weighted model is used below as a design parameter for increasing the compensator gain in chosen frequency ranges. Because the testbed performance metric requires displacement minimization, the weighted function (chosen iteratively in the LQG design) emphasizes acceleration at lower frequencies. The 8^{th} order weighted disturbance filter dynamics are

$$\begin{aligned} \dot{x}_w &= A_w x_w + L_w \xi \\ y_w &= C_w x_w \end{aligned} \tag{6.16}$$

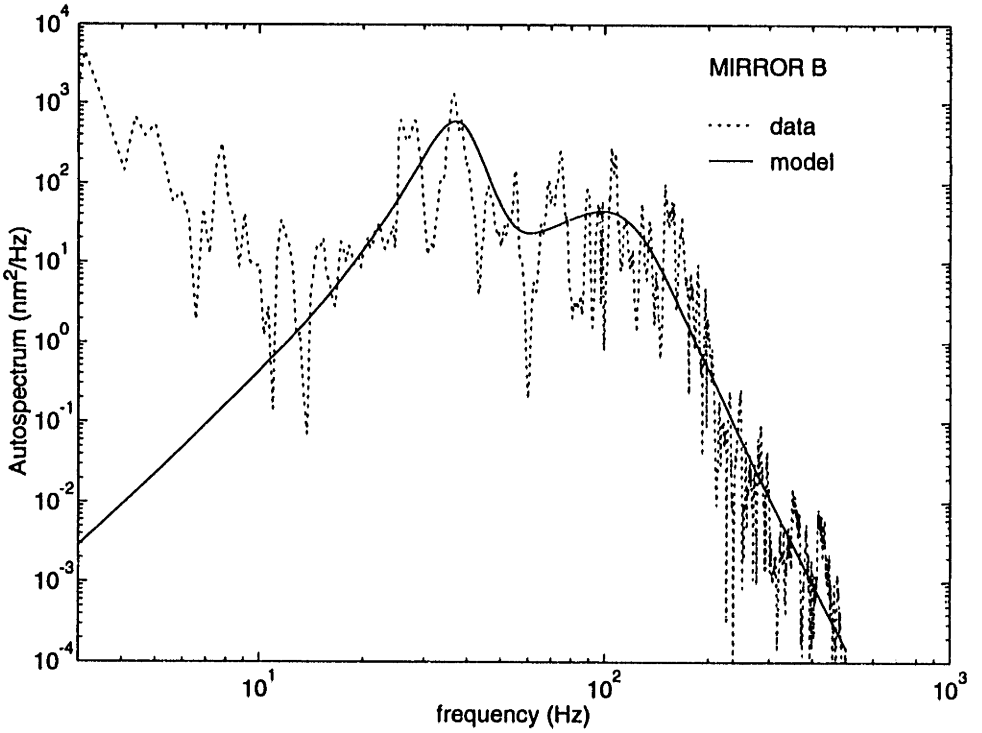

Figure 6.9: 8^{th} order model of disturbance at mirror B line of sight compared to accelerometer data, converted to displacement. Sensor noise is strong below 20 Hz.

6.4 Compensator Design

Compensators were designed based on the full 46^{th} order design model model G_D. Originally, only the hardware plant model G_h was included in the design plant model. The resulting compensators were characterized by high gain (60 dB), large dynamic range (necessary to force the acceleration transfer function, which increases with a slope of s^2, to roll off at s^{-1}), and notching of strongly coupled plant modes at 2.1 kHz. These compensators could not be implemented in the realtime computer, given limits on sample rate and dynamic range. Accordingly, the gain, high frequency notch and low pass filters (a total of three first order models) typical of the compensators were built in analog using op-amp circuits and simple RC networks. The LQG design method was used to select the "natural" dynamics of these analog filters, which could be placed anywhere in the circuit, for purposes of anti-aliasing, output smoothing of the D/A control output signal, and signal amplification.

The 6^{th} order analog circuit plant G_a was included in an augmented design plant

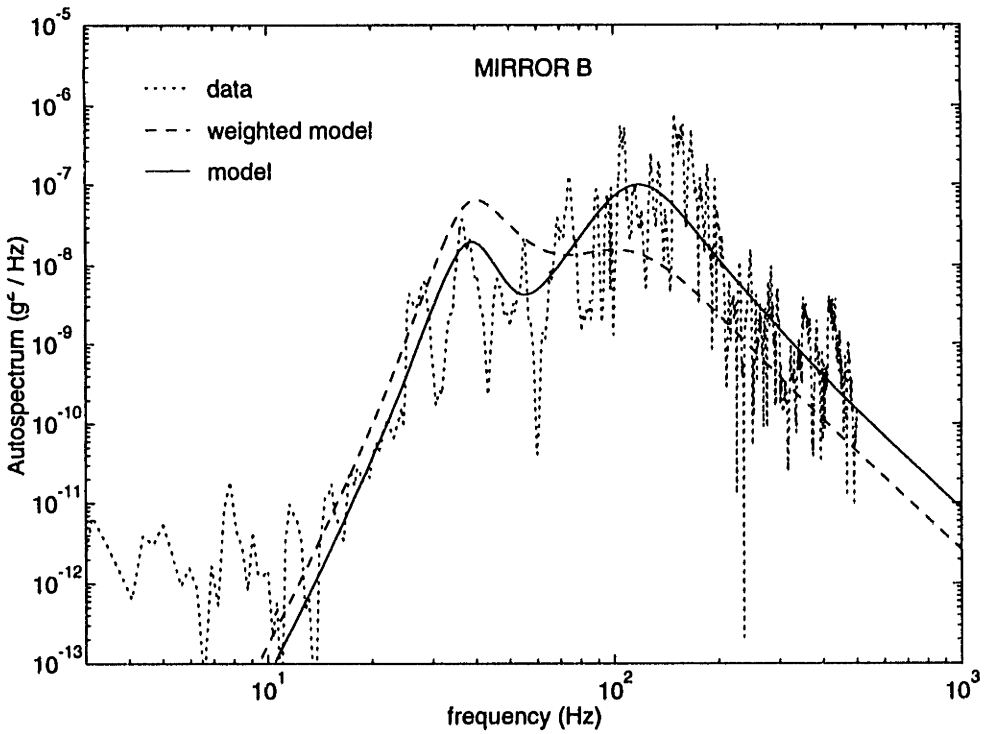

Figure 6.10: Model vs data of the acceleration spectrum at mirror B, plotted with the weighted disturbance spectrum used for loopshaping in the LQG design.

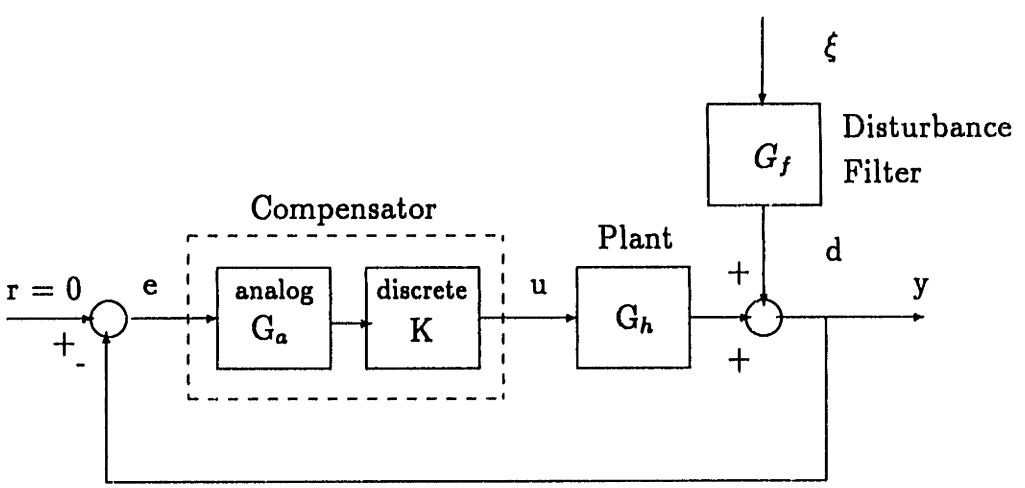

Figure 6.11: Compensator is comprised of analog and discrete elements. LQG methods are used to design discrete K based on new plant G_aG_h. Analog plant G_a is sixth order.

model G_D, and a set of compensators K were redesigned based on the new plant, as illustrated in Figure 6.11. These new compensators were characterized by low gain and low dynamic range, and could be easily reduced (in terms of model order and high frequency dynamics) because the 2.1 kHz notch was implemented in analog. Through a process of iteration, the analog circuit was finalized (and remained constant throughout the set of acceleration feedback experiments). The compensators K were designed for loop stability and loop shaping to increase gain in frequency bands of high disturbance energy. The compensator design and evaluation models presented below are shown for the continuous time compensator; for laboratory implementation these compensators are discretized using the Tustin transformation with prewarping, which induces small differences in gain and phase, which only affect the closed loop performance slightly.

6.4.1 LQG Design

The control penalty used in the LQG problem statement requires a penalty on output variables and input control. In this thesis, the output acceleration is frequency weighted in the estimator design step through the use of the weighted disturbance filter model (A_w, B_w, C_w). Similarly, a frequency weighted function of the control u is provided by the filter

$$\begin{aligned} \dot{x}_w &= A_w x_w + B_w u \\ u_w &= C_w x_w + D_w u \end{aligned} \tag{6.17}$$

The weighted input u_w is penalized in the regulator cost function. Figure 6.12 illustrates the control weight used for mirror B control designs, in order to force a decrease in the compensator gain at low frequencies, which was necessary to prevent amplifications of DC bias voltages in the circuit.

An augmented plant model is assembled which includes states x_p of to the design plant model, the weighted disturbance states x_w, and states x_u representing weighted control. The augmented state vector is $\tilde{x} = [x_p \ x_w \ x_u]^T$ with state dynamics

$$\dot{\tilde{x}} = \tilde{A}\tilde{x} + \tilde{B}u + \tilde{L}\xi$$

$$\tilde{y} = \tilde{C}\tilde{x} + \tilde{D}u + \tilde{N}\theta \tag{6.18}$$

where ξ is assumed to be a white noise process with covariance $\Xi = 1$, θ is sensor noise with covariance Θ, and the plant output $\tilde{y}$ is a two-element vector of plant acceleration and weighted control

$$\begin{aligned} \tilde{y} &= \begin{bmatrix} \ddot{y} \\ w \end{bmatrix} \\ &= \begin{bmatrix} \tilde{C}_a \\ \tilde{C}_w \end{bmatrix} \tilde{x} + \begin{bmatrix} 0 \\ \tilde{D}_w \end{bmatrix} u \end{aligned} \tag{6.19}$$

The design plant feedthrough term is zero, a convenient modelling assumption but one which is not required. The regulator cost function is expressed as

$$J = \int_0^\infty \left[\ddot{y}^T \ddot{y} + \rho u_w^T u_w \right] dt \tag{6.20}$$

where

$$\ddot{y}^T \ddot{y} = \tilde{x}^T \tilde{C}_a^T \tilde{C}_a \tilde{x} \tag{6.21}$$

and

$$u_w^T u_w = \tilde{x}^T \tilde{C}_w^T \tilde{C}_w \tilde{x} + \tilde{x}^T \tilde{C}_w^T \tilde{D}_w u + u_T \tilde{D}_w^T \tilde{D}_w u \tag{6.22}$$

Using these expressions the regulator cost function becomes

$$J = \int_0^\infty \left[\tilde{x}^T Q \tilde{x} + \tilde{x}^T S u + u^T R u \right] dt \tag{6.23}$$

where the state, control and cross-penalty matrices are defined by

$$\begin{aligned} Q &= \tilde{C}_a^T \tilde{C}_a + \rho \tilde{C}_w^T \tilde{C}_w \\ R &= \rho \tilde{D}_w^T \tilde{D}_w \\ S &= \rho \tilde{C}_w^T \tilde{D}_w \end{aligned} \tag{6.24}$$

Standard functions in the Matlab Robust Control Toolbox (Mathworks, Inc., 1988) are used to determine the Kalman filter gain H, compensator dynamics A_c, and output gain G for the model based compensator, expressed in state space form as

$$\begin{aligned} \dot{\hat{x}} &= A_c \hat{x} - He \\ u &= -G\hat{x} \end{aligned} \tag{6.25}$$

where the error $e = r - \ddot{y}$ is the difference between the output and the regulator command $r = 0$, and the compensator dynamics are

$$A_c = \tilde{A} - H\tilde{C}_a - \tilde{B}G \tag{6.26}$$

The model based compensator transfer function is

$$K(s) = \frac{u(s)}{e(s)} = G(sI - A_c)^{-1}H \tag{6.27}$$

Acceleration, instead of plant displacement, was chosen for the cost penalty because initial compensators K designed using a displacement penalty were themselves unstable. While implementable, it was decided to pursue a design procedure that did not lead to unstable compensators. Unstable compensator designs did not occur when acceleration (the actual plant output) was penalized in the regulator cost function.

Design Parameters: The design parameters used in the compensator design process fall into two broad categories: adjustment of sensor noise covariance Θ and frequency shaping of the disturbance spectrum in the estimator design; and secondly, adjustment of control penalty ρ and frequency weighting of control in the regulator design. The design procedure was to iterate on values of ρ and Θ until reasonable compensators were designed, then the ratio Θ/ρ was fixed. The designs then progressed by iteratively adjusting the control penalty ρ and by adjusting the weighting of the disturbance spectrum. In the final step, control penalty was added to limit compensator gain at low frequency.

The design and predicted performance of one high gain compensator for mirror B is documented below. Later, the measured performance of this control design is documented for the rigid test block and for the testbed.

6.4.2 Compensator Reduction and Evaluation

Compensator: The full and reduced order compensators (design CB7F) for mirror B at 6700 Hz are compared in Figure 6.13. The reduction was performed in two steps: first, a balanced realization of the compensator identified the matrix Hankel

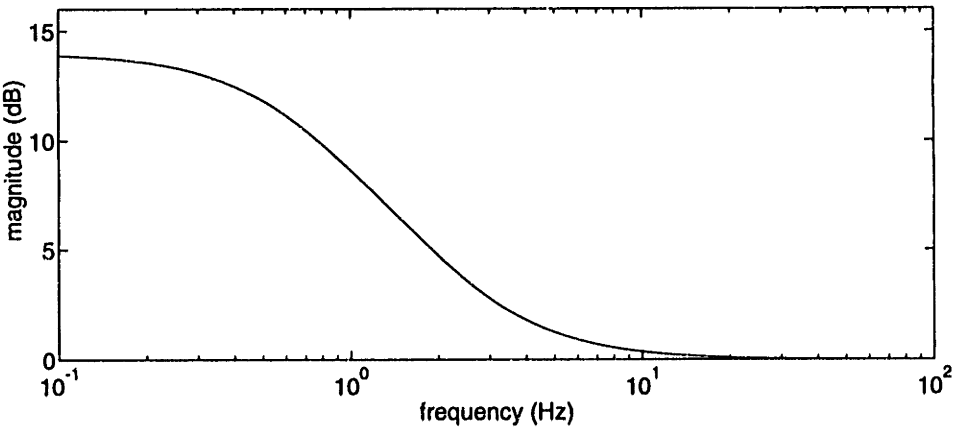

Figure 6.12: Control weight used to limit low frequency gain of the compensator.

singular values, and states with small singular values were reduced out of the model. Secondly, states with pole frequencies above 1 kHz were reduced from the model. A compensator order of 14 states was required in order to preserve the zero locations of the 550 Hz compensator notches. The reduction procedure leads to a small loss in gain and phase accuracy near crossover (330 Hz), as well as to a nonminimum phase compensator zero. The latter was not a performance or stability constraint, and did not occur for the majority of compensator designs. The total compensator KG_a, which includes the 6^{th} order analog filters, is plotted in Figure 6.14. Note the notch at 2.1 kHz provided by the analog filter compensator G_a.

Loop Gain: The loop gain in Figure 6.15 is obtained by applying the full and reduced order compensators to the design model G_D. Compensator notches gain stabilize the modes at 550 Hz, just above the 330 Hz crossover frequency, while plant modes at 1 kHz and 2.1 kHz are phase stabilized by the full order model. For the reduced order model, the 2.1 kHz mode is gain stabilized, and small losses in gain and phase margin are evident. The analog notch was placed just below the 2.1 kHz mode, using the phase lead of the notch to retain phase stabilization of this mode, should the gain of this lightly damped mode ever approach 0 dB. The fidelity of the design model is illustrated in Figure 6.16, which compares the loop gain using the reduced order compensator for both the design model G_D and the evaluation model G_E.

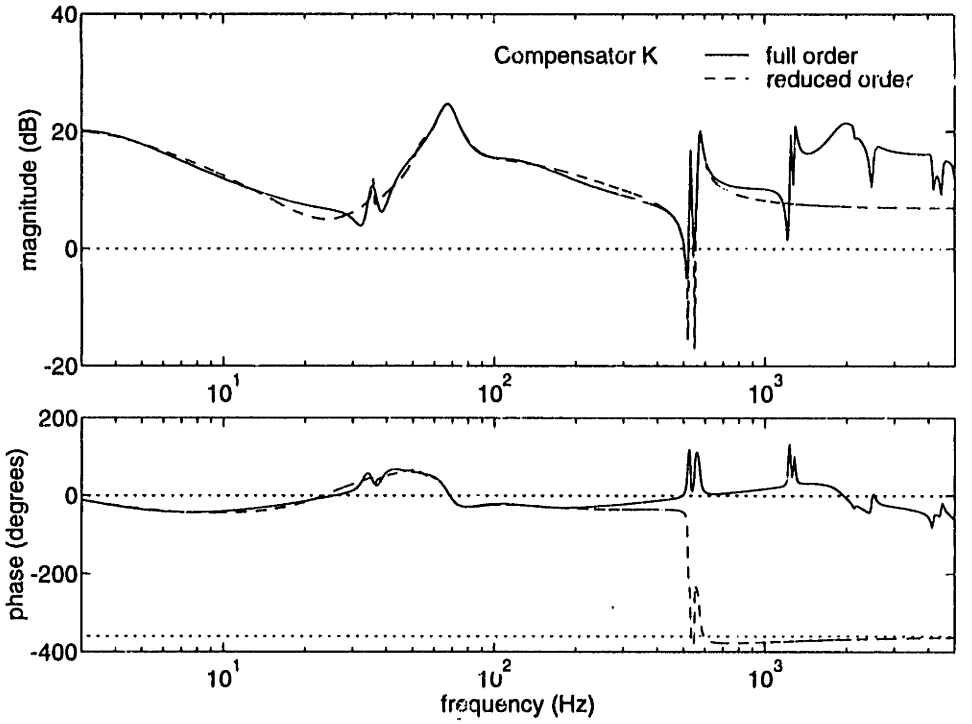

Figure 6.13: Full and reduced order compensators K for CB7F. Reduction from 46 states to 14 states induces small gain and phase errors near crossover, and results in nonminimum phase compensator zero at 550 Hz.

Model of Closed Loop Sensitivity: Figure 6.17 compares the predicted closed loop sensitivity using the design model G_D with the full and reduced order compensators. The reduction in gain and phase margin near crossover leads to an increase in closed loop sensitivity $S(s)$ in this frequency range. Note that for both compensators, the effects of the 1.2 kHz and 2.1 kHz modes are stabilizing, since these modes are phase stabilized. Figure 6.18 illustrates a model of the open and closed loop autospectra of acceleration (converted to displacement) at the mount, predicting a 13.4 dB improvement. The disturbance model is based on the state model (A_f, B_f, C_f) from Eq. 6.15.

6.4.3 Compensator Implementation

The continuous time compensator K shown above was converted to discrete time using the Tustin transform, with prewarping set at 550 Hz in order to correctly match the zeros and poles of the lightly damped compensator dynamics in this range.

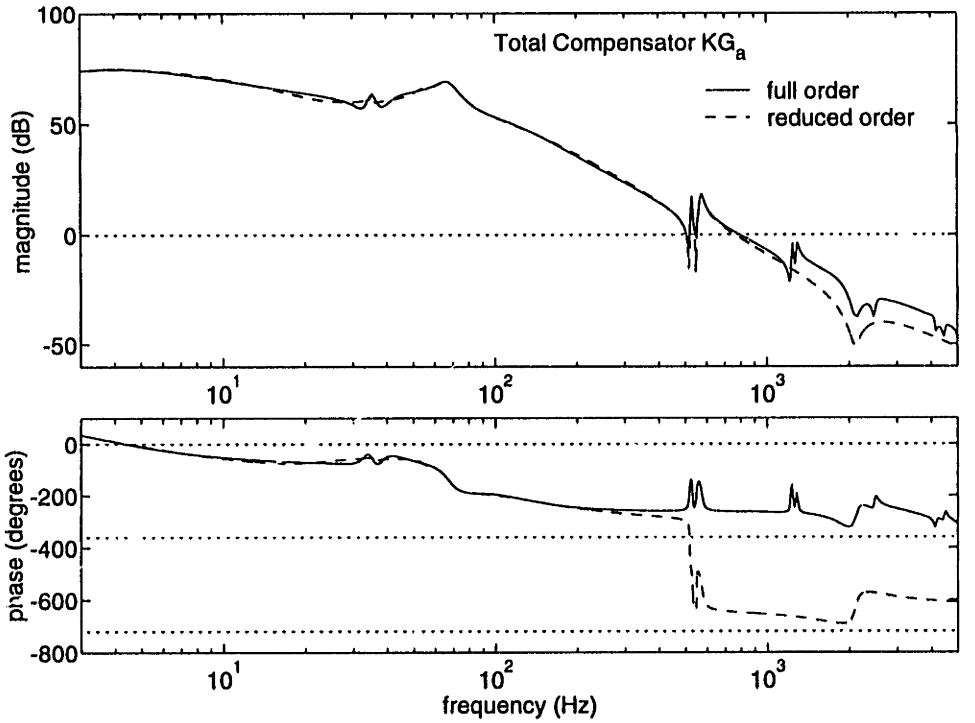

Figure 6.14: Total compensator KG_a (includes analog elements), reduced and full. Total compensator order is 20 states, of which 6 are implemented in analog.

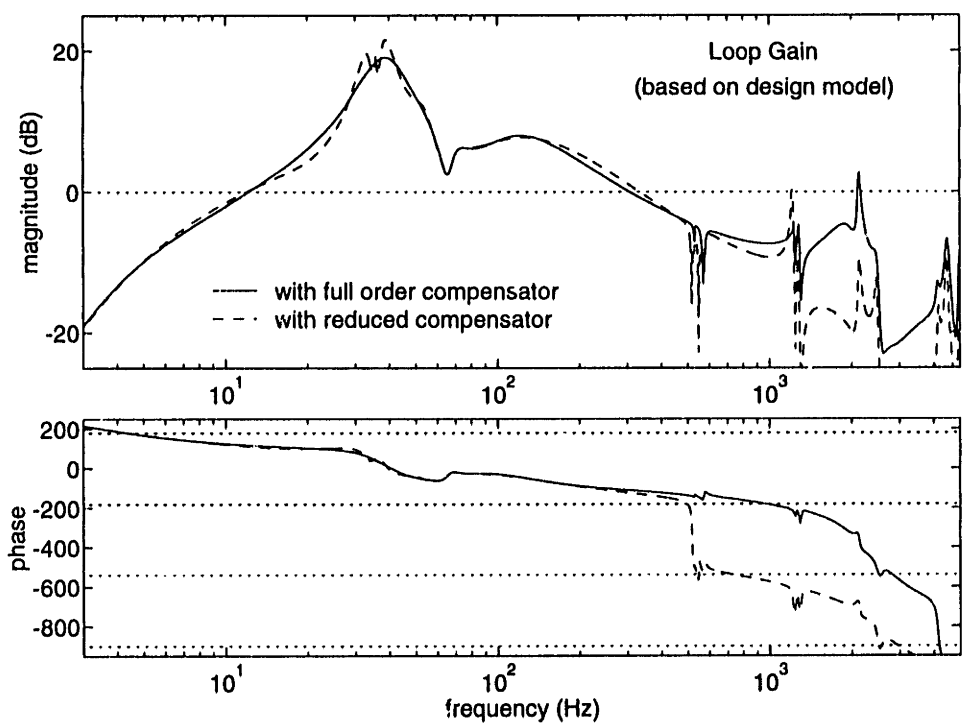

Figure 6.15: Loop transfer function for mirror B (CB7F, 6700 Hz). Full and reduced order compensator applied to design model.

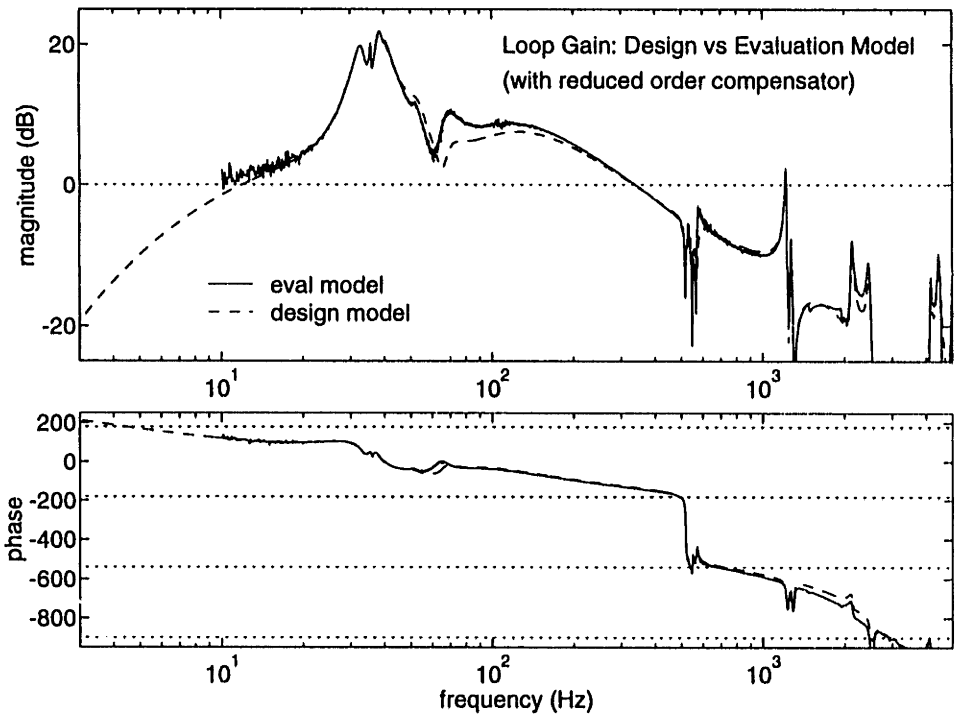

Figure 6.16: Loop transfer function for mirror B (CB7F, 6700 Hz). Reduced order compensator applied to G_D and G_E. 550 Hz modes are gain stabilized; 1.2 kHz modes are phase stabilized. Both gain and phase stabilization for 2.1 kHz mode.

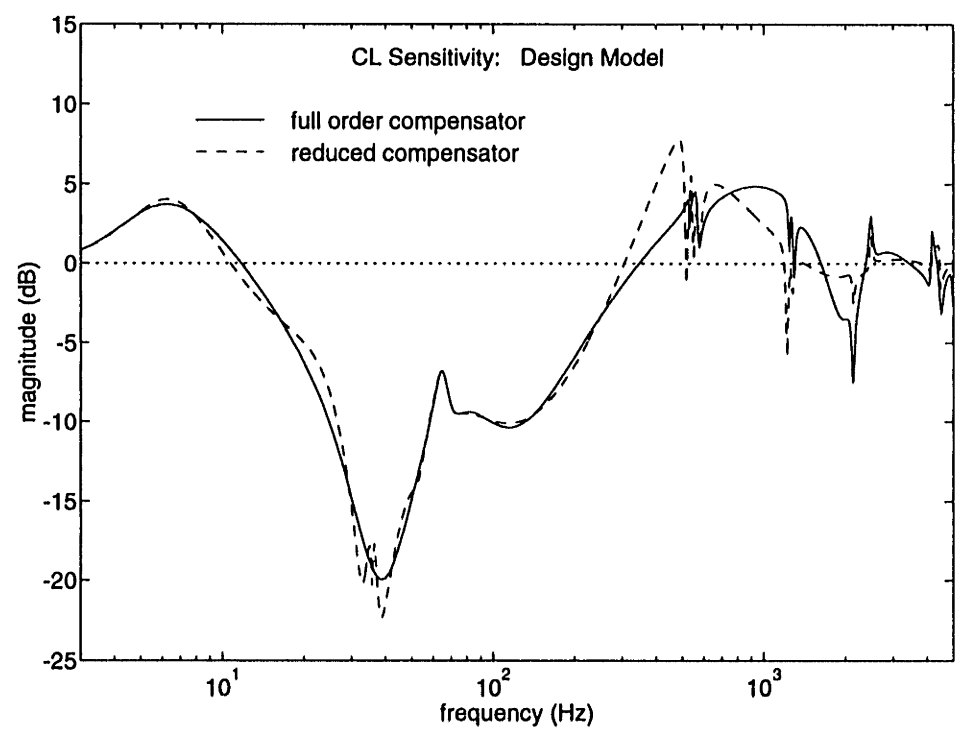

Figure 6.17: Closed loop sensitivity, full and reduced order compensators evaluated with design model G_D.

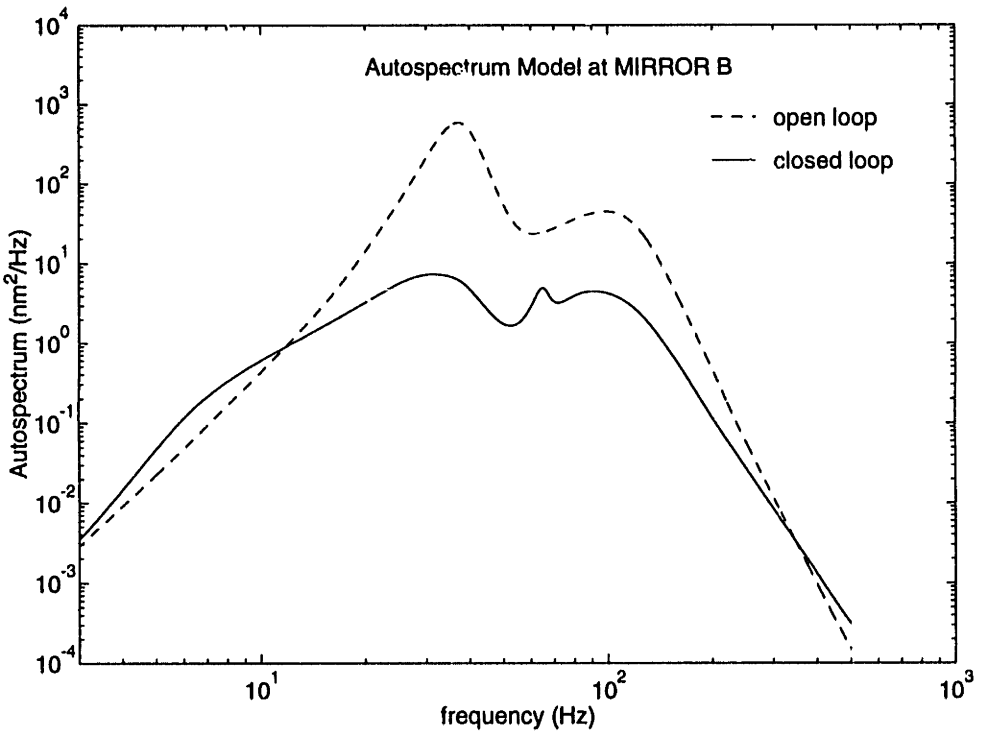

Figure 6.18: Disturbance model, open loop and closed loop (reduced compensator CB7F and design model). OL and CL disturbance models agree to measured data to within 1 dB in RMS 10-500 Hz. Compensator provides 13.4 dB reduction over 10 - 500 Hz.

Compensator transfer functions, measured through the input and output channels of the realtime computer, were checked against the model. The overall loop gain (including the compensator) was measured in the lab and compared to the design and evaluation models, as a final check before the feedback loop was closed.

6.5 Results of Acceleration Feedback

6.5.1 Rigid Block Mounting

LQG methods were used to design compensators for mirror B for the test block, at sample rates of 6700 Hz and 3100 Hz. The faster sample rate was found to be the maximum at which the realtime computer would operate for a compensator of 14 states (the anticipated compensator order number), while the lower sample rate was

required to handle two compensators of this order, with the additional input/output operations of the D/A converter.

Figures 6.19 and 6.20 compare the measured closed loop sensitivity functions with the prediction based on applying the reduced order compensator K to the design model G_D, for both 6700 Hz and 3100 Hz sample rates. The close agreement verifies the fidelity of the analytical design model G_D. The increase in the measured sensitivity below 10 Hz is due to interaction with the damped modes of the test block. The experimental sensitivity functions were obtained by injecting an artificial white noise disturbance at the sensor output, and by measuring the transfer function between this signal and the closed loop output.

The performance of the analytical model was calculated by applying the predicted closed loop sensitivity $S(s)$ to the measured disturbance autospectrum at mirror B:

$$\Phi_{\ddot{y}}^{CL}(s) = |S(s)|^2 \Phi_{\ddot{y}}^{OL}(s) \tag{6.28}$$

The open and closed loop autospectra were converted to displacement and the RMS performance improvement was tabulated over the frequency range of 10 to 500 Hz. A family of compensators, for different levels of control authority, is plotted in Figure 6.21. At lower values of ρ no reduced order compensators resulted in stable plants when applied to the design model G_D. The instability always occurred at 500 Hz (the closed loop sensitivity function became very large) due to a loss in gain and phase margin incurred during the compensator reduction step.

6.5.2 Flexible Testbed Mounting

The families of compensators, for 6700 and 3100 Hz sample rates, were re-implemented on the isolator when it was mounted to the flexible testbed at point B in Figure 4.1. The 6700 Hz compensators were stable for the truss mounting, but a reduction in gain and phase margin at 600 Hz led to a less stable design and to an increase in the closed loop sensitivity magnitude in this frequency range. Figure 6.22 compares $S(s)$ when mounted to the testbed, versus the design model prediction. The testbed data was measured by injecting an artificial white noise disturbance at the plant output.

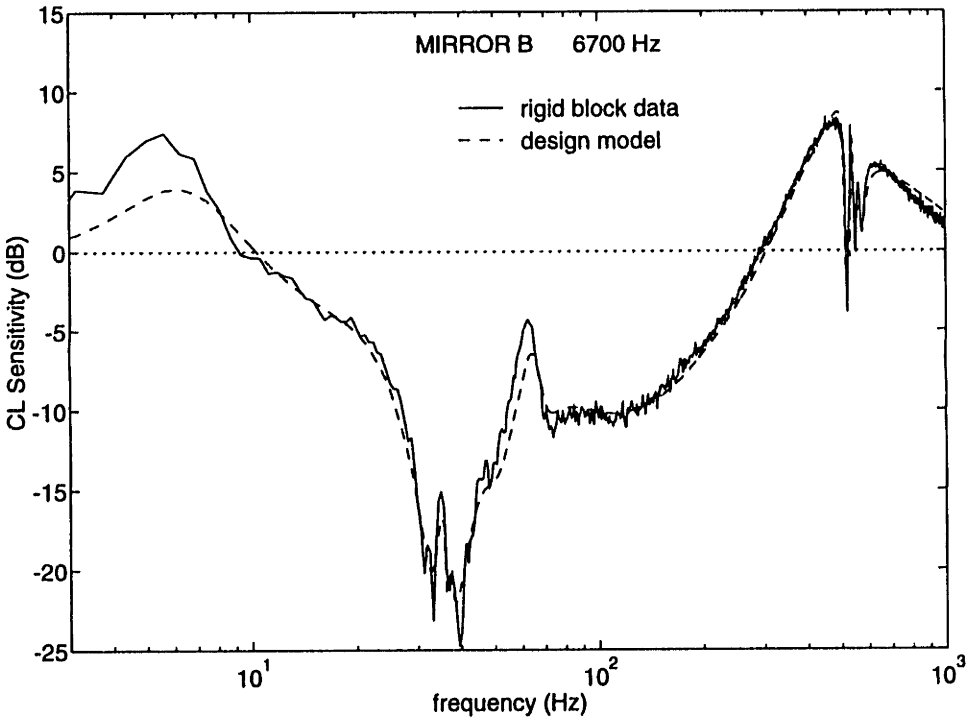

Figure 6.19: Closed loop sensitivity measured on rigid block for CB7F. Data closely agree with prediction based on design model G_D. Increase in $S(s)$ below 10 Hz due to damped resonance in test block.

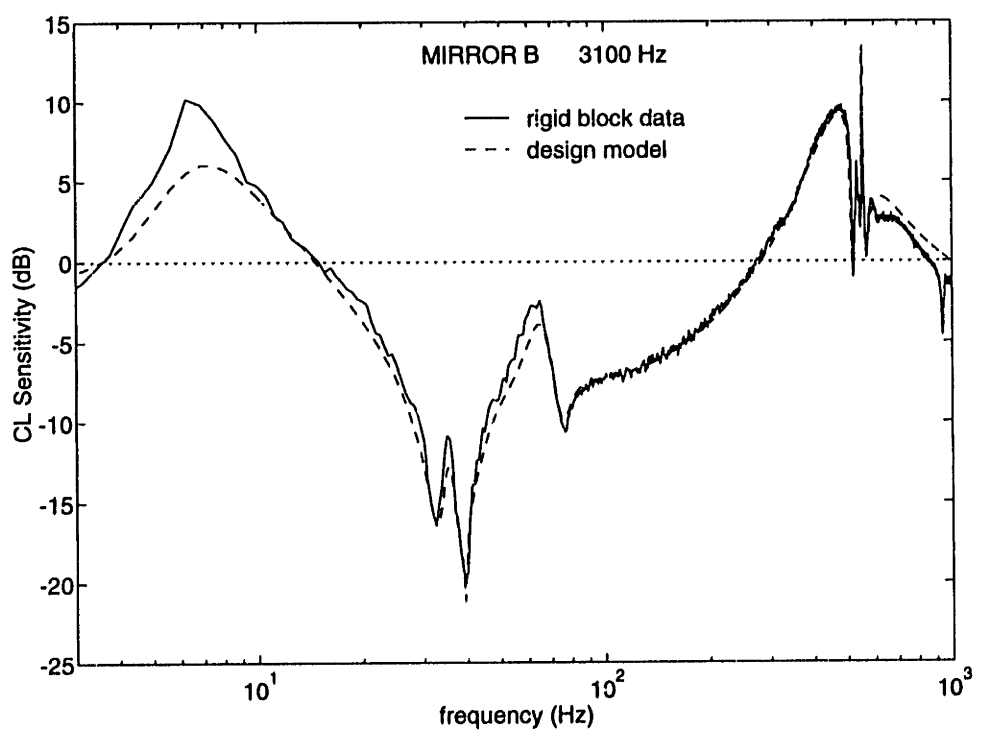

Figure 6.20: Compensator CB8E designed for mirror B on the rigid block at a sample rate of 3100 Hz. Compensator remains 14^{th} order.

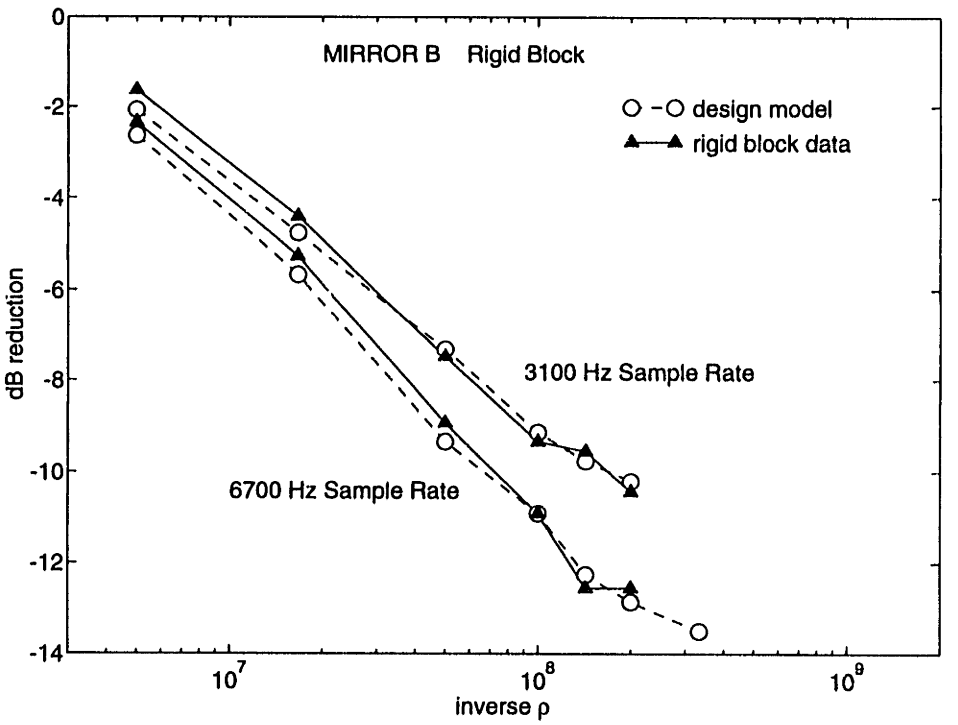

Figure 6.21: Performance summary for mirror B results on test block, versus prediction based on design model. Reduction in dB (RMS, 10 to 500 Hz) obtained by applying $S(s)$ (measured and modelled) to measured disturbance autospectrum on testbed at mirror B.

The same sensitivity function was measured when the standard disturbance source for the testbed was used.

The increase in sensitivity near 600 Hz is due to the frequency and damping shift of the lightly damped 550 Hz modes, as shown in the open loop transfer function in Figure 5.22 in Chapter 5. Figure 6.23 compares the new evaluation plant model G_E (based on testbed actuator measurement G_m) with the design model G_D, clearly showing the change in modal damping and frequency of the 550 Hz modes. These modes correspond to transverse blade flexure modes that couple with the base flexibility. Although the plant modes have changed, the lightly damped compensator modes remain at 550 Hz. Observe that below 10 Hz, the model and data agree more closely than they did for the rigid block tests, since the damped 8 Hz modes of the test block are absent, and the testbed exhibits no flexibility below 24 Hz (except for suspension modes near 2 Hz).

Figure 6.24 compares the performance of compensators for mirror B on the testbed,

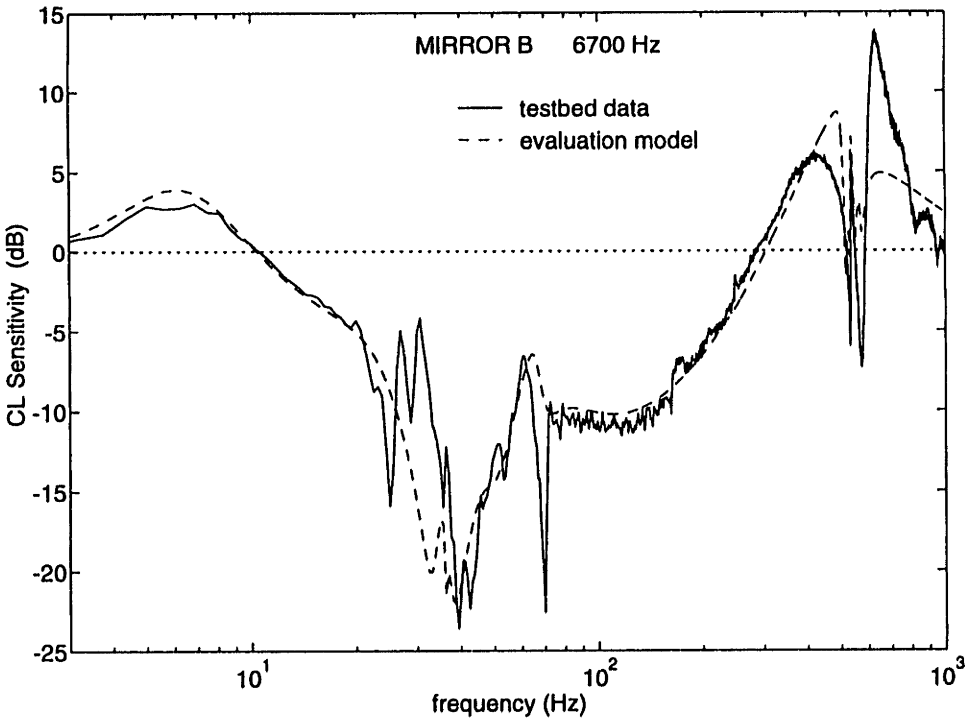

Figure 6.22: Closed loop sensitivity for testbed vs design model (with compensator CB7F). Flexible modes affect gain near 30 - 60 Hz; shift in 550 Hz modes leads to increase in sensitivity.

rigid block and for the design model G_D. The agreement is quite good despite the shift in 550 Hz modes. The testbed results are slightly inferior to the rigid block tests, due primarily to a reduction in plant gain between 20 and 40 Hz that is a result of base flexibility.

Performance of 3100 Hz Compensators: The family of 3100 Hz compensators was also implemented for the testbed mounting, but with less success. Figure 6.25 plots the dB performance improvement of these compensators for the design model, rigid block and testbed mountings. High gain compensators were unstable on the truss, because the compensator modes themselves at 550 Hz drove the closed loop plant unstable. Less phase margin was available in these designs due to the lower sampling rate and due to constraints imposed by the necessity to reduce the model order of the compensator.

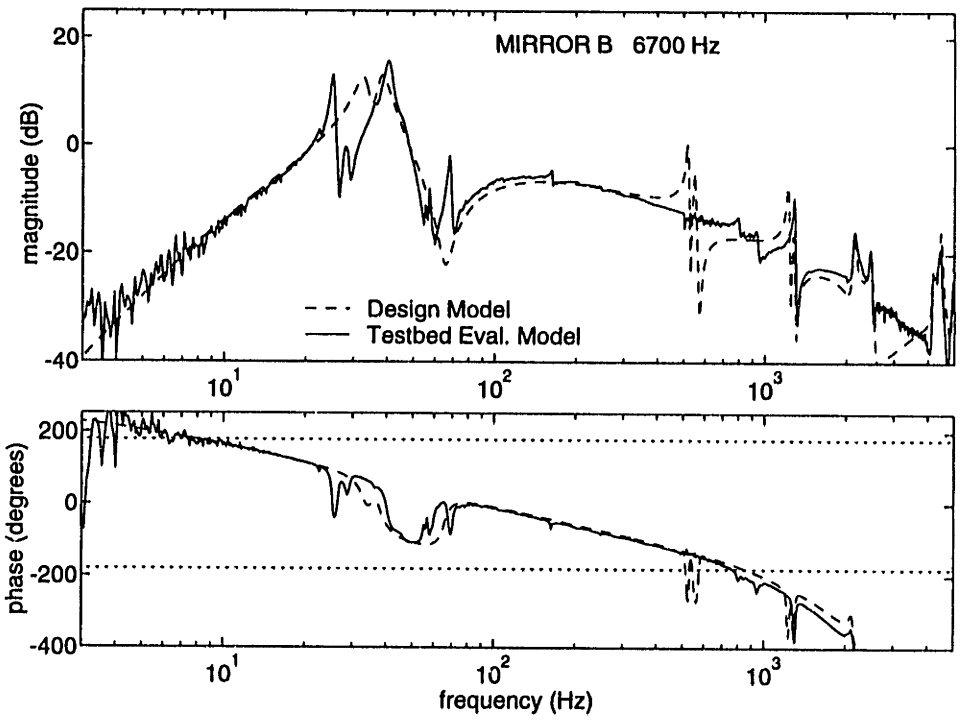

Figure 6.23: Design model G_D vs evaluation model G_E (using actuator transfer function G_m measured on testbed). Modes at 550 Hz are shifted and damped, due to coupling with base flexibility. Mode at 1.2 kHz has also shifted, probably due to handling.

Updated Design Model G_D: The design model G_D was updated as shown in Figure 6.26, by modifying the frequency and damping of the 550 Hz modes. Compensators for 6700 and 3100 Hz were redesigned using the new plant model, and compensation of the shifted modes was avoided by reducing all modes above 500 Hz from the reduced order compensators. A successful 3100 Hz closed loop sensitivity is illustrated in Figure 6.27, and the performance of a new family of 3100 Hz compensators is plotted in Figure 6.28. Much higher gains and dB reduction are obtained, since compensation of the lightly damped modes was no longer required. Also, compensator order was reduced significantly, to between 8 and 12 states. The reduction step was much easier since effort was no longer required to maintain the correct frequency of the zeros of the compensator at crossover, because notching of these modes was not retained in the new reduced order compensator design.

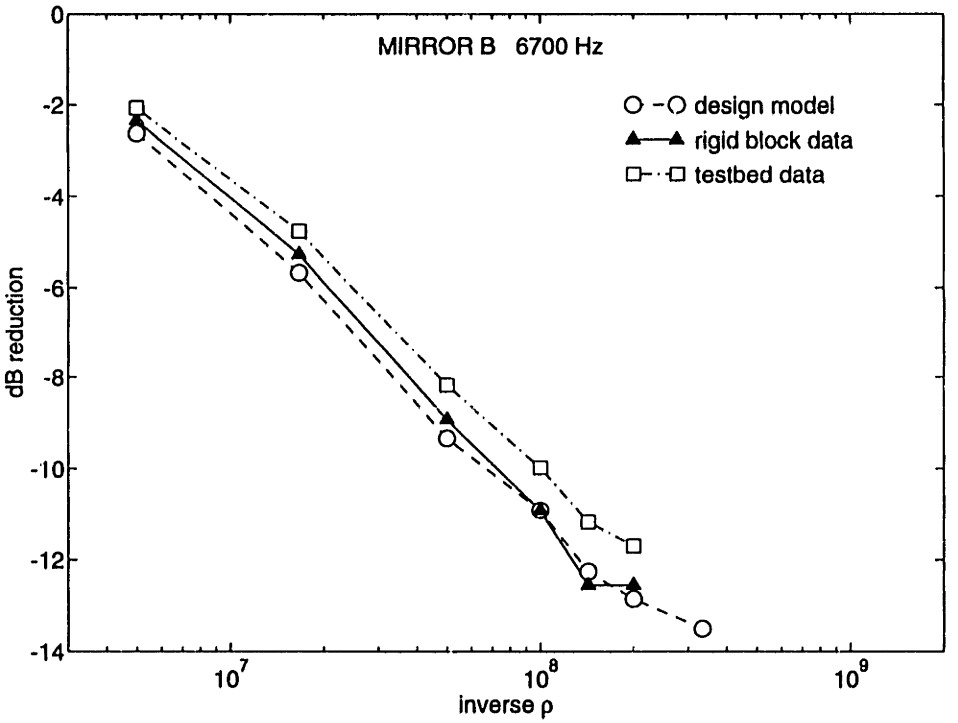

Figure 6.24: Family of compensators implemented for mirror B on testbed at 6700 Hz. Testbed data show only small performance loss compared to rigid block, mostly due to gain loss in 25-40 Hz range.

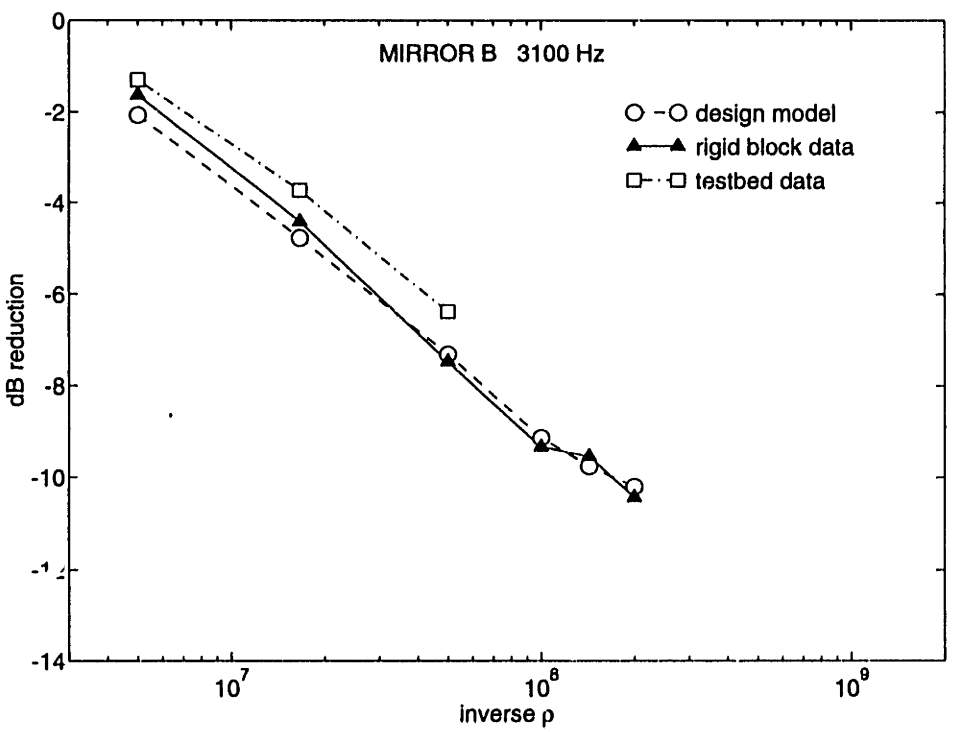

Figure 6.25: Family of compensators implemented for mirror B on testbed at 3100 Hz. Testbed implementation unstable for low ρ due to shift in plant modes. Compensator modes at 550 Hz caused instability.

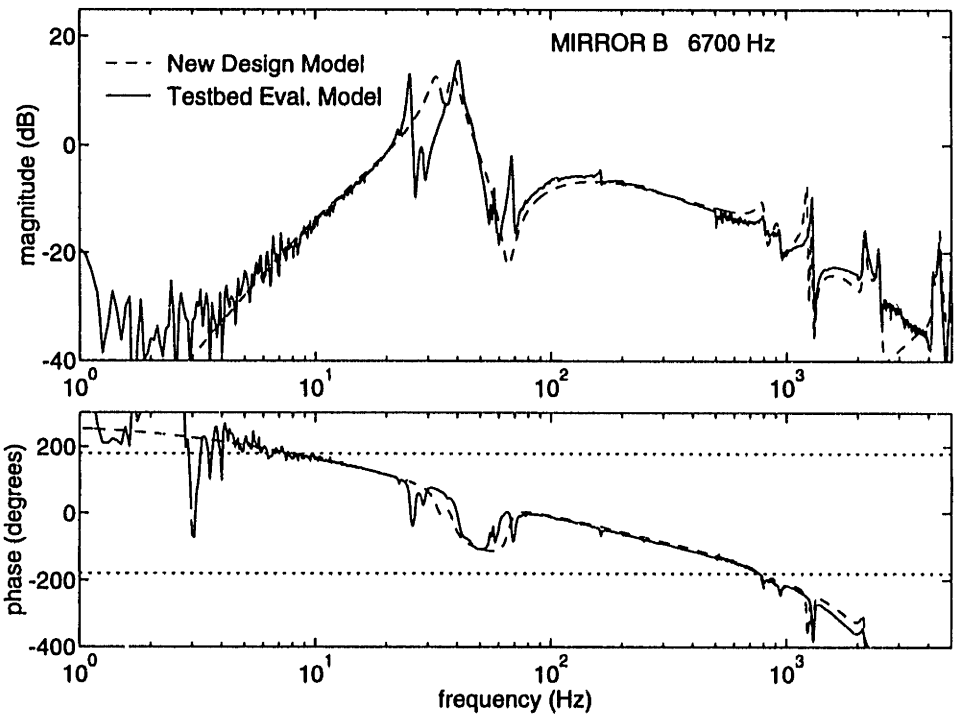

Figure 6.26: Updated design model G_D vs evaluation model based on testbed actuator transfer function G_m. Model update based on measured data.

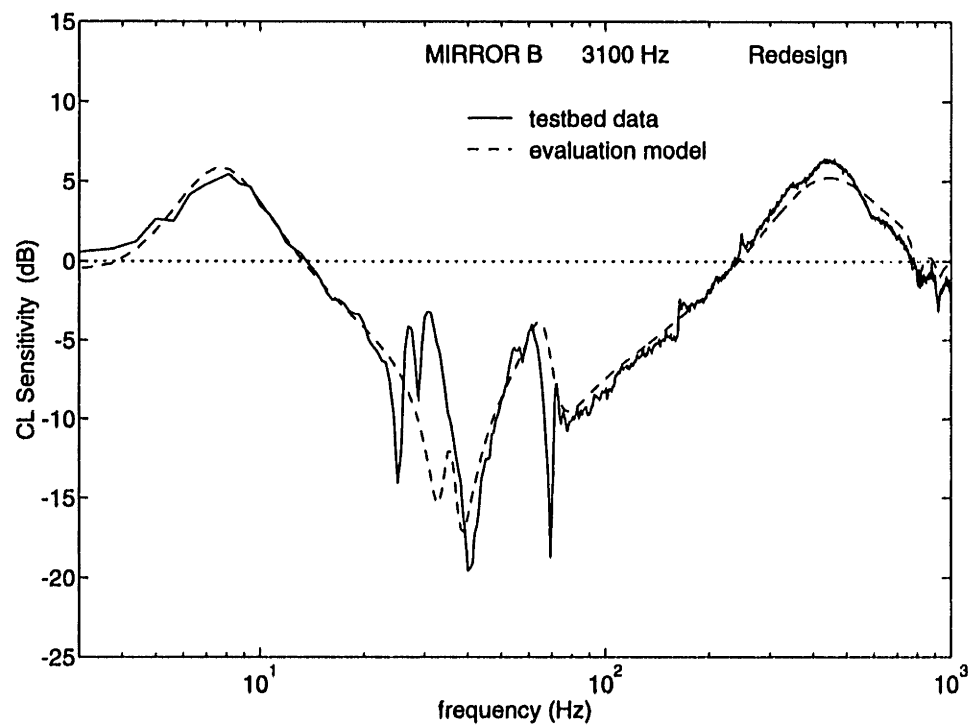

Figure 6.27: $S(s)$ on testbed vs model for mirror B at 3100 Hz, designed without compensation of plant modes at 550 Hz (now at 800 and 900 Hz). This compensator would not be stable on the test block.

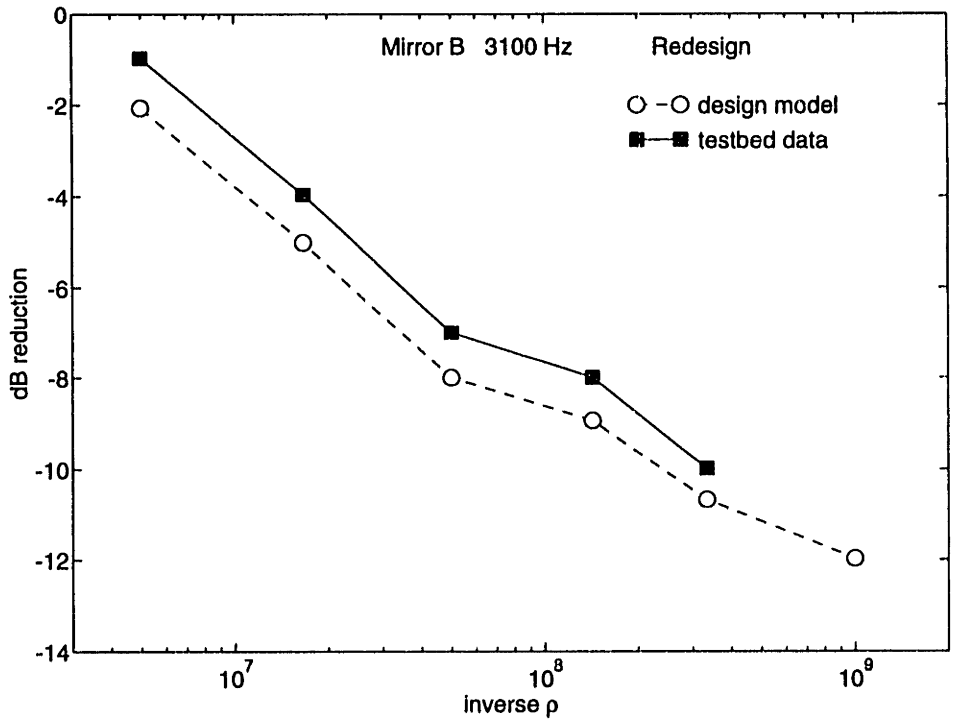

Figure 6.28: Family of compensators at 3100 Hz based on the updated design model. Dynamic compensation of the shifted 550 Hz modes is not included, resulting in compensators that are stable (and lower order) at much lower values of ρ.

6.5.3 Multiple Isolator Experiments

The 3100 Hz compensator designs for mirrors B and C, redesigned based on the updated design model, were implemented individually and then simultaneously on the testbed. Note that these compensators did not contain dynamic compensation of the uncertain modes near crossover. Figure 6.29 compares the individual and simultaneous controller implementations, indicating nearly independent control loops.

The MIMO plant is defined using the notation of Eqs. 6.5 to 6.8

$$G_{OL} = (H_5 H_4) G_m G_a K \tag{6.29}$$

where G_m is the 2×2 transfer function matrix from Figure 5.27

$$G_m = \begin{bmatrix} H_{BB} & H_{BC} \\ H_{CB} & H_{CC} \end{bmatrix} \tag{6.30}$$

and K is a diagonal compensator matrix

$$K = \begin{bmatrix} K_B & 0 \\ 0 & K_C \end{bmatrix} \tag{6.31}$$

Elements H_5, H_4, and G_a correspond to ZOH, time delay and analog elements that are identical for each loop.

The MIMO Nyquist theorem states that the closed loop system will be stable if and only if the clockwise origin encirclements of $\det[I + G_{OL}]$, as s travels once around the Nyquist contour D, equal the number of open loop poles in G_{OL}

$$N_x = -p_o \qquad \text{negative} = \text{counter-clockwise} \tag{6.32}$$

In this application, $p_o = 0$ so $N_x = 0$ implies closed loop stability.

For diagonal dominance of the matrix $[I + G_{OL}]$ [81] (matrix diagonal dominance is defined in Section 5.2.2), the origin encirclements of $\det[I + G_{OL}]$, as s travels once around the Nyquist contour D, equal the sum of the origin encirclements of the diagonal elements of the return matrix $[I + G_{OL}]$. Therefore, if the individual diagonal transfer functions are Nyquist stable, then diagonal dominance of $[I + G_{OL}]$ guarantees MIMO loop stability. The MIMO Nyquist stability theorem is applied below to the experimental data for the 2×2 plant for mirrors B and C mounted to the truss.

Figure 6.30 compares the individual SISO transfer functions for mirrors B and C for the highest gain compensators implemented stably, measured on the testbed. Each SISO plant is Nyquist stable in the model and experiment. The diagonal dominance of the return matrix $[I + G_{OL}]$ for the 2×2 plant is plotted in Figure 6.31, which indicates that the transfer function matrix is diagonally dominant at all frequencies, thus guaranteeing MIMO stability of the system. However, the diagonal dominance is weak near the 30 Hz modes.

Nyquist Plots: The implication of the diagonal dominance is illustrated in Figures 6.32, 6.33, and 6.34, which are plots of $\det[I + G_{OL}]$ for successively zoomed axes with respect to the origin. In Figure 6.32, the Nyquist plot follows a clockwise

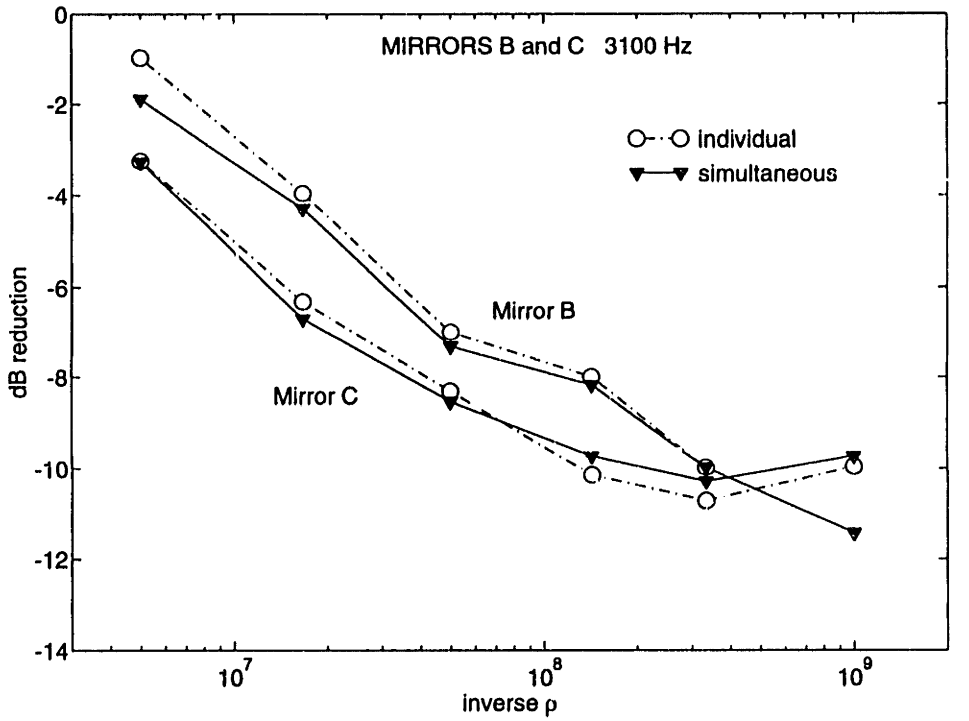

Figure 6.29: Comparison of independent and simultaneous performance of mirrors B and C mounted to truss. Coupling appears to be small.

rotation, with the large loop corresponding to frequencies immediately near the 40 Hz modes. A magnification of the origin in Figure 6.34 shows that no encirclements of the origin occur, but that stability bounds are very low (the next highest gain compensator was unstable). The three figures are overplotted with a dashed curve corresponding to $\det[I + G_{OL}]$ in which the off-diagonal terms in G_{OL} have been set to zero. The difference between the solid and dashed curves indicates the effect of the base coupling, which is small and does not perturb the curve in the direction of the origin, as shown in Figure 6.33. Even though diagonal dominance is weak in the 20 - 40 Hz region, the perturbations are not destabilizing.

6.6 Pathlength Control Experiments

6.6.1 Changes to Model and Compensator

Compensators were designed for absolute pathlength feedback for the three actuators based on the design models G_D developed for acceleration feedback. However, some

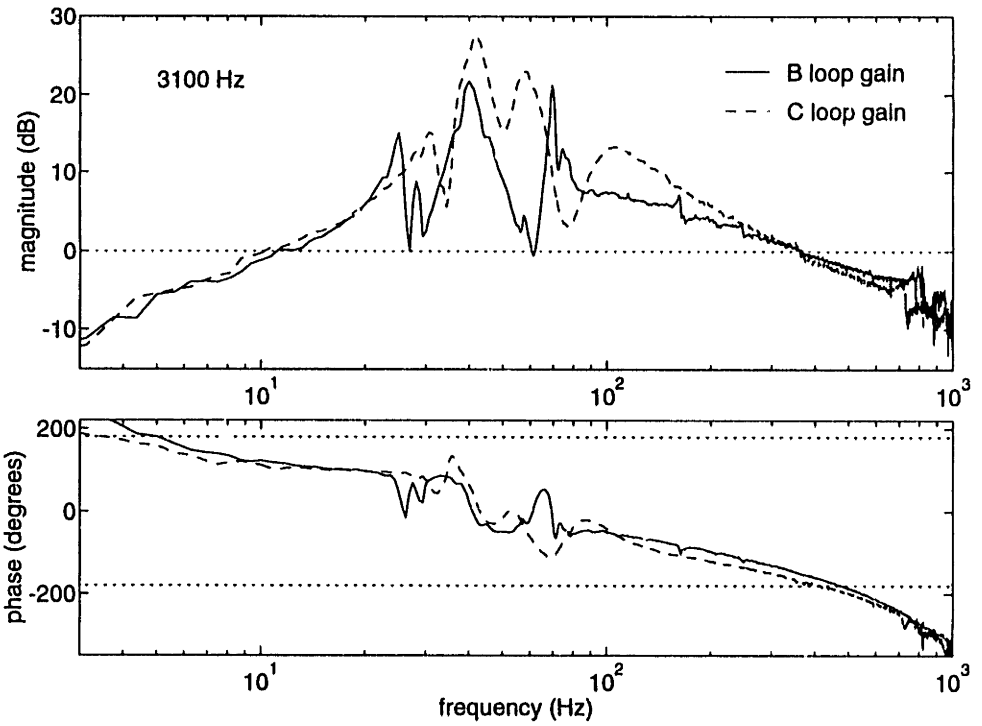

Figure 6.30: Comparison of loop gains (measured on the testbed) for mirrors B and C for moderate level of control authority, illustrating gain and phase margins.

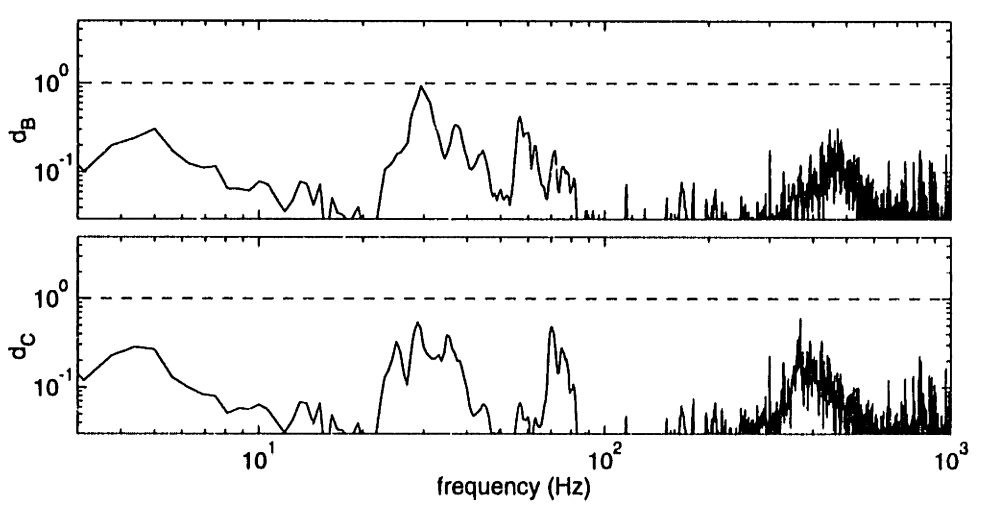

Figure 6.31: Diagonal dominance of the 2×2 return matrix $[I + G_{OL}]$ for the two isolators. Decoupling is high near 330 Hz crossover.

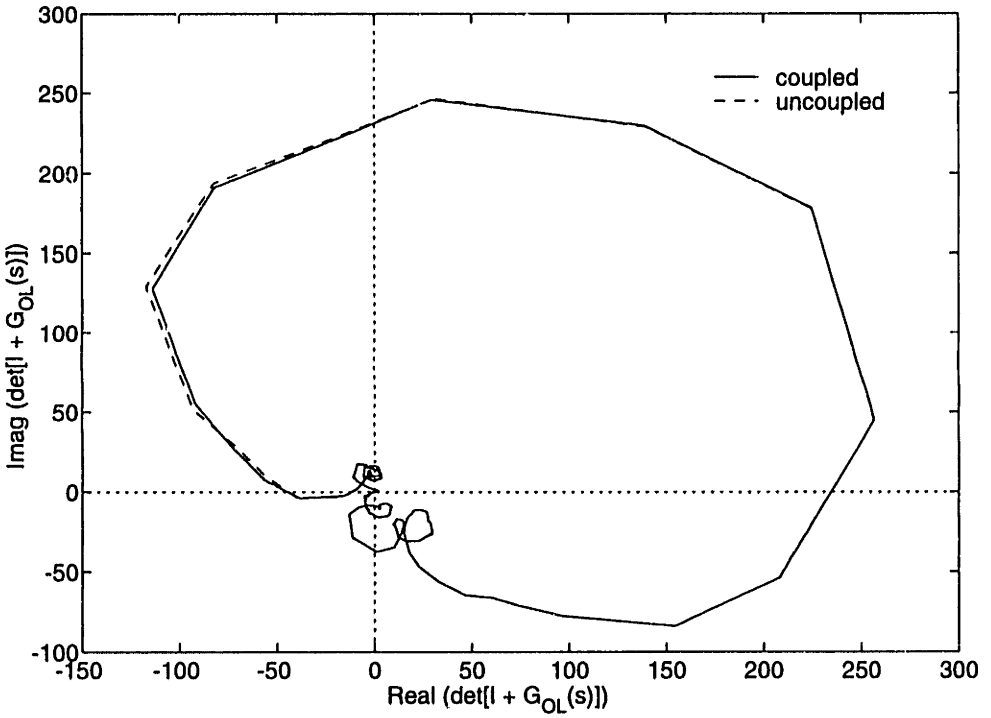

Figure 6.32: Plot of det$[I + G_{OL}]$ based on the experimental transfer functions, both with and without off diagonal terms in the plant G_D. Compensator K is diagonal. Overlay is nearly identical.

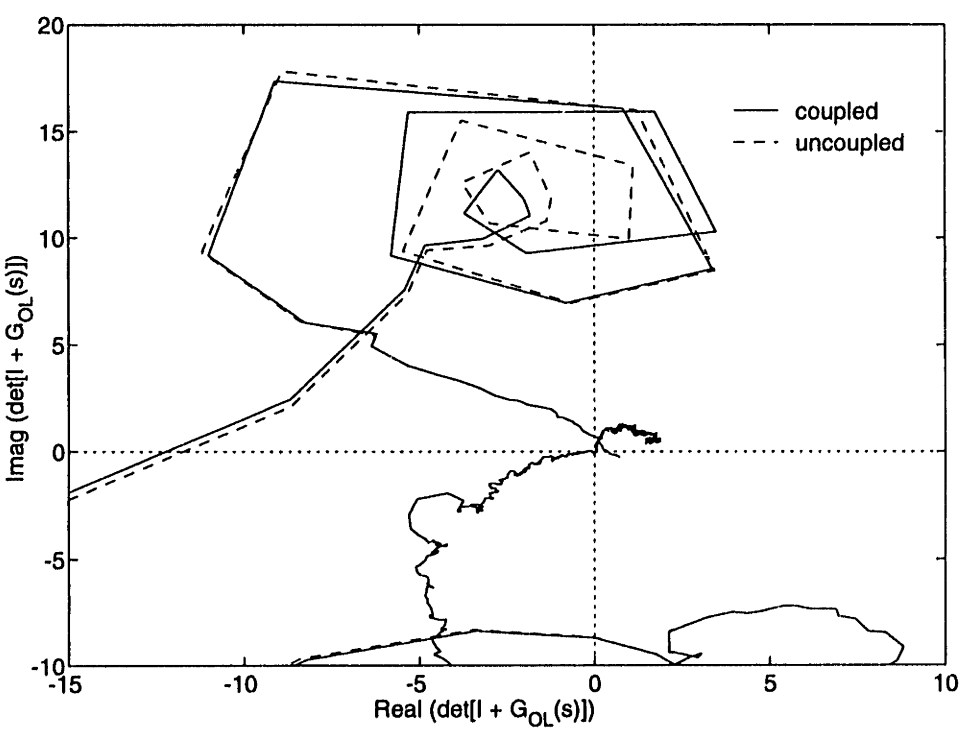

Figure 6.33: Blow- up of det $[I + G_{OL}]$ in the region near origin, showing slight differences for modes that correspond to resonances in the 20 - 60 Hz region. The perturbation is generally away from the origin.

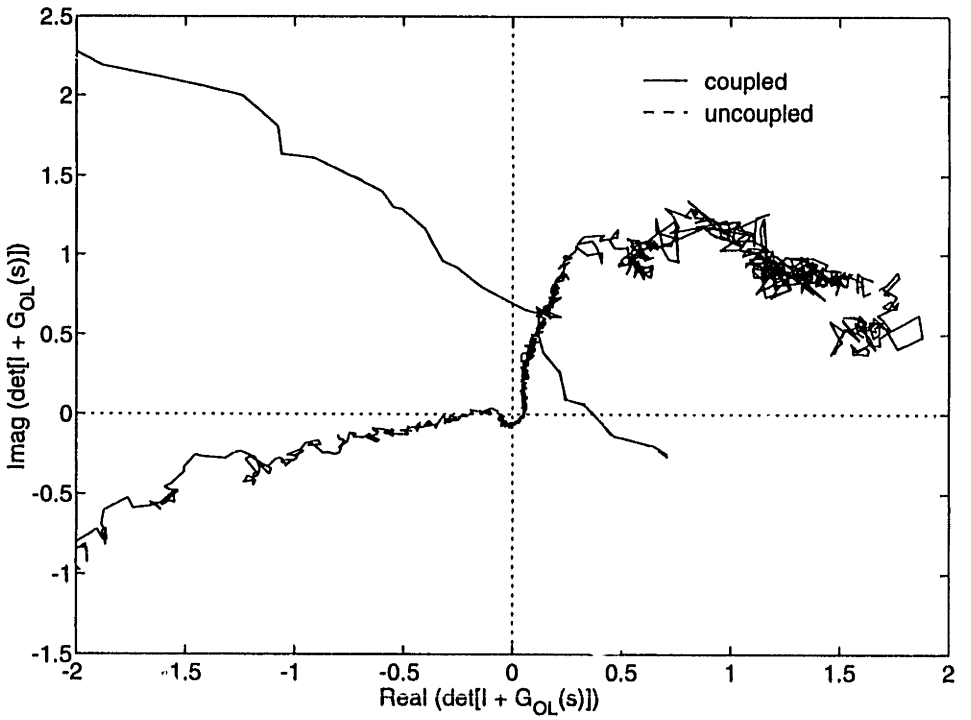

Figure 6.34: Further blow-up of $\det[I+G_{OL}]$ in the region near origin. No origin encirclements occur, implying MIMO Nyquist stability. However, margins are extremely low.

modifications were necessary because the laser transfer functions have a slope of roughly s^0, unlike the accelerometers. Accordingly, the analog circuit was reduced to only a notch at 2.1 kHz and a single real pole at 40 Hz. The laser output gain was set inside the realtime computer. Sensor noise was measured to be on the order of 7 nm RMS, which is near the discretization limit of 10 nm.

It is shown in Section 5.4.2 that the testbed measurements of acceleration and laser output closely agree once the s^2 term is accounted for. Thus, the design and evaluation models based on the acceleration models were used for compensator design (with s^2 removed). The updated design model, which includes the shifted 550 Hz modes, was used to design reduced order compensators (of order 4 or 6) that provided high performance on the truss. A documentation of a high gain compensator for mirror B is provided in Appendix E.

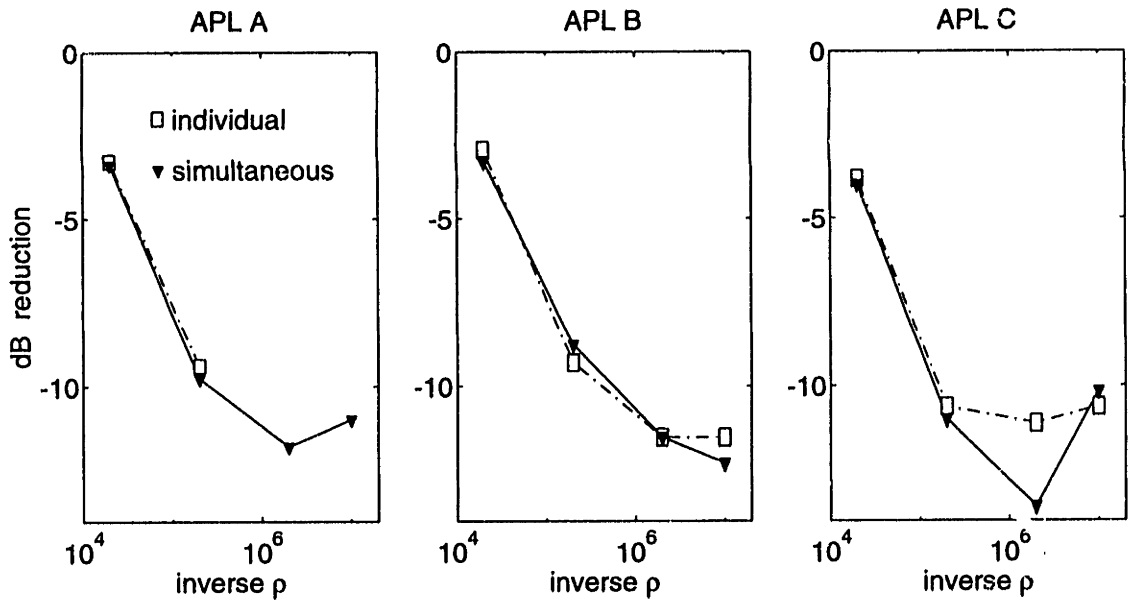

Figure 6.35: Performance improvement (due to laser feedback) for family of compensators implemented both individually (dashed) and simultaneously (solid) for three actuators mounted to the truss. Performance improvement is plotted for absolute pathlength.

6.6.2 Testbed Results Using Multiple Actuators

Performance for each mirror, at different values of control penalty ρ, is plotted in Figure 6.35 for independent and simultaneous implementation of the three actuators. The dB performance improvement is based on the measured RMS improvement in the 10 - 500 Hz absolute pathlength metric. The data indicate that the pathlength controllers are essentially decoupled on the truss. Note that the mirror A (SISO) control was not implementable for the two highest gain compensators, due to saturation problems in the control loop. However, when the loops for mirrors B and C were closed, the saturation problem for mirror A did not occur, permitting the implementation of high gain compensators for mirror A. The cause of this phenomenon was not identified. No compensators at lower values of control penalty ρ) were stable either for the design model or on the testbed. At high control gain, the performance in each loop was slightly better for simultaneous loop closure compared to individual control.

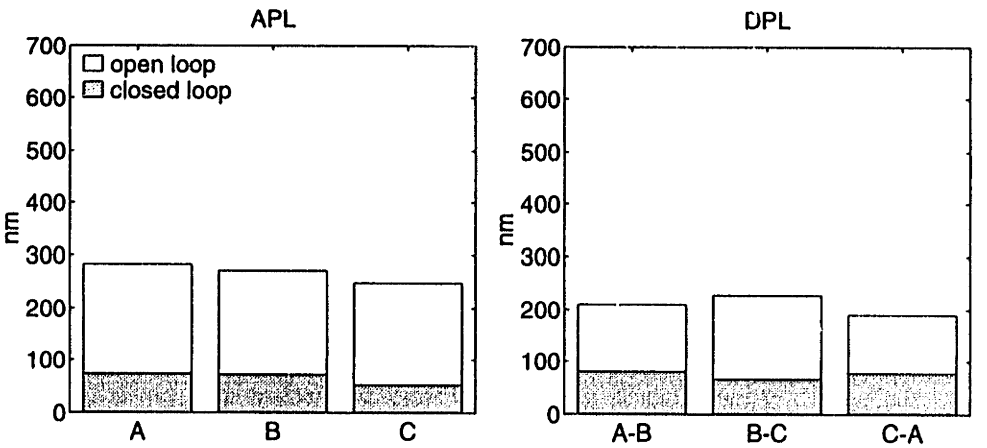

Figure 6.36: Performance metric improvement (nm RMS, 10 - 500 Hz) due to simultaneous pathlength control with three actuators. No D-struts or J-struts in truss.

6.6.3 Performance Metric Improvement

Figure 6.36 illustrates the performance metric improvement due to simultaneous pathlength control with the three actuators on the testbed. Improvement is highest in the absolute metric, since the absolute pathlengths were used as the regulated variables. The axes of the plot are consistent with the "original hardmount" metric summary presented in Chapter 4. No D-struts or J-struts were installed in the truss to provide damping for these measurements. In Appendix F, a layered design is presented in which 5 D-struts are added to the truss and the same pathlength controllers are re-implemented, providing approximately 20 percent greater reduction in the metric.

6.7 Combined Improvements to the Performance Metric

Figures 6.37 and 6.38 document the combined improvements to the testbed performance metric due to the experimental work in this thesis. Mechanical redesign of the original hardmounts removed local dynamics from the laser pathlength measurements; in particular, the cantilevered mode at 240 Hz of the original retro-reflector at mirror A was removed. The addition of the softmount passive isolation at each

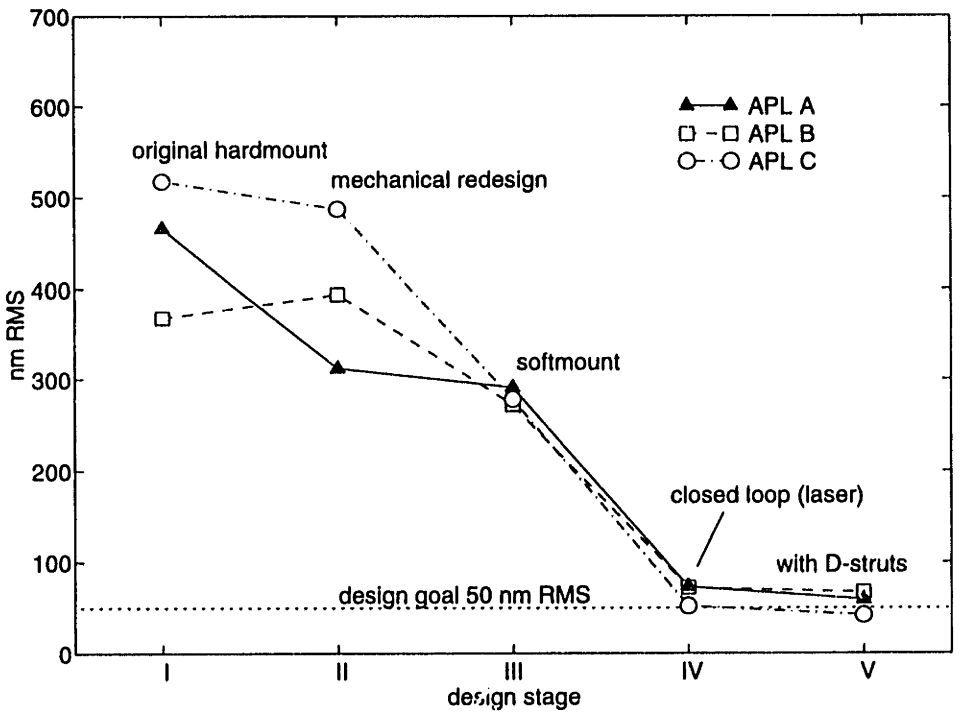

Figure 6.37: Summary of improvements to the absolute pathlength performance metric, 10 - 500 Hz. Replacement of optics at mirror A led to large improvement in that pathlength. Five D-struts were added to the truss and the same 3 pathlength control loops were again closed.

mirror provided only minor improvement to the metric, since the fourth vertex cat's eye was not passively isolated, and because the softmount was designed primarily to limit actuator reaction forces from entering the truss structure. The advantages of the decoupling design are evident in the performance metric improvement obtained using simultaneous, independent pathlength control with three actuators – using compensators that were a total of 7^{th} or 9^{th} order (analog plus discrete), and which were designed with only limited knowledge of the base structure dynamics. Further improvement was obtained by the addition of 5 D-struts to the testbed. Figure 6.39 presents the differential pathlength metric summary in a manner which highlights the performance gain due to the D-struts. The combination of passive isolation, passive damping and pathlength feedback reduced the performance metric to close to the stated design goal of 50 nm RMS in each of the differential pathlengths.

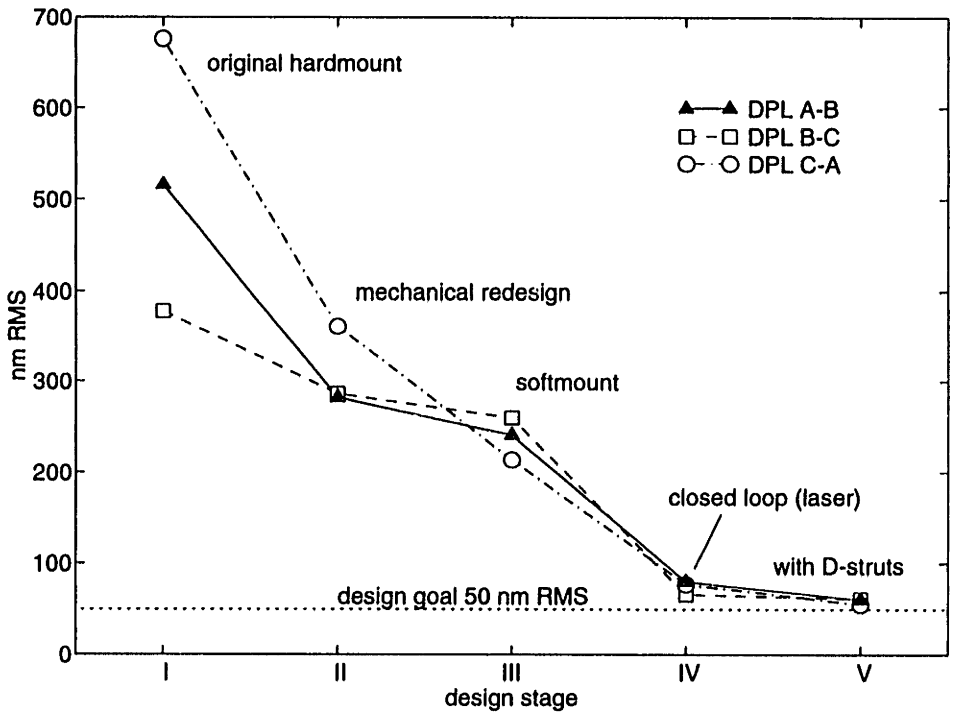

Figure 6.38: Summary of improvement to differential pathlength performance metric, 10-500 Hz. Mechanical redesign stiffened so that they did not occur within the disturbance bandwidth.

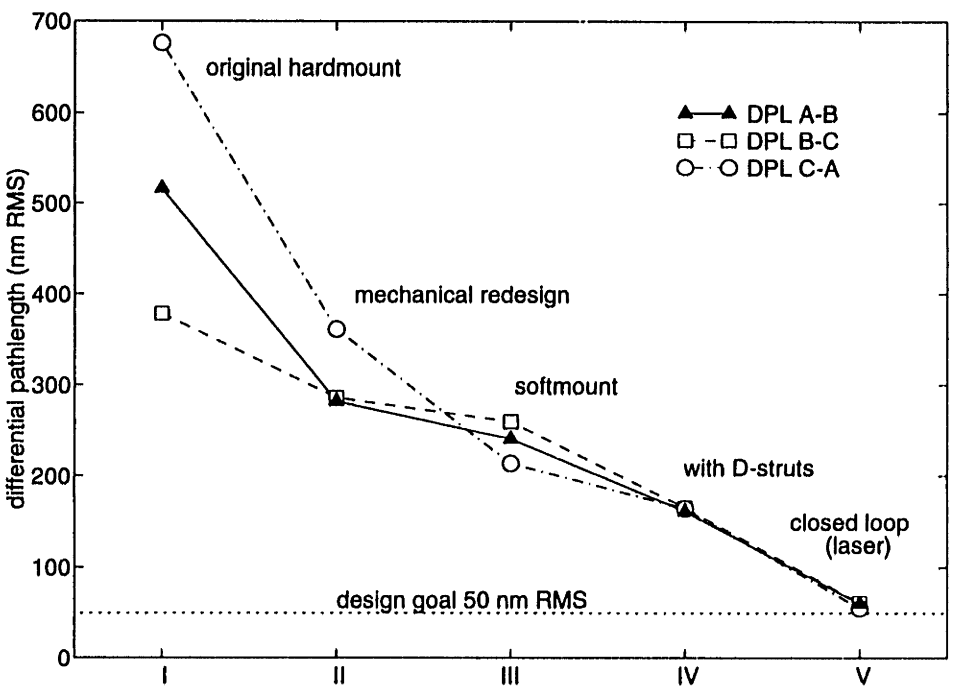

Figure 6.39: Differential pathlength improvement, emphasizing contribution of D-struts. Metric shown at step IV is open loop truss with 5 D-struts, before three laser loops were closed.

6.8 Summary

This chapter presents the control designs and closed loop results for active isolation both on a rigid test block and then for a flexible testbed mounting. An important result is that the closed loop actuator could be re-implemented on the testbed with little or no change to the compensator design. The results show that base modes are decoupled from the loop transfer function at high frequency, and thus do not pose a stability risk near crossover. Base modes that remain coupled at low frequency are not destabilizing due to the collocated nature of the isolator plant. In general, the agreement between model, rigid block stability, and testbed stability is good, which validates the control design approach taken. However, lightly damped modes in the softmount interface of the active mount, occurring near crossover frequency, were found to be a performance limit. Compensator dynamics, added to stabilize these modes for the rigid block, were destabilizing at high control gains on the testbed because base flexibility caused a shift in frequency and damping of these modes. Compensators with these dynamics removed were stable on the testbed. Pathlength control was implemented using absolute pathlength measurement as feedback, and provided a significant improvement in the testbed performance metric. A combined disturbance rejection design using 5 D-struts and 3 pathlength control loops reduced the performance metric to near the stated design goal of 50 nm RMS in each differential pathlength.

Chapter 7

Conclusions and Recommendations

7.1 Summary

This thesis investigates the problem of active vibration isolation and pathlength control of mirrors mounted to uncertain, flexible structures. An active mount incorporating passive isolation, a reaction stage and local acceleration feedback was designed so that it could be easily controlled on a flexible structure using a compensator that ignores the presence of unmodelled flexibility in the base structure. The closed loop stability was first validated on a rigid test block, and then implemented when mounted to a flexible structure. The experimental closed loop results of this thesis demonstrate the power of mechanical design for control, rather than control of difficult mechanical systems.

A general model for passive and active isolation was developed in order to study the effect of mechanical flexibility on passive and active isolation. It was shown that for passive isolation the mount *passive sensitivity* function $\mathcal{P}$ is the best function to describe the mount performance for flexible structures, since it directly relates the *isolated* variables of mount velocities and forces to their *unisolated* values, for both the force (input) and velocity (output) isolation problems. The effect of structural flexibility on the passive sensitivity function was characterized in terms of a dimen-

sionless perturbation parameter which is a function of modal damping, modal mass and isolated mass. Perturbations to the mount actuator/sensor transfer functions due to mechanical flexibility were also characterized in terms of the dimensionless parameter β, and the analysis revealed that the degree of coupling depends on the choice of output sensor as well as on the frequency of mount resonance. For values of the coupling parameter much less than one, it was shown that the perturbation effect on transfer functions was negligible. For base flexible modes with strong interaction, the perturbation to the transfer function was found to be stabilizing due to collocation, although near loop crossover, stability risks exist. Configurations for parallel actuation and series actuation were studied, and the results apply to both the force and velocity isolation problems. Dereverberated and average linear magnitude models of the base structure and equipment were shown to improve models for passive isolation performance and to improve models of the loop transfer functions for control design.

Based on these insights, a design approach for an active isolation mount was proposed, in which the compensator design is based on the plant model derived from a rigid base. The closed loop mount performance is verified first on a rigid test stand, and then installed on a flexible structure with the same compensator. The performance metric of the SERC Interferometer Testbed was used to determine the functional requirements for an active mount for isolation of three optical elements from the vibrating structure, as well as for articulation of these optics for direct pathlength control. Tests and analysis indicated that due to base modal flexibility, strong coupling between the three independent isolators was too great to permit decentralized control design for each mirror. To limit interaction, each mount was modified to include a softmounted reaction stage that decouples actuator reaction forces from the structure at frequencies near loop crossover.

Compensators were designed and implemented for an isolator mounted to a rigid base, and were implemented stably (with little or no change to the compensator) when the isolator was attached to the flexible testbed, thus validating the proposed control design approach. The closed loop results demonstrated that considerable attenuation could be achieved in the local acceleration and pathlength errors in the truss, using

simple compensators developed for the rigid base model. The combined layers of passive isolation, simultaneous (independent) pathlength control of three laser legs, and viscous damping in the truss using five D-struts, were used to reduce the open loop performance metric from 500 nm RMS in a 10 to 500 Hz bandwidth to less than 60 nm RMS in each laser pathlength measurement.

7.2 Conclusions and Contributions

1. This thesis has demonstrated the power of mechanical design for control, as opposed to control design for difficult mechanical systems. The mechanical design of an active isolation/articulation stage for a mirror, incorporating mount damping, passive isolation and mechanical reactuation, permitted the design of low order, high gain compensators that were robust to the presence of unmodelled flexibility in the base structure to which the isolator was mounted. The work complements and extends recent research on active force isolation for flexible structures by Watters *et al.* [82], Spanos *et al.* [71], and Swanson et al. [76] by explicitly characterizing the interaction between local mechanical design and base structure modal parameters. Furthermore, it was demonstrated experimentally and analytically how the decoupling naturally present in isolation control architectures, enhanced by mechanical design, allows a design approach in which a compensator is designed based only on the rigid base transfer functions, and then re-implemented stably when the isolator is mounted to a flexible base. It is concluded that a mechanical mount design which includes passive isolation, mount damping and possibly reactuation, provides not only passive performance improvement, but also conditions the local mount transfer functions to robustly accept low order, high gain control by decoupling uncertain base or equipment flexibility.

2. This research extends the work by Sykes [77] and Ruzicka [59] on the effect on passive isolator performance due to modal flexibility, by quantifying the perturbations in terms of a dimensionless parameter that is a function of modal damping, modal

mass and isolated mass. A further advance of the current work is that modal flexibility in the isolated equipment is shown to impact the isolator performance in a parametric form identical to that for base flexibility, thereby permitting the effect of both types of flexibility to be characterized by the same dimensionless parameter. The mount *passive sensitivity* function, a modified transmissibility function which accounts for base or equipment flexibility, is identified as a useful function for CST isolation design. The passive sensitivity function predicts the changes in all mount and structural variables due to the addition of passive isolation at either (force) input or (velocity) output locations.

3. A new method was proposed and validated, by simulation and experiment, in which *averaged mobility* models of the base structure are used to better estimate the improvement due to the addition of passive isolation, when structural flexibility is present in the base or equipment. A low order, frequency-averaged model of the linear magnitude of the base input mobility is substituted into a modified passive sensitivity function to predict the average vibration energy transmitted across the mount. The method is both more accurate than the rigid base estimate of isolator performance, and easier to use than the exact method based on full order models of the base structure, which may not be accurate – or even available – at early stages in a CST design. The proposed method is motivated by recent results obtained using dereverberated (log magnitude) averages of structural mobility in the wave and impedance matching literature [45], [43], and by concepts based on averaged structural response in Statistical Energy Analysis [44]. This result can be used to provide reasonable *a priori* estimates of structural response due to passive isolation, based only on a model of the isolator and on a coarse estimate of base input mobility at the isolator interface.

4. The effects of base and equipment flexibility on the local mount transfer functions for active isolation have been quantified parametrically in terms of the dimensionless parameter β that is a function of isolated mass, mount resonance, and base

modal mass and damping. The analysis both extends, and captures within a common framework, recent research on flexible coupling (studied for particular applications by Garcia et al [24], Watters et al. [82] and Spanos *et al.* [71]), and clarifies the individual decoupling effects of output sensor selection and local mount mechanical design. The general analysis framework revealed the similarities between the base and equipment flexible coupling, permitting effects of both to be represented by a common set of transfer functions and by the common dimensionless coupling parameter β. It was shown that for the dimensionless coupling parameter β much less than one, the rigid base transfer functions for active isolation were recovered. Decoupling from base flexibility was improved by increased damping in the isolator, damping in the base structure, soft passive isolation, and by reactionless actuation design. The analysis also demonstrated that strong modal coupling will always be present in an acceleration output signal when the sensor is mounted to the side of the interface which exhibts structural flexibility. Furthermore, transfer functions to interface force exhibit decoupling of both base and equipment modal flexibility at frequencies above mount resonance, where loop crossover is anticipated. This dimensionless parameter β provides a new means to quantify the degree of decoupling that can be expected from mechanical design of the mount, sensor selection, or modifications to the modal parameters of the base or equipment structures.

5. A parametric multiplicative error model that accounts for unmodelled flexibility was developed for active isolator control design, based on the dimensionless coupling parameter β. For the SISO case, the model predicts the gain and phase perturbations due to the base and equipment flexibility. This generalizes and extends the result of Garcia *et al.* [24] to the general isolation problem for different feedback sensors and for frequency ranges both above and below mount resonance. Another new, related result of this thesis is the use of low order, dereverberated mobility models of the base or equipment to improve the magnitude and phase of the rigid base transfer functions used for control design. The dereverberated mobility is easy to obtain at an early stage in the CST design process, and its use captures the true transfer function backbone

which is perturbed by the base or equipment flexibility. It is concluded that the backbone transfer function models incorporating the dereverberated mobility, along with the multiplicative error based on the dimensionless coupling parameter, permit the design of active isolation compensators based on rigid base transfer functions, which will then be stable when the isolator is mounted to flexible structures.

6. This thesis has demonstrated multiple, independent isolation and pathlength control of mirrors mounted to a common flexible structure. Because of the mount mechanical design for base modal decoupling, the structural interactions between three isolators mounted on the testbed were low enough near crossover frequency to permit decentralized control design for each isolator. Although the mounts were only reactuated at high frequency, and high coupling remained at low frequencies near the softmount resonances, implementation was possible due to the large phase margin in each loop in this frequency range. The importance of this result is that simultaneous, decentralized control designs are possible for both output and input isolation (for which reactuation is not possible, but only soft isolation mounting) and that at frequencies well below crossover, any remaining flexible interaction will not necessarily be destabilizing.

7.3 Recommendations for Future Work

1. The active isolation and pathlength control experiments in this thesis lend themselves to MIMO implementation for cases in which more than one output direction of the isolated equipment must be controlled. The MIMO application of the passive isolator performance has recently been investigated by Swanson [76]. The coupling analysis and multiplicative error model introduced in this thesis could be extended using matrix algebra to MIMO problems, which will highlight the directionality of the base input mobility and the directionality of the active stage. An open area of research is whether a decoupled control design can be implemented stably for two or more output directions for a single isolator mount, since the base input mobility

will introduce off-diagonal coupling unless some reactuation is introduced. Significant off-diagonal coupling may remain due to coupling within the mount itself. This topic has application to the design of multi-axis force isolation mounts for vibrating equipment, where typically three or more axes of vibration are important. Secondly, the isolation of proposed flight experiments such as SITE [11] will require multi-axis isolation of base disturbances from a massive sensitive payload.

2. A variation of the series isolator configuration used in this thesis could be used to isolate vibrating equipment from quiet base structures [12]. For this application he piezoelectric actuator must exhibit sufficient stroke to cancel the free disturbance velocity of the vibrating equipment. Feedback sensors of interface force or of acceleration of the reaction stage m_2 could be used for active control. However, in this case the reaction mass m_2 does not need to be large, and may only be the mass of an accelerometer mounted between the stiff piezoelectric actuator and the soft series spring. Base modes would be weakly coupled into the loop transfer function above the resonance provided by the soft series spring with the equipment mass. Equipment modes would also be weakly coupled, governed by the ratio of accelerometer mass m_2 to the individual modal masses of the equipment resonances.

3. Given the demonstrated decoupling of base modes from the loop transfer functions used in this thesis for control design, emphasis in the future should shift to mechanical designs in which damping is added to the modes in the isolated equipment and in the isolator hardware itself. The presence of these modes was a performance constraint encountered during the experimental work of this thesis. Damping of these modes will permit simpler compensators for the mount to be implemented, and will reduce the demands for well identified models of the isolator plant transfer functions.

References

[1] Allen, T. S., Havenhill, D. D., and Kral, K. D., "FEAMIS: A Magnetically Suspended Isolation System for Space-Based Materials Processing," *Annual AAS Guidance and Control Conference*, Keystone CO (1986).

[2] Anderson, E. H., Trubert, M., Fanson, J. L., and Davis, P., "Testing and Application of a Viscous Passive Damper for Use in Precision Truss Structures," *32rd AIAA/ASME/ASCE/AHS/ASC Structures, Structural Dynamics and Materials Conference*, Apr. 1991.

[3] Anderson, E. H., and How, J. P., "Implementation Issues in the Control of a Flexible Mirror Testbed," *SPIE Conference on Active and Adaptive Optical Systems*, San Diego CA, July 1991.

[4] Anderson, E. H., Blackwood, G. H., and How, J. P., "Passive Damping in the MIT SERC Controlled Structures Testbed," *International Symposium on Active Materials and Adaptive Structures*, Alexandria VA, November 1991.

[5] Anderson, E. H., "Robust Actuator and Damper Placement for Structural Control," PhD Thesis, MIT, February 1994.

[6] Bahcall, J. N., editor. *The Decade of Discovery in Astronomy and Astrophysics.* National Research Council, National Academy Press, 1991.

[7] Balmes, E., "Experimental/Analytical Predictive Models of Damped Structural Dynamics," PhD Thesis, Massachusetts Institute of Technology, May 1993.

[8] Balmes, E., "Experimental and Analytic Structural Dynamic Analysis Toolbox," *MATLAB^{TM} Toolbox*, The MathWorks, Inc., 21 Eliot St., South Natick, MA, 1993.

[9] Billing-Ross, J. A., and Wilson, J. F., "Pointing System Design for Low-Disturbance Performance," AIAA Paper 88-4106.

[10] Blackwood, G. H., Jacques, R., and Miller, D., "The MIT Multipoint Alignment Testbed: Technology Development for Optical Interferometry," *SPIE Conference on Active and Adaptive Optical Systems*, San Diego CA (1991).

[11] Blackwood, G., Hyde, T., Miller, D., Crawley, E., Shao, M., and Laskin, R., "Stellar Interferometer Tracking Experiment (SITE): A Proposed Technology Demonstration Experiment." *44th Congress of the International Astronautical Federation*, Oct 1993, Graz, Austria.

[12] Blackwood, G. H., and von Flotow, A. H., "Active Control for Vibration Isolation Despite Resonant Structural Dynamics: A Trade Study of Sensors, Actuators and Configurations," *Recent Advances in Active Control of Sound and Vibration*, Virginia Polytechnic Institute, Blacksburg VA, April 1993.

[13] Blevins, R. D., *Formulas for Natural Frequency and Mode Shape*, Robert E. Krieger Publishing Co., Inc., Malabar FL, 1979, pp. 101-113.

[14] Collins, S. A. and von Flotow, A. H., "Active Vibration Isolation for Spacecraft," *42nd Congress of the International Astronautical Federation*, Montreal, CA (1991).

[15] Collins, S. A., von Flotow, A. H., and Paduano, J. D., "An Analog Adaptive Vibration Cancellation System for Stirling Cryocoolers," *1993 Space Cryogenics Workshop*, San Jose, CA, July 20-21, 1993.

[16] Crandall, S. H., "Impedance and Mobility Analysis of Lumped Parameter Systems," *Colloquium on Mechanical Impedance Methods for Mechanical Vibrations*, ASME Annual Meeting, Dec. 1958, pp. 19-42.

[17] Crede, C. E., "Theory of Vibration Isolation," chapter 30 of *Shock and Vibration Handbook*, Harris, C. M., ed. New York: McGraw-Hill Book Co., 1961.

[18] Das, A. *et al.*, "ASTREX - A Unique Test Bed for CSI Research," *Proceedings of the 21st Conference on Decision and Control*, Dec. 1990, pp. 2018-2023.

[19] Doyle, J. C., Stein, G. S., "Multivariable Feedback Design: Concepts for a Classical/Modern Synthesis," *IEEE Transactions on Automatic Control*, Vol. AC-26, No. 1, Feb. 1981, pp. 4-16.

[20] Eyerman, C. E., Shea, J. F., "A Systems Engineering Approach to Disturbance Minimization for Spacecraft Using Controlled Structures Technology," Technical Report 2-90, MIT SERC, June 1990.

[21] Fanson, J. L., Chu, C-C., Smith, R. S., and Anderson, E. H., "Active Member Control of a Precision Structure with an $\mathcal{H}_\infty$ Performance Objective," *AIAA Dynamics Specialists Conference*, Long Beach CA, Apr. 1990.

[22] Fenn, R. C., Downer, J. R. Gondhalekar, V., and Johnson, B. G., "An Active Magnetic Suspension for Space-Based Microgravity Vibration Isolation," *ASME Winter Annual Meeting*, Dallas TX, pp. 49-56 (1990).

[23] Franklin, G. F., Powell, J. D., *Digital Control of Dynamic Systems*. Reading,

MA: Addison Wesley Publishing Company, 1980, pp. 82-84.

[24] Garcia, J. G., Sievers, L. A., and von Flotow, A. H., "High Bandwidth Position Control of Small Payloads Mounted on a Flexible Structure," *Journal of Guidance, Control and Dynamics*, Vol. 15, no. 4, Jul-Aug 1992, pp. 928-934.

[25] Germann, L., and Gupta, A. A., "The Six-DOF, Magnetic Suspended Fine Steering Mirror," *Proceedings of the Annual Rocky Mountain Guidance and Control Conference*, Keystone CO, Feb. 1990, pp. 155-167.

[26] Grodsinsky, C. M., and Brown, G. V., "Low Frequency Vibration Isolation Technology for Microgravity Space Experiments," *ASME Conference on Mechanical Vibration and Noise*, Montreal, pp. 295-302 (1989).

[27] Guillemin, *Introductory Circuit Theory.* New York: John Wiley & Sons, Inc., 1953.

[28] Gupta, A., and Germann, M., "Precision Pointing and Inertial Line-of-Sight Stabilization Using Fine-Steering Mirror, and Strap-Down Inertial Sensors," AAS Paper 89-036.

[29] Hain, H. L. and Miller, R., "Isolation Mounts for the HEAO-B Xray Telescope," *The Shock and Vibration Bulletin*, Vol. 48, Part 2, 1978, pp. 97-113.

[30] Hamilton, B. J., Andrus, J. H., and Carter, D. R., "Pointing Mount with Active Vibration Isolation for Large Payloads," *Advances in the Astronautical Sciences*, Vol. 63, 299-318 (1987).

[31] Harris, C. M., ed., *Shock and Vibration Handbook*, Harris, C. M., ed. New York: McGraw-Hill Book Co., 1961.

[32] Heusmann, H., "Spacelab Instrument Pointing Subsystem (IPS) On-Orbit Operations," *SPIE Shuttle Pointing of ElectroOptical Experiments*, Vol. 265, Los Angeles, CA (1981).

[33] Hixson, E. L., "Mechanical Impedance," Chapter 10 of *Shock and Vibration Handbook*, Harris, C. M., ed. New York: McGraw-Hill Book Co., 1961.

[34] Jones, D. I., Owens, A. R., and Owen, R. G., "A Microgravity Facility for In-Orbit Experiments," *ASME Winter Annual Meeting*, Dallas TX, 1990, pp. 67-73.

[35] Kaplow, C. F. and Velman, J. R., "Application of an Active Local Vibration Isolation Concept to a Flexible Space Telescope," *Journal of Guidance and Control*, Vol. 3, no. 3, 1980, pp. 227-233.

[36] Karnopp, D. C., "Active and Passive Isolation of Random Vibration," Isolation of Mechanical Vibration, Impact and Noise, ASME Design Engineering

Technical Conference, Cincinnati, Sept. 1973, pp. 64-86.

[37] Kekler, C. R., "ASPS Performance with Large Payloads Onboard the Shuttle Orbiter," *Journal of Guidance, Control and Dynamics*, Vol. 5, no. 1, 32-36 (1980).

[38] Laskin, R. A., Kopf, E. H., Sirlin, S. W., Spanos, J. T., and Wiktor, P. J., "Reactionless Gimbal Actuation for Precision Pointing of Large Payloads," *AAS/AIAA Astrodynamics Specialist Conference*, Kalispell MT, Aug. 1987.

[39] Laskin, R. A., and Sirlin, S. W., "Future Payload Isolation and Pointing System Technology," *Journal of Guidance and Control*, Vol. 9, no. 4, 1986, pp. 469-477.

[40] Laskin, R. A., and San Martin, M., "Control/Structure System Design of a Spaceborne Optical Interferometer," *AAS/AIAA Astrodynamics Specialist Conference*, Stowe VT, Aug. 1989.

[41] Lazarus, K. B., and Crawley, E. F., "Multivariable High-Authority Control of Plate-Like Active Structures," *33rd AIAA/ASME/ASCE/AHS/ASC Structures, Structural Dynamics and Materials Conference*, Apr. 1992.

[42] Lurie, B. J., Sirlin, S. W., O'Brien, J. F., and Fanson, J. L., "The Dial-a-Strut Controller for Structural Damping," *ADPA/AIAA/ASME/SPIE Conference on Active Materials and Adaptive Structures*, Alexandria VA, Nov. 1991.

[43] Lurie, B. J., Fanson, J. L., and Laskin, R. A., "Active Suspension for Vibration Isolation," *32nd AIAA/ASME/ASCE/AHS/ASC Structures, Structural Dynamics and Materials Conference*, Baltimore MD, Apr. 1991, pp. 2256-2260.

[44] Lyon, R. H., *Machinery Noise and Diagnostics: Theory and Applications*, The MIT Press, Cambridge MA, 1975.

[45] MacMartin, D. G., Miller, D. W., and Hall, S. R., "Structural Control Using Active Broadband Impedance Matching," *Recent Advances in Active Control of Sound and Vibration*, Apr. 1991, pp. 604-617.

[46] MacMartin, D. G., "A Stochastic Approach to Broadband Control of Parametrically Uncertain Structures," PhD Thesis, Massachusetts Institute of Technology, May 1992.

[47] Marston, R. M., *OP-AMP Circuits Manual.* Oxford: Heinemann Publishing Ltd., 1989.

[48] Marth, H., and Donat, M., "Latest Experience in the Design of a Piezoelectric Driven Fine Steering Mirror," *SPIE Active and Adaptive Optics Conference*, San Diego CA, July 1991, pp. 248-261.

[49] Miller, D. W., Hall, S. R., and von Flotow, A. H., "Optimal Control of Power

Flow at Structural Junctions," *Journal of Sound and Vibration*, Vol. 140, No. 3, 1990, pp. 475-497.

[50] Miller, D. W., de Luis, J., and Crawley, E. F., "Dynamics and Control of Multipayload Platforms: the Middeck Active Control Experiment (MACE)," *41st Congress of the International Astronautical Federation*, Oct. 1990.

[51] Molloy, C. T., "Four-Pole Parameters in Vibration Analysis," *Colloquium on Mechanical Impedance Methods for Mechanical Vibrations*, ASME Annual Meeting, Dec. 1958, pp. 43-68.

[52] Moore, B. C., "Principal Component Analysis of Linear Systems: Controllability, Observability, and Model Reduction," *IEEE Transactions on Automatic Control*, Vol. AC-26, Feb. 1981, pp. 17-32.

[53] Newsom, J. R., Layman, W. E., Waites, H. B., and Hayduk, R. J., "The NASA Controls-Structures Interaction Technology Program," *41st Congress of the International Astronautical Foundation*, Oct. 1990.

[54] Peterson, L. D., "Optimal Projection Control of an Experimental Truss Structure," *Journal of Guidance*, Control and Dynamics, Vol. 14, no. 2, Mar-Apr. 1991, pp. 241-250.

[55] Peterson, A. P., and Gross, E. E., *Handbook of Noise Measurement.* General Radio Company: Concord, MA pp 74-75.

[56] Phillips, D., and Collins, E. G. Jr., "Four Experimental Demonstrations of Active Vibration Control for Flexible Structures," *AIAA Guidance, Navigation and Control Conference*, Portland OR, Aug. 1990, pp. 1625-1633.

[57] Quadrelli, B. M., and von Flotow, A. H., "Modelling, Dynamics Analysis and Control of a Multi-Body Space Platform," MS Thesis, Massachusetts Institute of Technology, February 1992, pp. 59 to 64.

[58] Rodden, J. J., Dougherty, H. J., Reschke, L. F., Hasha, M. D., and Davis, L. P., "Line-of-Sight Performance Improvement with Reaction-Wheel Isolation," *Advances in the Astronautical Sciences*, Vol. 61, 1986, pp. 71-84.

[59] Ruzicka, J. E., and Cavanaugh, R. D., "Vibration Isolation of Non-Rigid Bodies," *Colloquium on Mechanical Impedance Methods for Mechanical Vibrations*, ASME Annual Meeting, Dec. 1958, pp. 109-124.

[60] Ruzicka, J. E., "Active Vibration and Shock Isolation," SAE Paper No. 680747, (1968).

[61] Ruzicka, J. E., and Derby, T. F., *Influence of Damping in Vibration Isolation.* Washington, D.C.: The Shock and Vibration Information Center, Naval Research Laboratory, 1971, p. 39.

[62] Scribner, K. B., Sievers, L. A., and von Flotow, A. H., "Active Narrowband Vibration Isolation of Machinery Noise from Resonant Substructures," *ASME Winter Annual Meeting*, Dallas TX, 1990.

[63] Sevaston, G. E., Socha, M. M., and Eisenman, A., "The Circumstellar Imaging Telescope Image Motion Compensation System: Ultra-Precise Control on the Space Station Platform," *Advances in the Astronautical Sciences*, Vol. 68, 291-310 (1989).

[64] Shao, M., Colavita, M. M., Hines, B. E., Staelin, D. H., Hutter, D. J., *et al.*, "The Mark III Stellar Interferometer," *J. Astron. Astrophys.* 193, 357-371, 1988.

[65] Skudrzyk, E., "The Mean-value Method of Predicting the Dynamic Response of Complex Vibrator," *The Journal of the Acoustical Society of America*, Vol. 67, No. 4, Apr. 1980, pp. 1105-1135.

[66] Shao, M., Colavita, M. M., "Long Baseline Optical and Infrared Stellar Interferometry," *Annu. Rev. Astron. Astrophys.*, 30:457-498, 1992.

[67] Sievers, L. A., and von Flotow, A. H., "Comparison and Extensions of Methods for Cancellation of Periodic Noise," *IEEE Transactions on Circuits and Systems II: Analog and Digital Signal Processing*, Vol. 39, no. 8, Oct. 1992.

[68] Sinha, A. and Wang, Y.-P., "Digital Control Algorithms for Microgravity Isolation Systems," *ASME Conference on Mechanical Vibration and Noise*, Miami FL, pp. 247-256 (1991).

[69] Sirlin, S. W., and Laskin, R. A., "Payload Isolation and Precision Pointing for the 1990's," *Advances in the Astronautical Sciences*, Vol. 57, 1985, pp. 39-60.

[70] Spanos, John T., "Control-Structure Interaction in Precision Pointing Servo Loops," *Journal of Guidance, Control and Dynamics*, Vol. 12, no. 2, Mar-Apr. 1989.

[71] Spanos, J., Rahman, Z., and von Flotow, A., "Active Vibration Isolation on an Experimental Flexible Structure," *Smart Materials and Intelligent Systems*, SPIE 1917-60, Albuquerque, 1993.

[72] Spanos, J., Rahman, Z., Chu, C., and O'Brien, J., "Control Structure Interaction in Long Baseline Space Interferometers," *12th IFAC Symposium on Automatic Control in Aerospace*, Ottobrunn, Germany, Sep. 1992.

[73] Stampleman, D. S., and von Flotow, A. H., "Microgravity Isolation Mounts Based Upon Piezoelectric Film," *ASME Winter Annual Meeting*, Dallas TX, pp. 57-65 (1990).

[74] Stein, G., and Athans, M., "The LQG/LTR Procedure for Multivariable Feedback Control Design," *IEEE Transactions on Automatic Control*, Vol. AC-32,

no. 2, Feb. 1987, pp. 105-114.

[75] Su, H., Rakheja, S., Sankar, T. S., "Vibration Isolation Characteristics of an Active Electromagnetic Force Generator and the Influence of Generator Dynamics," *Journal of Vibration and Acoustics*, Vol. 112, Jan. 1990, pp. 8-15.

[76] Swanson, D. A., Miller, L. R., and Norris, M. A., "Multi-dimensional Mount Effectiveness for Vibration Isolation," *33rd AIAA/ASME/ASCE/AHS/ASC Structures, Structural Dynamics and Materials Conference*, Apr. 1992, pp. 1764-1773.

[77] Sykes, A. O., "The Evaluation of Mounts Isolating Nonrigid Machines from Nonrigid Foundations," *ASME Shock and Vibration Instrumentation*, 1958, pp. 1-39.

[78] Tanaka, N., and Kikushima, Y., "Rigid Support Active Vibration Isolation," *Journal of Sound and Vibration*, Vol. 125, No 3., 1988, pp. 539-553.

[79] Thompson, A. G., "Optimal and Suboptimal Linear Active Suspensions for Road Vehicles,", *Vehicle System Dynamics*, Vol. 5, 1976, pp. 187-203.

[80] The EVIS Vibration Isolation System, 1993 Newport Catalog. The Newport Corporation: 18235 Mt. Baldy Circle, PO Box 8020, Fountain Valley, CA 92728-8020.

[81] Van De Vegte, John, *Feedback Control Systems*. Englewood Cliffs, NJ: Prentice-Hall, Inc., 1990, pp. 377-382.

[82] Watters, B. G., Coleman, R. B., Duckworth, G. L., and Berkman, E. F., "A Perspective on Active Machinery Isolation," *Proceedings of the 27th Conference on Decision and Control*, Austin TX., 1989.

[83] Wie, B., and Byun, K-W, "New Generalized Structural Filtering Concept for Active Vibration Control Synthesis," *Journal of Guidance*, Vol. 12, no. 2, March-April 1989, pp. 147-154.

[84] Wong, E., Rathbun, D., and Smith, K., "A Pointing System Design Concept for Space Station Attached Payloads," *AIAA Guidance, Navigation and Control Conference*, Boston, Aug. 1989, pp. 759-769.

Appendix A

Finite Element Model Frequencies

Table A.1 lists the truss modal frequencies below 100 Hz as predicted by a finite element model [7]. The frequencies were found to agree with those measured in a modal test to within 2% up to 150 Hz. The model uses one beam element per strut with axial strut stiffness based on component tests. Plate elements were used to model the siderostat plates and fourth vertex assembly.

Table A.1: Frequencies of finite element model (inter5) below 100 Hz.

mode no.	freq. (Hz)	mode no.	freq. (Hz)
1	0.30	18	57.51
2	0.30	19	60.03
3	0.42	20	63.34
4	1.95	21	63.86
5	2.31	22	65.72
6	2.46	23	68.69
7	24.89	24	72.09
8	26.32	25	74.27
9	28.06	26	76.79
10	29.68	27	80.29
11	33.96	28	86.72
12	36.23	29	89.57
13	36.36	30	90.76
14	38.00	31	94.94
15	43.87	32	97.43
16	54.02	33	98.48
17	56.02	34	99.75

Appendix B

Testbed Performance Metric Summary

Table B.1 lists the measured absolute and differential performance metric measurements made for a series of open and closed loop truss configurations in this thesis. The laser measurements were recorded at a sample rate of 4100 Hz and read from the screen of the Tektronix Fourier analyzer for the frequency range of 10 to 500 Hz.

Table B.1: Interferometer performance metric summary.

Truss State	Pathlength Error (nm RMS) 10 - 500 Hz					
	Absolute			Differential		
	A	B	C	A-B	B-C	C-A
1. Original Hardmount	465	368	518	516	378	676
2. New Hardmount	312	394	487	282	286	331
3. Softmount (SM)	291	272	278	241	260	214
4. SM Prior to CL Laser Tests	283	271	248	210	228	190
5. SM with D-Struts	235	215	201	161	165	164
6. SM with 3 CL Lasers (no D)	73	72	52	80	66	77
7. SM with 3 CL Lasers (+ D)	59	67	42	60	61	55

Appendix C

Accelerometer Noise Autospectra

Two accelerometers of each type were mounted back to back and were suspended on a 1 meter cable inside a plastic bag to reduce air currents. Signals were scaled by individual sensor calibration, and their sum was recorded an averaged autospectrum. One-half of the averaged autospectrum is plotted below. Data for a new, low mass (3 g), 500 Hz bandwidth Kistler accelerometer are also shown.

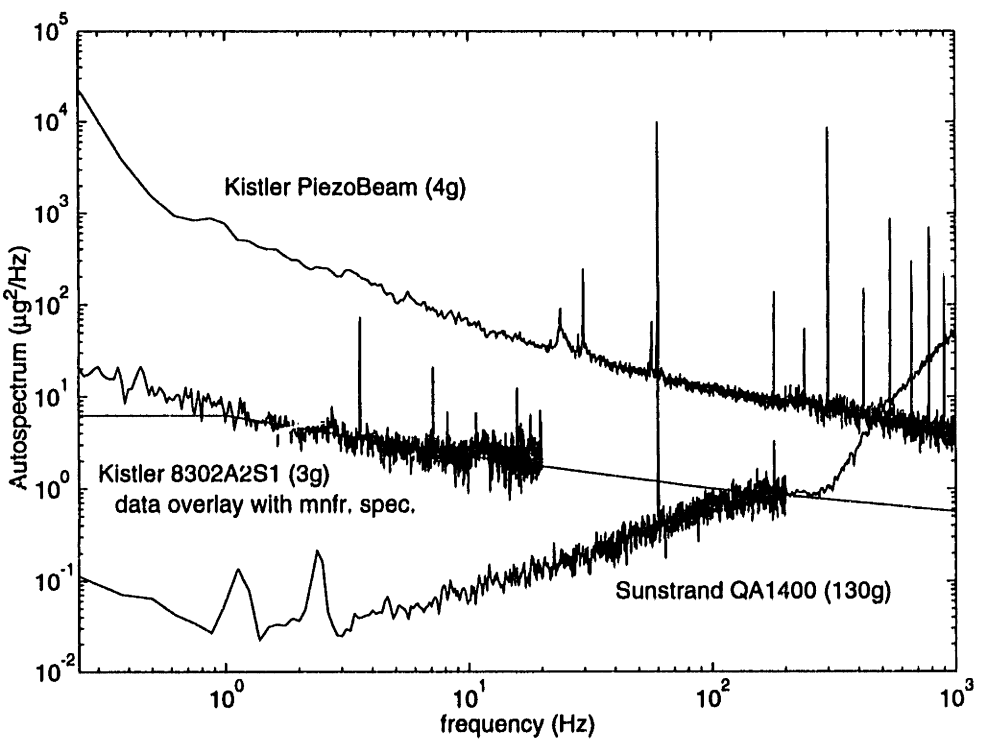

Figure C.1: Measured noise autospectra for three accelerometer models.

Appendix D

Transfer Functions to Laser Outputs

D.1 Transfer Function Data

Figure D.1 is a plot of the 3×3 transfer function matrix of the three hardmount isolators mounted to the truss structure. The input voltage V to each mount directed the mirror along the individual laser lines of sight, and the outputs u are the laser outputs. The transfer function matrix equation is given by Eq. 5.3. The softmount laser transfer functions are plotted in Figure D.2.

D.2 Diagonal Dominance of Transfer Function Matrix

Figures D.3 and D.4 are plots of the hardmount and softmount diagonal dominance ratio $d_i(s)$ defined by Eq. 5.6 in Chapter 5. The apparent jump in coupling above 500 Hz is due to noise in the data caused by a change in frequency windowing during the data collection.

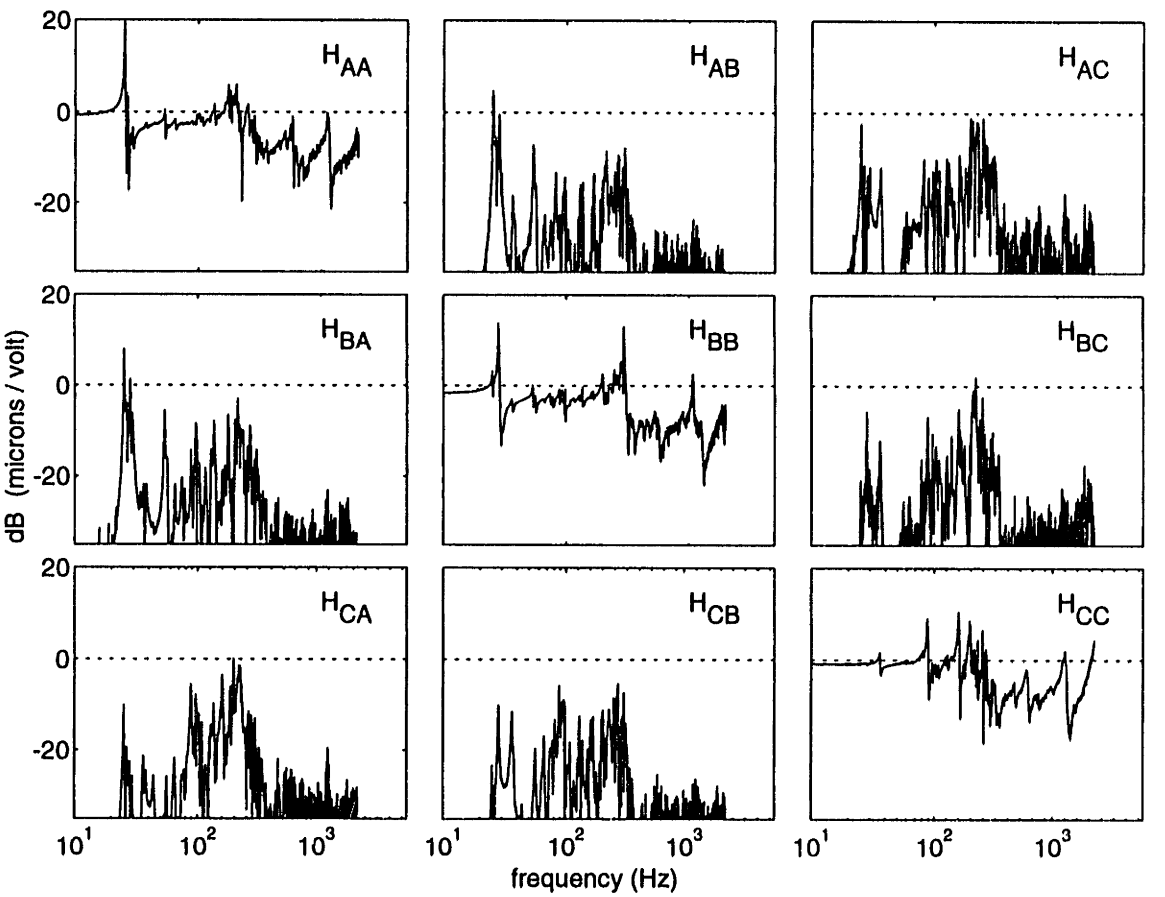

Figure D.1: Hardmount laser transfer function matrix for 3 mirrors actuated along lines of sight. Coupling with base flexible modes is strong both within the diagona transfer functions, as well as in the off-diagonal functions.

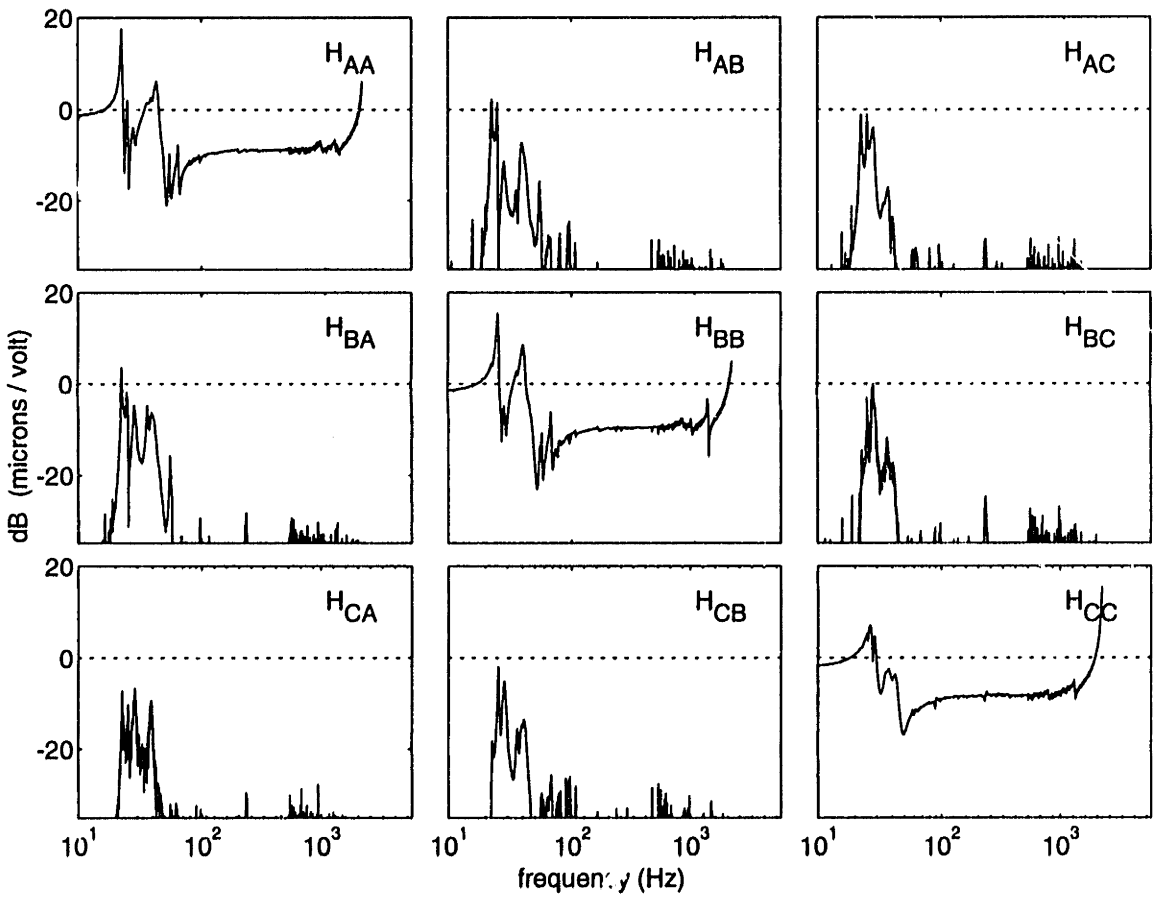

Figure D.2: Softmount laser transfer function matrix for 3 mirrors actuated along lines of sight. Decoupling is improved above 100 Hz in each of the diagonal functions, and off-diagonal coupling is attenuated.

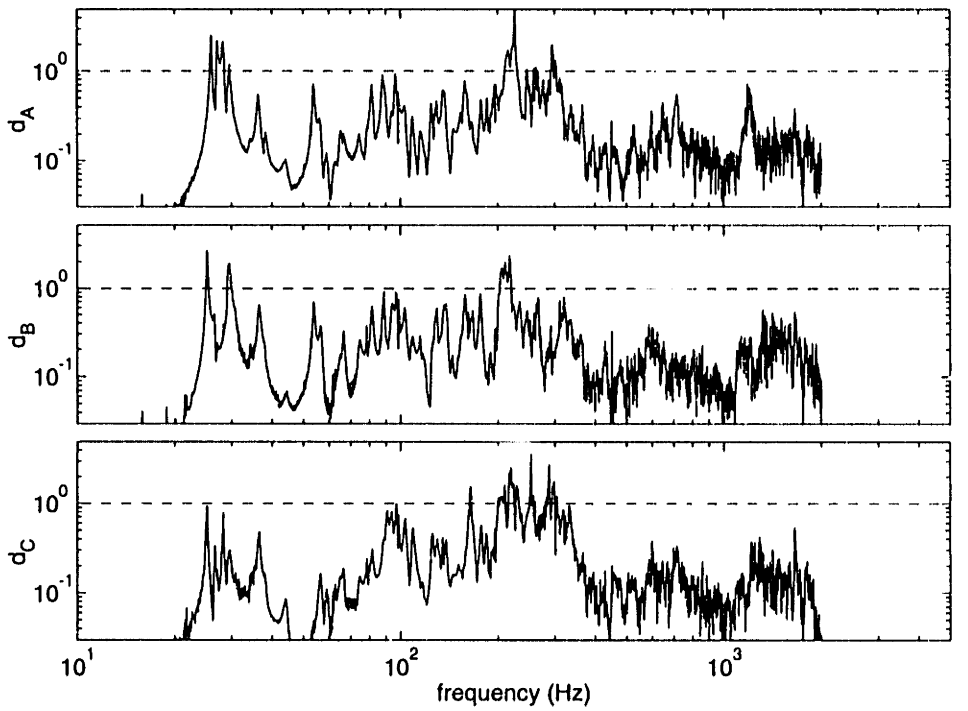

Figure D.3: Diagonal dominance ratios of the hardware plant transfer function matrix G_h, for hardmount isolators (laser output) on the testbed.

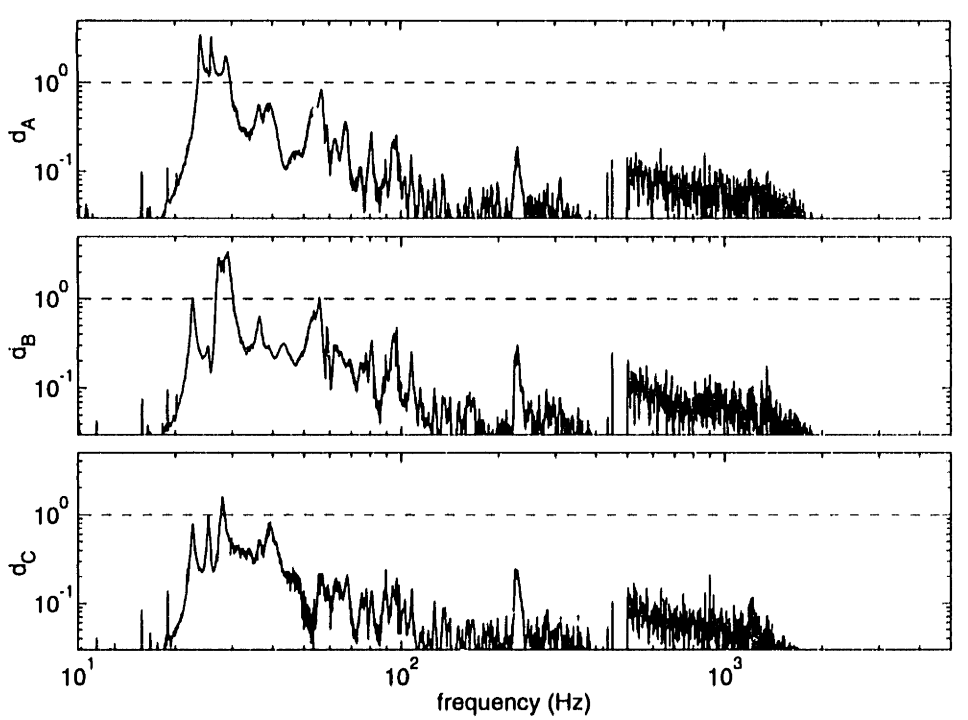

Figure D.4: Diagonal dominance ratios for softmount isolator (laser output) on testbed, showing improvement due to reaction mass. Frequency range near 30 Hz is not diagonally dominant.

Appendix E

Documentation of Pathlength Control Design

Documentation for laser feedback design for mirror B is presented below. The presentation and terminology follow Section 6.5 (acceleration feedback).

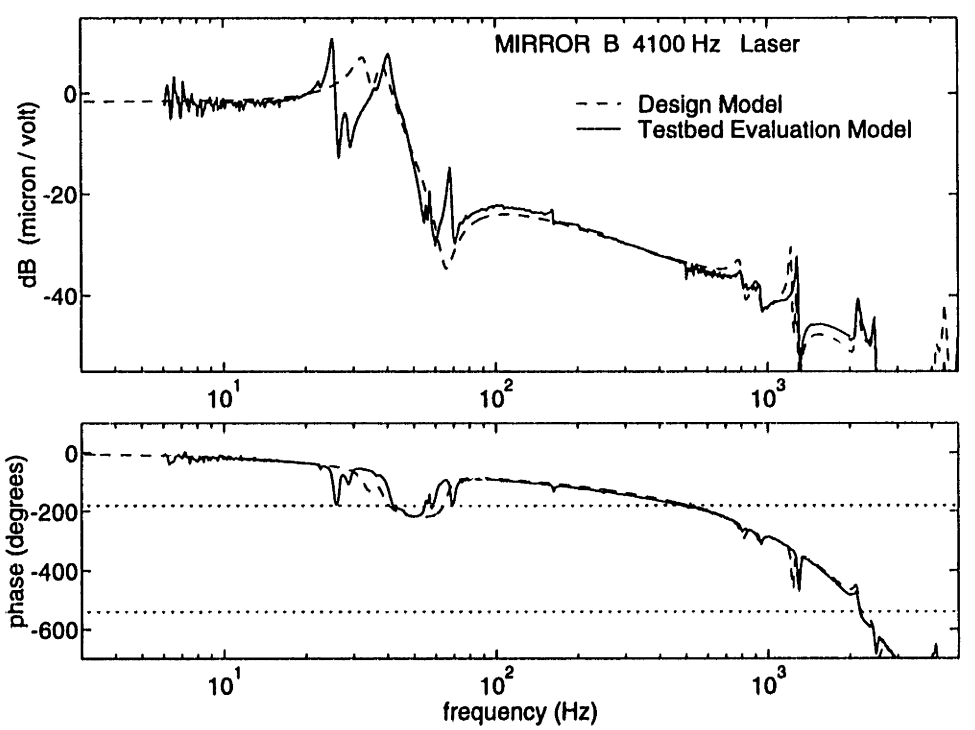

Figure E.1: Mirror B design model G_D (based on acceleration curve fit) compared to evaluation model G_E based on testbed measurement. Close agreement between laser and accelerometer output is shown in Section 5.4.2.

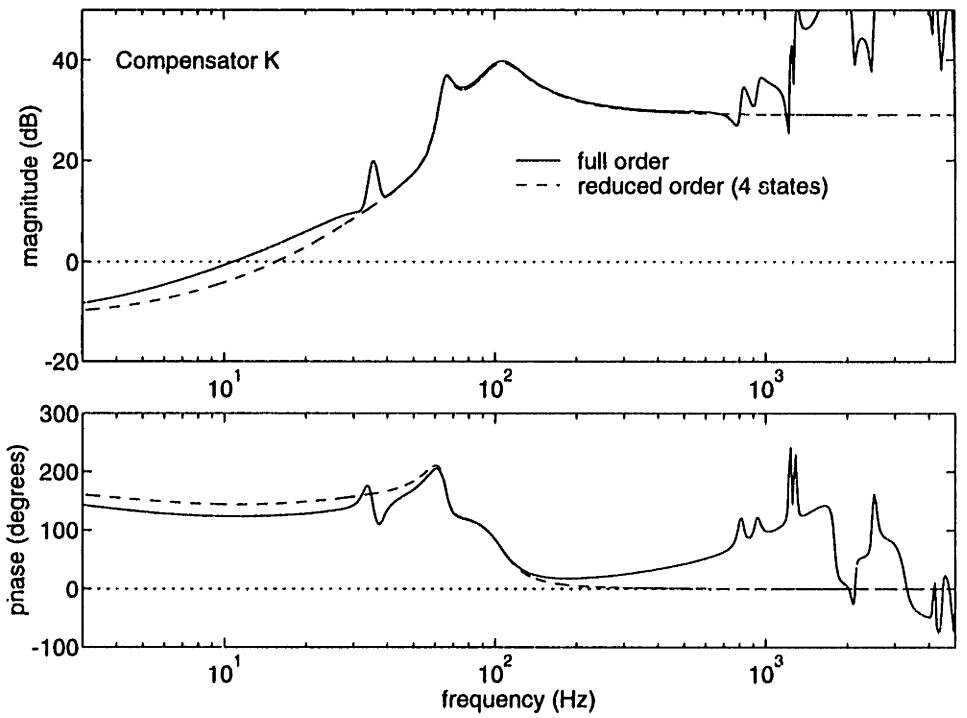

Figure E.2: Compensator K (LB1D) designed for real time computer implementation. Comparison of full order and reduced order (4 state) compensator.

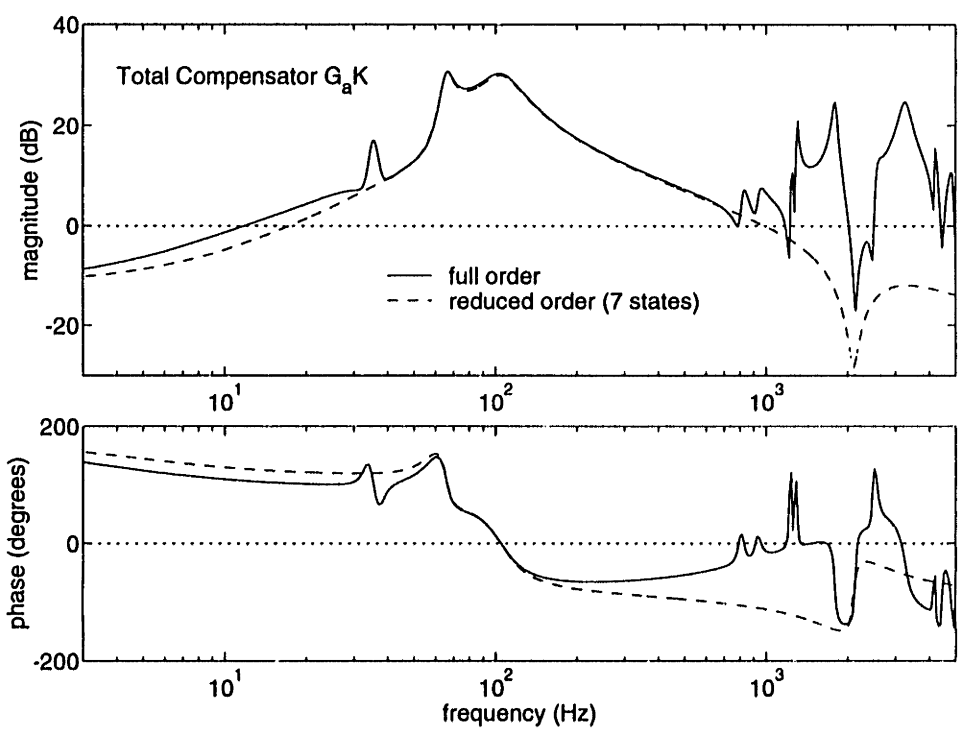

Figure E.3: Total compensator G_aK, which includes 3 analog states (1 real pole at 40 Hz, and 2.1 kHz notch).

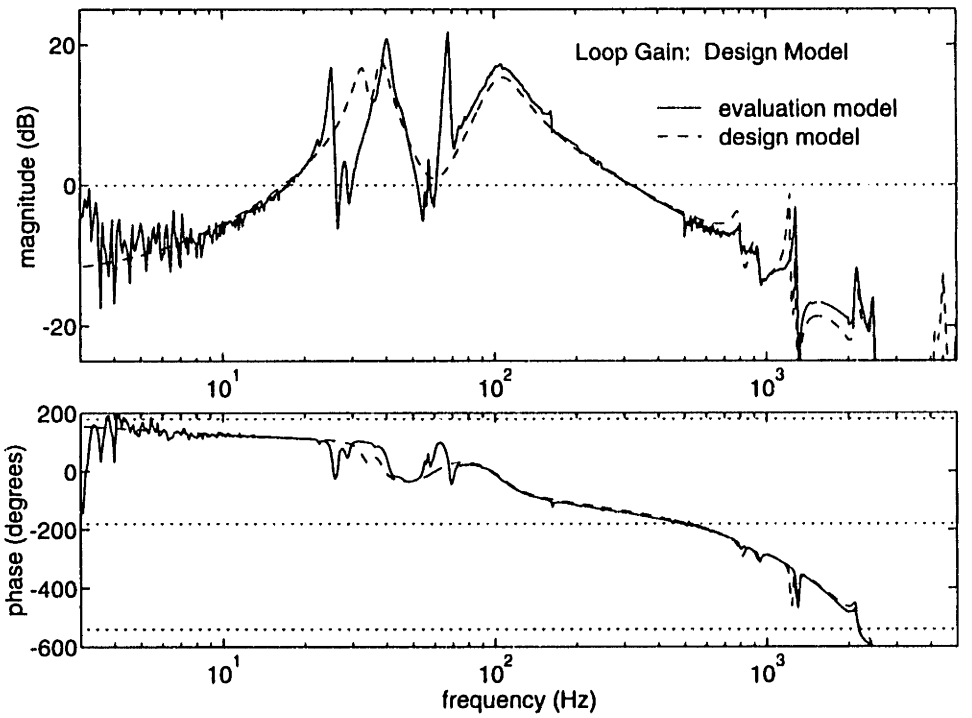

Figure E.4: Loop gain for pathlength control. Design model G_D is compared to the evaluation model G_E. Note that 1.2 kHz model is phase stabilized. Design model is based on rigid block accelerometer tests.

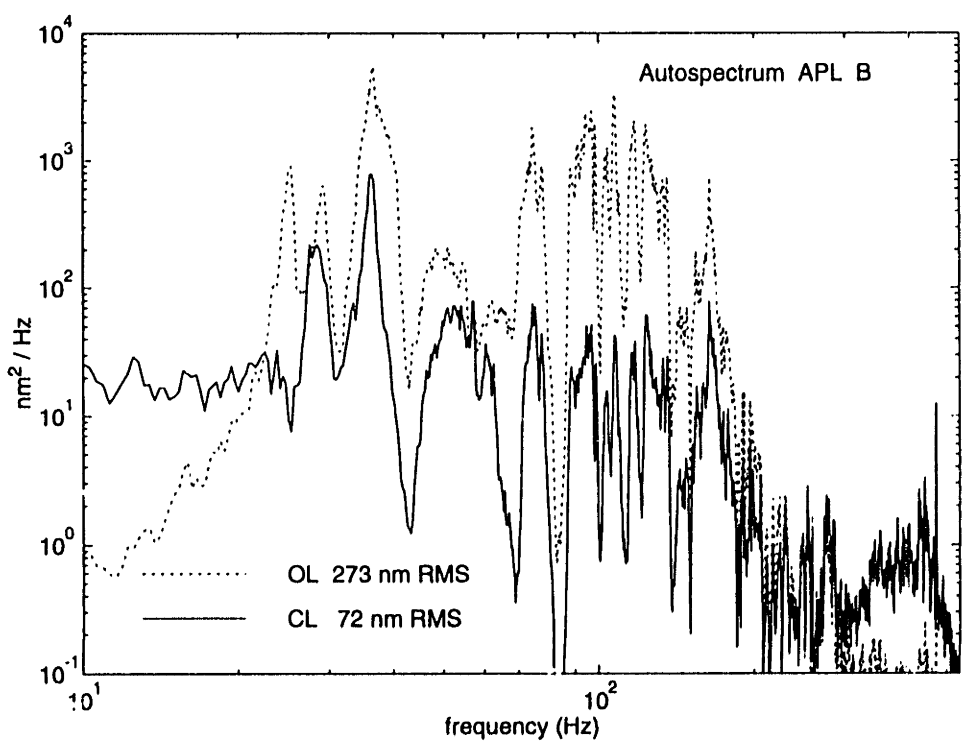

Figure E.5: Open and closed loop measurement of absolute pathlength leg B, for compensator LB1D.

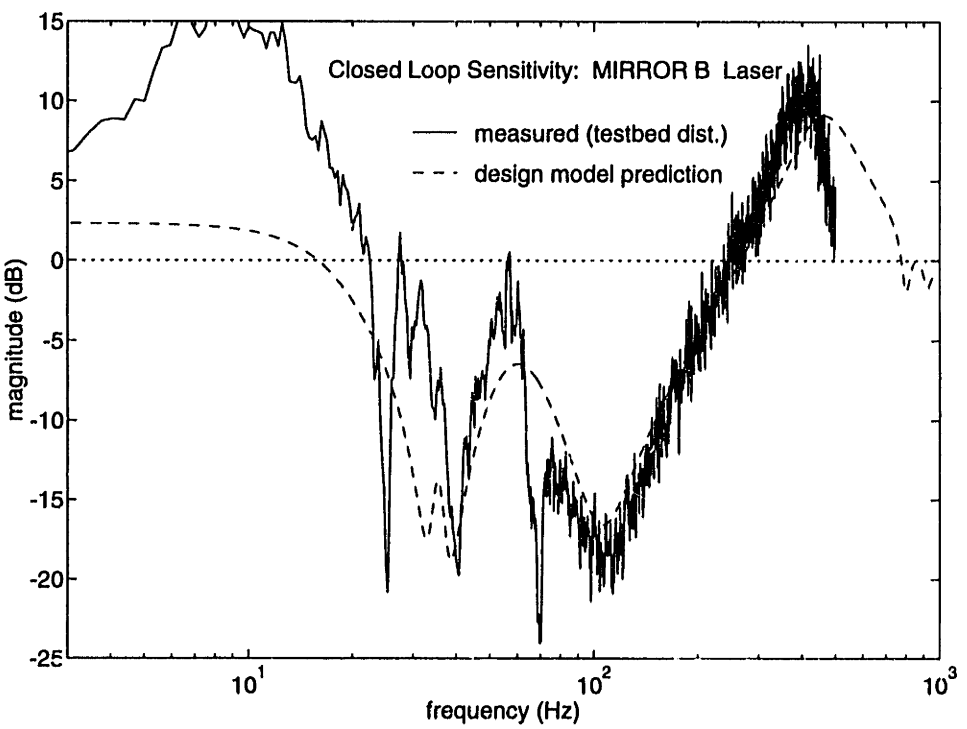

Figure E.6: Closed loop sensitivity for mirror B, absolute pathlength feedback. Comparison of measured and prediction based on design model G_D. Base flexibility reduces performance below 60 Hz, but does not affect high frequency crossover margins. Large sensitivity in 10 Hz region is due to extremely low disturbance level in this range.

Appendix F

Combination of D-Struts and Pathlength Control

The maximum performance metric improvement was achieved using both passive damping and 3 laser feedback controllers. Five D-struts were placed in the truss in order to maximize performance metric improvement in the differential pathlengths for frequencies below 80 Hz. The placement was based on the finite element model and a model of the uncertainty in the structural dynamics [5]. The laser pathlength controllers described in Section 6.6 and Appendix E, designed originally for the undamped truss, were re-implemented on the testbed without change. The damping reduced the dB performance improvement of the active control by up to 10 percent. Figure F.1 illustrates the performance improvement due solely to the D-struts, and Figure F.2 documents the further improvement obtained by simultaneously closing the three independent pathlength controllers. Performance in the laser loops was 0 - 1 dB lower with the D-struts in the truss, since the D-struts limit the dynamic response of the truss at the structural modes.

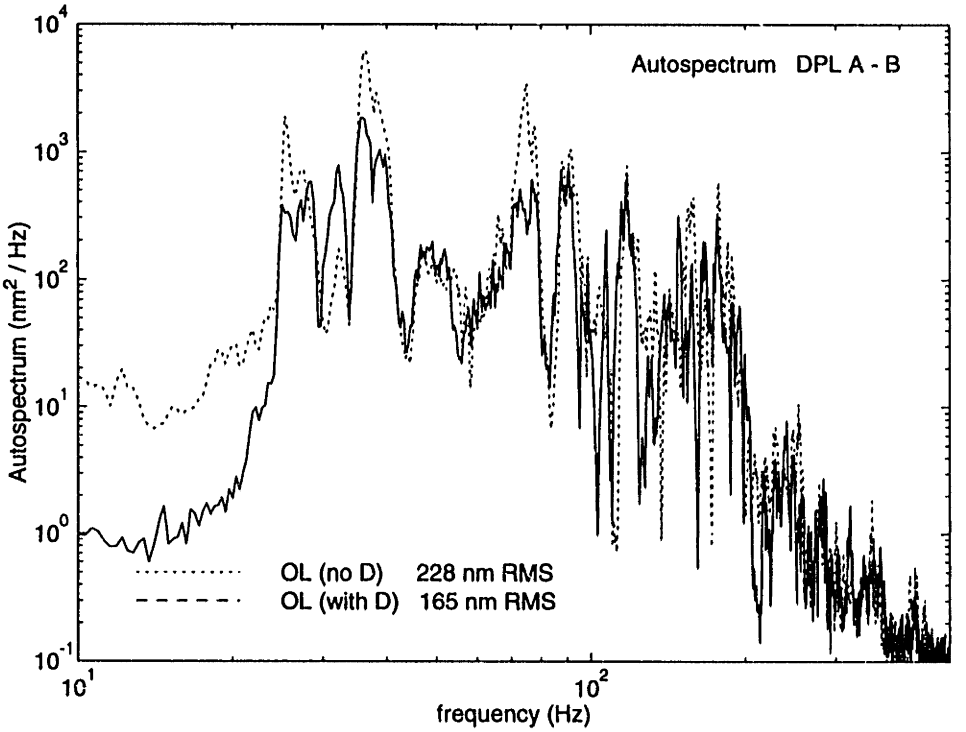

Figure F.1: Differential pathlength improvement due to the addition of 5 D-struts to the structure, placed for maximum energy dissipation in 20 - 80 Hz frequency range.

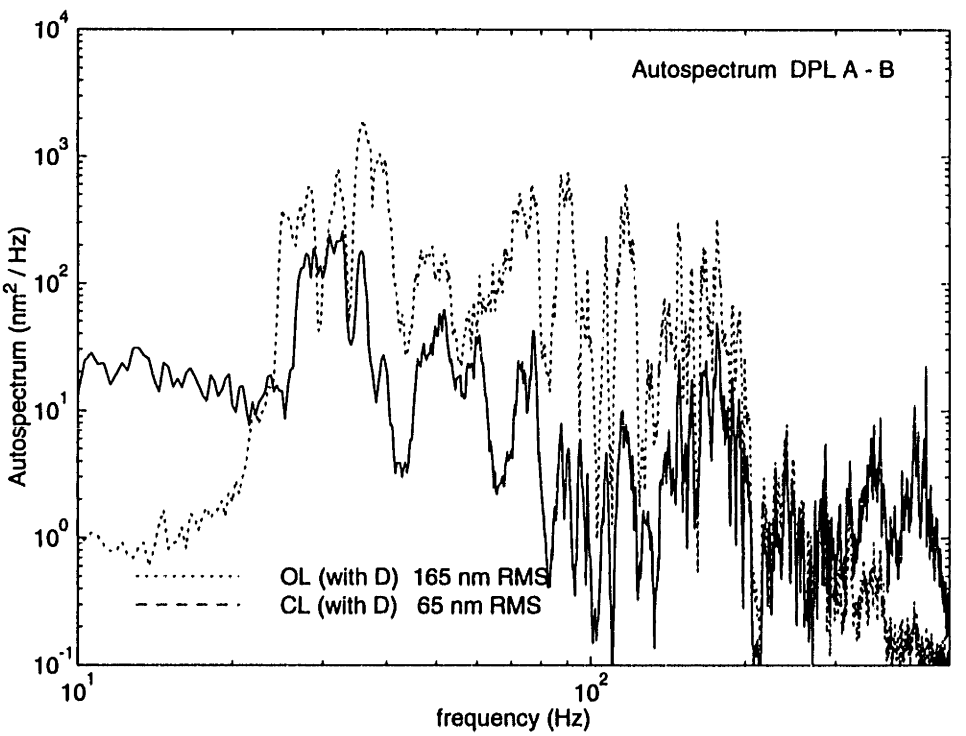

Figure F.2: Further improvement in DPL A - B obtained by simultaneous control of the three absolute pathlengths. Other pathlengths show similar improvement.